12-2016

# Hydrodynamics of swimming microorganisms in complex fluids

Gaojin Li
*Purdue University*

*Graduate School Form*
*30 Updated 12/26/2015*

**PURDUE UNIVERSITY**
**GRADUATE SCHOOL**
**Thesis/Dissertation Acceptance**

This is to certify that the thesis/dissertation prepared

By Gaojin Li

Entitled

HYDRODYNAMICS OF SWIMMING MICROORGANISMS IN COMPLEX FLUIDS

For the degree of Doctor of Philosophy

Is approved by the final examining committee:

| | |
|---|---|
| Arezoo<br>Chair | Ardekani |
| Pavlos | Vlachos |
| Steve | Wereley |
| John | Patterson |

To the best of my knowledge and as understood by the student in the Thesis/Dissertation Agreement, Publication Delay, and Certification Disclaimer (Graduate School Form 32), this thesis/dissertation adheres to the provisions of Purdue University's "Policy of Integrity in Research" and the use of copyright material.

Approved by Major Professor(s): Arezoo M. Ardekani

Approved by: Jay P. Gore 12/5/2016

Head of the Departmental Graduate Program Date

# HYDRODYNAMICS OF SWIMMING MICROORGANISMS IN COMPLEX FLUIDS

A Dissertation

Submitted to the Faculty

of

Purdue University

by

Gaojin Li

In Partial Fulfillment of the

Requirements for the Degree

of

Doctor of Philosophy

December 2016

Purdue University

West Lafayette, Indiana

# ACKNOWLEDGMENTS

First of all, I would like to express my thanks to my advisor Professor Arezoo Ardekani. It has been a great honor to be her Ph.D. student. She not only guided me through my PhD research and carefully reviewed all my writings, but also gave me freedom and support in my projects. I appreciate all her contributions, time, inspiration, and funding to make my Ph.D. experience stimulating and productive. During the past few years, I have been subconsciously influenced by her research passion, professionalism, and dedication, which were great asset to me. Her support is indispensable for me to complete the Ph.D. study.

I would also like to thank my committee members, Professor Steven Wereley, Professor Pavlos Vlachos, and Professor John Patterson for their time and helpful comments on my work. I thank all the professors at University of Notre Dame and Purdue University. Particularly, I want to thank Professor Sadegh Dabiri, Professor Gretar Tryggvason, and Professor Carl Wassgren for all their help in my research and teaching. I also thank Professor Paulo Arratia, Professor Morozov Alexander, Professor Saverio Spagnolie, Professor Lisa Fauci, and Professor Donald Koch for the helpful discussions. All students in our group are appreciated, in particular Alireza Karimi, Amin Doostmohammadi, Shiyan Wang, and Yuchen Zhang. I also want to thank my fellow graduate students and friends at University of Notre Dame and Purdue University.

I gratefully acknowledge the funding sources that made my Ph.D. work possible, specially to the National Science Foundation. I also appreciate the support from Center for Research Computing (CRC) at University of Notre Dame and Information Technology at Purdue (ITaP) at Purdue University.

Finally, I would like to give my thanks to my family for all their love and encouragement. Special thanks to my wife Wenjun Li and my parents in law whose love and support is invaluable to me.

TABLE OF CONTENTS

Page

# LIST OF FIGURES

# ABSTRACT

Li, Gaojin PhD, Purdue University, December 2016. Hydrodynamics of Swimming Microorganisms in Complex Fluids. Major Professor: Arezoo M. Ardekani, School of Mechanical Engineering.

Swimming motion of microorganisms, such as spermatozoa, plankton, algae and bacteria, etc., ubiquitously occurs in nature. It affects many biological processes, including reproduction, infection and the marine life ecosystem. The hydrodynamic effects are important in microorganism swimming, their nutrient uptake, fertilization, collective motions and formation of colonies. In nature, microorganisms have evolved to use various fascinating ways for locomotion and transport. Different designs are also developed for the locomotion of artificial nano- and microswimmers. In this study, we use several different computational models to investigate the behavior of microswimmers.

Microorganisms typically swim in the low Reynolds number regime, where inertia is negligible. They interact with each other, surfaces and external flow field. Microorganisms often swim in complex fluids, exhibiting non-Newtonian behavior, including viscoelasticity and shear-thinning viscosity. These biological materials contain network of glycoprotein fibers and gel-like polymers. Therefore on the scale of microorganisms, their fluid environments are heterogeneous rather than homogenous. In this study, we develop a computational platform to investigate swimming motion of a single and multiple microorganism(s) in the bulk fluid and near surfaces in complex fluids. We also investigate the role of fluid rheological properties and flow field on the migration of inert particles in a channel flow of viscoelastic fluids.

# 1. INTRODUCTION

Microorganisms are ubiquitous and vital in our life. In a milliliter of fresh water, there are typically one million bacterial cells. The number of the bacterial cells in the human body is approximately ten times the human cells. Bacteria are crucial in nutrients recycling in many ecosystems, such as the nitrogen fixation and putrefaction. The probiotic bacterial species in the normal human gut flora are beneficial in vitamins synthesis and converting sugars to lactic acid. Many bacteria are pathogenic and cause infectious diseases, including anthrax, cholera, syphilis, leprosy, etc. In marine ecosystems, microorganisms, include bacteria, algae, protozoa, etc, provide a crucial food source to large aquatic organisms. Plankton play an important role in the carbon cycle and oxygen production: about $50 \sim 85\%$ of the world's oxygen is estimated to be produced through phytoplankton photosynthesis.

Due to the small size of microorganisms, the locomotion at the microscale is dominated by viscous forces over the inertial forces. The physics that governs the microscale locomotion at low Reynolds numbers is very different from the macroscopic organisms at high Reynolds numbers. The Reynolds number is defined as $Re = \rho UL/\mu$, where $\rho$ is the fluid density, $\mu$ is the dynamic viscosity of the fluid, and $U$ and $L$ are the characteristic velocity and length scales of the flow, respectively. At low Reynolds number, the locomotion strategies employed by larger organisms, such as fish, birds or insects, are ineffective due to Purcell's scallop theorem [1]. This theorem states that if a low-Reynolds number swimmer in a Newtonian fluid displays a geometrically reciprocal motion, which means the sequence of its shape deformation is identical when viewed in a reversed time, then its net displacement must be zero independent of its deformation rate. In nature, microorganisms have evolved various propulsion strategies which are not invariant under time-reversal and thus they can propel themselves. For example, spermatozoa often have a single flagellum under-

going a nearly-planar beating motion; bacteria typically swim using rotating helical flagella; the green algae *Chlamydomonas* propels by beating its two anterior flagella in a breaststroke motion; the unicellular *Paramecium* and colonial algae *Volvox* use thousands of cilia on their surface for locomotion. Inner organs of superior animals widely use metachronal waves of cilia for the transport of biological fluids. In the far-field, the leading order effects of a freely swimming microorganism in a bulk fluid is equivalent to a force dipole. Depending on the sign of the force dipole, two different swimming types can be modeled: pusher, which propels themselves forward by pushing fluid behind their body such as bacteria and spermatozoa, and puller, which generates thrust by pulling fluid in front of their body such as *Chlamydomonas*. Overview of different propulsion mechanisms used by microorganisms can be found in [2–4].

The swimming motion of a low Reynolds number swimmer in an unbounded Newtonian fluid has been investigated. In 1951, Taylor analyzed the swimming motion of an infinitely long waving sheet of small amplitude [5], which is analogous to the beating flagellum of spermatozoa in two dimensions. The profile of the waving sheet is prescribed as $h = b\sin(kx - \omega t)$, where the propagation of the wave is along the $x$ direction, $k$ is the wave number, $\omega$ is the frequency, and $b$ is the amplitude which is small compared with the wavelength $2\pi/k$. Using a perturbation analysis, Taylor showed that the sheet moves in the opposite direction of the traveling wave and its swimming speed is $U = -\omega k b^2/2$. Taylor later considered a more realistic model of an infinitely long flagellum with a cylindrical cross section. In the limit of zero flagellum thickness, the swimming velocity is found to have the same form as the planar sheet [6]. The model has also been extended to a flagellum with three-dimensional deformations, such as a helical wave [7] as well as finite size swimmers. In 1960s, Lighthill [8] and Blake [9,10] developed an envelope model, where the swimmer surface is covered by a carpet of beating cilia under propagating waves, called squirmer, to model the swimming motion of ciliates such as *Paramecium* and *Volvox*. For a waving sheet of large amplitude, a resistive force theory was developed by Gray and Hancock [11]

and Lighthill [12]. This theory disregard the hydrodynamic interactions between the filament segments, and relates the filament velocity to the local resistive force on it via resistance coefficients. This method has been widely applied in studies of flagellar propulsion [13–17]. However, this approach is quantitatively correct when $1/\ln(L/a) \ll 1$, where $L$ and $a$ are the length and thickness of the flagellum, and may lead to large errors [18,19]. A more accurate approach, the slender body theory, was developed by Hancock [20], Batchelor [21]and Ligthhill [12,22] and was widely used by other researchers [18,23–26]. This method accounts for the nonlocal effects by replacing the filament with an appropriately determined distribution of singularities and the accuracy of the results is greatly improved [27]. If inertial effects are considered while the flow separation is disregarded, the swimming speed of a waving sheet becomes $U = -\omega k b^2[1 + F(Re)^{-1}]/4$, where $F(Re) = [1 + (1 + Re^2)^{1/2}]^{1/2}/2$, i.e. the speed monotonically decreases with the Reynolds number to half of its value at $Re = 0$ [28,29].

Note that the Taylor's swimming sheet and the squirmer model assume a prescribed kinematics, while in nature, the deformation of the swimmer is determined by the interplay between its internal actuation and the external forces. Many motile bacteria swim using a boundary actuation of their flagellum, in which the relative stiff flagellum is driven by a rotary motor. Studies on the propulsion of a rotating helix has been conducted using slender body theory [18,30] and finite element method simulations [31,32]. Experiments show that the flagellar motor has a nonlinear relation between the torque and rotating speed [33]: at low rotating speeds, the torque generated by the motor is approximately constant; at higher speeds, it decreases almost linearly with the rotating speed until becomes zero at about 300 Hz. This property is found to play an important role for the bacterium to achieve an enhanced swimming speed in a polymeric solution [34]. The other type of flagellum actuation is the distributed actuation, such as eukaryotic flagella, in which almost the entire filament is active driven by the molecular motors. The bending of the flagellum is produced by the relative sliding motion between the neighboring micro-

tubules inside the flagellum driven by dynein motors [35]. Camalet and Jülicher have developed an internally-driven flagellum model driven by a sliding force distribution to consider the interplay between the internally driven force, the elastic deformation of the flagellum and the hydrodynamic forces [36, 37]. The coordination of the dynein motors is suggested to be related to the mechanics of the motors and their interaction instead of chemical signaling [38]. The model of a swimming flagellum with a load-dependent motor detachment rate is found to be consistent with the observations [39]. In this dissertation, several different theoretical models, including squirmer model [8–10, 40], undulatory swimming sheet with prescribed kinematics [5] and internally driven mechanism [37], and self-propelled rod model [41] are used to describe and understand the swimming motion of microswimmers in Newtonian and complex fluids.

Microorganisms often swim in a complex fluid and interact with different environments, including wall surfaces and interfaces, non-Newtonian fluids, small particles suspended in the fluid media, external flow and turbulence, etc. Furthermore, many micro-scale swimmers, such as spermatozoa, often swim in high concentrations and interact with each other. Swimming motion and aggregation of bacteria near a surface and biofilm formation have been extensively studied for many years for its importance in many health and environmental problems [42]. Biofilms may be formed on almost all types of surface and are ubiquitous in natural and industrial environments. They cause enormous loss of life and economy around the world due to human and animal infections, medical implants contamination, industrial equipment damage, pipe clogging, and energy losses. Biofilms can also be beneficial in waste treatment and remediation, waste water filtration, spilled oil clean-up, etc. Biofilm, which are mainly made of extracellular polymeric substances of polysaccharides and proteins, often show both elasticity and shear-thinning behavior [43, 44]. At a micro-scale, biofilms generate a highly heterogeneous and porous fluid environment for the microorganisms [45, 46]. Non-Newtonian behavior of the fluid media greatly affects the swimming motion of the microorganisms and their interactions with surfaces, exter-

nal flow and other microorganisms, which are the focus of this thesis. The following sections will discuss these effects based on several different swimming models.

In chapter 2, we focus on the near-wall swimming motion of ciliates in a Newtonian fluid using a squirmer model. For a single squirmer near a wall, depending on the swimming mechanism, three different modes are distinguished: (a) the squirmer escaping from the wall, (b) the squirmer swimming along the wall at a constant distance and orientation angle, and (c) the squirmer swimming near the wall in a periodic trajectory. For a suspension of squirmers, near-wall accumulation is observed, which is consistent with previous experiments [47, 48]. Furthermore, we find that in the near-wall region, pullers repel each other, while pushers are attracted to each other and form clusters. This work has been published in Physical Review E, 2014 [49].

In chapter 3, we numerically study the effect of solid boundaries on the swimming behavior of a squirmer in a viscoelastic fluid. A Giesekus constitutive equation is utilized to describe both viscoelasticity and shear-thinning behavior of the background fluid. We found that the viscoelasticity strongly affects the near-wall motion of a squirmer by generating an opposing polymeric torque which impedes the rotation of the swimmer away from the wall. The shear-thinning effect is found to weaken the solvent stress and therefore, increases the swimmer-wall contact time. For a puller swimmer, the polymer stretching mainly occurs around its lateral sides, leading to reduced elastic resistance against its locomotion. The neutral and puller swimmers eventually escape the wall attraction effect due to a releasing force generated by the Newtonian viscous stress. In contrast, the pusher is found to be perpetually trapped near the wall as a result of the formation of a highly stretched region behind its body. This work has been published as an invited article in Rheologica Acta, 2014 special early career issue on novel trends in rheology [50].

In chapter 4, we investigate the migration of an inert spherical particle in a pressure-driven channel flow of viscoelastic fluids. The effects of inertia, elasticity, shear-thinning, secondary flows, and the block ratio are considered by conducting fully resolved direct numerical simulations in a wide range of parameters. We find

that elastic effects drive the particle towards the channel centerline. The equilibrium position depends on the interplay between the elastic and inertial effects. Particle focusing at the centerline occurs in flows of strong elasticity and weak inertia. Both shear-thinning effects and secondary flows tend to move the particle close to the wall. The effect is more pronounced as inertia and elasticity effects increase. A scaling analysis is used to explain these different effects. Besides the particle migration, the particle-induced fluid transport and transient motion of the particle during the flow start-up are also considered. The inertial effect, shear-thinning behaviour, and secondary flows, are found to enhance the effective fluid transport normal to the flow direction. Due to the oscillation in fluid velocity and strong normal stress difference during the flow start-up, the particle has a larger transient migration velocity. This work has been published in Journal of Fluid Mechanics, 2015 [51].

In chapter 5, we compare the effects of viscoelasticity and shear-thinning viscosity on an undulatory swimmer in an unbounded domain. In a pure viscoelastic fluid, the swimming speed and power consumption always decrease with increasing viscoelasticity, independent of flagellum amplitude. In an inelastic shear-thinning fluid, the shear Carreau number Cr, related to the typical shear rate, is found to mostly affect the swimming behavior. Therefore, both the beating frequency and amplitude are important. Our simulation results recover the analytical results for small amplitude flagellum [52], where speed is not affected and power is reduced. For a large amplitude flagellum, velocity enhancement and power reduction are observed. The swimming boost in a shear-thinning fluid occurs even for an infinitely long flagellum because it swims in a lower-viscosity fluid layer surrounded by a high-viscosity fluid. Two competing effects determine the speed enhancement: the viscosity and width of the inner layer. Increasing Cr reduces the viscosity of the inner layer, but enhances its width. Therefore, there exists a maximum swimming speed, dependent on the oscillation amplitude as well as the fluid rheological properties. The power consumption, on the other hand, follows a universal scaling law. Same mechanism is also found

for a swimmer in a heterogeneous fluid environment with particle suspensions. This work has been published in the Journal of Fluid Mechanics, Rapids, 2015 [53].

In chapter 6, we investigate the near-wall motion of an undulatory swimmer in both Newtonian and non-Newtonian fluids. Our results show that the undulatory swimmer have three types of swimming mode depending on its undulatory amplitude. The swimmer can be strongly attracted to the wall, swimming in close proximity of the wall, be weakly attracted to the wall with a relatively large distance away from the wall, or escape from the wall. The scattering angle of the swimmer and its hydrodynamic interaction with the wall are important for describing the near-wall swimming motion. The shear-thinning viscosity is found to increase the swimming speed and to slightly enhance the wall attraction by reducing the swimmer's scattering angle. The fluid elasticity, however, leads to strong attraction of swimmer's head towards the wall, reducing the swimming speed. The combined shear-thinning effect and fluid elasticity results in an enhanced swimming speed along the wall. This work has been submitted to the European Journal of Computational Mechanics.

In chapter 7, we investigate the elastohydrodynamics of a self-driven undulatory swimmer with a sliding force distribution [37, 54]. We show that the sliding force can capture the target curvature of the flagellum and the previous numerical results [55] can be recovered when neglecting the tangential contribution of the sliding force. Based on this model, we numerically investigate the swimming motion of an elastic kicker and burrower. Different swimming performance is observed for the swimmers with a fixed target curvature or a fixed sliding force. A stiff flagellum behaves similar to a flagellum with a prescribed kinematics. The dynamics of a soft flagellum, which is the case for many real microorganisms, is determined by the interplay between the flagellum elastic deformation and viscous forces. Our results also show that there exists an optimized distribution of sliding force that maximizes the swimming performance of a soft swimmer.

In chapter 8, we study the collective motion of a suspension of rodlike microswimmers in a two-dimensional film of viscoelastic fluid. We find that the fluid elasticity

has a small effect on a suspension of pullers, while it significantly affects the pushers. The attraction and orientational ordering of the pushers are enhanced in viscoelastic fluids. The induced polymer stresses break down the large-scale flow structures and suppress velocity fluctuations. In addition, the energy spectra and induced mixing in the suspension of pushers are greatly modified by fluid elasticity. This work has been published in Physical Review Letters, 2016 [56]. Finally, chapter 9 summarizes the thesis and recommends possible avenues for further research.

# 2. NEAR WALL MOTION OF MODEL CILIATE IN A NEWTONIAN FLUID[1]

## 2.1 Motivation and Previous Works

Biolocomotion near surfaces or in a confined environment is very important in many health and environmental problems [3, 57]. Such example include accumulation of bacteria near the surface and the biofilm formation which is closely related to many types of microbial infections [58], spermatozoa swimming in the female reproductive tract is another common example [59]. *H. pylori* colonizing the mucus layer covering the stomach [60], *B. burgdorferi* penetrating the connective tissues in skin [61, 62], and *C. elegans* swimming in the water-saturated soil [63]. As the first step to investigate these problems, microorganisms in a Newtonian fluid have been extensively studied. The presence of nearby boundaries affects various distinct aspects of microorganism locomotion, such as the changing in the swimming speed and energetic properties [64–66], the modification of the swimming trajectories [67] and the general attraction of organisms to surfaces and reorientation [47, 48, 68, 69]. The interactions between microorganisms can also be greatly affected by the presence of the wall, for example, pairs of *Volvox* show "waltz" or "minuet" motions when near a solid boundary [70].

The inertial effects are important for many of planktonic swimmers in marine environments, such as larvae and *Pleurobrachia*. Small organisms use inertia to change their swimming direction, attack a prey or escape from a predator [71, 72]. Wang and Ardekani [73, 74] analytically quantified the inertial effects by deriving the fundamental equation of motion for small organisms swimming in an unbounded quiescent fluid environment. Their results showed that the history force and added mass force

[1]This chapter has been reprinted (abstract/excerpt/figure) with permission from "Hydrodynamic interaction of microswimmers near a wall", by G. Li and A. M. Ardekani, in Physical Review E, 90(1): 013012, 2014 (DOI: 10.1103/PhysRevE.90.013010). Copyright (2014) by the American Physical Society.

are of the same order as the steady Stokes force for an unsteady swimmer such as *Paramecium* escaping from an aggression. For two nearby swimming organisms, the inertial effects cause two puller-type swimmers to attract to each other and swim in circular trajectories. The role of boundaries on the swimming of small organisms in a nonzero-Reynolds-number regime is of great importance. For example, the accumulation of larvae near the surface has a significant influence on the metamorphosis and survival of larvae [75].

The swimming dynamics of a single swimmer has been investigated based on various simplified swimmer models. Zargar et al. [76] used a three-sphere swimmer and analyzed its dynamics in the close proximity of a boundary. It is shown that the swimmer can either be attracted to or escape from the wall, depending on the initial angle and distance from the wall. The work of Or et al. [77] studied the dynamics of swimmers of rotating spheres attached by rigid rods. In their simulation, the interactions between the particles and the wall were approximated only considering the far-field hydrodynamic interactions. Their results show that the swimmer may have a marginally stable motion or a periodic motion depending on the arrangement of the spheres. Similar swimming dynamics was reported in the work of Crowdy and Or [78] for a two-dimensional treadmill swimmer model near a no-slip wall. The treadmill swimmer was also utilized to study the swimming dynamics near a wall with a gap. Stable equilibrium points for the swimmer near the gap, Hopf bifurcations, and periodic attracting states were observed [79]. The work of Dunstan et al. [80] modeled a bacterial cell by using two spheres of different radii at a constant distance. The effect of the flagella was modeled by imposing a force on the tail sphere as well as adding equal and opposite torques on the two spheres. Their results show three different swimming behaviors depending on the initial condition: swimming in circles in contact with the wall, swimming in circles at a finite distance from the wall and swimming away from the wall. Spagnolie and Lauga [81] provided a detailed comparison of the hydrodynamics of micro-swimmers near a boundary using far-field approximations and numerical solutions of the Stokes equation. They showed that

the far-field approximation is surprisingly accurate for spherical swimmers when the distance between the center of the swimmer and the wall is larger than its diameter. However, the fundamental singularities of the Stokes equation cannot accurately account for the near-field effects when the swimmer comes close to the boundary. Here in this work, Navier-Stokes equations are directly solved to capture the hydrodynamic interaction of a single swimmer and a suspension of swimmers near a wall in a small, but nonzero, Reynolds number regime.

However, microorganisms are usually observed in high concentrations, where the interaction between microorganisms are important and they often exhibit collective behaviors resulting in swarms and vortices of large scales [2]. Previous experiments show that a suspension of microorganisms results in the variation of fluid viscosity [82], increase in the short-time mass diffusion [83], and enhanced mixing [84]. Hydrodynamic interaction of spherical particles near a wall or between two walls in a zero-Reynolds-number regime has been extensively studied using multipole expansion method and Stokesian Dynamics [85–87]. The algorithm developed by Bhattacharya et al. accurately calculates the many-particle friction matrix by using spherical and Cartesian representation of Stokes flow to capture the interaction of the fluid with the particles and walls, respectively [87]. Based on the dumbbell swimmer model of two beads connected by a rigid rod, Underhill et al. [88] studied the diffusion and spatial correlation of swimmers as well as the correlations of stress and velocity [89]. Using the same model, Hernández-Ortiz et al. [90, 91] studied the dynamics of suspension of swimmers between two walls and found that the swimmers aggregate near the wall at low concentrations, while at high concentrations, this distribution is disrupted by large-scale coherent motions. The diffusion and spatial correlation of swimmers are also affected by the confined geometry. Their model treated the swimmers as point force dipoles and the swimmer-swimmer and swimmer-wall interactions are approximated using an excluded volume force, therefore the near-field hydrodynamic interactions are not accurately captured. Wensink and Löwen [92] studied the suspension of self-propelled colloidal rods in a channel using two-dimensional Brown-

ian dynamics simulation. Their results show that the aggregated self-propelled rods near the channel wall form "hedgehog"-shaped clusters with most of the rods pointing towards the wall.

Here we investigate the dynamics of a single and a collection of squirmer(s) near a no-slip wall in a low-Reynolds-number regime. By directly solving the Navier-Stokes equation, the inertial effects are included and the motion of small swimming organisms near a solid surface is accurately captured.

## 2.2 Squirmer Model

In this study, we adopt an axisymmetric model microswimmer with tangential velocity on its surface to characterize the swimming strategy of ciliated microorganisms, such as *Volvox* and *Paramecium*, near a solid wall. The so-called squirmer model, first proposed by Lighthill [8] and Blake [9], has been widely utilized in numerical investigations of biolocomotion in various environmental conditions (e.g. see [93–95]). The overall ciliary movement can be idealized as a continuous velocity distribution along the exterior surface of a self-propelled spheroid [96],

$$u_s(\theta) = \sum_{n=1}^{\infty} B_n V_n(\cos\ \theta), \tag{2.1}$$

where $\theta$ is the polar angle measured from the swimming direction, $B_n$ represents the magnitude of $n$th mode of squirming motion, and the function $V_n$ is defined as,

$$V_n(x) = \frac{2\sqrt{1-x^2}}{n(n+1)} \frac{d}{dx} P_n(x), \tag{2.2}$$

with $P_n(x)$ denoting the $n$th order Legendre polynomial. In a Newtonian fluid under Stokes flow conditions, the swimming speed of a squirmer in an unbounded domain is $U_0 = 2B_1/3$ [9]. Conforming with previous studies employing this approach, we assume $B_n = 0$ for $n > 2$. Hence, we can define the ratio of the second to the first squirming mode, $\beta = B_2/B_1$, to distinguish three types of swimming mechanisms: $\beta > 0$ corresponds to pullers generating thrust by pulling fluid in front of their body such as *Chlamydomonas nivalis*, $\beta < 0$ corresponds to pushers propelling forward

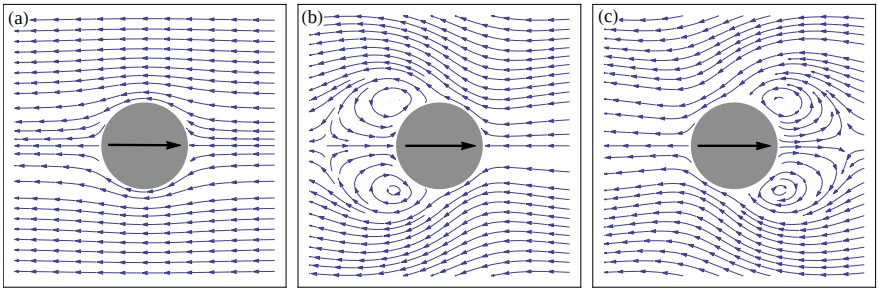


Figure 2.1. Flow streamlines around squirmers in the comoving frame of reference for (a) neutral squirmer, (b) puller, and (c) pusher. The black arrow indicates the swimming direction.

by pushing fluid behind their body such as *Escherichia coli*, and $\beta = 0$ corresponds to a neutral squirmer with net ciliary motion such as *Volvox*. Fig. 2.1 demonstrates the flow field arisen from the swimming motion of these three types of squirmers in the unbounded Newtonian fluids. While a neutral squirmer gives rise to a potential flow in the surrounding fluid, the squirming motion of a puller (pusher) results in a formation of a positive (negative) force dipole which its magnitude decays quadratically with the distance from the swimmer's body. Since the sedimentation velocity of the microorganisms is commonly much smaller than their swimming speed [97], we assume the squirmer to be neutrally buoyant.

The squirmer model has been widely used to study the dynamics of a single microswimmer, nutrient uptake [98,99], bio-mixing [100], unsteady propulsion of small organisms [74] as well as the effects of density stratification on the self-propulsion [101]. Recently, Zhu et al. [102] studied the locomotion of a squirmer in a capillary tube and found that a neutral squirmer generally follows a helical trajectory; a puller displays a stable locomotion along the tube, while a pusher crashes into the wall. Ishikawa, Pedley, and coworkers have studied the dynamics of multiple squirmers in an unbounded fluid in the Stokes regime, including the hydrodynamic interaction between two squirmers [97], rheology and diffusion of a suspension of squirmers

[103, 104], collective behavior [105], and vertical dispersion of squirmers in a shear flow [106].

### 2.3 Governing Equations and Numerical Method

The governing equations of the incompressible flow in a viscoelastic fluid in dimensionless form are,

$$\nabla \cdot \mathbf{u} = 0, \tag{2.3a}$$

$$Re\left(\frac{\partial \mathbf{u}}{\partial t} + \mathbf{u} \cdot \nabla \mathbf{u}\right) = -\nabla p + \nabla \cdot \boldsymbol{\tau}, \tag{2.3b}$$

where $Re = \rho U_0 a/\mu$ is the Reynolds number, $\rho$ is the fluid density, $\boldsymbol{u}$ is the fluid velocity, and $p$ is the pressure. $\boldsymbol{\tau} = \mu(\nabla \boldsymbol{u} + \nabla \boldsymbol{u}^{\mathrm{T}})$ is the deviatoric stress. Here, the length is scaled by the radius of the spherical squirmer $a$, velocity by $U_0$, time by $a/U_0$, and pressure and stresses by $\mu U_0/a$, where $\mu$ is the dynamic viscosity of the fluid.

The distributed Lagrange multiplier based finite volume method is used in this study and details of the method can be found in [107, 108]. A rigid particle and a self-propelled particle can be modeled by adding a source term to the Navier-Stokes equation. The forcing term in each iteration is calculated as

$$\boldsymbol{f} = \boldsymbol{f}^* + Re\frac{\rho\phi}{\Delta t}(\boldsymbol{U}_P + \boldsymbol{\Omega}_p \times \boldsymbol{r} + \boldsymbol{u}_i - \boldsymbol{u}), \tag{2.4}$$

where $\boldsymbol{U}_P$ is the translational velocity of the particle (inert or self-propelled), $\boldsymbol{\Omega}_p$ is the particle angular velocity, $\boldsymbol{u}_i$ is the imposed velocity causing the self-propulsion, $\boldsymbol{f}^*$ is the force calculated in the previous iteration, $\phi$ is the volume fraction occupied by the particle in each computational cell ($\phi = 1$ inside, $\phi = 0$ outside and $0 < \phi < 1$ for the cells at the surface of the particle). The velocity field $\boldsymbol{u}$ is obtained by solving Eq. (2.3). To recover the tangential velocity $u_\theta^s$ on the surface of the squirmer (given in Eq. (2.1)), we impose the following solenoidal velocity $\boldsymbol{u}_i$ inside the squirmer

$$\boldsymbol{u}_i = (r^m - r^{m+1})(u_s \cot\theta + \frac{du_s}{d\theta})\boldsymbol{e}_r + \left[(m+3)r^{m+1} - (m+2)r^m\right] u_s^\theta \boldsymbol{e}_\theta,$$

where $\boldsymbol{e}_r$ and $\boldsymbol{e}_\theta$ are the unit vectors along $r$ and $\theta$ directions, $m$ is an arbitrary positive integer, where the simulation results are independent of its value. It should be noted that $= \boldsymbol{u}_i$ is zero for an inert particle. $\boldsymbol{U}_p$ and $\boldsymbol{\Omega}_p$ are determined by

$$\boldsymbol{U}_P = \frac{1}{M_p}\int_{V_P}\frac{\rho_p}{\rho}\boldsymbol{u}dV, \qquad \boldsymbol{\Omega}_P = \mathbf{I}_p^{-1}\int_{V_P}\frac{\rho_p}{\rho}(\boldsymbol{x}-\boldsymbol{X}_p)\times\boldsymbol{u}dV, \tag{2.5}$$

where $V_P$ is the particle volume, $\rho_p/\rho$ is the ratio of the particle density to the fluid density, which is equal to unity in all our simulations since the density of microorganisms is usually close to the background fluid. $M_p$ and $\mathbf{I}_p$ are the dimensionless mass and moment of inertia of the particle, respectively. Particle mass and moment of inertia are scaled by $\rho H^3$ and $\rho H^5$, respectively. The imposed velocity leads to a zero translational and rotational velocity for the particle (i.e $\int_{V_p}\boldsymbol{u}_i dV = 0$ and $\int_{V_p}\boldsymbol{r}\times\boldsymbol{u}_i dV = 0$). Iterations are repeated until the maximum of Euclidean norm of $(\boldsymbol{f}-\boldsymbol{f}^*)/\boldsymbol{f}$ and the normalized residual falls below the specified tolerance of $10^{-3}$. The normalized residual is defined as

$$\frac{\int_{V_P}\left|\boldsymbol{U}_P+\boldsymbol{\Omega}_p\times\boldsymbol{r}+\boldsymbol{u}_i-\boldsymbol{u}\right|\phi dV}{U_0 V_p}. \tag{2.6}$$

The velocity field inside the particle for the converged solution is $\boldsymbol{u} = \boldsymbol{U}_P+\boldsymbol{\Omega}_p\times\boldsymbol{r}+\boldsymbol{u}_i$. It is straight forward to demonstrate that the converged solution is the equivalent of the particle equation of motion:

$$M_p\frac{d^2\mathbf{x}_p}{dt^2} = \int_{\partial V_p}(-p\mathbf{I}+\boldsymbol{\tau})\cdot\mathbf{n}dS, \tag{2.7}$$

where $dS$ is the surface differential element. Combining Eqs. (2.4)-(2.5), one can show that $\int_{V_p}\boldsymbol{f}dV = 0$. Integrating Eq. (2.3$a$) over the particle volume and using the Reynolds transport theorem lead to:

$$\frac{d}{dt}\int_{V_p}\boldsymbol{U}_P+\boldsymbol{\Omega}_p\times\boldsymbol{r}+\boldsymbol{u}_i dV = Re\int_{V_p}\nabla\cdot(-p\mathbf{I}+\boldsymbol{\tau})dV, \tag{2.8}$$

which is equivalent to Eq. (2.7). This method has been extensively used for the motion of inert particles in viscous fluids and verified in our previous publications.

Simulations are conducted using a finite volume method on a fixed staggered grid. A conventional operator splitting method is applied to enforce the continuity equation.

The second-order TVD (total variation diminishing) Runge-Kutta method is used for time marching. The spatial derivatives in the convection term are evaluated using the QUICK (Quadratic Upstream Interpolation for Convective Kinetics) scheme and the diffusion terms are discretized using the central difference scheme.

When the squirmer approaches the wall or another squirmer, the high pressure in the thin film between the squirmers and the wall prevents any unphysical overlaps. However, a very small grid resolution is needed to properly capture this dynamic process and consequently it is computationally expensive. As mentioned in [81], the hydrodynamic interactions between squirmer and the wall are not sufficient to prevent squirmer-wall or squirmer-squimrer overlaps in some cases and a short-range repulsive force [109] is necessary. The repulsive force during the squirmer-wall or squirmer-squirmer collision is defined as:

$$\boldsymbol{F}_r = \frac{C_m}{\varepsilon}\left(\frac{d - d_{min} - dr}{dr}\right)^2 \boldsymbol{e}_c, \tag{2.9}$$

where $C_m = M_p U_0^2/a$ is the characteristic force, $\varepsilon = 10^{-4}$ is a small positive number, $d$ is the distance between the center of the squirmer and the wall or the distance between two squirmers, $d_{min} = a$ or $2a$ is the corresponding minimum possible distance, $dr$ is the force range and is usually set to be the smallest grid size $\Delta$ in the computational domain [109]. The direction of the repulsive force $\boldsymbol{e}_c$ is normal to the wall or along the line of center of the two squirmers. The above mentioned repulsive force has been widely used to handle the collision between particles and walls [109, 110].

## 2.4 Results and Discussion

### 2.4.1 Single Squirmer Swimming Near a Wall

Fig. 2.2 shows the trajectory as well as the time history of orientation angle $\alpha$ and swimming speed $U$ of the squirmer for different values of $\beta$. The squirmer collides with the wall at $t \simeq 0.8$, then it swims along the wall for a certain period of time referred to as the "contact time" and finally swims away from the wall. The contact

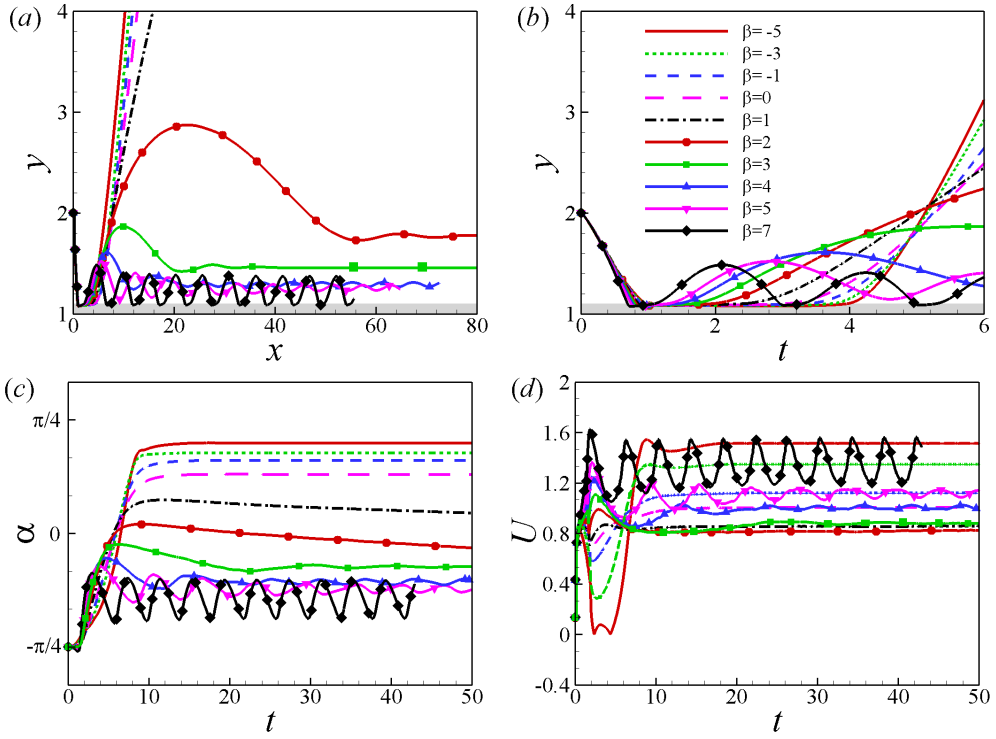


Figure 2.2. (*a*) Trajectory and (*b*) temporal evolution of distance away from the wall $y$, (*c*) orientation angle $\alpha$ and (*d*) swimming speed $U$ for squirmers of various $\beta$ at $Re = 1$, initially located at $h_0 = 2$ and $\alpha_0 = -\pi/4$.

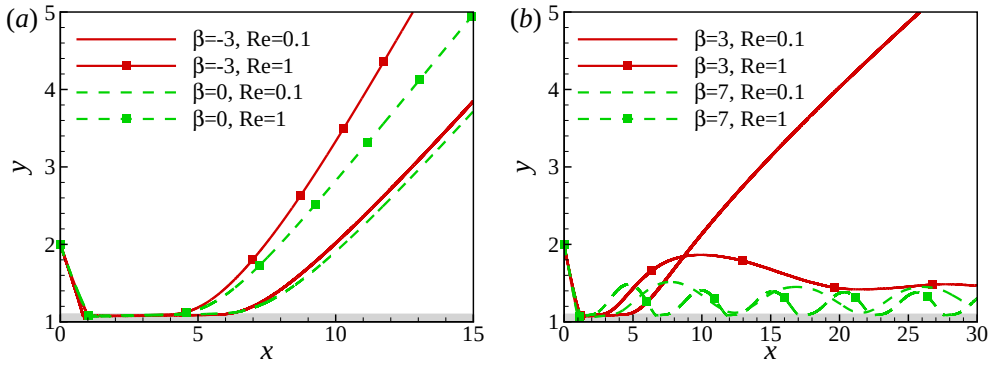


Figure 2.3. Trajectory of squirmers of (*a*) $\beta = -3$ and 0 (*b*) $\beta = 3$ and 7 at different Reynolds numbers.

time decrease as $\beta$ increases. When squirmers detached from the wall, three different swimming modes are observed depending on the values of $\beta$: (1) Squirmers of $\beta \leq 1$ will swim away from the wall with a positive angle. (2) Squirmers of $2 \leq \beta \leq 5$ oscillate near the wall and eventually swim along the wall with a constant distance and a negative angle. It should be noted that the damping ratio for the cases of $\beta = 4$ and 5 is small and their oscillations is not fully damped during the simulation time. (3) Squirmers of $\beta \geq 7$ will swim in a cyclic motion, bouncing on the wall. The amplitude of the cyclic motion is small compared to the wavelength. Similar steady and periodic swimming modes along the wall have been observed in [77] using a three-sphere swimmer model. For the squirmers swimming away form the wall, the swimming speed is recovered to its value for a squirmer in an unbounded domain. For $\beta \leq 1$, the swimmers escape from the wall and their steady swimming speed decreases as $\beta$ increases, which is consistent with analytical results of inertial squirmer in an unbounded domain [74]. On the other hand, pullers of $\beta > 2$ are trapped near the wall and their swimming speed increases with $\beta$.

The far field solution of a swimming organism in the low Reynolds number regime can be approximated using the superposition of fundamental singularities in the Stokes regime. At $Re = 0$, the velocity field generated by a squirmer in an unbounded quiescent fluid can be decomposed into three singularities at the location of the squirmer center: the Stokeslet dipole $\mathbf{G_D}$, the source dipole $\mathbf{D}$, and the source quadrupole $\mathbf{Q}$, respectively. The velocity generated by the squirmer centered at $\boldsymbol{r}_0$ swimming along the direction $\boldsymbol{e}$ is given as

$$\boldsymbol{u}(\boldsymbol{r}_p) = p_{GD}\mathbf{G_D} + p_D\mathbf{D} + p_Q\mathbf{Q}, \tag{2.10}$$

where $\boldsymbol{r}_p$ is the position at which the velocity is evaluated. The strength of each singularity is given as [74]

$$p_{GD} = -\frac{3\beta}{4}, \quad p_D = \frac{1}{2}, \quad p_Q = \frac{\beta}{4}, \tag{2.11}$$

and

$$\mathbf{G_D} = \frac{1}{r^2}(-\frac{\boldsymbol{r}}{r} + \frac{3(\boldsymbol{r}\cdot\boldsymbol{e})^2\boldsymbol{r}}{r^3}), \tag{2.12a}$$

$$\mathbf{D} = \frac{1}{r^3}(-\boldsymbol{e} + \frac{3(\boldsymbol{r}\cdot\boldsymbol{e})\boldsymbol{r}}{r^2}), \tag{2.12b}$$

$$\mathbf{Q} = \frac{3}{r^4}(-\frac{2(\boldsymbol{e}\cdot\boldsymbol{r})\boldsymbol{e} + \boldsymbol{r}}{r} + \frac{5(\boldsymbol{r}\cdot\boldsymbol{e})^2\boldsymbol{r}}{r^3}), \tag{2.12c}$$

where $\boldsymbol{r} = \boldsymbol{r}_p - \boldsymbol{r}_0$ and $r = |\boldsymbol{r}|$. For more details see [81].

When the singularities are close to a plane wall, a collection of image singularities are placed at the image point on the other side of the wall to satisfy the no-slip boundary condition at the wall. Here, we use $\mathbf{G}^*_{\mathbf{D}}, \mathbf{D}^*$, and $\mathbf{Q}^*$ to represent the image singularity collections for $\mathbf{G}_{\mathbf{D}}, \mathbf{D}$ and $\mathbf{Q}$, respectively, and $\boldsymbol{u}^*$ represents the velocity field induced by the image singularities. According to the Faxén's law, the motion of a spherical particle due to the presence of the wall can be exactly determined using the velocity $\boldsymbol{u}^*$ and its gradient at the center of the sphere. The translational and rotational velocities of the spherical swimmer located at $\boldsymbol{r}_0$ due to $\boldsymbol{u}^*$ can be written as [111]

$$\widetilde{\boldsymbol{u}} = \boldsymbol{u}^*|_{\boldsymbol{r}_0} + \frac{1}{6}\nabla^2\boldsymbol{u}^*|_{\boldsymbol{r}_0}, \tag{2.13a}$$

$$\widetilde{\boldsymbol{\Omega}} = \frac{1}{2}\nabla\times\boldsymbol{u}^*|_{\boldsymbol{r}_0}. \tag{2.13b}$$

Therefore, the translational and rotational velocities of the squirmer can be approximated as

$$\boldsymbol{u} = \boldsymbol{e} + p_{GD}\widetilde{\boldsymbol{u}}_{GD} + p_D\widetilde{\boldsymbol{u}}_D + p_Q\widetilde{\boldsymbol{u}}_Q, \tag{2.14a}$$

$$\boldsymbol{\Omega} = p_{GD}\widetilde{\boldsymbol{\Omega}}_{GD} + p_D\widetilde{\boldsymbol{\Omega}}_D + p_Q\widetilde{\boldsymbol{\Omega}}_Q. \tag{2.14b}$$

It should be noted that the velocity distribution on the surface of the squirmer is changed due to the velocity field induced by the wall and its influence increases as the squirmer gets closer to the wall. Therefore, Eq. (2.14) performs well only when the squirmer is far away from the wall and the numerical simulation is necessary for the near-wall motion of the squirmer.

In the present simulation, the squirmer swims in the $x$-$y$ plane, and its rotational velocity $\Omega$ is around the $z$-axis. The velocity components in the $x$ (wall-parallel) and

$y$ (wall-perpendicular) directions and rotational velocity in the $z$ direction induced by the image singularities are:

$$\widetilde{u}_{GD} = \frac{3\sin 2\theta}{8h^2}(1-\frac{1}{2h^2}), \quad \widetilde{v}_{GD} = \frac{-3+9\sin^2\theta}{8h^2}(1-\frac{1}{2h^2}), \quad \widetilde{\Omega}_{GD} = \frac{-3\sin 2\theta}{16h^3}, \tag{2.15a}$$

$$\widetilde{u}_{D} = \frac{-\cos\theta}{4h^3}(1-\frac{1}{h^2}), \quad \widetilde{v}_{D} = \frac{-\sin\theta}{h^3}(1-\frac{1}{2h^2}), \quad \widetilde{\Omega}_{D} = \frac{3\cos\theta}{8h^4}, \tag{2.15b}$$

$$\widetilde{u}_{Q} = \frac{-3\sin 2\theta}{16h^4}, \quad \widetilde{v}_{Q} = \frac{15+3\sin^2\theta}{16h^4} - \frac{5+5\sin^2\theta}{8h^6}, \quad \widetilde{\Omega}_{Q} = 0. \tag{2.15c}$$

The translational velocities induced by $\mathbf{G}^*_{\mathbf{D}}, \mathbf{D}^*$ and $\mathbf{Q}^*$ are of order $\mathrm{O}(1/h^2)$, $\mathrm{O}(1/h^3)$ and $\mathrm{O}(1/h^4)$, respectively and the corresponding rotational velocities are $\mathrm{O}(1/h^3)$, $\mathrm{O}(1/h^4)$ and 0, respectively. When the squirmer is far away from the wall, i.e. $h \gg 1$, the wall induced motion of the squirmer is dominated by the images of Stokeslet dipole $\mathbf{G}^*_{\mathbf{D}}$. For the pusher, the wall-induced rotation tends to align the squirmer parallel to the surface. When $\theta < 0$, the pusher rotates away from the wall and a puller rotates towards the wall [3]. However, when the squirmer is close to the wall, the motion of the squirmer is determined by the combined effects of all the image singularities and the rotation of the squirmer is determined by both $\mathbf{G}^*_{\mathbf{D}}$ and $\mathbf{D}^*$. The rotational velocity of squirmer induced by $\mathbf{D}^*$ is to rotate the squirmer away from the wall and a stable angle of $\theta = \pi/2$ is obtained. When $\theta < 0$, both $\mathbf{G}^*_{\mathbf{D}}$ and $\mathbf{D}^*$ rotate the pusher away form the wall, while for a puller, $\mathbf{G}^*_{\mathbf{D}}$ and $\mathbf{D}^*$ have opposite and competing effects on the rotation and different swimming modes are observed depending on the magnitude of $\beta$.

The inertia effects on the trajectories of squirmers are compared inn Fig. 2.3. The pusher and neutral swimmer escape from the wall for both values of Reynolds number, whereas puller of $\beta = 3$ escapes from the wall at $Re = 0.1$ and is entrapped near the wall at $Re = 1$. At larger values of $\beta$, the puller is entrapped for both values of Reynolds number, but the one at $Re = 1$ has a larger bouncing frequency. In summary, the inertial effect decreases the initial wall contact time independent of the squirming type, but it leads to a stronger attraction towards the wall for the puller.

### 2.4.2 Multiple Squirmers between Two Walls

We examine the swimming dynamics of suspension of squirmers between two walls. The simulation is conducted in a cubic domain of $[0, 13.89] \times [0, 13.89] \times [0, 13.89]$ with two no-slip walls at $y = 0$ and $y = 13.89$. Periodic conditions are used along $x$ and $z$ directions. Without any overlap, squirmers are initially randomly placed in a fluid otherwise at rest and their orientations are also randomly initialized. Three cases of $\beta = 0, 3$, and $-3$ at volume concentration $c = (4\pi N)/(3L^3) = 0.1$ are simulated. The case of $\beta = 0$ at $c = 0.4$ is also studied to consider the role of concentration. $N = 64$ and 256 squirmers are modeled for the two concentrations, respectively. Across the diameter of the squirmer, there are around 20 grid points for cases of $c = 0.1$ and 10 grids for $c = 0.4$, the time step is $\Delta t = 1 \times 10^{-3}$. The Reynolds number is $Re = 1$ for all cases.

Fig. 2.4 shows the spatial distribution of squirmers at $t = 100$ at which the system reaches a statistical steady state. White and black points show the front and trailing ends of symmetry axes of squirmers, respectively. At concentration $c = 0.1$, squirmers are accumulated near the walls for all values of $\beta$. Aggregation of pushers and pullers near the wall is stronger compared to the neutral squirmers. At high concentrations, squirmers are closely packed and the accumulation near the walls is not obvious from Fig. 2.4. Another interesting phenomena is that there is a strong tendency for squirmers to orient towards the walls in the near-wall region.

We now quantitatively characterize the hydrodynamic interaction between the squirmers and the walls. Fig. 2.5($a$) shows the probability distribution function of the vertical position of squirmers. Thee probability distribution function $f(\phi)$ is defined as

$$f(\phi) = \frac{1}{N\Delta\phi} \sum_{n=1}^{N} \langle \delta(\phi_n - \phi) \rangle, \tag{2.16}$$

and

$$\delta(\phi_n - \phi) = \begin{cases} 1, \phi - \frac{\Delta\phi}{2} \leq \phi_n < \phi + \frac{\Delta\phi}{2}, \\ 0, \text{otherwise}, \end{cases} \tag{2.17}$$

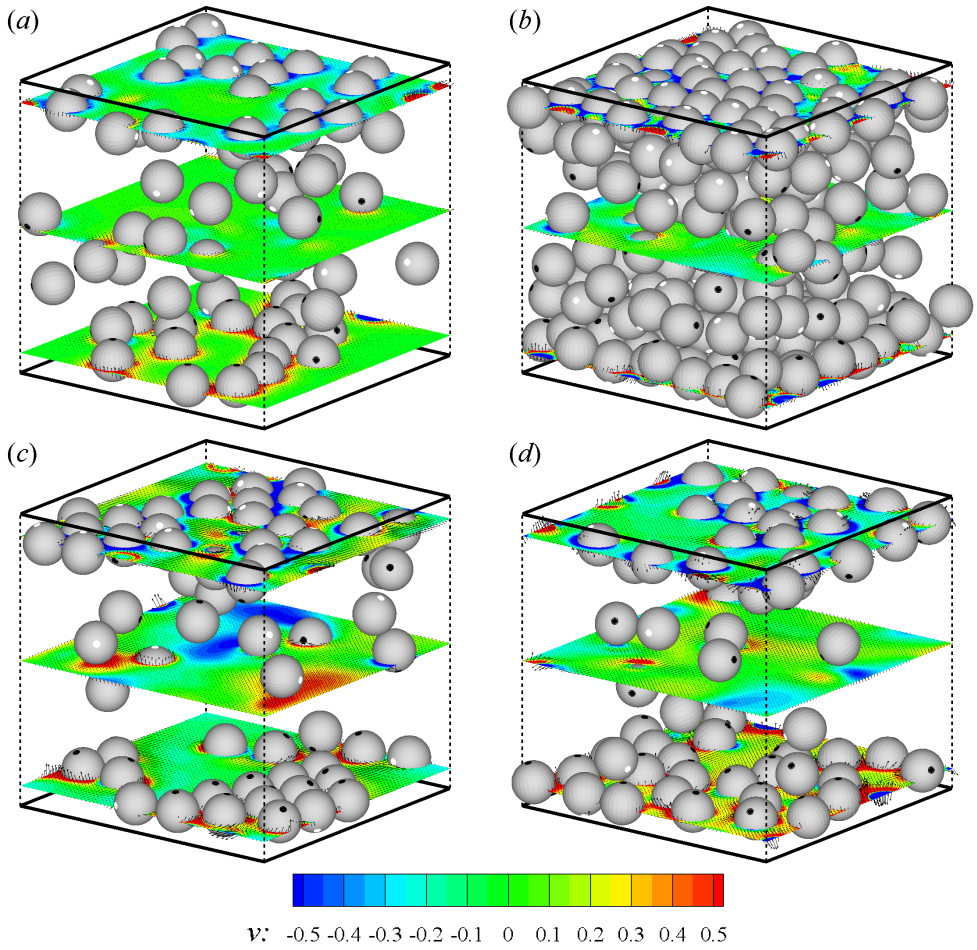


Figure 2.4. Distribution of squirmers of $(a)$ $\beta = 0, c = 0.1$, $(b)$ $\beta = 0, c = 0.4$, $(c)$ $\beta = -3, c = 0.1$, and $(d)$ $\beta = 3, c = 0.1$. Thick solid lines on the top and bottom show the plane walls, dashed lines show the computational domain. The front and trailing ends of symmetry axes of squirmers are shown with white and black points, respectively. The contourplot of $v$ and the velocity vectors on horizontal planes are shown on three slices at $y = 1, 6.94$, and $12.89$. The data is shown at every two points for cases of $c = 0.1$.

where $\phi$ is the vertical position $y$, orientation angle $\alpha$ and velocity components in Figs. $2.5(a)\sim(f)$, and $\Delta\phi$ is the interval of $\phi$ which is set to $\Delta y = 1.389$, $\Delta\alpha = 0.05\pi$ and $\Delta u = \Delta v = \Delta w = 0.1$. The choice of $\Delta\phi$ does not qualitatively change the results. The symbol $\langle\rangle$ represents a time-averaged quantity.

The squirmers are accumulated near the walls and the probability distribution function rapidly falls away from the walls. When close to the wall, pushers and pullers have stronger tendencies to accumulate near the wall compared to neutral squirmers. This result is predictable since the stresslet (strongest far-field interaction) is absent in the case of neutral squirmer [81]. It also agrees with the results for a single squirmer near the wall, in which both pusher and puller stay a longer time near the surface than the neutral squirmer (see Fig. 2.2($b$)). At high concentrations, the peaks of $f(y)$ near the two walls are lower than the cases of $c = 0.1$ because the layer of the squirmers close to the wall is nearly saturated and the concentration in the middle of the channel grows. Similar results have been reported in [90, 91]. In Fig. 2.6, we quantitatively compare our simulation results of pusher of $\beta = -3$ and $c = 0.1$ with published experimental/analytical results. The volume concentration of the cells in the experiments were reported in the range of $c = 0.01 - 0.1$ and the ratio between the channel width and the cell radius is around 40 for bull spermatozoa [47], 20-80 for *E. coli* [48], 66 for *C. crescentus* [68,69] and 6.6 for *C. crescentus* [69], respectively. All the results show an increase in concentration of microorganisms near the wall, and the wall attraction is stronger for the smaller channel width. Our results show good agreements with the results of *C. crescentus* which is performed at a small channel width [69]. The analytical results solely based on the dipole interaction with the wall [48] overestimates the probability distribution of swimmers near the wall compared to the results of direct numerical simulation.

Fig. 2.5($b$) shows the probability distribution function of the orientation angle of the swimmers $f(\alpha)$. A peak near $\alpha = -\pi/2$ is observed for all the cases. For squirmers of $\beta = 0$ at $c = 0.1$, another peak occurs near $\alpha = 0$. To better visualize the results, the probability distribution function of the orientation angle $f(\alpha)$ is plotted for the squirmers near the wall and in the bulk region in Figs. 2.5($c$) and 2.5($d$), respectively. The near-wall squirmers are strongly oriented normal to the wall (see Fig. 2.4). Interestingly for squirmers away from the wall, two different types of behavior are observed: for cases of $\beta = 0$ and 3 at $c = 0.1$, $\alpha$ is mostly between $-\pi/4$ and $\pi/4$ and

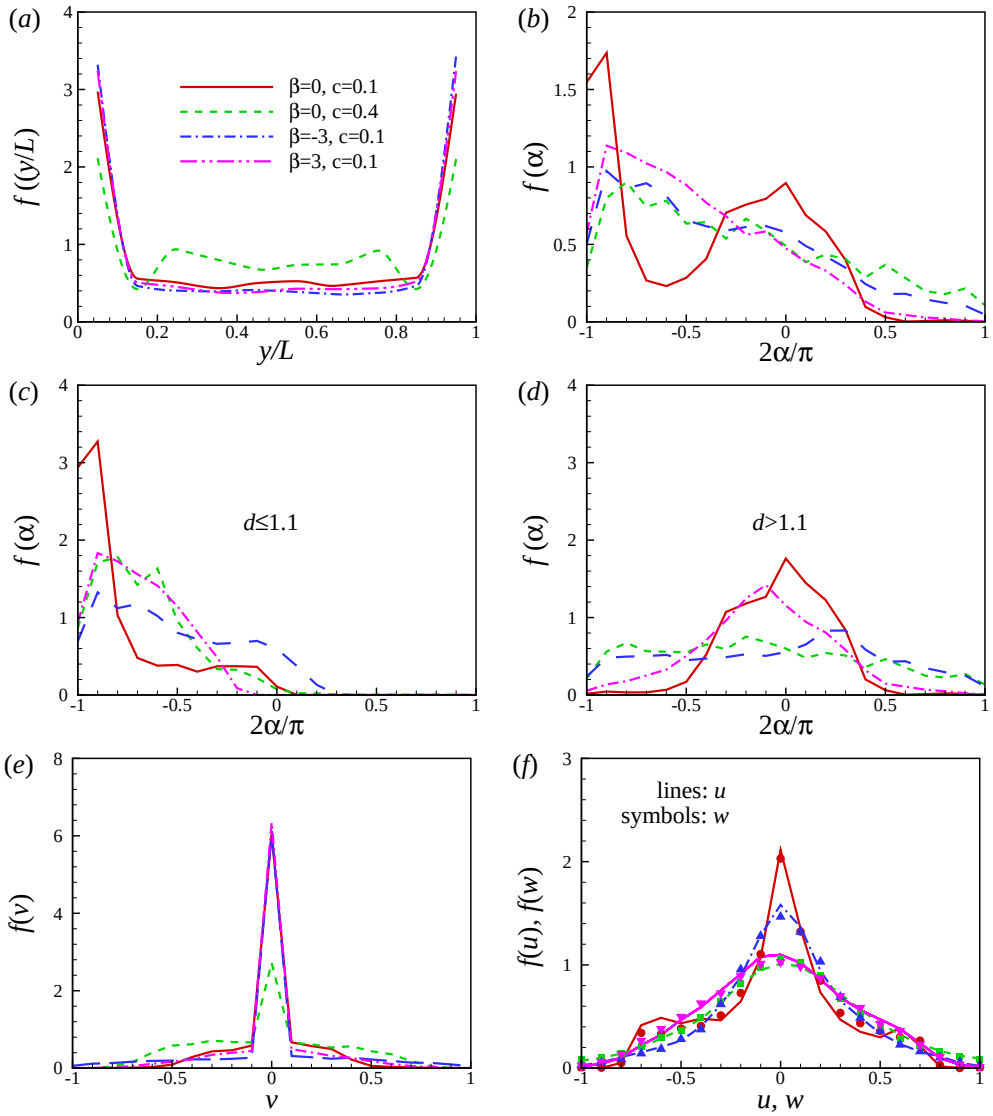


Figure 2.5. The probability distribution function of $(a)$ vertical position of squirmers, $(b)$ orientation angle $\alpha$ with respect to the nearest wall, $(c)$ $\alpha$ for the near-wall squirmers, $(d)$ $\alpha$ for the squirmers in the bulk region, $(e)$ vertical velocity component $v$ and $(f)$ velocity components $u$ and $w$.

there is a clear peak at $\alpha = 0$; and for cases of $\beta = -3, c = 0.1$ and $\beta = 0, c = 0.4$, $f(\alpha)$ is almost uniformly distributed over $-\pi/2$ to $\pi/2$. From the results of a single squirmer in Fig. 2.2$(b)$, after the initial wall contact, all the squirmers detach from the

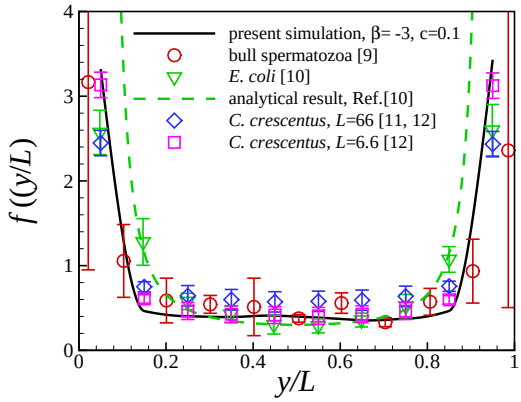


Figure 2.6. Comparison of vertical distribution of microorganisms between present simulation results and previous experimental/analytical studies.

wall with the finial angle between $-\pi/4$ to $\pi/4$ (0.56, 0.41, and -0.24 for $\beta = -3, 0,$ and 3, respectively). We have also shown that the finial angles are independent of the initial impact angle of the squirmer if a close contact between the squirmer and the wall occurs. Therefore, when squirmers swim into the bulk region, their orientation angle is mainly between $-\pi/4$ and $\pi/4$. However, for cases of $\beta = -3, c = 0.1$ and $\beta = 0, c = 0.4$, squirmers collide with each other more frequently, which leads to a more uniform distribution in the orientation angle. As shown in Fig. 2.5($e$), the distribution of vertical velocity component $v$ dominates at 0, which also indicates the high percentage of the near-wall squirmers. Similar results can be also found in Fig. 2.5($f$) for $u$ and $w$ components of velocity.

Hydrodynamic interaction between squirmers generates large scale flows and leads to a collective motion [105, 112]. To show this, we investigate the spacial correlation function $g(r)$, which is defined as

$$g(r) = \frac{L^3}{N(N-1)V(r_{m,n})} \sum_{m=1}^{N} \sum_{\substack{n=1 \\ n \neq m}}^{N} \langle \delta(r_{m,n} - r) \rangle,$$
$$\delta(r_{m,n} - r) = \begin{cases} 1, & r - \frac{\Delta r}{2} \leq r_{m,n} < r + \frac{\Delta r}{2}, \\ 0, & \text{otherwise}, \end{cases} \tag{2.18}$$

where $r_{m,n}$ is the distance between squirmers $m$ and $n$, $V(r_{m,n}) = (4\pi/3)((r_{m,n} + \Delta r/2)^3 - (r_{m,n} - \Delta r/2)^3)$ is the volume of spherical shell of radius $r_{m,n}$ and thickness $\Delta r$. Figs. 2.7 $(a)$ and $(b)$ show the pair distribution function for squirmers close to the wall and in the bulk region, respectively. For the squirmers near the wall, $g(r)$ peaks at around $r = 2$ and 4, referring to the cluster formation of squirmers on the wall. The curve of $\beta = -3$ has the highest peak at $r \simeq 2$, meaning that a larger number of pushers are in close contact (see Fig. 2.4$(c)$). On the contrary, pullers are distributed further away from each other. This can be explained by the side-by-side interactions between two pushers, which is an attractive force, and two pullers, which is a repulsive force [3]. All curves have similar distributions for the bulk squirmers, the pair distribution function has a peak near $r = 2$ corresponding to the squirmers in close contact. Similar results were reported for the suspension of passive particles [113], bubbles [114] and two-dimensional swimming particles [112] in an unbounded domain.

The flow field near the bottom wall ($y = 0$) generated by pushers ($\beta = -3$) and pullers ($\beta = 3$) is plotted in Fig. 2.8. The contourplot of the vertical velocity component $v$ is shown in the plane of $y = 2.5$. For clarity, the squirmers above the plane is not shown here. Near-wall pushers accumulate near each other and form large scale coherent structures. Previous studies have shown that these coherent structures can increase the mass transport [83, 84]. On the contrary, near-wall pullers are more scattered due to the side-by-side repelling force between them.

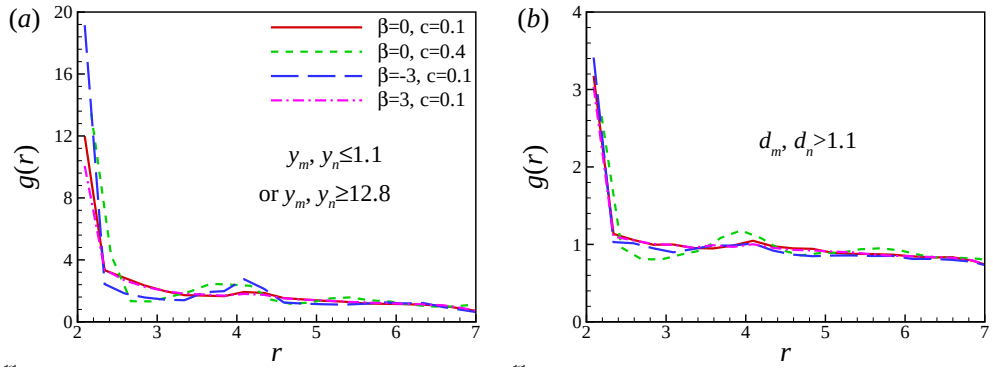


Figure 2.7. Pair distribution function for the squirmers ($a$) close to either walls or ($b$) in the bulk region.

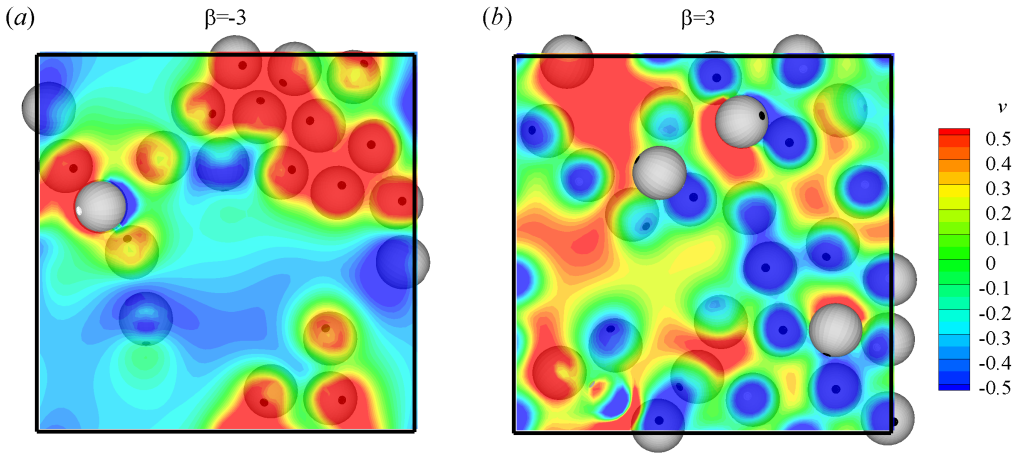


Figure 2.8. Top view of the flow field near the bottom wall of a suspension of ($a$) pushers ($\beta = -3$) and ($b$) pullers ($\beta = 3$). Contour-plots show the distribution of velocity component $v$ on the plane of $y = 2.5$.

## 2.5 Concluding Remarks

We have studied the dynamics of a single and multiple low-Reynolds-number swimming organism(s) near a wall by conducting a three-dimensional direct numerical simulation. Each swimmer is modeled as a squirmer, which consists of a spherical body that propels itself by a tangential velocity distribution on its surface.

When a single squirmer is initially oriented towards the wall, three different modes are observed for $Re = 1$: $(a)$ squirmers of $\beta \leq 1$ escapes from the wall, $(b)$ squirmers of $2 \leq \beta \leq 5$ oscillate near the wall and eventually swim along the wall keeping a constant distance and orientation angle and $(c)$ squirmers of $\beta \geq 7$ bounce on the wall. At a smaller Reynolds number, $Re = 0.1$, the initial wall contact time is increased independent of the swimming type, but a weaker attraction towards the wall is observed for the puller. The dynamics of suspension of squirmers between two walls is also studied. Similar to the observation of previous experiments [47,48,68,69], we found that the squirmers are strongly attracted to the walls. At a relatively small concentration of $c = 0.1$, around $60 \sim 80\%$ of the squirmers are accumulated near the wall, the attraction of pushers and pullers is stronger than neutral squirmers. At a high concentration, $c = 0.4$, around 40% of the squirmers are near the wall. In the near-wall region, the squirmers mostly orient normal to the walls, while in the bulk region, the orientation angle of squirmers are more uniformly distributed or they orient in the direction parallel to the wall. The wall leads to the decrease of the average swimming speed of the squirmers. The pair distribution function shows that suspensions of pushers form large scale clusters near a wall, which is not the case for pullers.

It is interesting to extend the results of this paper by including higher-order squirming modes which will affect the near-wall motion of the squirmer. In our simulations, the squirmer model is used to reduce the complexities of real microorganisms. The first two squirming modes capture the most important features of pusher- and puller-type microswimmers. Previous experiments of *E. Coli* near a surface [48, 70] show that a stresslet and its image singularities, included to satisfy the boundary conditions on the wall, describes the measured flow around a bacterial cell near a wall with good accuracy. Since higher-order squirming modes will extensively expand the parameter space, our simulation as well as most of the previous studies [97, 99, 101–106] only considered the first two squirming modes.

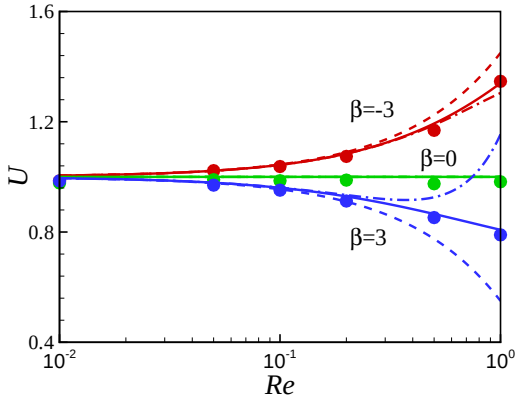


Figure 2.9. Comparison of the results for the steady swimming of a squirmer in an unbounded domain at finite $Re$. Symbols: present numerical results, dashed lines: Eq. (39) from [74] (first order), dashdot lines: Eq. (40) of [115] (second order), solid lines: Eq. (41) of [115]. The domain size for the computational results is $40\times40\times40$.

## 2.6 Appendix: Validation of the Numerical Method

We first validate the motion of a single squirmer in an unbounded fluid at a finite Reynolds number defined as $Re = \rho U_0 a/\mu$. The comparison between the present numerical results for the steady swimming speed and the analytical results, obtained using perturbation theory, [74,115] is illustrated in Fig. 2.9. The first order solution for the swimming speed of a squirmer in an unbounded domain is $U \approx 1 - 0.15\beta Re$ [74]. The swimming speed $U$ of the neutral squirmer does not change with the Reynolds number. The swimming speed of a pusher increases with $Re$ and our results are in good agreement with the analytical results at small values of Reynolds number. The swimming speed of a puller decreases with $Re$. At $Re > 0.2$, the first-order solution of Wang and Ardekani [74] and the second-order solution of Khair and Chisholm [115] starts to fail. Our results agree with Eq. (41) of [115]. Additional validation tests are included in the appendix. More detailed descriptions of the numerical method and some other relevant validation and verification tests using this code can be found in our previous publications [108, 110, 116].

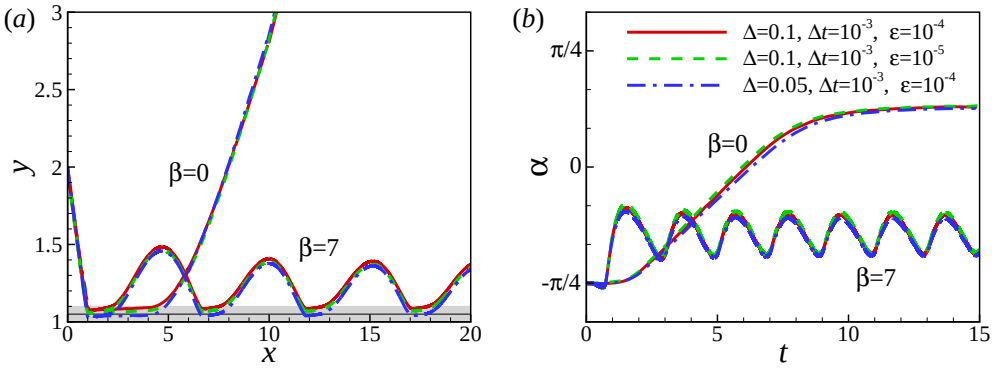


Figure 2.10. $(a)$ Trajectory and $(b)$ temporal evolution of orientation angle $\alpha$ for squirmers of $\beta = 0$ and 7 at $\alpha_0 = -\pi/4, h_0 = 2$, and $Re = 1$. Gray area and the dark gray line in $(a)$ show the area inside which the gap between the squirmer and the wall is less than one mesh size of $\Delta = 0.1$ and $\Delta = 0.05$.

To check the convergence of the results, simulations of the near-wall motion of a neutral squirmer are conducted for different values of mesh size, time step and magnitude of repulsive force . The size of computational domain is $64 \times 25.6 \times 12.8$. The no-slip boundary condition is used on the wall and the far field boundary condition is used at other boundaries of the domain. The squirmer is initially located at $h_0 = 2, \alpha_0 = -\pi/4$ and $Re = 1$. As shown in Fig. 2.10, the computed results are independent of the grid size, time step and magnitude of the repulsive force. Consequently, for the calculations presented in this work, twenty grid points are used across the squirmer diameter and the time step is set to $\Delta t = 1 \times 10^{-3}$.

# 3. NEAR WALL MOTION OF MODEL CILIATE IN A VISCOELASTIC FLUID[1]

## 3.1 Motivation and Previous Works

Bacteria primarily live within microscopic colonies embedded inside a self-secreted matrix of polymers and proteins. These microbial biofilms form on natural and man-made surfaces and interfaces and play important roles in various health and environmental issues [42]. Previous experimental studies have indicated the significance of bacterial motility mechanisms in the colonization process and the subsequent biofilm formation [117–123]. In particular, flagellar mediated swimming is crucial in approaching the surface and initiating the adhesion process [124] and pili-mediated motility highly promotes the surface exploration [125]. The swimming capability of a subpopulation of cells endures even after the establishment of the biofilm structure. For instance, the epifluorescence microscopic observations by Nielsen et al. [126] showed that the *Pseudomonas putida* cells rapidly swim in circular trajectories inside the microcolonies and some of them may swim out of the "liquefied" inner region of the biofilm. Furthermore, Houry et al. [123] showed that during the growth of *Bacillus cereus* biofilms, the recruited motile planktonic cells penetrate deeply inside the biomass instead of staying at its surface. The locomotion of cells may lead to their accumulation on the surface of the biomass as shown by Vlamakis el al. [127] for the *Bacillus subtilis* aggregates where the newly born motile cells move to the edge and the base of the biofilm.

The biofilm structure is strengthened by a protective matrix which is primarily composed of bacteria-produced extracellular polymeric substances (EPS). Dispersion of associated polysaccharides and proteins in the surroundings impart viscoelasticity

[1]The results of this chapter have been published in "Effect of solid boundaries on swimming dynamics of microorganisms in a viscoelastic fluid" by G. Li, A. Karimi and A. M. Ardekani in Rheologica Acta, 53: 911, 2014 (DOI: 10.1007/s00397-014-0796-9) (With permission of Springer).

into the ambient fluid. In addition, there exist ubiquitous examples in nature where fluid habitat of microorganisms is complex and shows non-Newtonian behavior, such as the spermatozoa in the mammalian female reproductive tract swimming through the cervical mucus [59], *Helicobacter pylori* colonizing the mucus layer covering the stomach [60], spirobacteria such as *Borrelia burgdorferi* penetrating the connective tissues in skin [61, 62], and the nematode *Caenorhabditis elegans* swimming in the water-saturated soil [63]. In these instances, the elastic effects become predominant when the Weissenberg number, $Wi$, defined as the ratio of polymer relaxation time to the characteristic time scale of the swimming, is larger than unity. Based on the rheological measurements of the biofilms, the corresponding relaxation time ranges from $10^{-2}$ s to $10^{2}$ s [43, 128], or even up to $10^{3}$ s [129]. Also, the typical relaxation time of the mucus layer varies in the $1 - 10$ s range [130]. Given the oscillation frequency of cilia $f \sim 5 - 50$ Hz [131] or the actuation frequency of spermatozoa $f \sim 20 - 50$ Hz [131], we can deduce that the associated Weissenberg number is $O(1)$ or much larger.

The study of motile microorganisms swimming in complex fluids has received significant attention in recent years. It has been shown that in viscoelastic media, both enhancement and inhibition of swimming speed occurs depending on the swimming strategy and the rheological characteristics of the background fluid. For example, helical bacteria such as *Leptospira* and *B. burgdorferi* swim faster in a viscoelastic fluid compared to a Newtonian fluid of the same viscosity [132, 133], whereas *C. elegans* which undulates its body in a planar wave swims with a slower pace [134]. Taylor's waving sheet [5] as an idealized model of an undulating swimmer has been utilized in several theoretical studies to investigate the kinematics and energetics of swimming in viscoelastic environments. The corresponding outcomes exhibit strong dependence on the waving stroke and the constitutive properties of the fluid. While the analytical study of Lauga [135] indicates that the viscoelasticity hinders the locomotion of an infinite swimming sheet oscillating with small amplitude, numerical results of Teran et al. [136] demonstrates enhancement of swimming speed and efficiency of a

waving sheet with finite length within a favorable range of undulation pattern and polymer relaxation time. For an undulating swimmer, the maximum speed emerges at $Wi \sim 1$ [136] where the decaying time of elastic stresses matches the period of swimming strokes. For self-propelled helical bodies, both experiments [137] and simulations [138] show that the swimming speed peaks at Weissenberg number of $O(1)$, and the speed enhancement with respect to Newtonian fluids is more pronounced for helices with large pitch angles. Simulations conducted on axisymmetric bodies with tangential squirming motion [94, 95] indicate that for ciliated cells, the swimming speed in shear-thinning polymeric solutions is always smaller compared to Newtonian fluids and the Weissenberg number associated with minimum velocity depends on the specific swimming gait of the microorganism. The hydrodynamic efficiency, however, is enhanced in viscoelastic fluids regardless of the squirming mode or the value of Weissenberg number.

The viscoelasticity of the ambient fluid, not only alters the swimming behavior of a single microorganism, but also affects the hydrodynamic interactions and collective motion of a population of motile cells. For example, Ardekani and Gore [139] demonstrated that in a bacterial suspension subjected to a background vortical flow, viscoelasticity results in steady rotation and aggregation of microorganisms on a limit cycle. Also, using a mean-field kinetic model, Bozorgi and Underhill [140, 141] analyzed the effect of viscoelasticity on the instability conditions of a suspension of extensile microwimmers.

Understanding the swimming strategy of bacteria in confined geometries is shown to be a decisive factor in identifying the adhesion rate and elucidating the subsequent colonization process. However, a large majority of studies focused on the swimming behavior of motile cells in complex fluids have been conducted assuming the cells' habitat to be an unbounded domain and thus, the boundary induced effects, such as surface trapping and wall accumulation, are poorly understood. On the contrary, the significance of the solid boundaries is well received in the context of particulate viscoelastic flows. Several computational [142–145] and experimental [146–148] in-

vestigations have been carried out to shed light on the dynamical behavior of rigid particles moving in close proximity of a solid surface in non-Newtonian fluids. In particular, it is found [142] that in the second-order fluids, a strong attraction force is developed which draws a solid sphere towards the corresponding wall. Also, the shear-thinning effects are shown [148] to be determinant in raising the acceleration of the particles moving away from the nearby surfaces. Although the physical mechanisms underlying the interaction of solid surfaces with rigid particles are different than those affecting the dynamics of self-propelled cells, the experimental and computational methodologies developed in the aforementioned studies are of potential use in order to explore the impact of the walls on the swimming motion of motile microorganisms in viscoelastic media.

In the current study, we conducted a series of three-dimensional direct numerical simulations in order to investigate the near-wall swimming motion of a squirmer in viscoelastic fluids. We scrutinize the effects of fluid elasticity, shear-thinning, and polymer viscosity on the swimming speed, inclination, and trapping period of various types of squirmers with different locomotive gaits. Utilizing a decomposition of force and torque exerted on swimmer's body, the dynamical behavior of a squirmer adjacent to a solid boundary is rationalized. To the best of our knowledge, the results presented below are the first three-dimensional simulations analyzing the effect of a rigid surface on the self-propelled motion in complex fluids.

## 3.2 Governing Equations

The governing equations of the are the same as for squirmers in Newtonian fluid,

$$\nabla \cdot \mathbf{u} = 0, \tag{3.1a}$$

$$Re\left(\frac{\partial \mathbf{u}}{\partial t} + \mathbf{u} \cdot \nabla \mathbf{u}\right) = -\nabla p + \nabla \cdot \boldsymbol{\tau}, \tag{3.1b}$$

The differences come form the deviatoric stress $\boldsymbol{\tau}$, which can be split into solvent and polymer components as $\boldsymbol{\tau} = \boldsymbol{\tau}^s + \boldsymbol{\tau}^p$. The Newtonian viscous stress is defined as $\boldsymbol{\tau}^s = \beta_s(\nabla \mathbf{u} + \nabla \mathbf{u}^{\mathrm{T}})$ with $\beta_s = \mu_s/\mu$ being the ratio of the solvent viscosity to

the zero-shear viscosity of the polymeric solution. The dynamic viscosity of the fluid includes contributions form both Newtonian solvent and polymers, $\mu = \mu_s + \mu_p$.

To characterize the evolution of the polymer stress, we adopt the Giesekus constitutive model [149] which specifies the constrained elongation of the polymers and the shear-thinning behavior of the polymeric solution. In dimensionless form, the associated equation can be written as,

$$\boldsymbol{\tau}^p + Wi\,\overset{\triangledown}{\boldsymbol{\tau}}^p + \frac{Wi\,\alpha_m}{1-\beta_s}\boldsymbol{\tau}^p \cdot \boldsymbol{\tau}^p = (1-\beta_s)(\nabla\mathbf{u} + \nabla\mathbf{u}^{\mathrm{T}}), \tag{3.2}$$

where $Wi = \lambda U_0/a$ is the Weissenberg number with $\lambda$ being the polymer relaxation time. The mobility factor, $\alpha_m$, represents the anisotropic hydrodynamic drag exerted on the polymer molecules by the surrounding solute molecules. Based on the thermodynamic analysis, the mobility factor must lay in the range of 0 to 1/2 [150]. For special case of $\alpha_m = 0$, the Giesekus model reduces to the Oldroyd-B model. In this work, unless otherwise stated, we set $\alpha_m = 0.2$ in accordance with previous studies regarding the squirming motion in unbounded viscoelastic media [94,95]. The notation $\overset{\triangledown}{\mathbf{A}}$ represents the upper-convected derivative,

$$\overset{\triangledown}{\mathbf{A}} = \frac{\partial \mathbf{A}}{\partial t} + \mathbf{u}\cdot\nabla\mathbf{A} - \nabla\mathbf{u}^{\mathrm{T}}\cdot\mathbf{A} - \mathbf{A}\cdot\nabla\mathbf{u}. \tag{3.3}$$

The range of parameters considered in the current study are $Re = 0.1$, $Wi = 0-6$, $\beta_s = 0.1-0.3$, $\alpha_m = 0-0.3$, and $\beta = -3, 0, 3$.

### 3.3 Results and Discussion

In this section, the effects of the fluid viscoelasticity on the swimming motion of different types of squirmers near a rigid wall is investigated. In our previous study, two types of swimming modes are distinguished for the near wall motion of a single squirmer at $Re = 0.1$ in a Newtonian fluid: (a) the squirmer with $\beta \leq 3$ escapes the wall and (b) the squirmer with $\beta > 3$ swims in the close proximity of the wall [50]. We have also found that the long-time swimming modes are not affected by the initial angle and the initial position of the squirmer. Thus in present study, the initial height

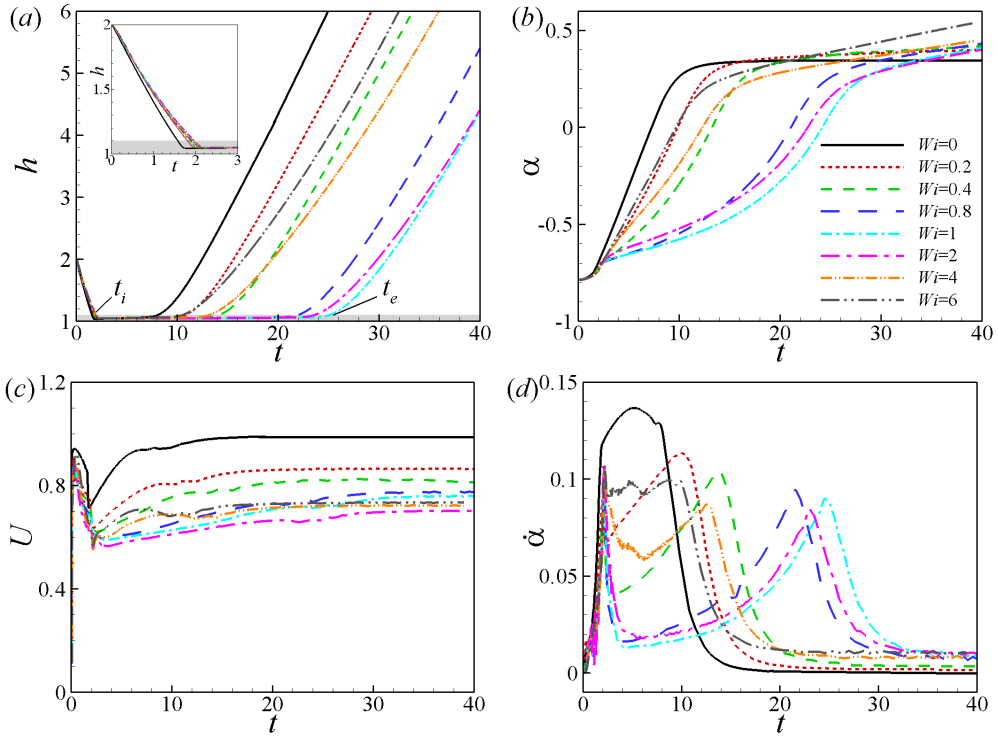


Figure 3.1. Temporal evolution of (a) distance from the wall, (b) orientation angle, (c) swimming speed, and (d) angular velocity for the neutral squirmer with $\beta = 0$.

and the initial orientation of the squirmer are fixed at $h_0 = 2$ and $\alpha_0 = -\pi/4$ and we only focused on the effect of the viscoelasticity of the background fluid on the interaction of the model swimmer and the solid surface.

### 3.3.1 Neutral Squirmer

The time history of the vertical position of a neutral squirmer in Newtonian and viscoelastic fluids are shown in Fig. 3.1($a$). In general, the viscoelasticity of the background fluid does not alter the near-wall swimming behavior of a neutral squirmer qualitatively. At all Weissenberg numbers, the squirmer initially approaches the wall in an oblique direction and then collides with the surface at time $t_i$. Next, due to synergetic effects of hydrodynamic interactions and collision, the squirmer reorients

and swims parallel to the wall for a limited time interval. Whilst the squirmer is trapped by the surface, it gradually rotates away from the wall and thus, the orientation angle $\alpha$ increases. Finally the squirmer escapes the wall at time $t_e$ where $\alpha$ becomes positive. Here, we define the impact time $t_i$ and the escape time $t_e$ of the squirmer at which the distance to the surface is $h_c = 1.1$. Based on this value of $h_c$, in the contact regime, the squirmer is 10% of a cell size away from the wall which agrees with experimental observation of Drescher et al. [70]. They found that, while trapped by the nearby surface, an *Escherichia coli* cell is about 1-3 $\mu$m away from the wall. The specific choice of $h_c$ affects the residence time quantitatively, but the qualitative trend will remain the same. As the inset in Fig. 3.1(a) demonstrates, the impact time $t_i$ of the squirmer is postponed in the viscoelastic fluid since the overall swimming speed of the squirmer is smaller compared to the Newtonian fluid (see Fig. 3.1(c)) [95]. The trapping period $\Delta t_e = t_e - t_i$ in which the squirmer is in a close contact with the wall increases for $Wi < 1$ and reaches a peak value around $Wi = 1$. The prolonged trapping time at $Wi = 1$ originates from the diminished angular velocity of the squirmer in this case as delineated in Fig. 3.1(d).

In order to elucidate the hydrodynamic interaction of the squirmer with the nearby wall, the temporal profiles of the torque and the vertical force exerted on the squirmer are calculated and illustrated in Fig. 3.2. After collision with the wall and reorientation of the squirmer, the polymer stress momentarily induces a large torque in negative $z$ direction which reduces the angular velocity and impedes the growth of the inclination angle $\alpha$. As demonstrated in the inset of Fig. 3.2(a), the magnitude of this opposing torque reaches its maximum at $Wi = 1$ and decays for higher values of $Wi$. The slower rotation and longer residence time of the squirmer when its swimming characteristic time is on the order of the polymer relaxation time can be rationalized considering the inhibiting effect of the polymer stress which generates an adverse torque at the early stage of swimmer-wall interaction. In order to illustrate the elastic wake around the squirmer, we calculated the first normal stress difference, $N_1 = \tau_{XX} - \tau_{YY}$, which is a measure of the polymer stretching. The snapshots of $N_1$

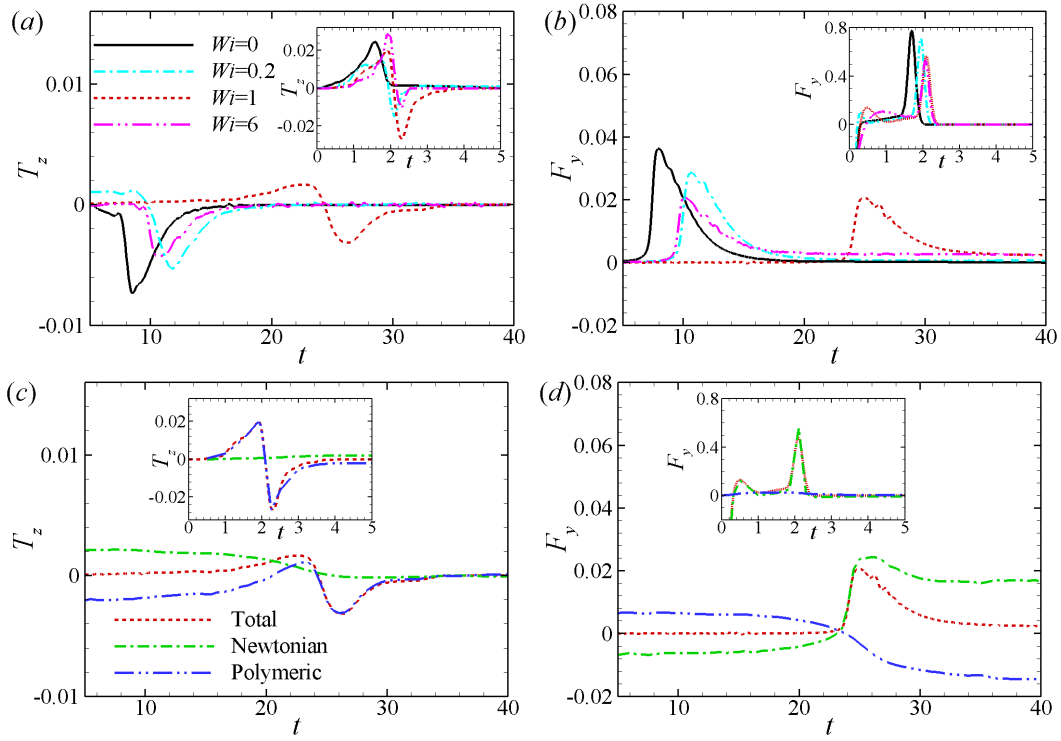


Figure 3.2. Temporal evolution of the torque and the vertical force exerted on the neutral squirmer with $\beta = 0$. The panels show (a) variation of the torque for different values of $Wi$, (b) variation of the vertical force for various values of $Wi$, (c) decomposition of the torque for the case of $Wi = 1$, and (d) decomposition of the vertical force for the case of $Wi = 1$.

around the cell body immediately after the impact, as shown in Fig. 3.3, exhibit a larger region of elongated polymers and a pronounced elastic wake in case of $Wi = 1$. For higher values of polymer relaxation time corresponding to $Wi > 1$, the region of largest elongation becomes thinner and thus, the squirmer encounters reduced elastic resistance against reorientation.

During the trapping period, the region of elongated polymers shrinks and thereby, the magnitude of the polymeric torque exerted on the squirmer diminishes. On the other hand, a high shear region in the gap between the swimmer and the wall evolves which strengthens the effect of the Newtonian stress. The resulting imbalance in the distribution of the shear stress gives rise to a strong torque in $z$ direction which coun-

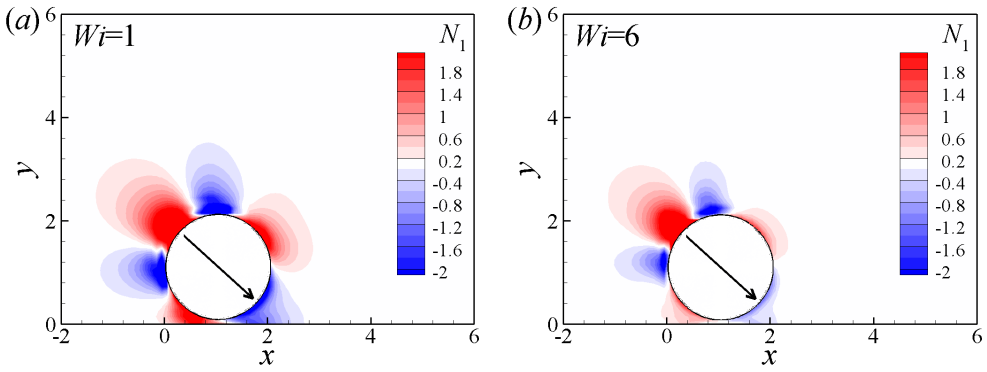


Figure 3.3. Distribution of the first normal stress difference at plane $z = 0$ around the neutral squirmer with $\beta = 0$. The snapshots are taken immediately after the impact at $t = 2$ and correspond to (a) $Wi = 1$, and (b) $Wi = 6$.

teracts the impeding effect of the polymeric torque. The overall effects of Newtonian and polymeric stresses on the surface of the squirmer result in counter-clockwise rotation of the cell and facilitates propelling towards the bulk fluid. As soon as the inclination of the squirmer becomes horizontal, a large vertical force arising from the asymmetric distribution of the Newtonian shear stress is developed which negates the wall attraction effect and leads to departure from the vicinity of the surface. This driving force emerges at the time when the squirmer starts to swim parallel to the wall. Hence, the residence time of the swimmer is contingent upon the torque balance and angular kinetics of the ciliated cell.

The effect of the constitutive properties of the background fluid on the squirmer dynamics near a wall is investigated. The impact of shear-thinning behavior on the residence time of the squirmer is depicted in Fig. 3.4(a). It is evident that by increasing the degree of shear-thinning, the trapping period of the squirmer will grow. This is closely related to the escaping mechanism of the swimmer resulting from the imbalance in the distribution of the Newtonian viscous stress. In fluids with a high degree of shear-thinning, the elevated shear rate in the constriction between the squirmer and the wall leads to a local decline in the fluid viscosity and consequently,

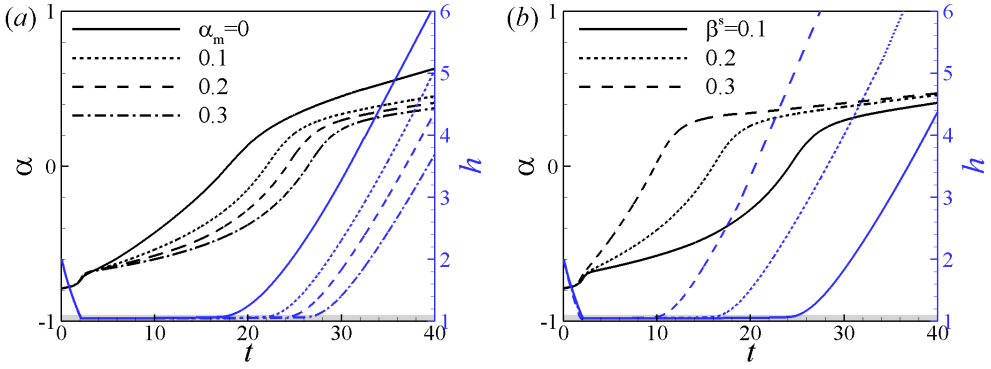


Figure 3.4. Temporal evolution of the orientation angle and vertical distance of a neutral squirmer for various values of (a) mobility factor, and (b) viscosity ratio. The corresponding parameters are $\beta = 0$, $Wi = 1$, and (a) $\beta_s = 0.1$, and (b) $\alpha_m = 0.2$.

a lower value of the Newtonian torque. Thus, the squirmer should spend a longer period of time near the wall to become capable of overcoming the impeding effect of the polymeric torque and reorienting away from the surface. In particular at $Wi = 1$, the residence time of a neutral squirmer swimming in a Giesekus fluid with $\alpha_m = 0.2$ is about 25% longer compared to an Oldroyd-B fluid.

The other important characteristic of the viscoelastic fluids is the viscosity ratio which describes the relative importance of the Newtonian and polymeric contributions in the fluid viscosity. By increasing the value of $\beta_s$, the role of solvent viscosity in kinetics of the swimmer gains more significance which leads to earlier release of the cell from the wall attraction (see Fig. 3.4(b)). Since the inhibiting impact of the polymeric torque is lessened for elevated values of $\beta_s$, the squirmer reorientation accelerates and the cell escapes the wall faster.

### 3.3.2 Puller

In this section, the dynamical behavior of a puller with $\beta = 3$ in the vicinity of a solid surface is investigated. The swimming trajectory of the puller swimmer is qualitatively akin to the neutral squirmer, i.e. it approaches the wall due to hydro-

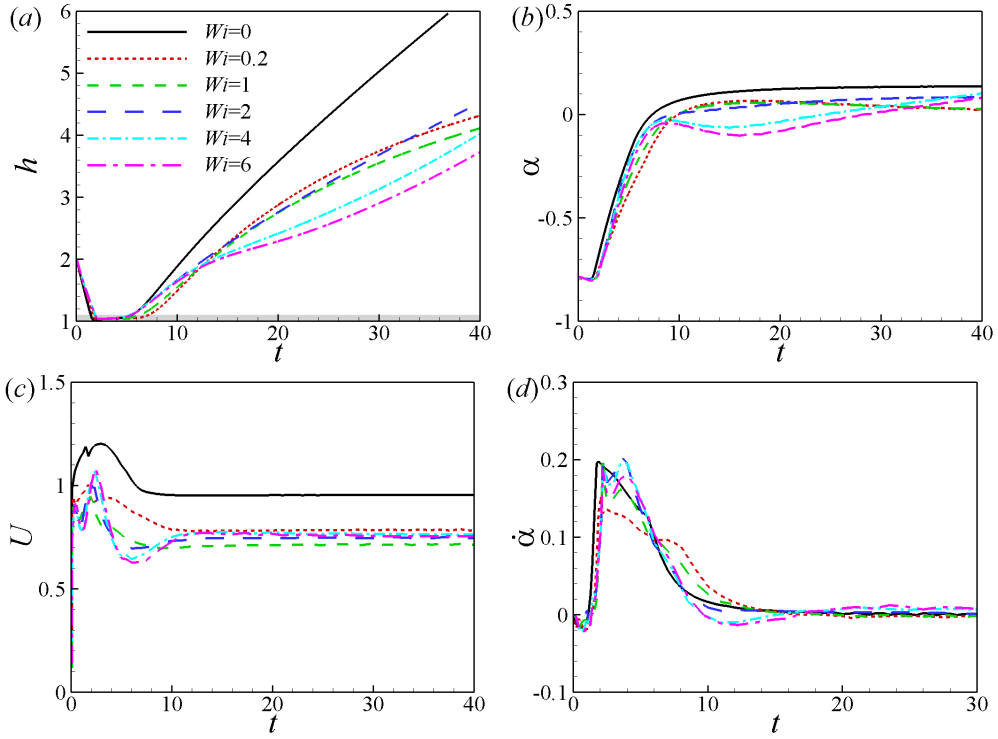


Figure 3.5. Temporal evolution of (a) vertical distance, (b) inclination angle, (c) swimming speed, and (d) rotation rate for a puller swimmer with $\beta = 3$.

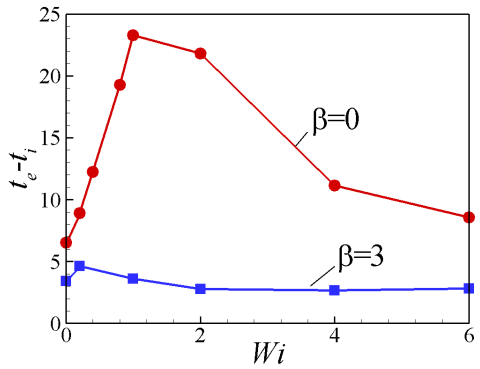


Figure 3.6. Residence time of the swimmer as a function of the Weissenberg number for puller $\beta = 3$ (squares, blue) and neutral squirmer $\beta = 0$ (circles, red).

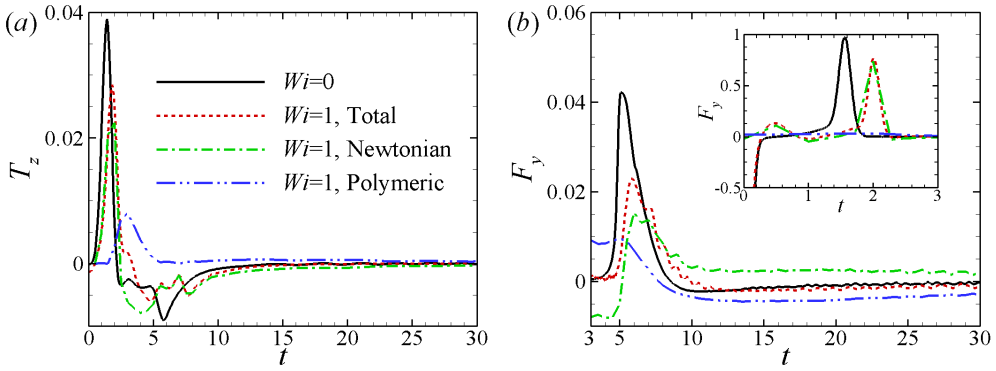


Figure 3.7. Time history of the decomposition of (a) torque and (b) vertical force exerted on the puller swimmer with $\beta = 3$ and $Wi = 1$. The inset in panel (b) demonstrates the evolution of the vertical force in short time.

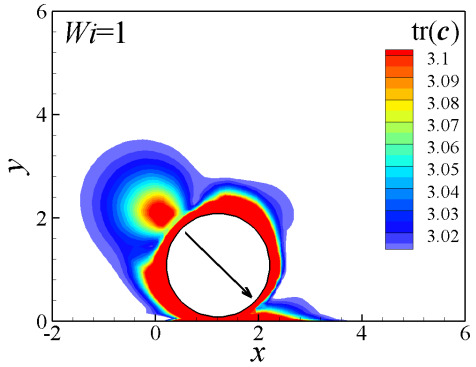


Figure 3.8. (Color online). Distribution of tr($\mathbf{C}$) at plane $z = 0$ around the puller with $\beta = 3$. The snapshot is taken at $t = 2$ immediately after the impact and the corresponding Weissenberg number is $Wi = 1$.

dynamic interactions, spends a brief period of time in the close proximity of the wall, and eventually escapes the wall. The temporal profiles of the vertical distance and inclination angle, shown in Figs. 3.5(a) and 3.5(b), clearly demonstrate this swimming strategy. However, the residence time of the puller swimmer is about one order of magnitude smaller compared to a neutral squirmer (see Fig. 3.6). Also, viscoelasticity of the background fluid does not alter the trapping time of a puller substantially, in

contrast to a neutral squirmer with analogous conditions. This discrepancy stems from the absence of polymeric negative torque after the impact of the puller with the wall as shown in Fig. 3.7(a). Due to specific swimming gait of a puller which imposes inward surface deformation, the polymer stretching around the swimmer poles is symmetric and no sizable elongated region is established behind the squirmer to pull it backward. The trace of the polymer conformation tensor, $\mathbf{C}$, defined as,

$$\mathbf{C} = \frac{Wi}{1-\beta_s}\boldsymbol{\tau}^p + \mathbf{I}, \tag{3.4}$$

indicates the intensity of polymer stretching. The snapshot of tr($\mathbf{C}$) shown in Fig. 3.8 shows that the locomotion of a puller, instead of rendering an elastic wake in the rear side, engenders stretching of the polymers mainly around its lateral sides perpendicular to the swimming direction. After a brief time interval, due to the growth of shear rate in the separating gap, the Newtonian shear stress significantly amplifies; leading to development of a vertical force, as depicted in Fig. 3.7(b), which provides sufficient thrust to escape the wall attraction. After separating from the nearby surface, a puller recovers its free swimming characteristics considerably faster than a neutral squirmer as illustrated in Figs. 3.5(c) and 3.5(d). The time scale of attaining steady state swimming behavior that is unaffected by the presence of the wall depends on the polymer relaxation time and slightly increases with Weissenberg number.

### 3.3.3 Pusher

The fluid viscoelasticity has a more dramatic effect on the near wall swimming motion of a pusher with $\beta = -3$. As depicted in the time history plots of the vertical distance and orientation angle shown in Figs.3.9(a) and 3.9(b), after approaching the surface, the pusher swimmer is strongly trapped by the wall and continues its swimming trajectory while maintaining a constant distance from the nearby boundary. Although in steady state, the pusher holds a small orientation angle ($\sim 5^\circ - 10^\circ$) away from the wall, it is incapable of escaping the confining effect of swimmer-wall hydrodynamic interaction. This behavior is in stark contrast with swimming strat-

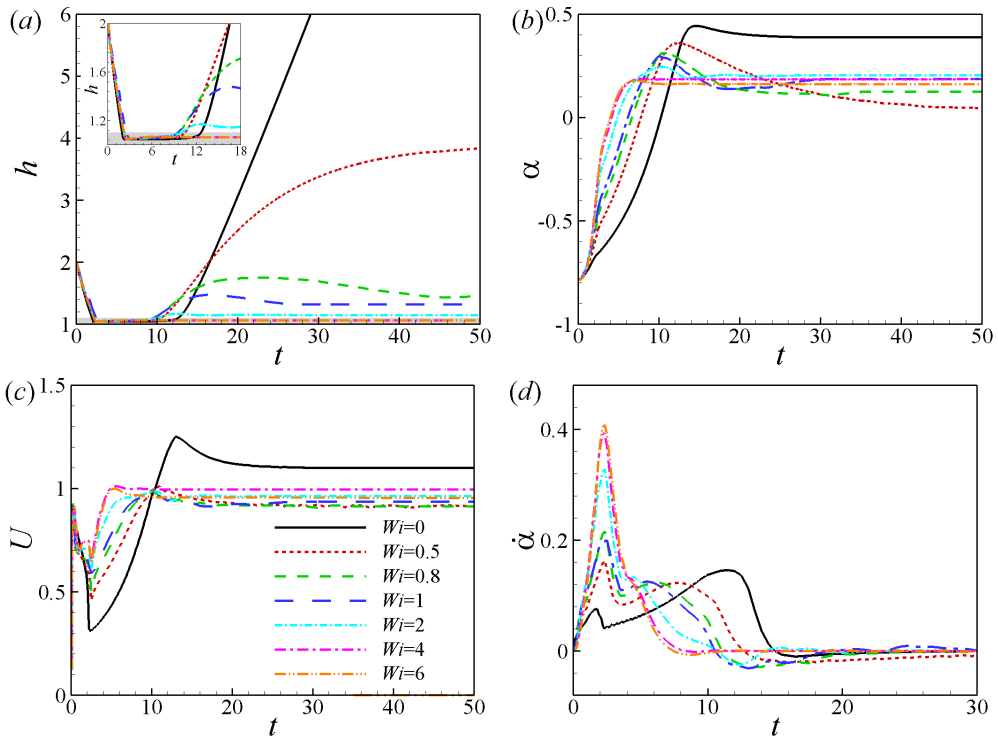


Figure 3.9. Temporal evolution of (a) separation distance, (b) orientation angle, (c) swimming speed, and (d) angular velocity for the pusher swimmer with $\beta = -3$. The inset in panel (a) illustrates the variation of the vertical distance over the trapping period.

egy of a pusher in a Newtonian fluid wherein the swimmer eventually reorients away and departs the nearby wall. The time scale of arriving at steady state decays with increasing the Weissenberg number. The steady state values of the vertical distance, inclination angle, and the velocity components for various values of $Wi$ are depicted in Figs. 3.10(a) and 3.10(b). The separation length scale dramatically decays with increasing $Wi$, however, the angle $\alpha$ varies within a limited range. Fig. 3.10(b) shows that in viscoelastic fluids, unlike the Newtonian case, the pusher swims along the horizontal direction parallel to the attracting boundary. The viscoelasticity also hinders the swimming speed compared to a Newtonian fluid. Further, by increasing the polymer relaxation time, the swimming speed grows and reaches a peak at $Wi = 4$.

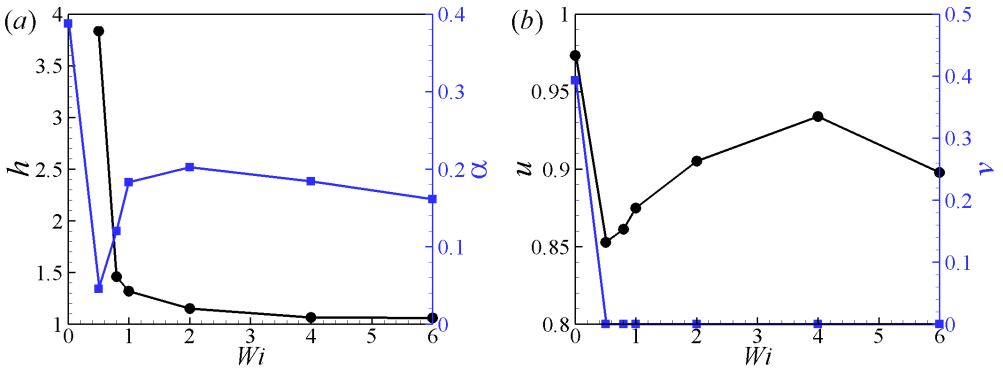


Figure 3.10. Steady state values of (a) vertical distance (black circles) and orientation angle (blue squares), and (b) velocity components in $x$ and $y$ directions (blacks circles and blue squares, respectively) as functions of the Weissenberg number for the pusher with $\beta = -3$.

In order to quantify the boundary effects on the pusher swimmer, we calculated the temporal profiles of torque and vertical force exerted on the squirmer. The results are shown in Figs. 3.11(a) and 3.11(b). Immediately after the impact, analogous to the neutral squirmer, a large polymeric torque is developed in negative $z$ direction which impedes the reorientation of the cell towards the fluid bulk. Subsequently, high values of shear rate arise in the constriction between the wall and the squirmer, leading to the formation of a positive torque due to the Newtonian viscous stress. The balance of these two torques leads to rotation of the cell away from the wall while maintaining a close distance with the surface. Contrary to the neutral squirmer where the viscous force becomes sufficiently strong to overcome the elastic drag, in case of the pusher swimmer, a wide region of stretched polymers is developed behind the squirmer's body which results in high elongational viscosities and thus, a large elastic drag which the Newtonian viscous force is unable to overcome. Since at steady state, the pusher is oriented away from the wall, the force generated due to the concentration of stretched polymers behind the squirmer draws it toward the nearby surface. On the other hand, the viscous force tends to separate the pusher from the wall and lessen the shear rate in the gap region. therefore, squirmer attains a kinetic balance

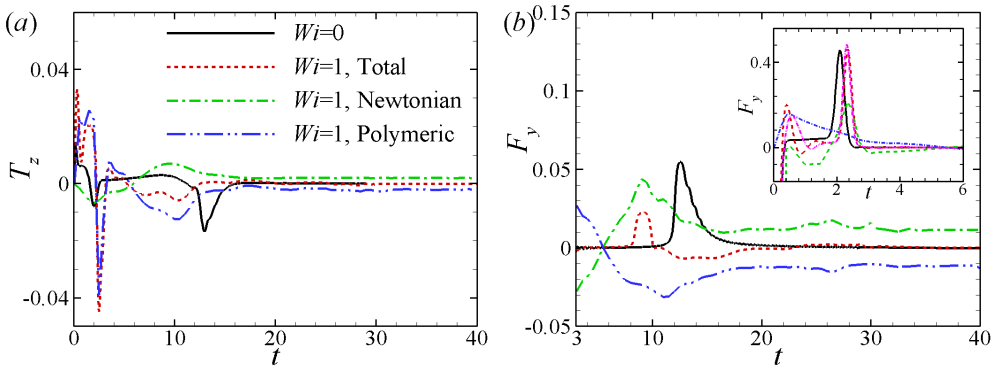


Figure 3.11. Time history of the decomposition of (a) torque and (b) vertical force exerted on the pusher with $\beta = -3$. The inset in panel (b) shows the evolution of the vertical force around the impact time.

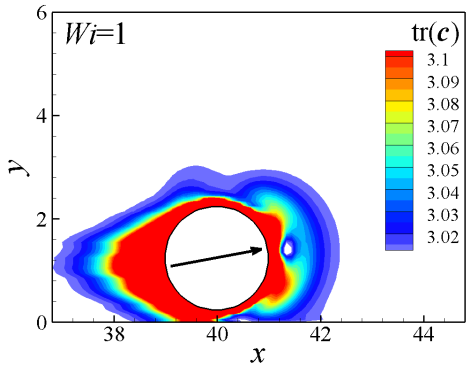


Figure 3.12. Distribution of tr($\mathbf{C}$) at plane $z = 0$ around the pusher squirmer with $\beta = -3$. The snapshot is taken at $t = 50$ and the corresponding Weissenberg number is $Wi = 1$.

and continues to swim in the vicinity of the surface. The distribution of the trace of the conformation tensor at steady state as depicted in Fig. 3.12 displays the strong elastic wake in the aft of the squirmer.

## 3.4 Concluding Remarks

In this work, we presented numerical results to demonstrate how the fluid viscoelasticity affects the swimming behavior of small organisms in the vicinity of rigid

surfaces. Studying this phenomenon is of prime importance in order to gain fundamental insights regarding the hydrodynamic interplay of motile cells with nearby substrates. Using the Giesekus constitutive model, we elucidated the near-wall dynamics of three types of squirmers with different swimming gaits, i.e. neutral squirmer (potential swimmer), puller (contractile swimmer), and pusher (extensile swimmer). These model swimmers cover a wide range of locomotion strategies typical of motile cells. Employing direct numerical simulations, the characteristics of the polymeric flow arising from swimmer-wall interactions are revealed and the underlying physical mechanisms affecting the swimmer dynamics are analyzed in depth.

In case of the neutral squirmer, we showed that the swimmer is capable of escaping the wall attraction due to the synergetic effects of the Newtonian viscous torque and vertical force. The former reorients the squirmer away from the surface, and subsequently the latter counterbalances the restraining effect of the stretched polymers. To better illustrate the spatial structure of the viscoelastic stresses and the configuration of elongated polymers, in Fig. 3.13, we have plotted ellipsoids that represent the geometric structure of the conformation tensor. The principal axes of the ellipsoids are aligned with the eigenvectors of $\mathbf{C}$, the axis lengths are scaled by corresponding eigenvalues, and the coloring is based on the value of the first normal stress difference ($N_1$) at the center of the ellipsoids. This visualization illustrates the distribution of polymer stretching and the associated stresses around the swimmer's body. All the snapshots are obtained at $t = 2$ immediately after the collision with the wall. Fig. 3.13(a) shows a strong polymer stress concentration and relatively high elongation viscosities in the aft of the neutral squirmer. The elongation field is asymmetric in vertical direction with more stretching in the lower portion of the swimmer near the rigid surface. The elastic drag generated by the elevated values of polymer stress behind the squirmer results in backward pulling and relatively long residence time of the swimmer in the proximity of the nearby wall.

Fig. 3.13(b) depicts the elongation and stress fields around a puller swimmer after its impact with the wall. Due to inward surface deformation of the puller,

around the swimmer's poles little stretching arise which is mostly in the tangential direction. In this case, polymer stretching predominantly occurs perpendicular to the swimming plane in the neighborhood of the squirmer's equator in $YZ$ plane. This kinetic configuration of the polymers combined with excessive shear stress beneath the squirmer lead to shorter trapping time and faster release of the puller compared to the neutral squirmer. Thus, the contractile ciliated microorganisms are expected to be least affected by the wall attraction and exhibit lower surface accumulation.

The geometric distribution of the eigenstructure of the conformation tensor for a pusher, as shown in Fig. 3.13(c), reveals that due to outward tangential deformation of an extensile swimmer, the polymers become highly stretched on the cell surface along the swimming direction. In particular, a largely elongated localized region is formed around the rear pole of the pusher, inducing an elastic drag which resists the locomotion of the swimmer. This configuration remains unchanged after reorientation of the cell and counteracts the releasing force which stems from the Newtonian viscous contribution. Hence, unlike the Newtonian case, the pusher is unable to escape the wall attraction in viscoelastic fluids. It is noticeable that, compared to other swimming gaits, the self-propulsion of the pusher engenders the highest rate of polymer elongation, especially around the swimmer's poles.

While the near-wall motion of bacteria in Newtonian fluids has been experimentally investigated in numerous studies [70,151,152], to the best of our knowledge, the cell-surface interactions in complex fluids still await experimentation. The insights gained through the present study can be corroborated by comparing the simulation results with experimental measurements in terms of the residence time and the cell trajectory after collision with wall. However, employing microorganisms incorporates complex biological factors in the experimental investigation and renders further difficulty to compare the outcomes with the results stemming from the simulation of squirmers. To remedy this problem, Thutupalli et al. [153] introduced a novel experimental technique which utilizes self-propelling liquid droplets to mimic the surface deformations of a squirmer. This methodology can be employed to further our

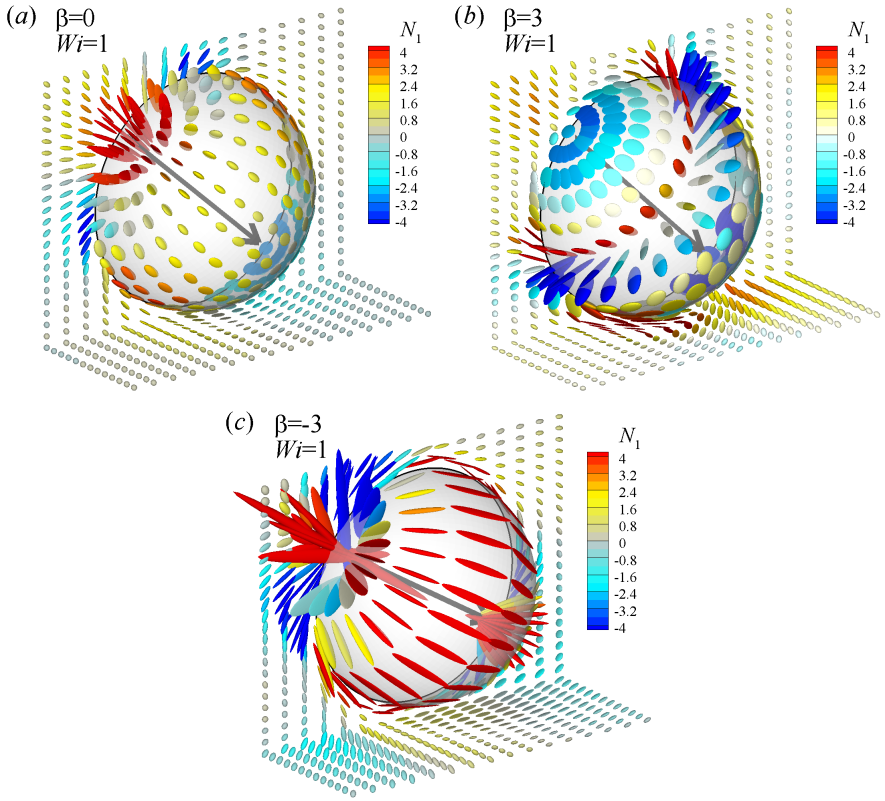


Figure 3.13. Snapshots of the conformation tensor and the polymer stress around (a) neutral squirmer with $\beta = 0$, (b) puller with $\beta = 3$, and (c) pusher with $\beta = -3$. The principal axis of each ellipsoid is aligned with the principal eigenvector of $\mathbf{C}$ and its length is scaled based on the associated eigenvalue. The minor axes correspond to the second and third eigenvectors of $\mathbf{C}$. The coloring is based on the value of the first normal stress difference at the centroid of each ellipsoid. The snapshots are taken at $t = 2$ after the collision and the corresponding Weisenberg number is $Wi = 1$.

knowledge regarding the hydrodynamic interaction solid walls with nearby squirmers swimming in viscoelastic media.

In this study, we quantified the impact of the Weissenbrg number on the residence time of the swimmers in proximity of solid surfaces. The associated outcomes can be utilized to enhance our understanding regarding the adhesion rate of the bacterial cells constituting a microbial community in viscoelastic media. In addition, this

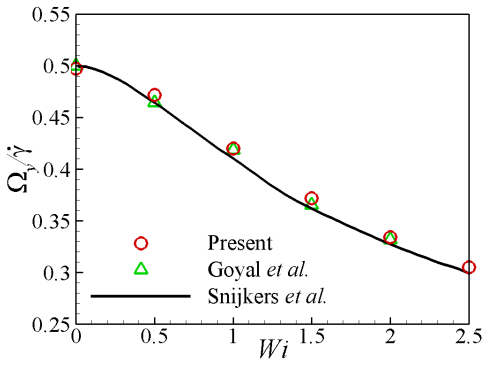


Figure 3.14. (Color online) Comparison of the steady angular velocity as a function of $Wi$ with the results of Snijkers et al. [154] and Goyal et al. [155].

investigation sheds light on the polymeric effects opposing the locomotion of three types of self-propelled particles near rigid walls. The insights gained through this study pave the way to design more efficient artificial swimmers via minimizing the unfavorable concentration of stretched polymers. The results presented in this work can be extended in several directions. For example, instead of using an idealized model of cell locomotion, more realistic models of microorganisms could be taken into account. Specifically, the helical structure and the rotation of flagella should be considered in more comprehensive simulations of motile bacteria. Further, the cell deformation could be captured more precisely by considering cell as a soft matter and simulating the associated fluid-structure interaction problem. Finally, hydrodynamic interactions of a group of swimmers pose an important theoretical challenge in order to resolve the collective behavior of microorganisms in viscoelastic media.

## 3.5 Appendix: Validation of the Numerical Method

In an Oldroyd-B fluid, we simulate the rotation of a single sphere in a shear flow to validate our numerical platform. Simulation is conducted in a rectangular domain of $[-2a, 2a] \times [-2a, 2a] \times [-4a, 4a]$ where $a$ is the radius of the sphere and the

sphere centered at (0,0,0). The flow is driven by two parallel plates at $z = -4a$ and $z = 4a$ moving opposite in $x$-direction with the same speed $U$. Periodic boundary conditions are applied in $x$ and $y$ directions. The mesh size is $\Delta = a/16$ and the time step is $\Delta t = 10^{-3}a/U$. The shear rate of the flow is $\dot{\gamma} = U/4a$, the Weissenberg number $Wi = \lambda\dot{\gamma}$ and the viscosity ratio $\beta_s = 0.5$. Fig. 3.14(a) shows the time evolution of the angular velocity of the sphere at different $Wi$. It is seen that for the Newtonian case, the sphere asymptotically reaches to its steady state of $\Omega_y = 0.5\dot{\gamma}$ while for viscoelastic cases, overshoots can be observed around $t\dot{\gamma} = 0.2$. In Fig. 3.14(b), the steady angular velocity as a function of $Wi$ is compared with previous experimental [154] and numerical [155] results. It is evident that our simulation results are in good agreement with the previous results.

The simulation is performed on a non-uniform structured grid with the smallest mesh size of $\Delta = D/40$ near the squirmer, where $D$ is the diameter of the spherical squirmer. The computational domain is $[-40a, 40a] \times [-40a, 40a] \times [-40a40a]$ and the squirmer is initially placed at (0,0,0). The time step is $\Delta t = 10^{-5}$. The Reynolds number defined as $Re = U_0 a/\nu$ is 0.01 in all the simulations, and $U_0 = 2B_1/3$. According to the analysis of a squirmer at finite Reynolds number, the swimming speed of a squirmer is determined by $U/U_0 \simeq 1 - 0.15\beta Re$ [74], thus the effects of the inertia on the swimming speed can be neglected in our simulation. The viscosity ratio is $\beta_s = 0.5$ and mobility factor is $\alpha_m = 0.2$. The Weissenberg number is defined as $Wi = \lambda B_1/a$. The swimming speed of the squirmer $U$ is plotted in Fig. 3.15 for squirmers with $\beta = -5$, 0, and 5. Our results show good agreement with the results obtained by Zhu et al. [95].

Convergence studies have been performed to examine the consistency of our simulations. As two typical cases, the near-wall motion of squirmers with $\beta = 0$ and $-3$ are calculated under different grid sizes and different time steps. Fig. 3.16 shows the time history of the distance $h$ away from the wall, orientation angle $\alpha$ and the swimming speed $U$ of the squirmer. The results from these different computations

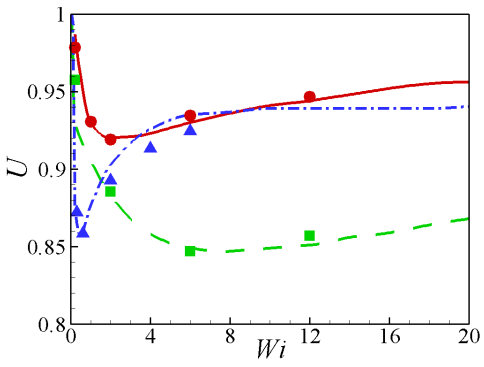


Figure 3.15. (Color online) Swimming speed $U$ as a function of the Weissenberg number $Wi$, for the neutral squirmer $\beta = 0$ (solid line: Ref. [95] and circles: present results), pusher $\beta = -5$ (dashed line: Ref. [95] and squares: present results) and puller $\beta = 5$ (dashdot line: Ref. [95] and triangles: present results). The Reynolds number is $Re = 0.01$ and the swimming speed is scaled by the squirmer's speed $U_0$ in a Newtonian fluid.

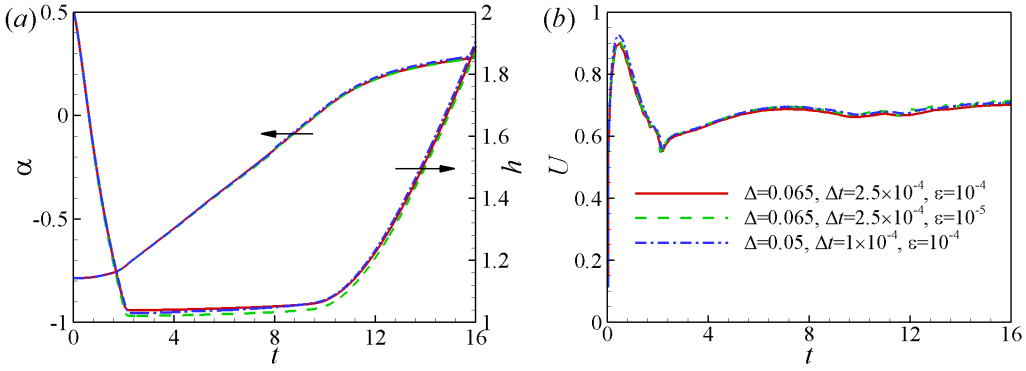


Figure 3.16. (Color online) Time history of (a) vertical distance $h$ and orientation angle $\alpha$ and (b) swimming speed $U$ of the neutral squirmer calculated using different grid sizes, different time steps and different values of the parameter $\epsilon$. The corresponding parameters are $Wi = 6$ and $Re = 0.1$ and the squirmer is initialized at $h_0 = 2$ and $\alpha_0 = -\pi/4$.

agree well with each other. It is confirmed that the computed results are independent of the mesh size and the time step.

When the squirmer lies in the close proximity of the surface, due to the lubrication effect and other non-hydrodynamic phenomena such as electrostatic charges, a repulsive force is developed which prevents intrusion of the swimmer's body into the wall. To capture the associated hydrodynamic squeezing effect, exceedingly fine grid resolutions are needed which make the corresponding simulations computationally highly demanding. In addition, as indicated in Ref. [81], hydrodynamic interactions are inadequate to prevent the swimmer-wall interference in some settings. Hence, in order to avoid overlapping of the squirmer's body and the nearby wall, we impose a short-range repulsive force [109] defined as,

$$\mathbf{F}_r = \frac{C_m}{\epsilon}\left(\frac{h - h_{\min} - h_r}{h_r}\right)\mathbf{e}, \tag{3.5}$$

where $h_{\min} = a$ is the minimum possible distance from the wall and $h_r$ represents the range over which the force is acting and is normally set to be the smallest grid size $\Delta$ in the computational domain [109]. The direction of the repulsive force $\mathbf{e}$ is considered to be perpendicular to the wall. The parameters $C_m = M_p U_0^2/a$ and $\epsilon = 10^{-4}$ denote a scaling factor and a small positive number, respectively, with $M_p$ being the mass of the squirmer. As demonstrated in Fig. 3.16, changing the value of $\epsilon$ have a negligible impact on the simulation results.

# 4. PARTICLE MIGRATION IN A CHANNEL FLOW OF VISCOELASTIC FLUIDS[1]

## 4.1 Motivation and Previous Works

Particle transport in a channel flow of Newtonian and non-Newtonian fluids has been widely studied for its importance in many industrial and biological applications. Depending on the flow conditions, inertial effect, proximity of the channel wall, fluid elasticity, shear-thinning, particle deformability, and particle-particle interaction may affect the dynamics of the particle motion and the flow field. Interplay between these effects result in various interesting phenomena, such as cross-streamline particle migration [156], particle focusing at the channel centerline [157, 158], wall-surface accumulation of particles [159, 160], self-assembly of two particles [161], and the particle-induced lateral transport of the fluid [162]. These phenomena have been successfully used for the manipulation of cells and particles suspended in microfluidic platforms.

The two most important dimensionless parameters of the problem are the flow Reynolds number and the Weissenberg number, quantifying inertia and elasticity effects, respectively. The flow Reynolds number is defined as $Re = \rho U_c H/\mu$, where $U_c$ is the characteristic flow velocity, such as the velocity at the channel centerline, $H$ is the characteristic length scale in the channel cross-sectional plane, $\rho$ is the fluid density, and $\mu$ is the fluid zero shear viscosity. The Weissenberg number is defined as $Wi = \lambda U_c/H$, where $\lambda$ is the relaxation time of the fluid. The ratio between these two parameters gives the elasticity number $El = Wi/Re = \lambda\mu/\rho H^2$, which only depends on the channel dimension and fluid properties. Other important parameters

[1]This chapter has been published in "Dynamics of particle migration in channel flow of viscoelastic fluids", by G. Li, G. H. Mckinley and A. M. Ardekani, in Journal of Fluid Mechanics, 785: 486-505, 2015 (reproduced with permission).

include, the geometry of the channel, the strength of the shear-thinning effect, the initial position of the particle, and the block ratio defined as $d/H$, where $d$ is the particle diameter.

Cross-streamline migration of particles was first observed in a Newtonian fluid ($El = Wi = 0$) by [156]. In a tube flow, initially randomly distributed particles gradually pinch into a narrow annulus at around 0.6 radius, resulting in the "tubular pinch" effect. This phenomenon was later confirmed in several experimental [163, 164], analytical [165] and numerical [166,167] studies. Similar phenomenon occurs in square- and rectangular-shaped channels, where particles accumulate at the center of each wall [168–172]. Inertia is necessary for this phenomenon, and the balance of two competing effects, the shear-gradient lift force [173] and the wall repulsive force [174], determines the equilibrium position of the particles. These two forces scale differently in the centerline and near-wall regions and both depend on the Reynolds number [164] and block ratio [171, 175]. By properly designing the geometry of apparatus, this effect is used in cell and particle focusing, sorting, separation, filtration, enrichment, and trapping. Review articles by [176] and [177] provide a comprehensive discussion of the progress and future directions in this area.

In a channel flow of viscoelastic fluids, the particle migration shows a different behavior depending on the fluid rheology. For example, particles move towards the centerline in viscoelastic fluids of constant viscosity, whereas they move towards the walls in a shear-thinning fluid [159, 160]. Particles also move towards the centerline in solutions of moderately cross-linked polymers, whereas little or no migration is observed in solutions of highly cross-linked polymers [178]. Under the assumption of zero Reynolds number and small block ratio, [179] showed that a lateral force, originated from the normal stress difference, drives the particle towards the lower-shear region in a second-order fluid. This conclusion has been verified in other experiments and simulations, where particles move to the central axis of a circular tube [157, 180, 181] and to both centerline and corners in a rectangular channel [182]. The shear-thinning behavior of the fluid is found to have a large effect when the inertia or

elasticity is large [183]. Based on simulations of Geisekus and Phan Thien-Tanner constitutive equations, [184,185] and [180] observed a bistable dynamics of the particle in shear-thinning fluids, i.e. the particle may move towards the channel centerline or the closest wall depending on its initial position. The same behavior is also observed in experiments [186]. The second normal stress difference induces a secondary flow in a non-circular channel, which may directly affect the particle motion [185]. A recent review article about particle dynamics in viscoelastic fluids can be found in [187].

These studies are mostly conducted in flows with dominated elastic effects, where the Reynolds number is small ($El > 0, Re \simeq 0$). The synergetic effect of elastic and inertial forces ($El > 0, Re > 0$) result in a different particle migration behavior. For example, even in a weak inertia regime in a rectangular channel of viscoelastic fluid, the equilibrium positions at the corners become unstable and particles focus only at the channel centerline [182]. This elasto-inertial particle focusing in the range of low Reynolds number ($Re \sim 10^{-2} - 10^{-1}$) and high elasticity number ($El \sim 10^{1} - 10^{2}$) is destabilized as the channel Reynolds number increases beyond order unity [157,182]. On the contrary, a recent study by [158] show that stable particle focusing at the channel centerline can be achieved in weakly viscoelastic flows at a high Reynolds number ($El \sim 0.1, Re \sim 2000$). Their experiments illustrated particle focusing at very high flow rates. Another recent study by [188] showed that the flow rate, block ratio and shear-thinning properties of viscoelastic fluids have complex effects on the particle migration in a square microchannel in the presence of elastic and inertia effects.

Despite the above mentioned numerical and experimental studies, there exist gaps in the parameter space, where the mechanism of particle migration due to combined effects of rheological properties of viscoelastic fluids, flow conditions, and particle-fluid interaction is poorly understood. Experiments have some limitations in providing all the detailed information, and most previous simulations are conducted in flows with

either inertia ($El = 0$) or elastic ($Re = 0$) effects, and the synergetic effects of the two forces for spherical particles have not been numerically investigated.

In the present study, we investigate the particle migration in a square channel by means of three-dimensional direct numerical simulations. Our simulations include the effects of the fluid elasticity, shear-thinning and normal stress coefficients in a relatively large range of parameters by using Oldroyd-B and Geisekus constitutive equations. Besides the migration dynamics of the particle, we also study some other less-explored aspects of the problem such as the particle-induced fluid transport and the transient behavior during the flow start-up.

## 4.2 Mathematical Model and Numerical Method

In this study, we consider the motion of a rigid particle in a straight square channel filled with a viscoelastic fluid. A Cartesian reference frame is considered with its origin at the center of the channel cross-section. The computational domain spans over $[-L/2, L/2]$ in $x$, $[-H/2, H/2]$ in $y$ and $[-H/2, H/2]$ in $z$ directions. Initially, the fluid is at rest and a constant pressure gradient $G$ is imposed along the $x$-direction at time $t = 0$ to drive the channel flow. In what follows, the length is scaled by the channel width $H$, velocity by $U_0 = 4kGH^2/\pi^3\mu$, time by $H/U_0$, shear and angular velocity by $U_0/H$, density by $\rho$ and pressure and stress by $\mu U_0/H$, where $k$ is a constant, depending on the geometry of the channel. For a square-shaped channel, $k = \sum_{n,odd}^{\infty} \frac{1}{n^3}(1 - \operatorname{sech}\frac{n\pi}{2}) \simeq 0.571$. In Newtonian and Oldroyd-B fluids, $U_0$ is equal to steady centerline velocity of the channel $U_c$ [189], whereas in shear-thinning fluids $U_c > U_0$. The particle is neutrally buoyant and has a spherical shape with diameter $d$. The block ratio is set to $\kappa = d/H = 0.25$, unless otherwise stated. The particle has zero translational and rotational velocity and is initially located at $\boldsymbol{X}_p^0 = (0, 0.25, 0)$, unless otherwise stated. The rigid-body motion of the particle is described by the translational velocity $\boldsymbol{U}_p = (U_p, V_p, W_p)$ and angular velocity $\boldsymbol{\Omega}_p = (\Omega_x, \Omega_y, \Omega_z)$.

A distributed Lagrange multiplier method is used in our simulations and details of the method can be found in [108]. The entire domain is treated as a fluid, and a forcing term $\boldsymbol{f}$ is added inside the particle domain to enforce the rigid body motion of the particle. The dimensionless governing equations for an incompressible fluid are

$$Re_G(\frac{\partial \boldsymbol{u}}{\partial t} + \boldsymbol{u}\cdot\nabla\boldsymbol{u}) = -\nabla p + \nabla\cdot\boldsymbol{\tau} - \frac{\pi^3}{4k}H(t)\boldsymbol{e}_x + \boldsymbol{f}, \tag{4.1a}$$

$$\nabla\cdot\boldsymbol{u} = 0, \tag{4.1b}$$

$$\boldsymbol{u}\mid_{y,\, z=\pm 0.5} = 0, \qquad \frac{\partial \boldsymbol{u}}{\partial x}\mid_{x=\pm L/H} = 0, \qquad \boldsymbol{u}\mid_{t=0} = 0 \tag{4.1c}$$

$$\boldsymbol{X}_p\mid_{t=0} = \boldsymbol{X}_p^0, \qquad \boldsymbol{U}_p\,,\ \boldsymbol{\Omega}_p\mid_{t=0} = 0, \tag{4.1d}$$

where $Re_G = \rho U_0 H/\mu = 4k\rho G H^3/\pi^3\mu$ is the Reynolds number based on the pressure gradient. The flow Reynolds number is equal to $Re = Re_G$ in Newtonian and Oldroyd-B fluids, while $Re > Re_G$ in shear-thinning fluids. Here, $\boldsymbol{u}$ is the fluid velocity, $p$ is the pressure, $\boldsymbol{\tau}$ is the total deviatoric stress tensor, $H(t)$ is the Heaviside function, and $\boldsymbol{e}_x$ is the unit vector along the $x$-direction. The forcing term $\boldsymbol{f}$ is calculated in an iterative procedure to ensure the rigid motion of the particle

$$\boldsymbol{f} = \boldsymbol{f}^* + Re_G\frac{\phi}{\Delta t}(\boldsymbol{U}_p + \boldsymbol{\Omega}_p\times(\boldsymbol{x}-\boldsymbol{X}_p) - \boldsymbol{u}), \tag{4.2}$$

where $\boldsymbol{f}^*$ is the force from the previous iteration, $\phi$ is the volume fraction occupied by the particle in each computational cell ($\phi = 1$ inside, $\phi = 0$ outside and $0 < \phi < 1$ for the cells at the surface of the particle), $\boldsymbol{U}_p$ and $\boldsymbol{\Omega}_p$ are determined by

$$\boldsymbol{U}_P = \frac{1}{M_p}\int_{\mathbb{P}}\frac{\rho_p}{\rho}\boldsymbol{u}dV, \qquad \boldsymbol{\Omega}_P = \mathbf{I}_p^{-1}\int_{\mathbb{P}}\frac{\rho_p}{\rho}(\boldsymbol{x}-\boldsymbol{X}_p)\times\boldsymbol{u}dV, \tag{4.3}$$

where $\mathbb{P}$ represents the particle domain, $\rho_p/\rho$ is the ratio of the particle density to the fluid density, which is equal to unity in all our simulations. $M_p$ and $\mathbf{I}_p$ are the dimensionless mass and moment of inertia of the particle, respectively. Particle mass

and moment of inertia are scaled by $\rho H^3$ and $\rho H^5$, respectively. Eq. (4.1), (4.2) and (4.3) recover to the Newton's second law for the particle as shown in [49].

The total deviatoric stress tensor, $\boldsymbol{\tau}$, can be split into contributions from solvent and polymer as $\boldsymbol{\tau} = \boldsymbol{\tau}^s + \boldsymbol{\tau}^p$. The Newtonian viscous stress is defined as $\boldsymbol{\tau}^s = \beta^s(\nabla \boldsymbol{u} + \nabla \boldsymbol{u}^{\mathrm{T}})$, where $\beta^s$ is the ratio of the solvent viscosity to the zero shear viscosity of the polymeric material. In all our simulations of viscoelastic fluids, $\beta^s = 0.1$. To characterize the evolution of the polymer stress, we utilize the Giesekus constitutive equation [149] which captures the constrained elongation of the polymers and the shear-thinning behavior of the polymeric material. In a dimensionless form, the associated equation can be written as

$$\boldsymbol{\tau}^p + Wi_G \overset{\triangledown}{\boldsymbol{\tau}}^p + \frac{Wi\,\alpha}{1-\beta^s}\boldsymbol{\tau}^p \cdot \boldsymbol{\tau}^p = (1-\beta^s)(\nabla \boldsymbol{u} + \nabla \boldsymbol{u}^{\mathrm{T}}), \tag{4.4}$$

where $Wi_G = \lambda U_0/H = 4k\lambda GH/\pi^3\mu$ is the Weissenberg number and $\lambda$ is the polymer relaxation time. The mobility factor, $\alpha$, represents the anisotropy of the hydrodynamic drag exerted on the polymer molecules by the surrounding solute molecules. Based on the thermodynamic analysis, the mobility factor must be in the range of 0 to 1/2 [150]. For special case of $\alpha = 0$, the Giesekus model reduces to the Oldroyd-B model. Similar to the Reynolds number, $Wi = Wi_G$ in Newtonian and Oldroyd-B fluids, and $Wi > Wi_G$ in a Giesekus fluid. The notation $\overset{\triangledown}{\mathbf{A}}$ represents the upper-convected derivative

$$\overset{\triangledown}{\mathbf{A}} = \frac{\partial \mathbf{A}}{\partial t} + \boldsymbol{u} \cdot \nabla \mathbf{A} - \nabla \boldsymbol{u}^{\mathrm{T}} \cdot \mathbf{A} - \mathbf{A} \cdot \nabla \boldsymbol{u}. \tag{4.5}$$

Simulations are conducted in a non-inertial frame moving with a velocity $U_p \boldsymbol{e}_x$ so that the center of the particle is fixed in $x$-direction. The velocity of the fluid in the non-inertial frame becomes $\boldsymbol{u}' = \boldsymbol{u} - U_p \boldsymbol{e}_x$ and the governing Eq. (4.1) can be rewritten for variable $\boldsymbol{u}'$. The finite volume method based on the staggered grid is used for the computations. A conventional operator-splitting method is applied to enforce the continuity equation. The second-order total variation diminishing (TVD) Runge-Kutta method is used for time marching. The spatial derivatives in

the convection term are evaluated using the quadratic upstream interpolation for convective kinetics (QUICK) scheme and the diffusion terms are discretized using the central difference scheme. The viscoelastic stress is solved using a commonly used formulation denoted as elastic and viscous stresses splitting (EVSS) method [190]. The grid size $\Delta = 0.0125$ (20 grids across the particle diameter) is uniform in $y$-, $z$-directions and in a domain $x_f \in [-0.2, 0.2]$ near the particle in the $x$-direction. The grids are gradually stretched in the $x$-direction outside this domain moving away from the particle. The computational domain along the $x$-direction is $[-8, 8]$, and the dimension of the channel cross section in $y$-$z$ plane is $[-0.5, 0.5] \times [-0.5, 0.5]$. The time step is $\Delta t = 10^{-5} - 10^{-4}$ depending on the Reynolds number.

This method has been extensively used for the motion of particles in fluids and verified in our previous publications of inert particles in Newtonian fluids of homologous density [108, 116] and density-stratified fluids [110], and active squirming particles in Newtonian [49] and viscoelastic fluids [50]. Convergence studies have been performed to assess the effects of grid resolution, time step, and domain size. The computed results are independent of the mesh size, time step, and domain size as shown in figure 4.1. The calculations in a non-inertial frame are also compared with the same case performed in a laboratory-fixed frame. In the laboratory-fixed simulation, the particle is able to freely move in all three directions. Uniform grid is used in the entire computational domain and periodic boundary conditions are used at both inlet and outlet of the channel. The migration velocity of the particle in the laboratory-fixed simulation has some oscillations because of the relative motion of the particle and the fixed grid that is intrinsically caused by the numerical method [191]. By conducting the simulations in a particle-fixed coordinate system (only fixed in the $x$-direction), the oscillations can be greatly reduced since the relative motion of the particle and the grid in the streamwise direction is zero.

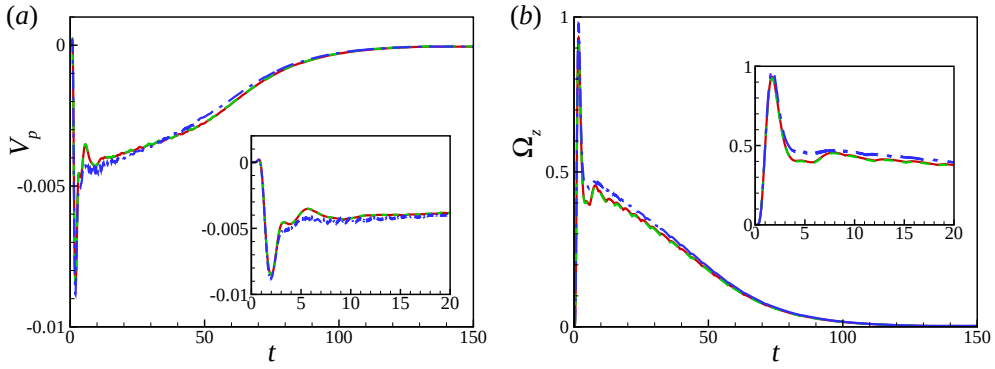


Figure 4.1. Comparison of the time history of $(a)$ migration velocity $V_p$ and $(b)$ angular velocity $\Omega_z$ of the particle. The corresponding parameters are $Re_G = 18.9, El = 0.05, \alpha = 0.0$ and $\kappa = 0.25$. Red solid lines: finest grid size $\Delta = 0.0125$ with 20 grids across the particle diameter, time step $\Delta t = 10^{-4}$, the domain size in the $x$-direction is $x \in [-8, 8]$ and the domain size with a uniform fine grid is $x_f \in [-0.2, 0.2]$. Green dashed lines: $\Delta = 0.00625$, $\Delta t = 2 \times 10^{-5}$, $x \in [-12, 12]$ and $x_f \in [-0.4, 0.4]$. Blue dashdot lines: $\Delta = 0.0125$, $\Delta t = 10^{-4}$ and $x = x_f \in [-1.6, 1.6]$.

## 4.3 Results

In this section, the simulation results of the particle migration in a channel flow of a viscoelastic fluid is discussed. The simulation parameters are: $Re_G \sim 3 - 300, El \sim 0 - 0.2, Wi_G \sim 0 - 3, \alpha = 0, 0.1$ and $0.2$, and $\kappa = 0.25$ and $0.125$, the flow Reynolds and Weiseenberg numbers are $Re \sim 3 - 1000$ and $Wi \sim 0 - 15$. We first show the steady flow field for three different cases. We then discuss the dynamics of particle migration in section 4.3.2. In section 4.3.3, the particle-induced fluid transport in the channel will be investigated. Finally in section 4.3.4, we will discuss the transient behavior of the flow field during the flow start-up as well as its effects on the particle migration.

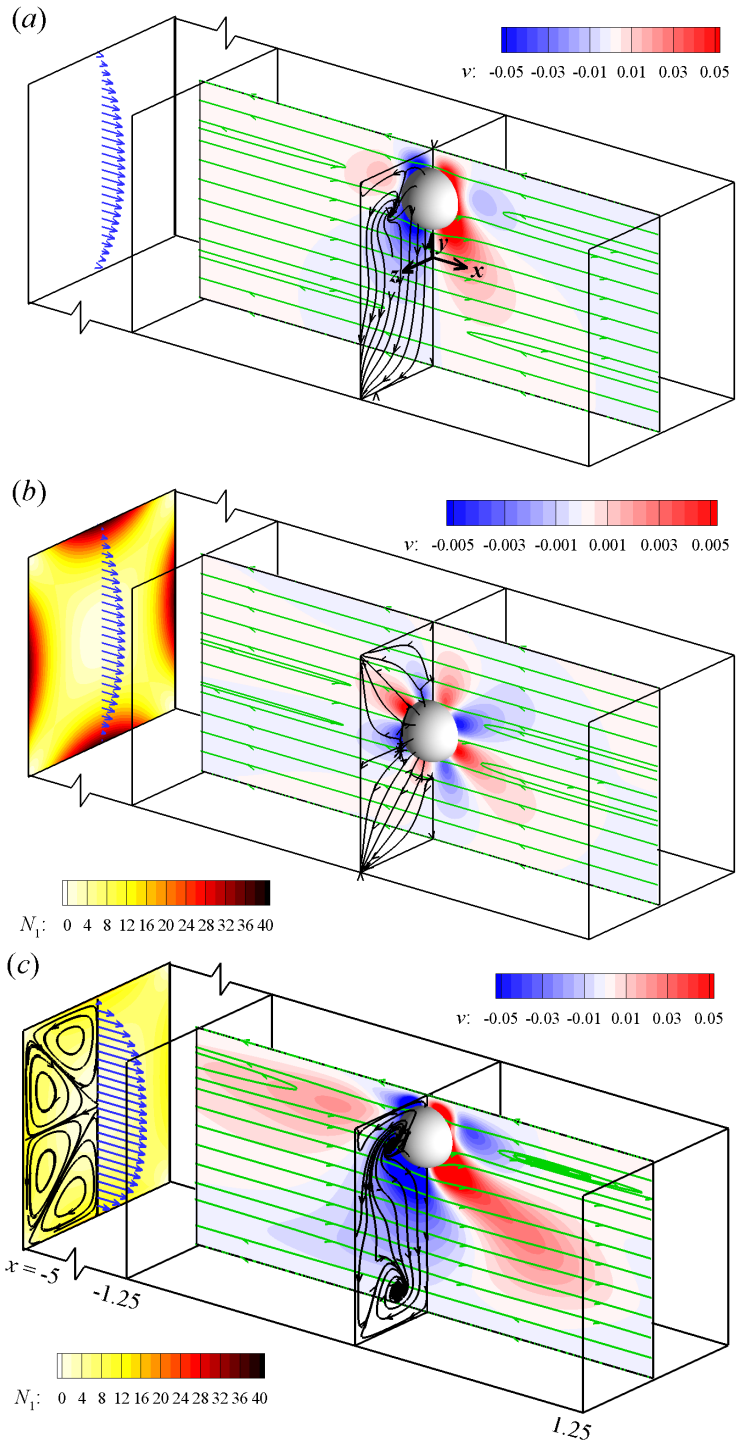


Figure 4.2. Steady flow field around the particle in a channel filled with ($a$) Newtonian, ($b$) Oldroyd-B fluid of $El = 0.05$ and ($c$) Giesekus fluid of $El = 0.05, \alpha = 0.2$. The Reynolds number in all cases is $Re_G = 18.9$. The far left planes show the velocity profile, first normal stress distribution, and secondary flow at the inlet of the channel. In the $z = 0$ plane, streamlines (green lines) are plotted in the frame of reference fixed to the particle center. In the $x = 0$ plane, streamlines (black lines) are plotted using the velocity field projected on the $x = 0$ plane.

### 4.3.1 Steady Flow Field

Figure 4.2 shows the steady flow field in a channel of Newtonian, Oldroyd-B and Geisekus fluids after the particle has reached to its equilibrium position. The Reynolds number is the same in all cases $Re_G = 18.9$, the elasticity number is $El = 0.05$ in both Oldroyd-B and Giesekus fluids, and $\alpha = 0.2$ for the Geisekus fluid. Far away from the particle, the flow velocity (blue arrows) in the Oldroyd-B channel shows the same distribution as in the Newtonian Poiseuille flow in a square channel [189]. While in a Geisekus fluid, the velocity profile is more flat near the center of the channel and a larger maximum velocity is achieved due to the shear-thinning effect. A secondary flow consisting of eight vortices (black lines) is generated because of the second normal stress difference. These vortices induce a fluid flow from the channel centerline to the wall center; it then returns to the centerline from the corners. The first normal stress difference, defined as $N_1 = \tau_{xx} - \tau_{yy}$ is non-zero in viscoelastic fluids and its spatial gradient leads to the elasto-migration of the particle [179, 192]. The first stress difference is mainly generated near the four walls of the channel, whereas it is much weaker at the center and four corners of the channel. This particular distribution in a rectangular channel is considered to be the main reason behind the particle accumulation at the channel center and corners [182, 188]. The shear-thinning effect reduces the first normal stress difference. We will illustrate that, in a Geisekus fluid, a different particle migration occurs compared to that in an Oldroyd-B fluid due to the variation in the distribution of the first normal stress difference and secondary flows.

The equilibrium position of the particle may be close to the wall, as in Newtonian and Geisekus fluids, or at the centerline, as in an Oldroyd-B fluid. In all three cases, the streamlines in the $z = 0$ plane (green lines) are reversed due to the confinement of the flow [162, 193], indicating a particle-induced convection along the flow direction. In the cross-sectional plane of $x = 0$, the streamlines (black lines) show particle-induced convection of different flow patterns depending on the fluid prop-

erties. In Newtonian and Geisekus fluids, in-plane vortices are generated and the flow has an overall net transport towards the negative $y$-direction. In an Oldyroyd-B fluid, the fluid flows away from the particle. Besides the difference in flow patterns, the contourplots of $v$ in the $z = 0$ plane show that the magnitude of $v$ is an order of magnitude smaller in an Oldroyd-B fluid compared to Newtonian and Giesekes fluids. In a Geisekus fluid, the flow field shows more asymmetry around the particle in the $x$-direction compared to a Newtonian fluid. Since both enhanced velocity magnitude and flow asymmetry around the particle increase the particle-induced lateral transport in a channel, we expect a better fluid transport property in a Geisekus fluid. The particle-induced transport will be quantified in more details in section 4.3.3.

### 4.3.2 Dynamics of Particle Migration

Figure 4.3 shows the time history of the particle lateral position $Y_p$ under different flow conditions, where particles are released from the initial position $Y_p^0 = 0.25$ or $Y_p^0 = 0.1$. In a Newtonian fluid, the particle gradually migrates to a place near the channel wall with the equilibrium position $Y_p^e \simeq 0.3$, which is the same as the result of [171] at a similar Reynolds number. This equilibrium position is determined by the balance between two opposing forces: (1) the shear-gradient lift force originating from the curvature of velocity profile in confined flows which moves the particles away from the centerline of the channel [173], and (2) the wall repulsion force arising from the asymmetry of the corresponding wake vorticity distribution which pushes the particles away from the walls [174].

In viscoelastic fluids, the particle migration is much more complex, and it depends on the fluid rheological properties. Besides the two forces in a Newtonian fluid, the elastic force, shear-thinning effects and secondary flow may affect the particle migration. In Oldroyd-B fluids, particle moves towards the centerline and its equilibrium position dependents on both the Reynolds number and elasticity number. In flows of small $Re_G$ and $El$, the migration stops before the particle reaches the centerline.

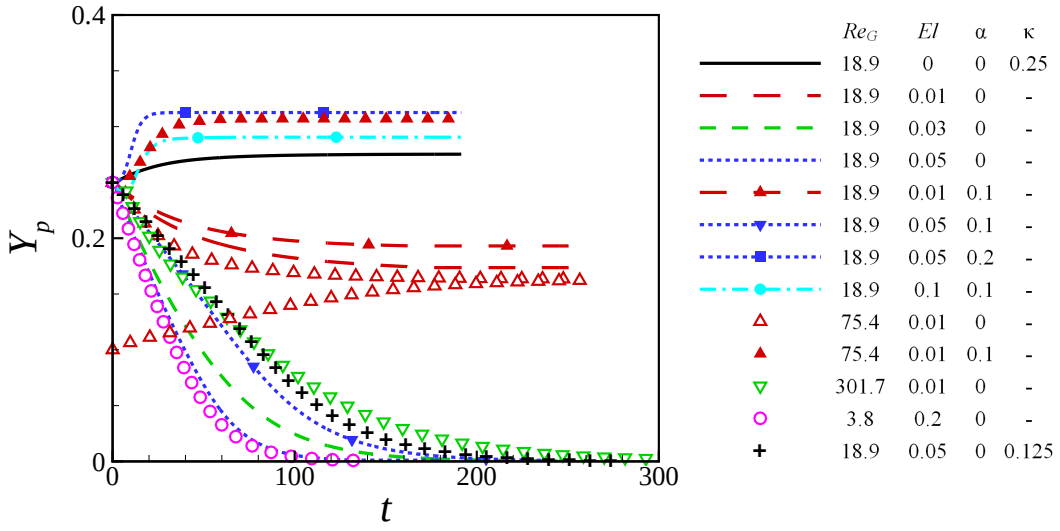


Figure 4.3. Time history of lateral position of the particle $Y_p$ at different flow conditions.

There exist multiple equilibrium positions for the particle between the wall and the centerline, depending on the flow parameters. At higher $Re_G$ or higher $El$, for example $Re_G = 18.9, El = 0.05$ and $Re_G = 301.7, El = 0.01$, particle eventually migrates to the centerline of the channel, i.e. particle focusing is achieved. This elasto-focusing phenomena has been observed in channel flows of $Re \sim 0 - 10^{-1}, El \sim 10^{0} - 10^{2}$ in experiments [157, 180–182, 192] and simulations [180, 184, 194], and recently in flows of $Re \sim 10^{3}, El \sim 10^{-1}$ [158]. Here we show that the critical elasticity number $El_c$ for particle focusing is of the order $O(10^{-2})$. For a given $Re_G$ and $El$, the particle migrates slower in a channel with a smaller block ratio $\kappa$, as observed in previous experiments [157, 158]. Compared to the two-dimensional cases in [195], particle focusing in a three-dimensional channel is easier for large particles. In their simulations, a particle with a block ratio of $\kappa = 0.25$ is attracted to the wall at $Re_G = 5$ and $Wi = 0.2$, even if released at the centerline of the channel. This is due to a strong elastic force generated from the compression of streamlines for a large block

ratio, which pushes the particle towards the wall [195]. In a three-dimensional case, however, the compression of the streamlines is weaker.

When the Reynolds number $Re_G$ increases, the equilibrium position of the particle $Y_p^e$ moves towards the channel wall in a Newtonian fluid, whereas in an Oldroyd-B fluid of a given elasticity number, it moves towards the centerline (see the inset of figure 4.4($a$)). The equilibrium position of the particle is independent of its initial position in an Oldroyd-B fluid [195]. Here, we quantify the dependence of the particle equilibrium position $Y_p^e$ on $Re_G, El$ and $Wi$. The critical elasticity number $El_c$, beyond which particle focusing occurs, are high at small Reynolds numbers, but it decreases dramatically at higher $Re_G$. The critical Weissenberg number $Wi_c$ increases with Reynolds number and roughly shows a linear relationship with $Re_G$. Another interesting phenomenon shown in both figure 4.3 and the inset of figure 4.4($a$) is that equilibrium position for most particles in an Oldroyd-B fluid is either at $Y_p \lesssim 0.15$ or at the channel centerline. The reason for such a behaviour is due the peak of inertial force at $Y_p \simeq 0.15$, and it can be explained by the following analysis. In elasticity dominated flows, [179] showed that the elastic force drives the particle migration to the region of lower normal stresses, in a two-dimensional second-order fluid, the viscoelastic force on the particle is given by

$$F_e^* = -\frac{20\pi}{3}\frac{d^3}{H}Y_p\left(\Psi_1 - 2\Psi_2\right)\left(\frac{U_c}{H}\right)^2, \tag{4.6}$$

in which $Y_p$ is the dimensionless vertical position of the particle from the channel centerline. Superscript $*$ refers to dimensional variables. $\Psi_1$ and $\Psi_2$ are the first and second normal stress coefficients of the fluid, respectively. The negative sign indicate the force drives the particle towards the center of the channel. If we further assume $\Psi_1 = 2\mu(1-\beta_s)\lambda$ and $\Psi_2 = 0$ as in a Poiseuille channel flow of Oldroyd-B fluid, the above equation further reduces to

$$F_e^* = -\frac{40}{3}\pi\rho U_c^2 d^2 \kappa El\left(1-\beta_s\right)Y_p. \tag{4.7}$$

These equations and the corresponding expression for the migration velocity have been widely used in pervious experimental studies of elasticity dominated channel

flows [178, 180–182, 188, 192]. Particularly, [181] showed that a modification of Eq. (4.7) can provide a very good estimate for the migration velocity in a circular channel at very low Reynolds and high elasticity numbers.

In Newtonian fluids, the inertia effects push the particle away from both the walls and the center. [171] showed that the inertia force follows two different scaling laws in near-wall and center regions. The shear-gradient lift force, which causes the particle to migrate away from the central axis, has the formula

$$F_i^{s*} = \rho U_c^2 d^2 \kappa C_2(Y_p), \qquad Y_p \lesssim 0.3. \tag{4.8}$$

The wall repulsion force, which pushes the particle away from the walls and prevents the wall collision, has the formula

$$F_i^{w*} = -\rho U_c^2 d^2 \kappa^4 C_1(Y_p), \qquad Y_p \gtrsim 0.3. \tag{4.9}$$

$C_1, C_2$ are two positive functions of $Y_p$. $C_1$ has a maximum value of around 0.05 at $Y_p \simeq 0.15$, and it is equal to zero at both $Y_p = 0$ and $Y_p \simeq 0.3$; $C_2$ increases monotonically from 0 at $Y_p \simeq 0.3$ to around 12 when particle reaches to the wall [171]. Similar results can also be found in the analysis of [196] for a two-dimensional Poiseuille flow at low Reynolds number $Re \ll \kappa^2$, in which the scaling is given as $F_i^* = C_3(Y_p)\rho U_c^2 d^2 \kappa^2$ in the entire domain and the peak of $C_3$ occurs around 0.24 at $Y_p \simeq 0.15$. The particle migration is mainly determined by the competition between the elastic force $F_e^*$ and the inertia force $F_i^{s*}$ caused by the shear-gradient lift force. The peak value of $F_i^{s*}$ can determine whether or not the particle can be focused at the centerline. In flows of high $El$, the elastic force overcomes the maximum inertia force and the particle migrates towards the centerline. However in flows of low $El$, the particle stops at a location before $F_i^{s*}$ reaches its maximum. A balance between (4.7) and (4.8) at $Y_p \simeq 0.15$ leads to an estimate for the critical elasticity number $El_c \simeq 0.01$ for an Oldroyd-B fluid. The analysis of [196], on the other hand, leads to $El_c \simeq 0.04\kappa$, which gives the same estimate for $\kappa = 0.25$. This prediction agrees with the present simulation results for high $Re$ as shown in figure 4.4. The prediction fails

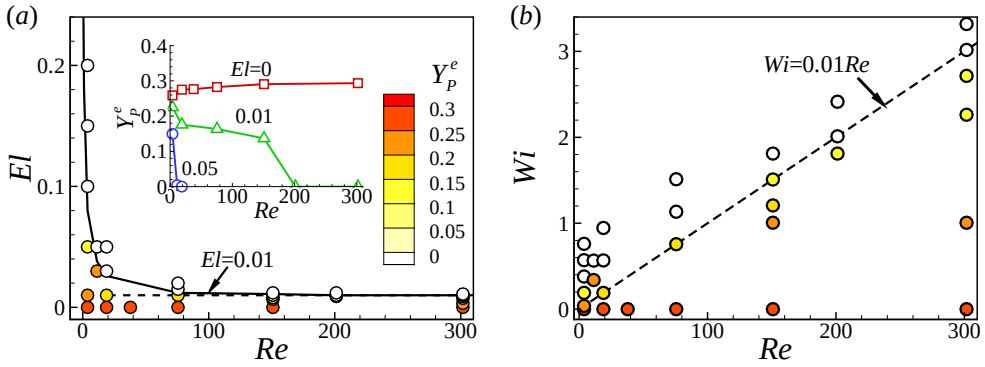


Figure 4.4. Dependence of the particle equilibrium position on $(a)$ $Re, El$ and $(b)$ $Re, Wi$. Please note that $Re = Re_G$ and $Wi = Wi_G$ in Newtonian and Oldroyd-B fluids. The inset in $(a)$ shows the dependence of $Y_P^e$ on $Re$ for three different elasticity numbers.

at relatively low Reynolds numbers, indicating a stronger coupling between the two effects.

For non-zero $\alpha$, the particle migration shows a more complex behavior in a viscoelstic fluid. At fixed $Re_G = 18.9$ and $El = 0.05$, the particle migrates towards the centerline for $\alpha = 0.1$. While for $\alpha = 0.2$, the particle migrates in the opposite direction and gets closer to the wall. This phenomenon is due to the interplay between the shear-thinning effects [183,185] and the secondary flow generated due to the second normal stress difference [185]. The shear-thinning properties affect the particle migration in two ways: (1) reduces the elastic force by decreasing the fluid viscosity, and (2) increases the inertia force by increasing the flow velocity $U_c$, and therefore, the equilibrium position of the particle moves closer to the wall in shear-thinning fluids. The secondary flow, whose velocity magnitude is comparable to the particle migration velocity in flows of relatively large $El$ and $\alpha$, drives the particle towards the wall. For example, in a Geisekus fluid of $El = 0.05, Re_G = 18.9$ and $\alpha = 0.1$, the maximum value of the far-field $v$-velocity component, which occurs at $y \simeq 0.33$, is $2.7 \times 10^{-4}$. While in the flow of $\alpha = 0.2$ at the same $El$ and $Re_G$, the corresponding maximum is $3.4 \times 10^{-3}$, the same order as the particle migration velocity. When

increasing $Re_G$ or $El$, the particle moves towards the wall, illustrating that the role of shear-thinning effect and secondary flow is stronger in flows of larger inertia and/or elastic effects. We should also emphasize that unlike the case of Oldroyd-B fluid, the equilibrium position of the particle in a Giesekus fluid is dependent on its initial location [180,185]. Previous simulations of a zero-Reynolds-number channel flow show that there exists a core region surrounding the centerline of the channel, inside which the particle moves to the center, while outside it the particles moves towards the wall and eventually collides with it. This core region shrinks with increasing the mobility factor $\alpha$. Our simulations follow the same trend in the presence of inertial effects, except in all our simulations, the particle stops before hitting the wall due the wall repulsion.

The migration velocity of the particle is the most important index of particle focusing, and its dependence on the particle size has been used for the particle separation [157,186,197]. In figures 4.5, we plot the particle migration velocity $V_p$ as a function of particle position $Y_p$ in Oldroyd-B and Geisekus fluids, respectively. During the start-up under a constant pressure gradient, the particle has a large transient migration velocity. After the channel flow reaches a steady state, the migration velocity monotonously decreases and eventually goes to zero when the particle reaches its equilibrium position. In this section, we mainly focus on the particle migration velocity after the flow has reached the steady state. The transient behavior during the flow start-up will be discussed in section 4.3.4. The magnitude of the dimensionless migration velocity $O(10^{-3} - 10^{-2})$ is of the same order as the experimental measurements of [158], and is one order of magnitude larger than in the Stokes regime $Re \sim 0$ [180,181]. In a Geisekus fluid at $El = 0.01$, the migration velocity decreases as $\alpha$ increases. At $El = 0.05$ and $\alpha = 0.1$, the particle still moves to the centerline but at $\alpha = 0.2$, it migrates towards the wall. An approximately linear relation between $V_p$ and $Y_p$ exists before the particle reaches its equilibrium position. This linear relationship holds very well in flows of small elasticity numbers and low

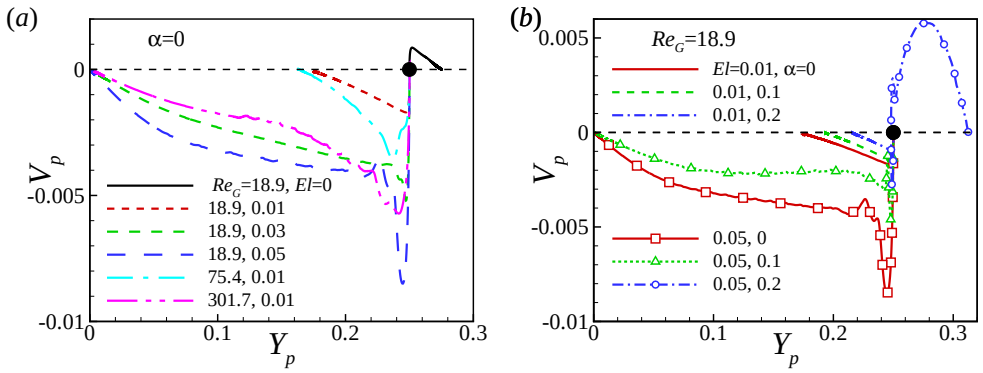


Figure 4.5. Dependence of migration velocity $V_p$ on the particle position $Y_p$ in $(a)$ Newtonian and Oldroyd-B fluids at different $Re_G$ and $El$ and $(b)$ Geisekus fluid at $Re_G$=18.9. Black dot shows the initial location of the particle.

Reynolds numbers. Similar results has been obtained for the particle migration in a circular pipe of a Giesekus fluid at $Re \sim 0$ and $El \sim 10^2$ [181].

The relative motion of the particle and surrounding fluid in the steady state are shown in figure 4.6. The distribution of streamwise velocity $u$ and vorticity $\omega_z = \partial v/\partial x - \partial u/\partial y$ in the $z = 0$ plane are plotted at two different locations: $x = 0$ across the particle center and $x = -5$ far from the particle. In Newtonian and Oldroyd-B fluids, the far-field velocity shows the same profiles. In a Geisekus fluid, however, the flow velocity increases due to the shear-thinning effects, and more remarkable enhancement is observed at higher elasticity numbers (see the inset in figure 4.6$(a)$). The flow disturbance due to the particle is relatively restricted to a small area close to the particle (one radius away from the particle). Particularly for the case of $El = 0.05$ and $\alpha = 0$, in which particle equilibrium position is at the center of the channel and the particle does not rotate, the velocity quickly recovers to its far-field value. The velocity distributions clearly show that the translational velocity of the particle is smaller than the far-field velocity at the same lateral position, i.e. the particle lags the flow. The experiments of [158] show that the centerline-focused particles lead the viscoelastic fluid in the presence of weak or strong shear-thinning

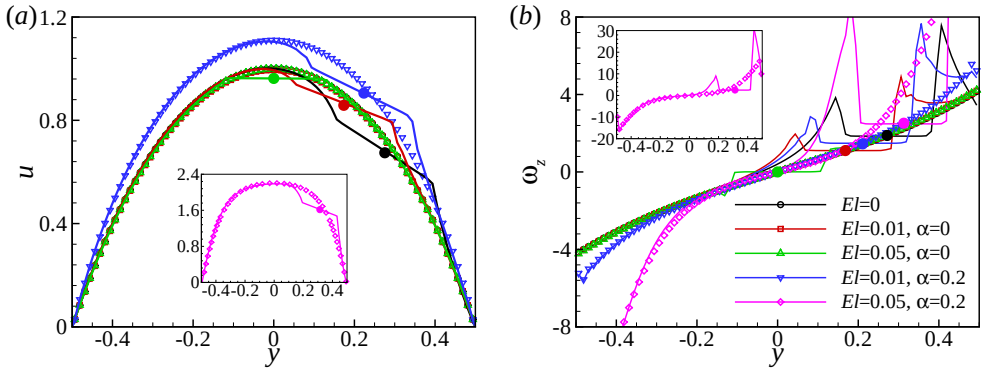


Figure 4.6. Steady distribution of ($a$) velocity $u$ and ($b$) vorticity $\omega_z$ in fluids of different $El$ and $\alpha$ at $Re = 18.9$. Symbols correspond to the velocity profile at $x = -5$ far from the particle, lines correspond to the velocity profile at $x = 0$ across the particle center, filled circles mark the center of the particle.

effects. At relatively large block ratios as in our cases, the wall effect, which tends to increase the drag force acting on the particle [198], overcomes the viscoelastic effect [199]. Therefore, the particle is lagging the fluid. These results indicate that the lateral migration of the particle is not directly related to the slip velocity.

The vorticity $\omega_z$, on the other hand, show a different behavior depending on the fluid properties. In Newtonian and Oldroyd-B fluids as well as in Geisekus fluids of low elasticity numbers, half the angular velocity of the particle $1/2\Omega_z$ is equal to the far-field vorticity. Whereas in a Geisekus fluid of $El = 0.05$ and $\alpha = 0.2$, it is smaller than the far-field vorticity due to the reduction of the fluid viscosity and consequently the viscous torque on the particle in the presence of shear-thinning effects. We also observe that the shear-thinning effect increases the background vorticity in the near-wall region, whereas in the centerline region, it is almost the same as in the Newtonian and Oldroyd-B fluids. Because $\partial v/\partial x$ is very small compared to $\partial u/\partial y$ when away from the particle, the shear rate $\dot{\gamma} = \partial v/\partial x + \partial u/\partial y$ of the fluid has a similar distribution as $-\omega_z$ (results not shown here).

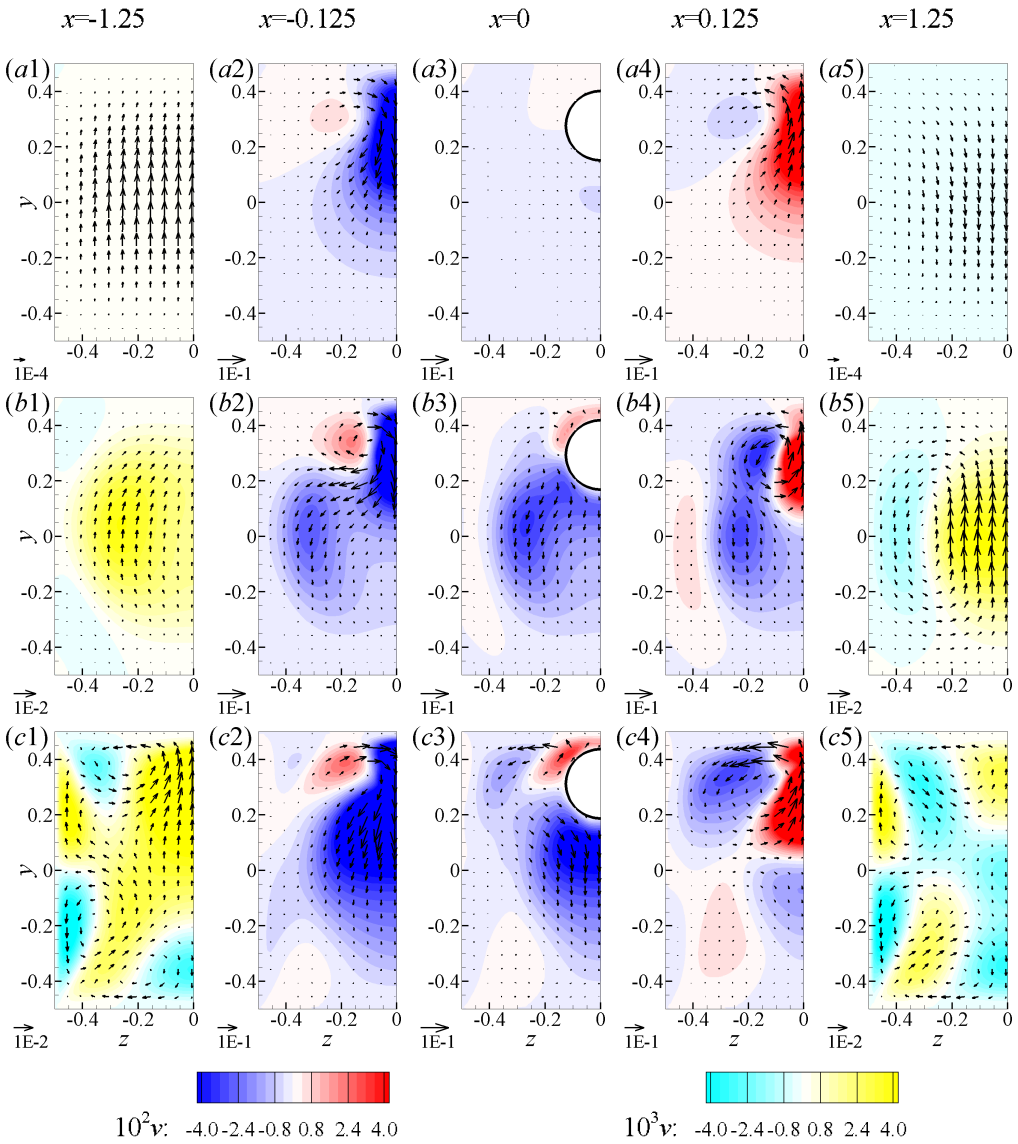


Figure 4.7. Particle-induced lateral flows at different $x$-locations for (*a*) $Re_G = 18.9, El = 0$, (*b*) $Re_G = 301.7, El = 0$ and (*c*) $Re_G = 18.9, El = 0.05$ and $\alpha = 0.2$. Contourplots show the distribution of the velocity component $v$. Vectors show the in-plane projection of the velocity field.

### 4.3.3 Particle-induced Fluid Transport

Besides the dynamics of particle migration in a channel flow, the effect of the particle on the fluid transport is another interesting topic, but it has been much less

explored in the literature. The fore-aft symmetry around the particle in a Stokes flow is broken in a Newtonian fluid with finite inertia, and a net recirculating flow perpendicular to the primary flow direction is created due to the combined effects of the near-field flow, particle rotation and the channel confinement. This net lateral transport of the fluid, which resembles the well-known Dean flow, occurs in a straight channel and has been successfully applied to perform fluid switching and mixing [162]. As shown in section 4.3.1, in an Oldroyd-B fluid, the particle-induced lateral flow is greatly inhibited due to the absence of the particle rotation. In a Geisekus fluid, the pattern of the lateral flow shows a remarkable difference from the one in a Newtonian fluid, and the flow has a stronger fore-aft asymmetry. In this section, we mainly focus on the flow field after the particle has reached to its equilibrium position.

For three cases: $(a)$ $Re_G = 18.9, El = 0$, $(b)$ $Re_G = 301.7, El = 0$ and $(c)$ $Re_G = 18.9, El = 0.05$ and $\alpha = 0.2$, we compare the flow field in the $z$-$y$ plane at different locations at $x = \pm 1.25, \pm 0.125$ and $x = 0$ in figure 4.7. The lateral flow generally shows similar flow pattern for the two Newtonian cases. At the upstream far from the particle, the fluid has a weak tendency to flow along the positive $y$-direction. Due to the particle rotation, the flow is driven to the negative $y$-direction when approaching the particle, and it is reversed downstream of the particle. Downstream of the particle away from it, the flow starts to recover, and velocity has an opposite sign compared to the upstream velocity. Around the particle, the magnitude of the lateral flow is of the order of $\omega_z a \sim 0.1$, and it decays away from the particle. At higher Reynolds numbers, the flow decays more slowly, particularly downstream of the particle, and the flow is in the positive $y$-direction in the middle of the channel (see figure 4.7($b$5)). In a Geisekus fluid, the flow shows a strong fore-aft asymmetry due to both inertia and viscoelastic wake, similar to the flow field around a settling sphere [200–202]. The secondary flows interact with the particle-induced flow, and further enhance the fluid mixing.

To quantitatively compare the fluid transport, we calculate the net velocity $\langle v \rangle_{x,y}$ averaged in both $x$ and $y$ directions and compare the distribution over the channel

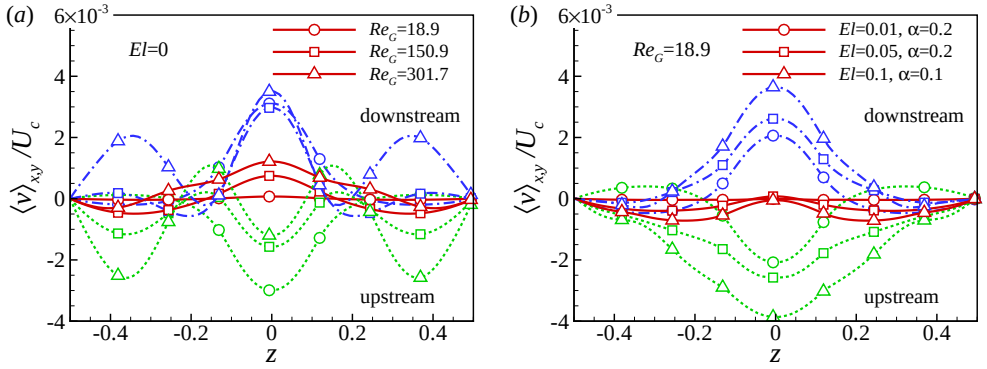


Figure 4.8. The distribution of the fluid velocity over the channel width $z$ for $(a)$ Newtonian fluid and $(b)$ Geisekus fluid. The integration in $y$-direction is over the entire channel height [-0.5, 0.5], and integration in $x$-direction are performed for different regions: upstream region [-1.25, 0] (green dotted lines), downstream region [0, 1.25] (blue dashdot lines) and central region [-1.25, 1.25] (red solid lines).

width $z$. In a Newtonian fluid, the net flow velocity has a peak at the centerline both upstream and downstream of the particle (see figure 4.8$(a)$). As $Re_G$ increases, two additional peaks appear near the walls. In the upstream region, the magnitude of the net flow decreases at the centerline with Reynolds number, while at the downstream region, it increases. The contribution from the downstream wins, and the net fluid transport, which mainly occurs in the middle of the channel, drives the fluid towards the particle side. The fluid transport of a Geisekus fluid is shown in figure 4.8$(b)$. The net fluid transport in the domain [-1.25, 1.25] occurs mainly in two regions between the centerline and the channel walls and the flow direction is away from the particle. Figure 4.9 shows the net averaged velocity $\langle v \rangle_{x,y,z}$ over the domain $[-1.25, 1.25] \times [-0.5, 0.5] \times [-0.5, 0.5]$ for different flow conditions. In a Newtonian fluid, the net fluid transport increases with the flow Reynolds number. In a viscoelastic fluid, it has a complex relationship with the Reynolds number ($Re$ and $Re_G$), elasticity number $El$ and mobility factor $\alpha$. However, the net velocity shows an approximately linear relationship with the flow Weissenberg number $Wi$.

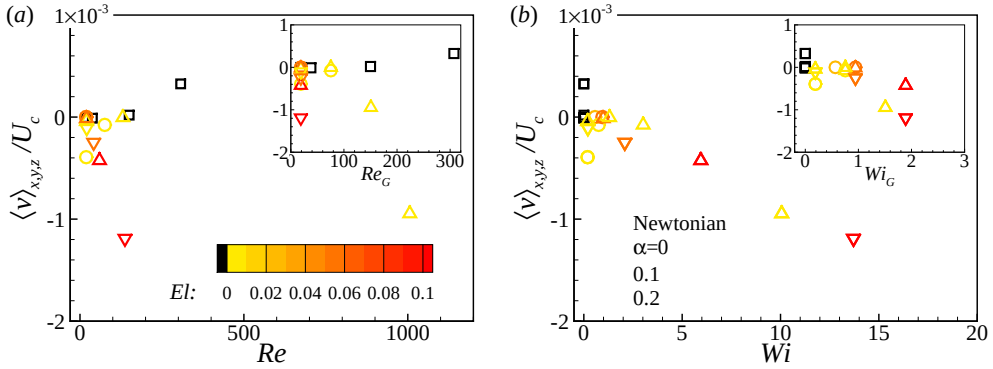


Figure 4.9. Dependence of the averaged velocity $\langle v \rangle_{x,y,z}$ over the domain $[-1.25, 1.25] \times [-0.5, 0.5] \times [-0.5, 0.5]$ on $(a)$ $Re$ and $Re_G$ (inset), and $(b)$ $Wi$ and $Wi_G$ (inset).

### 4.3.4 Migration Behavior during a Flow Startup

The elasticity and shear-thinning effects have significant impact on the transient behavior of both fluid flow and particle motion [203]. In a poiseuille flow of viscoelastic fluids, the velocity oscillation can be observed during the flow start-up [189] because of the propagation of stress waves in the channel [204]. Transient velocity oscillations also occurs for a particle settling in viscoelastic fluids, and often causes the particle to "rebound" during the first oscillation [155, 205]. The blood circulating flow is an important example of unsteady channel flow of a non-Newtonian fluid. However, recent studies have not reported the transient behavior. In this section, we discuss the transient behavior of the particle migration during the flow start-up.

Figure 4.10$(a)$ shows the time history of the particle migration velocity for different flow conditions. At relatively large $Re$ and $El$, the migration velocity oscillates during the flow start-up. In a shear-thinning fluid, the particle initially migrates towards the centerline, but after the growth of the secondary flow, the particle moves towards the wall. In figure 4.10$(b)$, we compare the channel centerline velocity $U_c$ far from the particle, the particle streamwise velocity $U_p$, and the migration velocity $V_p$ during the flow start-up for the case of $Re_G = 18.9, El = 0.05$ and $\alpha = 0$. The fluid velocity

oscillates at $t < 10$ before it reaches to a steady state, and the peak velocity occurs at $t \simeq 2$. The particle streamwise velocity $U_p$ follows this oscillation until $t \sim 10$, it then slowly increases as the particle moves towards the centerline region. The migration velocity $V_p$, however, shows a more complex time dependence. At $t < 1$, the migration velocity is towards the wall because the viscoelastic stresses are still very weak and the inertia effect dominates the flow. As the viscoelastic stress grows, $V_p$ quickly grows and overshoots at the same time instant as $U_c$ and $U_p$, and then after some oscillations, its magnitude gradually decreases. The magnitude of the overshoot of $V_p$, which is about twice its steady value, is larger than the corresponding values for $U_c$ and $U_p$. Figure 4.11 shows the distribution of first normal stress difference $N_1$ at time $t = 3$. The normal stress difference in the gap between the particle and the wall is stronger than the other side. Furthermore, a strip of large normal stress difference is generated near the upstream wall, due to the relative motion of the particle and the wall as well as the particle rotation. This strip disappears as the particle approaches its equilibrium position and moves away from the wall. In summary, the larger transient migration velocity of the particle is a result of both the flow velocity oscillation during the flow start-up and the strong normal stress difference due to the particle-wall interaction.

## 4.4 Concluding Remarks

Particle migration in a pressure-driven channel flow of viscoelastic fluids is affected by the interplay between several effects: inertia, elasticity, shear-thinning and secondary flow induced by the second normal stress difference in a non-circular channel. In an Oldroyd-B fluid, the competition between the inertia force and the elastic force determines the particle migration. The elastic force, which drives the particle towards the channel centerline, decreases monotonically as the particle reaches the centerline. The inertia force, which has a peak at $Y_p \simeq 0.15$, pushes the particle towards the wall. If the elastic force is weaker than the inertia force, the particle

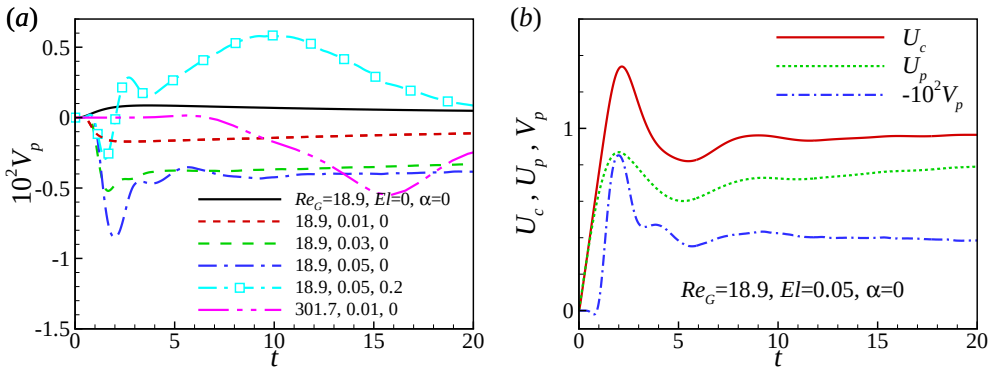


Figure 4.10. ($a$) Time history of particle migration velocity for different flow conditions. ($b$) Time history of the channel centerline velocity $U_c$ far away from the particle, particle streamwise velocity $U_p$, and migration velocity $V_p$ at flow start-up. The flow conditions are $Re_G = 18.9, El = 0.05$ and $\alpha = 0$.

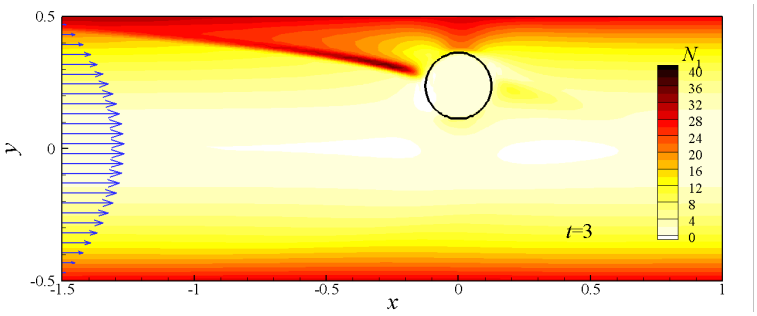


Figure 4.11. First normal stress difference around the particle at $t = 3$. The flow conditions are $Re_G = 18.9, El = 0.05$ and $\alpha = 0$.

migration stops at a location where two forces are balanced. Once the elastic force overcomes the maximum inertia force, the particle moves till it reaches the centerline. A scaling analysis of the force balance provides a good estimate for the critical elasticity and Weissenberg numbers for particle focusing in flows of relative large Reynolds numbers. Both the shear-thinning effect and the corresponding secondary flow tend to move the particle closer to the wall, and their effects are more pronounced with stronger inertia and elasticity. Besides the particle migration, we have also consid-

ered the particle-induced fluid transport and the transient behavior of the particle motion during the flow start-up. An effective fluid transport perpendicular to the flow direction can be achieved in flows with strong inertia and shear-thinning effects. The particle has a larger transient migration velocity during the flow start-up due to the streamwise velocity oscillation and the strong normal stress difference.

# 5. UNDULATORY SWIMMING IN NON-NEWTONIAN FLUIDS[1]

## 5.1 Motivation and Previous Works

Microorganisms often swim in complex fluids which show non-Newtonian behavior [3]. Such examples include bacteria forming biofilms composed of bacteria-produced extracellular polymeric substances (EPS) [42], spermatozoa swimming through cervical mucus in the mammalian female reproductive tract [59], *H. pylori* colonizing the mucus layer covering the stomach [60] and *B. burgdorferi* penetrating the connective tissues in skin [62]. In marine environments, bacteria abundance and productivity is elevated within aggregates mainly composed of transparent exopolymer particles (TEPs) referred to as oceanic gel [206]. It contribute to fluxes of carbon into the deep ocean and significantly affect the world's carbon balance. Rheological measurements show that many biological fluids exhibit both viscoelasticity and shear-dependent viscosity [43, 207].

Depending on the swimming strategies and the rheological properties of the background fluid, both swimming enhancement and reduction are possible. Helical bacteria swim faster in a viscoelastic fluid compared to a Newtonian fluid of the same viscosity [132], whereas *C. elegans*, with a planar wave undulation, swim slower [134]. In recent years, the effects of fluid elasticity have been widely investigated for different types of swimmers, such as squirmers [50, 95], swimming sheets undergoing planar beating motion [135, 136, 208, 209] and rotating helical flagellum [137, 138]. The speed enhancement up to about $20 \sim 30\%$ occurs for helices of large pitch angle and small filament radius [137, 138], and for soft flagella undergoing planar beating motion [208, 209].

[1]Part of this chapter has been published in "Undulatory swimming in non-Newtonian fluids", by G. Li and A. M. Ardekani, in Journal of Fluid Mechanics, 784: R4, 2015 (reproduced with permission).

The role of shear-dependent viscosity of biological fluids, which usually behaves as shear-thinning fluids, is less understood compared to its viscoelasticity. The non-Newtonian viscosity has been considered as the reason behind the enhancement of the bacteria speed in early studies [132, 210]. Based on the concept that a slender body under longitudinal and transversal motions experiences two different apparent viscosities, [211] used a modified resistive force theory and showed enhancement in both the swimming speed and efficiency with an increase in viscosity in a certain range. Using scaling arguments, a recent study by [52] suggested the shear-dependent viscosity is likely to play a more important role than elastic effects. An experimental study by [34] shows that the enhanced swimming of *E. Coli* in polymeric solutions is not related to fluid elasticity, instead it is due to the fast-rotating flagella of *E. Coli* encountering a lower viscosity than the cell body. Swimming enhancement is also observed in simulations of a sperm cell in a shear-thinning fluid [212, 213]. For a *C. elegans*, the swimming speed and kinematics are only determined by the effective fluid viscosity around it, independent of shear-thinning behavior of the fluid [214]. Surprisingly, however, the flow field is found to be affected by the fluid shear-thinning property. A similar conclusion is derived in the analysis of an inextensible swimming sheet of very small amplitude [52]. A reduction in swimming speed is also observed in experiments of a cylindrical waving sheet in shear-thinning viscoelastic fluids [215]. Further studies need to be conducted to better understand the different observations reported in the literature.

In this work, we use numerical simulations to investigate the effects of non-Newtonian fluid properties on the swimming motion of a planer waving flagellum. We first compare the effects of viscoelasticity and shear-thinning behavior of the fluid on a Taylor's swimming sheet. We then investigate the role of shear-thinning behavior and our results bridge previous numerical [212, 213] and analytical studies [52]. A new scaling relation for the power consumption is proposed to extend the analysis of [52] for a small amplitude flagellum to large amplitude oscillations. We also compare the present results against previous experiments. Since many mi-

croorganisms and biological systems, such as spermatozoa, bacteria and beating cilia experience non-Newtonian fluids, our findings help us better understand the motion of low-Reynolds-number swimmers in complex fluids.

## 5.2 Taylor's Swimming Sheet in Non-Newtonian Fluids

We model the swimmer as an inextensible infinitely long two-dimensional flagellum immersed in a non-Newtonian fluid. The prescribed motion of the Taylor's swimming sheet [5] is described by a left-moving traveling wave $y = A\sin(x - t)$, where $A$ is the dimensionless amplitude. In all our results, the length is scaled by $1/k$, time by $1/\Omega$, velocity by $\Omega/k$, shear rate by $\Omega$, and pressure and stress by $\mu\Omega$, where $k$ is the wavenumber, $\Omega$ the angular frequency, and $\mu$ is the fluid viscosity. At length and velocity scales relevant to microorganisms, inertial effects are neglected. The dimensionless equations for conservation of momentum and mass are

$$\nabla p = \nabla \cdot \boldsymbol{\tau} + \boldsymbol{f}, \qquad \nabla \cdot \boldsymbol{u} = 0, \tag{5.1}$$

where $\boldsymbol{u}$ is the velocity vector, $p$ is the pressure, and $\boldsymbol{\tau}$ is the deviatoric stress tensor. In a Newtonian fluid, the stress tensor is simply determined by the shear rate tensor $\dot{\boldsymbol{\gamma}} = \nabla\boldsymbol{u} + \nabla\boldsymbol{u}^{\mathrm{T}}$ and fluid viscosity, i.e., $\boldsymbol{\tau} = \dot{\boldsymbol{\gamma}}$ in dimensionless form. The forcing term $\boldsymbol{f}$, acting as a Lagrange multiplier [108], is calculated in an iterative way to ensure the no-slip boundary condition on the flagellum. Simulations are conducted using a finite volume method based on the staggered grid. A conventional operator-splitting method is applied to enforce the continuity equation. The spatial derivatives in the diffusion terms are discretized using the central difference scheme. The computational domain is $2\pi \times 40\pi$ for an infinitely long flagellum. The grid size $\Delta = \pi/256$ is uniform along the flagellum ($x$-direction) and in the domain of $[-2\pi, 2\pi]$ normal to the flagellum ($y$-direction). The grids are gradually stretched in the $y$-direction outside this domain moving away from the flagellum. The time step is $dt = 10^{-4}$. A second-order total variation diminishing (TVD) Runge-Kutta method is used for time marching. Periodic boundary conditions are used at $x = 0$ and $x = 2\pi$ boundaries of

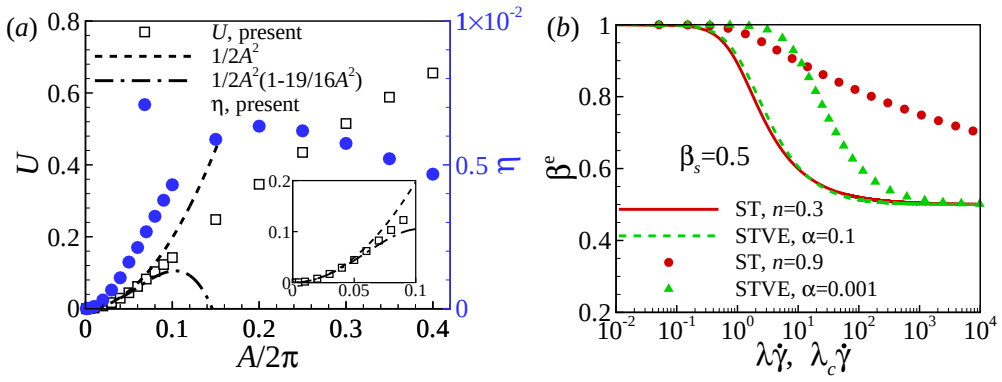


Figure 5.1. ($a$) Swimming speed $U$ and efficiency $\eta$ for an infinitely long flagellum of different amplitudes in a Newtonian fluid. ($b$) Shear-dependent viscosity of Giesekus and Carreau models in a simple shear flow.

the computational domain. At $y = -20\pi$ and $y = 20\pi$ boundaries, $\partial \boldsymbol{u}/\partial y$ is set to zero.

The swimming speed $U$ and the hydrodynamic efficiency $\eta$ for an infinitely long flagellum in a Newtonian fluid are shown in figure 5.1($a$). The efficiency is defined as $\eta = U^2/P$, where $P = \int_\Gamma \mathbf{f} \cdot \boldsymbol{u}_\Gamma d\Gamma$ is the hydrodynamic power, $\boldsymbol{u}_\Gamma$ is the velocity along the flagellum surface $\Gamma$. The numerical results agree well with the second and fourth order analytical results for a small amplitude flagellum [5] up to $A = 0.1\pi$. Within this range, the maximum difference between our simulations and the fourth-order analytical results is less than 0.5%. Interestingly, the efficiency of the flagellum peaks at around $A = 0.4\pi$, which lies inside the range of typical biological observations, such as *C. elagans* [214] and sperms [13]. The typical beating frequency ranges from 2 to 30Hz.

To model the elasticity and shear-thinning properties of biological fluids, we use the Giesekus constitutive relation [149], in which $\boldsymbol{\tau}$ can be split into solvent and polymer contributions as $\boldsymbol{\tau} = \boldsymbol{\tau}^s + \boldsymbol{\tau}^p$, where $\boldsymbol{\tau}^s = \beta_s \dot{\boldsymbol{\gamma}}$,

$$\boldsymbol{\tau}^p + \mathrm{De}\, \overset{\triangledown}{\boldsymbol{\tau}}^p + \frac{\mathrm{De}\,\alpha}{1-\beta_s} \boldsymbol{\tau}^p \cdot \boldsymbol{\tau}^p = (1-\beta_s)(\nabla \mathbf{u} + \nabla \mathbf{u}^{\mathrm{T}}), \tag{5.2}$$

$\beta_s$ is the ratio of the solvent viscosity to the zero-shear-rate viscosity of the polymeric solution. This ratio is equal to the ratio of the infinite-shear-rate viscosity and zero-shear-rate viscosity. The Deborah number $\mathrm{De} = \lambda/t_c$ is the ratio of the polymer relaxation time $\lambda$ and the characteristic flow time scale $t_c = 1/\Omega$. Another important dimensionless number for swimming in viscoelastic fluids is the Weissenberg number $\mathrm{Wi} = \lambda\dot{\gamma}_c$, where the characteristic shear rate in this study is $\dot{\gamma}_c = \Omega A$. The mobility factor $\alpha$, which is in the rage of 0 to 1/2, represents the anisotropic hydrodynamic drag exerted on the polymer molecules by the surrounding solute molecules and affects the viscosity of the polymeric solution. At $\alpha = 0$, the Giesekus constitutive equation recovers to the Oldroyd-B model and has a constant viscosity. At non-zero $\alpha$, the fluid has a shear-thinning viscosity. In a simple shear flow of Giesekus fluid, the effective viscosity is [216]

$$\beta^e = \beta_s + (1-\beta_s)\frac{(1-k)^2}{1+(1-2\alpha)k}, \tag{5.3}$$

where $k = [1-\chi]/[1+(1-2\alpha)\chi]$ and $\chi^2 = [(1+16\alpha(1-\alpha)De^2|\dot{\gamma}|^2)^{1/2}-1]/[8\alpha(1-\alpha)De^2|\dot{\gamma}|^2]$. The notation $\overset{\triangledown}{\mathbf{A}}$ represents the upper-convected derivative. The viscoelastic stress is solved using a commonly used formulation denoted as elastic and viscous stresses splitting (EVSS) method [190].

We use the Carreau constitutive model [217] to investigate the motion in a shear-thinning inelastic fluid

$$\boldsymbol{\tau} = \beta^e\dot{\boldsymbol{\gamma}}, \tag{5.4a}$$

$$\beta^e = \beta_s + (1-\beta_s)(1+\mathrm{Cu}^2|\dot{\gamma}|^2)^{\frac{n-1}{2}}, \quad (0 < n \leq 1) \tag{5.4b}$$

where $\beta_e$ is the normalized effective viscosity, $\dot{\boldsymbol{\gamma}}$ is the shear rate tensor, $|\dot{\gamma}| = \sqrt{\dot{\boldsymbol{\gamma}} : \dot{\boldsymbol{\gamma}}/2}$ is the effective shear rate. The Carreau number $\mathrm{Cu} = \lambda_c\Omega$ (Similar to De) is the ratio between the characteristic time scale $\lambda_c$ of the solution and the typical flow time scale $1/\Omega$, where $\lambda_c$ is the inverse of the shear rate at which the fluid transitions from Newtonian-like to power-law behavior. Similar to the Weissenberg number, the shear Carreau number is related to the shear rate $\mathrm{Cr} = \mathrm{Cu}A$. The power-law index $n$ determines how fast the viscosity decreases with increasing the

shear rate. The larger $n$ is, the slower the viscosity thins. At $\beta_s = 1$, Cu $= 0$, or $n = 1$, the model recovers to the Newtonian fluid. In biological materials, such as biofilm and mucus, $\lambda$ and $\lambda_c$ vary from O(10) to O($10^3$) seconds, $n$ from 0.1 to 0.9, and $\beta_s$ from O($10^{-3}$) to O($10^{-1}$). Therefore, for microorganisms, De, Wi, Cu and Cr vary in a very wide range, from O(1) to O($10^4$). In figure 5.1($b$), we compare the shear-thinning behavior of the Giesekus and the Carreau models (5.4b) in a simple shear flow. The shear rate corresponding to the transition from Newtonian-like to power-law behavior in a Giesekus fluid is determined by both $\lambda$ and $\alpha$, whereas the shear-thinning rate remains the same [216]. We can match the effective viscosity of the Carreau fluid to the Giesekus fluid to unravel the effect of both elasticity and shear-thinning behavior (see figure 1($b$)).

## 5.3 The Role of Viscoelasticity and Shear-thinning Viscosity

We first compare the role of fluid elasticity (VE), shear-thinning behavior (ST) and combined shear-thinning viscoelastic effects (STVE) on an undulatory swimming flagellum (see figure 5.2). We assume $\beta_s = 0.5$, except for small amplitude oscillations in a Carreau fluid, where we set $\beta_s = 0$ to directly compare the results with the analytical results. Unless otherwise stated, we set $n = 0.3$ in the Carreau fluid. Our results recover the analytical results for a small amplitude flagellum in both viscoelastic and shear-thinning fluids. In an Oldryod-B fluid, both the swimming speed and hydrodynamic power decreases monotonically as [135]

$$U/U_N = P/P_N = \frac{1 + \beta_s \mathrm{De}^2}{1 + \mathrm{De}^2}, \tag{5.5}$$

where $U_N$ and $P_N$ are the speed and power in a Newtonian fluid, respectively. The same scaling law approximately applies to a large amplitude flagellum. In a Carreau fluid, the swimming speed of a small amplitude flagellum does not change up to O($A^4$) and the power follows [52]

$$P/P_N = 1 + \frac{3}{16}(n-1)\mathrm{Cu}^2 A^2. \tag{5.6}$$

The above relations agree well with numerical results in the limit of small Cu. At large Cu, numerical results show a small enhancement in speed. Eq. (5.6) is not valid for Cu$A > 2.7$ and leads to a negative power. For a large amplitude flagellum ($A = 0.4\pi$), shear-thinning effects result in a speed enhancement, with the maximum increase of 20% at Cu $\simeq 1.2\pi$. [212] predicted an optimum velocity enhancement at Cr $= 1.6\pi$ for a finite-length undulatory sperm-like swimmer including a head. Shear-thinning effects lead to a significant enhancement in the swimming speed. In a shear-thinning viscoelastic fluid, the velocity follows the same relation as in an Oldroyd-B fluid when the oscillation amplitude or De are small. The shear-thinning effect is more important at higher shear rates, but the speed is still hindered. The power consumption is less affected by shear-thinning effects in a Giesekus fluid.

The mean-squared polymer distention field tr($\boldsymbol{\tau}^p$), computed as the trace of the polymer stress tensor, in Oldryod-B and Giesekus fluids are compared in figures 5.3($a$) and ($b$). Previous studies of a planar finite length flagellum in a viscoelastic fluid have shown that the swimming enhancement is related to the concentrated polymer stress distribution at the tail [136, 208]. Here, we see that the polymer stress is mostly stretched along the front-side of an infinitely long flagellum. In a Giesekus fluid, the polymer stress is attenuated, but the distribution is qualitatively the same. In figures 5.3 ($c$) and ($d$), we compare the effective viscosity in Giesekus and Carreau fluids. Effective viscosity of the Giesekus fluid is evaluated by calculating the effective shear rate [216]. The fluid viscosity around the flagellum is reduced and gradually recovers to the zero-shear viscosity away from the flagellum. There are some similarities between the two cases, but near the flagellum, the Giesekus fluid is less thinned and forms finer structures.

## 5.4 Scaling Law in Shear-thinning Fluids

To fully understand the shear-thinning effects on a swimming flagellum, we conduct a series of simulations of various oscillation amplitudes $A$ and viscosity ratios

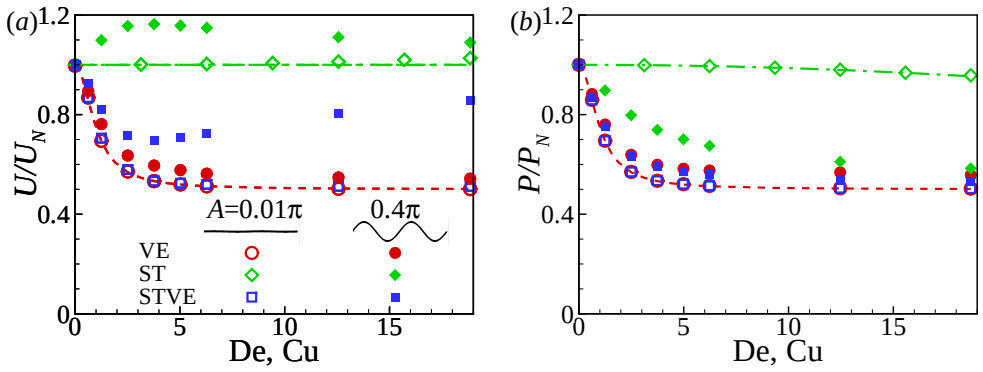


Figure 5.2. The normalized (a) swimming speed and (b) hydrodynamic power as a function of De (or Cu) for an infinitely long flagellum of small ($A = 0.01\pi$) and large amplitudes ($A = 0.4\pi$). The dashed and dashdot lines correspond to Eq. (5.5) and (5.6), respectively.

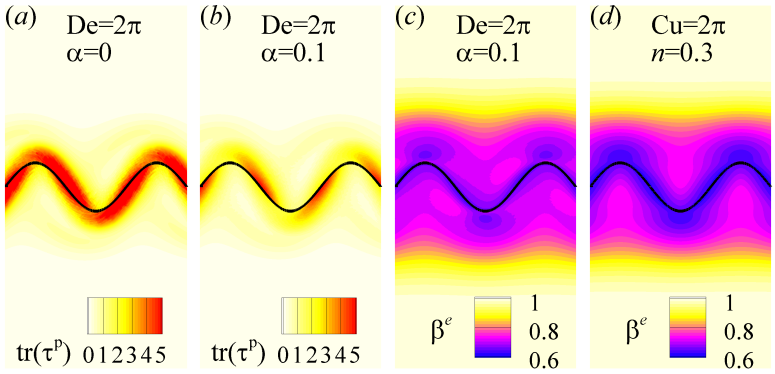


Figure 5.3. Distribution of trace of the polymeric stress tensor $\mathrm{tr}(\boldsymbol{\tau}^p)$ in $(a)$ Oldryod-B and $(b)$ Giesekus fluids. Distribution of effective viscosity in $(c)$ Giesekus and $(d)$ Carreau fluids. $A = 0.4\pi$ and $\beta_s = 0.5$ in all cases.

$\beta_s$. In figure 5.4, we plot the normalized swimming speed and power as a function of Cr. It is clear that using Cr instead of Cu leads to a much better collapse of the data. The swimming speed is less affected at small values of Cr ($< 0.1$), since the fluid viscosity does not vary at such a low shear rate. The analysis of [52] is valid in this range. With increasing Cr, the increase in the swimming speed becomes noticeable. There is a maximum speed for cases with non-zero $\beta_s$. In the limits of zero

and infinity Cr, the swimming speed of the flagellum is the same as its Newtonian value because the normalized viscosity is constant in both cases, equal to 1 and $\beta_s$, respectively. The maximum speed and the corresponding Cr number, $\mathrm{Cr}_{max}$, depend on the oscillation amplitude $A$, as well as the viscosity ratio $\beta_s$. Larger speed enhancement and $\mathrm{Cr}_{max}$ are observed for larger $A$ and smaller $\beta_s$. The value of $\mathrm{Cr}_{max}$ ranges from order of O(1) to O($10^2$), which corresponds to the range where the fluid viscosity is effectively thinned but before reaching the infinite-shear-rate plateau (see figure 5.1($b$)). Interestingly, experiments show that the circulation generated by *C. elegans* first increases with Cr and then decreases [214]. In the limit of zero $\beta_s$, the swimming speed monotonically increases due to the absence of infinite-shear-rate plateau.

The power consumption of an undulating flagellum follows a universal scaling law. As shown in figure 5.4($b$), all the data collapse into solid curves defined as

$$\frac{1 - P/P_N}{1 - \beta_s} = 1 - (1 + \frac{3}{8}\mathrm{Cr}^2)^{(n-1)/2}, \tag{5.7}$$

in which the constant 3/8 is chosen so that the first term of Taylor expansion of Eq. (5.7) matches the power consumption calculated for small amplitude oscillations, i.e., Eq. (5.6). The power consumption of an undulating flagellum is equal to the energy dissipation integral $P = \int_S \beta^e |\dot{\gamma}|^2 dS$, where $\beta^e = 1$ in a Newtonian fluid. Using Eq. (5.4b), we can derive $(1 - P/P_N)/(1 - \beta_s) \sim 1 - (1 + \mathrm{Cu}^2|\dot{\gamma}|^2)^{(n-1)/2}$, which will be simplified to Eq. (5.7) if the shear rate scales with oscillation amplitude ($\dot{\gamma} \propto A$). Later, we will confirm this assumption.

The present numerical results extend the analytical results by [52] for small amplitude flagellum. Our results are also consistent with the simulations of [212,213] for a finite sperm-like swimmer, in which the velocity peaks at a certain Cr. [213] related this velocity peak with the maximal viscosity gradient along the flagellum, but their explanation does not hold for an infinitely long flagellum. Here, we propose another explanation for the speed enhancement caused by shear-thinning viscosity. The fluid viscosity around the flagellum is reduced due to the high values of shear rate and it gradually recovers to the zero-shear viscosity away from the flagellum (figure

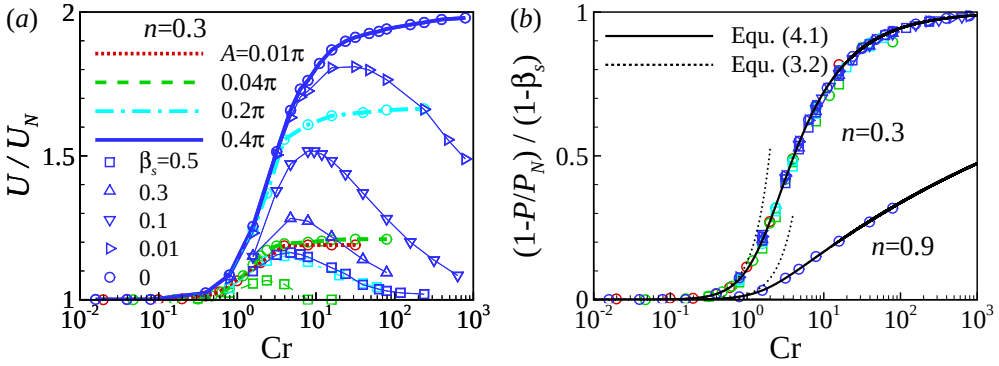


Figure 5.4. Normalized ($a$) swimming speed and ($b$) hydrodynamic power as a function of Cr.

$5.5(a-c)$). As a result, the flagellum swims inside a corridor of small viscosity fluid surrounded by a higher viscosity fluid. If $\beta_s = 0$, the fluid viscosity can be reduced to the solvent viscosity, which is infinitesimal compared to the unstirred fluid. The flagellum swims as if it is inside a confined channel and gains an enhanced speed due to the confinement [64]. The differences in the streamlines of two cases with different Cu are shown in figures $5.5(d)$ and $(e)$. The effect of this corridor of small viscosity fluid is weakened with increasing $\beta_s$ due to the increased viscosity ratio inside and outside the channel, but the same mechanism still exists. The further decrease in the fluid viscosity inside the channel at larger Cr strengthens the confinement effect. On the other hand, the enlarged shear-thinning region, weakens the confinement effect by increasing the width of the low-viscosity layer. These two competing effects lead to a peak in the swimming speed.

In figure 5.6, we plot the distribution of $|\dot{\gamma}|, u, v$ and $\beta^e$ along the $y$-direction at $x = \pi/2$. Independent of the fluid rheology and the oscillation amplitude, the magnitude of shear rate roughly follows the same relation (light gray line)

$$|\dot{\gamma}| = 2Aye^{-y}, \tag{5.8}$$

which confirms the assumption we used for the derivation of Eq. (5.7). This scaling is the same as the small amplitude analytical results, in which the first and second order

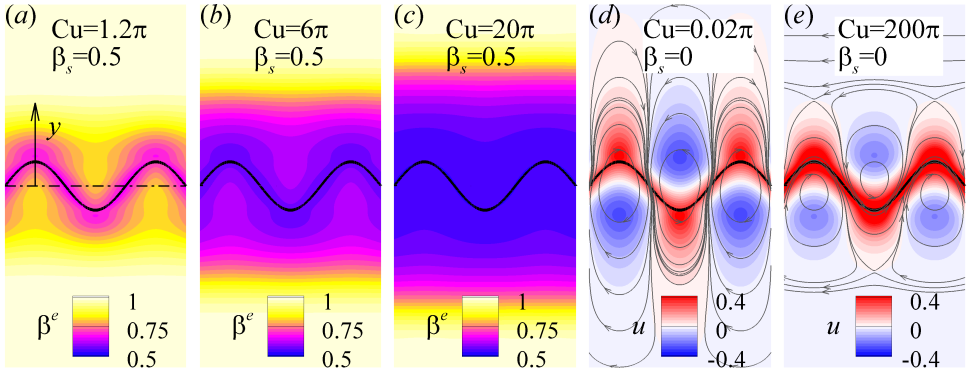


Figure 5.5. $(a-c)$ Distribution of effective viscosity around a flagellum at $\beta_s = 0.5$. $(d)$ and $(e)$ The velocity field and streamlines around a flagellum at $\beta_s = 0$. In all the cases, $A = 0.4\pi$.

velocities are not affected by shear-thinning effect. In this case, the shear-dependence of the viscosity affects the third and higher orders of shear rate [52]. The $u$ velocity component for the case with maximum speed changes its direction earlier than other cases, and $v$ component is the lowest, indicating the strongest confinement effect in this case. The effective viscosity $\beta^e$ of Carreau fluid can be derived as a function of Cr and $y$ using Eq. (5.4b) and (5.8) (Light gray lines in figure 5.6$(b)$). The effective viscosity obtained from Eq. (5.4b) and (5.8) has a minimum at $y = 1$, which agrees well with our numerical results for a small amplitude flagellum. For a large amplitude flagellum at low Cr, the viscosity near the flagellum is lower than the above mentioned prediction and its location is shifted further away from the flagellum. At high Cr, where the viscosity reaches its minimum value near the flagellum, the prediction holds well.

Using this prediction, we can estimate $\mathrm{Cr}_{max}$ by evaluating the strength of the shear-thinning effect, $(1-\beta^e_{min})/d$. Here, $\beta^e_{min}$ is the minimum effective viscosity, $d$ is the thickness of the shear-thinning layer, which is defined as the location where the viscosity recovers to the zero-shear viscosity. Figure 5.7$(a)$ shows $(1-\beta^e_{min})/d$ as a function of Cr. The Cr corresponding to the maximum value of $(1-\beta^e_{min})/d$ is close to $\mathrm{Cr}_{max}$ obtained from our numerical simulations. At $n = 0.3$, $\mathrm{Cr}_{max}$ is

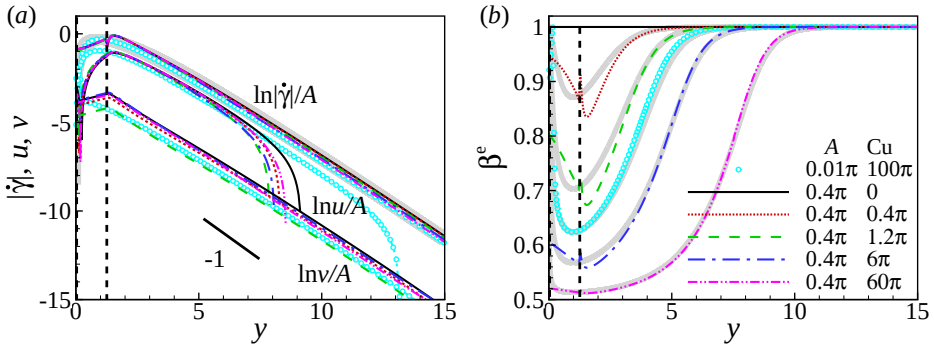


Figure 5.6. Distribution of $(a)$ $|\dot{\gamma}|, u$ and $v$ and $(b)$ $\beta^e$ along the $y$-direction at $x = \pi/2$. The light gray lines correspond to Eq. (5.8) in $(a)$ and Eq. (5.4b) in $(b)$ after substituting Eq. (5.8) for the effective shear rate. The vertical dash lines represent the flagellum of $A = 0.01\pi$ and $0.4\pi$, respectively. $\beta_s = 0.5$ in all cases.

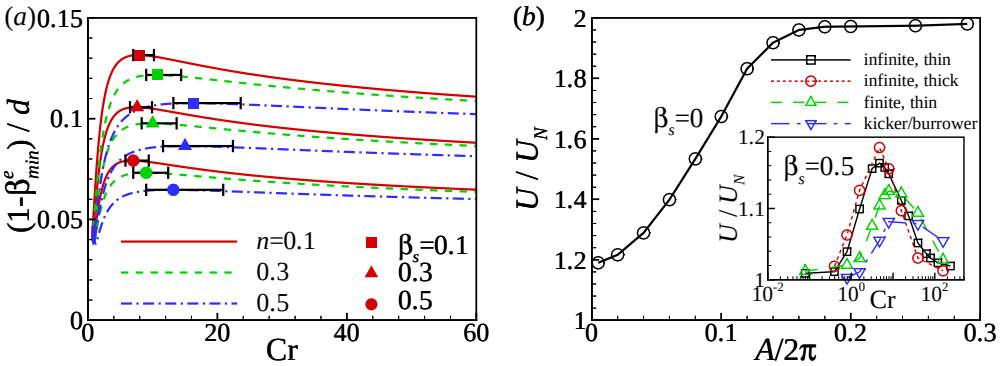


Figure 5.7. $(a)$ The strength of shear-thinning effect, $(1 - \beta^e_{min})/d$ as a function of Cr for different $n$ and $\beta_s$. Symbols show maximum value of $(1 - \beta^e_{min})/d$ with $d$ being the distance where the effective viscosity is 95% of the zero-shear viscosity. The left and right error bars span the range of $d$ corresponding to 91% and 99% of the zero-shear viscosity, respectively. $(b)$ The normalized swimming speed as a function of amplitude $A$ at Cu $= 200\pi$ and $\beta_s = 0$. (inset) The normalized swimming speed for various flagella as a function of Cr at $A = 0.4\pi$ and $\beta_s = 0.5$.

around 10 and increases with decreasing $\beta_s$ and increasing $n$. In typical biological fluids, where the viscosity ratio $\beta_s$ is usually low, we expect the microswimmers to

benefit from the speed enhancement. In figure 5.7($b$), we plot the normalized speed as a function of amplitude at Cu = $200\pi$ and $\beta_s = 0$. This is approximately the maximum speed enhancement of microswimmers due to shear-thinning effects. For a small amplitude flagellum, about 20% speed enhancement is achieved. For a large amplitude flagellum, the speed is almost doubled. At last, we check whether the thickness, finite length and the swimming stroke affect the results. The thickness of the thick flagellum is $0.16\pi$, similar to the measurements of *C. elegans* [214]. For the finite length swimmer, the flagella have one complete waving form. Linearly increasing/decreasing amplitude toward the tail is chosen for the kicker/burrower swimmers. As shown in the inset of figure 5.7($b$), the swimming enhancement occurs for all the cases. The flagellum thickness does not affect the speed; the finite length of flagellum leads to larger $\mathrm{Cr}_{max}$ and weaker speed enhancement. Kicker and burrower swimmers have the same swimming speeds.

## 5.5 Swimming Motion in a Suspension of Particles

The mechanism of speed enhancement for a swimmer moving in a corridor of small viscosity fluid surrounded by a higher viscosity fluid also exists when it swims inside a heterogeneous fluid environment. Biological material, such as mucus and biofilm, are typically heterogeneous, composed of a porous media filled with fluids inside it. For example, cervical mucus contains a network composed of glycoprotein fibers with diameters around 100nm, the pore size of the network ranges from hundreds of nanometers to around $25\mu$m [45, 46]. A sperm typically has a cell body of $5\mu$m, the flagella is around $40\mu$m. Therefore, the size of the microstructure in the mucus fluid is comparable to the sperm size. For the ruminants, the size of the food particles must be about 1 mm to escape the rumen for cattle and sheep [218]. Symbiotic gut microflora help vertebrates to digest the cell wall and the end products, primarily small size fatty acids, are comparable to bacteria size. Another example is nematode

*C. elegans* that often swims in saturated soil in nature, where soil particles are of the same size as the organism.

We conduct simulations of an infinitely long flagellum of amplitude $A = 0.4\pi$ swimming in a Newtonian fluid with suspended small particles of radius $a = 0.04\pi$ and particle number $N = 200$. As shown in figure 5.8, four cases are considered: $(a)$ particles are initially uniformly distributed inside a rectangular domain of $-2\pi < y < 2\pi$ (dashed lines), $(b)$ particles are initially distributed inside the domains of $0.6\pi < y < 1.6\pi$ and $-1.6\pi < y < -0.6\pi$, $(c)$ particles are located and fixed at the same location as $(b)$, and $(d)$ without particles. The time history of the swimming speed of the flagellum is shown in figure 5.9. From Einstein's results [219], the viscosity of a dilute suspension of small particles (in a Newtonian fluid) is calculated as $\mu^e = \mu(1+2.5\phi)$, where $\phi$ is the volume fraction of particles, i.e. the presence of the particles increases the fluid viscosity. A uniformly distributed particles around the flagellum does not strongly affect the average swimming speed (figure 5.8$(a)$), while the particle-free region around the flagellum enhances the swimming speed (figure 5.8$(b)$). When the particles are fixed (figure 5.8$(c)$), the effective confinement effect is strong, therefore results in a larger swimming speed compared to the swimmer moving thought freely suspended particles. These observations are consistent with our previous findings in a shear-thinning fluid.

## 5.6 Concluding Remarks

We have numerically investigated the effects of rheological properties of the fluid on the swimming motion of a infinitely long planar waving flagellum. In a viscoelastic fluid, the swimming speed and power consumption always decreases with the Deborah number, independent of flagellum amplitude. In an inelastic shear-thinning fluid, the shear Carreau number Cr, related to the typical shear rate, is found to mostly affect the swimming behavior. Therefore, both the beating frequency and amplitude are important. Our simulation results recover the analytical results for small amplitude

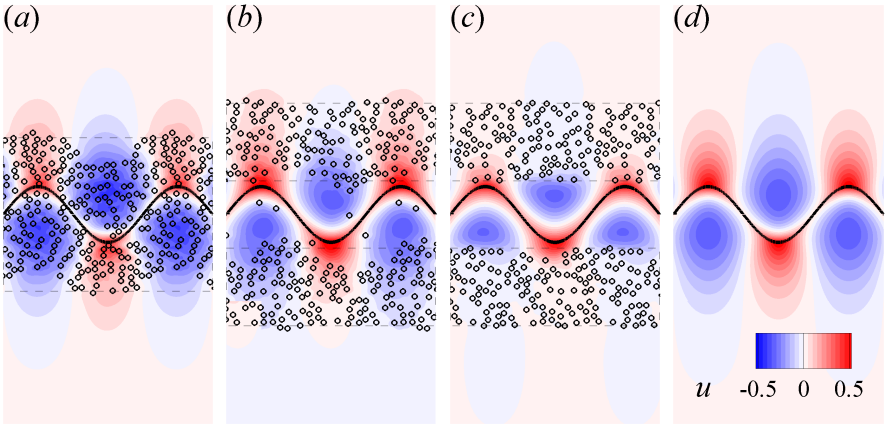


Figure 5.8. Distribution of the particles and the velocity field around a flagellum of $A = 0.4\pi$ in a Newtonian fluid of $(a) - (c)$ 200 particles initially distributed inside the regions covered by the dashed lines and $(d)$ without particles.

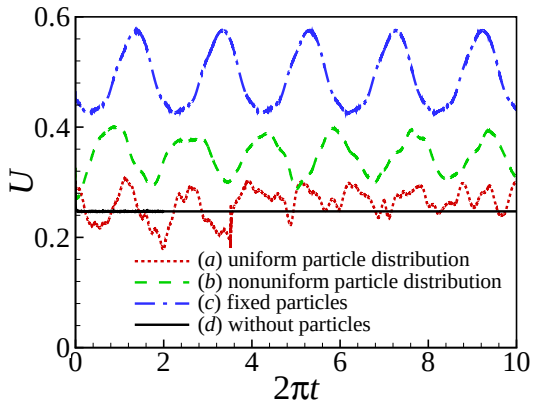


Figure 5.9. Time history of the swimming speed of the flagellum in different fluids.

flagellum [52], where speed is not affected and power is reduced. For a large amplitude flagellum, velocity enhancement and power reduction are observed. The swimming boost in a shear-thinning fluid occurs even for an infinitely long flagellum because it swims in a lower-viscosity fluid layer surrounded by a high-viscosity fluid. Two competing effects determine the speed enhancement: the viscosity and width of the inner layer. Increasing Cr reduces the viscosity of the inner layer, but enhances

its width. Therefore, there exists a maximum swimming speed, dependent on the oscillation amplitude as well as the fluid rheological properties. Same mechanisms also exists in a heterogeneous fluid environment with particles suspensions. The power consumption, on the other hand, follows a universal scaling law.

There are some differences between the simulation results and the experimental measurements of *C. elegans* by [214]. Even though experiments show that the circulation generated by *C. elegans* first increases with Cr and then decreases, the swimming speed is reported to be the same as the one in the Newtonian fluid. The difference may come from the fact that the swimming speed of *C. elegans* depends on the fluid viscosity, even in Newtonian fluids, while in the simulations, the swimming speed is the same. If we compare the experimentally measured swimming speeds in Newtonian and shear-thinning fluids at the same zero-shear-rate viscosity, we would see a higher speed in shear-thinning fluids which is consistent with our study. Further experimental results are required to investigate the existence of optimum speed for *C. elegans*.

# 6. NEAR WALL MOTION OF UNDULATORY SWIMMERS[1]

## 6.1 Motivation and Previous Works

Near-surface accumulation of microorganisms have been widely observed for spermatozoa [220, 221], bacteria [67], *C. elegans* [222] and Chlamydomonas [223]. Many different effects are involved in the wall-induced attraction of swimming microorganisms. The far field hydrodynamic effects on a swimmer depend on the swimmer type. A pusher, which generates thrust behind its body such as most bacteria, is attracted to the wall by the wall induced flow velocity when it swims parallel to the surface. A puller, on the other hand, reorients itself in the direction perpendicular to the surface [48, 81]. The Brownian diffusion enhances the wall accumulation [68, 70] and this effect is more important as the swimmer size decreases. More details on the near wall motion of swimmers in the Stokes regime can be found in recent review articles [3, 4]. Beyond the Stokes regime, small but non-negligible inertial effects has been considered by [49, 224].

When a swimmer gets close to a wall, the short-range hydrodynamic interaction and the contact with the wall are important in accurate prediction of the near-surface behavior. Experiments show that the contact between the cilia and the surface determines the scattering behavior of bull spermatozoa and *Chlamydomonas* algae from a solid boundary [223]. Spermatozoa accumulate close to a surface [220]. Their flagella beat in a three-dimensional waveform of conical shape or in a nearly planar wave form [221]. Numerical simulation shows that the near-wall swimming motion of a sperm depends on its initial location and angle [225]. The wall attraction of the sperm is affected by the flagellar wavenumber but not the shape of the head [226].

[1]Part of this chapter has been submitted as a research article "Near wall motion of undulatory swimmers in non-Newtonian fluids", by G. Li and A. M. Ardekani, to European Journal of Computational Mechanics.

It swims at a distance of about the swimmer size away from the wall [225]. Wall attraction of a sperm is also observed in the simulations based on the multiparticle collision dynamics [227]. However, these results show that the sperm is in a close contact with the wall. A sperm, whose flagellum has chiral asymmetry, swims in a circular trajectory [227]. Similar behavior was also observed for bacteria swimming near a wall [67]. For a hyper-activated sperm, its large undulatory amplitude and asymmetric waveform greatly affect the near-wall motion and the binding dynamics to the wall [228, 229].

Besides confinement and boundary effects, the fluid environment of microorganisms is often complex and shows both shear-thinning and viscoelastic properties [207, 230]. Such examples can be found in bacteria within biofilms which occur on almost all the surfaces [42], the spermatozoa in the female reproductive tract swimming through the cervical mucus [59], *H. pylori* colonizing the mucus layer covering the stomach [60] and *B. burgdorferi* penetrating the connective tissues in skin [62]. The effects of fluid elasticity on the microorganisms swimming in an unbounded domain have been widely investigated. Depending on the swimming strategy, flexibility of the flagellum, and the rheological properties of the background fluid, both speed enhancement and reduction have been observed [134–136, 208, 231]. For a finite planer flagellum, the speed enhancement due to the fluid elasticity occurs for a soft kicker swimmer with an amplitude increasing from its head to the tail [208]. However, it should be noted that the speed of a soft undulatory flagellum is much smaller than a stiff swimmer [232].

Recent studies show that shear-thinning viscosity may have a more important effect on the microorganism swimming behavior [52, 53]. A peak in the swimming speed of bacteria at a certain polymer concentration was observed in a solution of high molecular weight polymers [34]. The enhanced swimming speed of bacteria is found to be related to the reduced viscosity encountered by its fast-rotating flagella instead of fluid elasticity [34]. For a *C. elegans* in a shear-thinning fluid, its swimming speed and kinematics are less affected by the shear-thinning behavior of the fluid, while its

flow field and power consumption are greatly modified [214,233]. A similar behavior is observed using the analysis of small amplitude waving sheet [52]. Numerical simulations, on the other hand, show speed enhancement of a sperm in a shear-thinning fluid [212,213]. Our recent studies illustrate that the speed enhancement occurs at large oscillation amplitudes as undulatoray flagellum creates a corridor of low-viscosity fluid around it, leading to a similar effect as confinement. [53]. A spherical squirmer, on the other hand, may swim faster and slower in a shear-thinning fluid depending on the slip velocity on its surface [234].

Motion near a wall greatly affects the hydrodynamics of a microorganism in both Newtonian and non-Newtonian fluids. Analytical results show that an infinitely long flagellum swims faster but less efficient when close to a wall in a Newtonian fluid [64]. This speed enhancement is weakened by the fluid elasticity [235]. The boundary attraction effects, which are important for bacteria and spermatozoa, are not considered in these studies. The wall effects on passive particles in viscoelastic and shear-thinning fluids have been extensively studied [51,142,147]. However, the near-wall swimming of a self-propelled microorganism in non-Newtonian fluids is still poorly understood. Based on a squirmer model, the analytical results of Yazdi *et al.* [236] showed that the fluid elasticity breaks down the time-reversibility of the phase portraits of a squirmer in a Newtonian fluid. The periodic trajectories for a pusher and puller in a Newtonian fluid change into spirals in the presence of weak elasticity in the background fluid. For a squirmer with an oscillating tangential surface velocity, both pullers and pushers in a viscoelastic fluid swim towards the no-slip boundary if they are initially located within a small attraction region near the wall [237]. In a fluid with strong fluid elasticity, direct numerical simulations showed that the neutral squirmer in viscoelastic fluids stays near a wall for a longer time, while a puller is less affected. A pusher is found to be permanently trapped near the wall because of a highly stretched region of polymer molecules formed behind its body [50].

In this work, we investigate the near-wall motion of an undulatory swimmer in Newtonian and non-Newtonian fluids using a two-dimensional direct numerical sim-

ulation. We simulate the swimmer as a finite-length flagellum with a kinematically specified waving form, and two types of swimmer, kicker and burrower are studied to model the sperm and *C. elegans*, respectively. Wall attraction of the swimmer as well as its effect on the swimming performance is analyzed. The effects of shear-thinning fluid viscosity and fluid elasticity on the near-wall motion of a swimmer are both considered. In particular, we find that an enhanced swimming speed can be achieved by combination of wall effects, fluid elasticity and shear-thinning viscosity.

In this chapter, we model the swimmer as a two-dimensional stiff flagellum of finite length immersed in a fluid. An undulatory swimmer with its waving plane perpendicular to the wall were observed for sperm [223] and *C. elegans* [222]. The prescribed motion of the waving flagellum [5] is given by a traveling wave $y = a(s)\cos[2\pi(s/l - t/T)]$, where $t$ is the time, $a(s)$ is the dimensionless amplitude, $l$ is the swimmer length, and $s \in [0, l]$ is the length measured from the head of the swimmer. Two undulatory swimmer types are considered by varying the amplitude profile. For the kicker swimmer, its amplitude linearly increases from the head to tail as $a(s) = As/l$, and for the burrower, the undulation amplitude decreases toward the tail as $a(s) = A(1 - s/l)$. In all our results, the length is scaled by $l$, time by the waving time period $T$, velocity by $l/T$, and pressure and stress by $\mu/T$, where $\mu$ is the fluid dynamic viscosity. At length and velocity scales relevant to microorganisms, inertial effects are neglected.

Simulations are conducted using a finite volume method on a fixed staggered grid implemented in the code developed by Sadegh Dabiri and coworkers [238–241]. A conventional operator-splitting method is applied to enforce the continuity equation. The spatial derivatives in the convection term are evaluated using the QUICK (Quadratic Upstream Interpolation for Convective Kinetics) scheme and the diffusion terms are discretized using the central difference scheme. The viscoelastic stress is solved using a commonly used formulation denoted as elastic and viscous stresses splitting (EVSS) method [190]. The computational domain is $10.24 \times 20$ with the grid size being $\Delta x = 0.01$ uniform in $x$-direction and for $y < 3$, where the flagellum motion

occurs, and is gradually stretched outside this region. The time step is $\Delta t = 10^{-3}$ and a second-order total variation diminishing (TVD) Runge-Kutta method is used for time marching. At the bottom boundary at $y = 0$, a no slip boundary condition is imposed. Periodic boundary conditions are imposed at the left and right sides of the computational domain and far-field boundary conditions are imposed at the top side. The flagellum is modeled using a series of Lagrangian points immersed inside the fluid domain. The forcing term along the flagellum is calculated iteratively to impose the prescribed undulatory velocity and is then distributed back to the fluid [108].

When the swimmer approaches the wall, the high pressure in the thin film between the swimmer and the wall prevents any unphysical overlaps. However, a very small grid resolution is needed to properly capture this dynamic process and consequently it is computationally expensive. A short-range repulsive force [109] is added if the distance of any point on the swimmer from the wall is smaller than a certain value

$$\boldsymbol{F}_r = \frac{F_R}{\varepsilon}\left(\frac{d - dr}{dr}\right)^2 \boldsymbol{e}_z, \tag{6.1}$$

where $F_R$ is the characteristic force, $\varepsilon = 10^{-4}$ is a small positive number, $d$ is the distance between the point on the swimmer and the wall, $dr$ is the force range and is usually set to the smallest grid size $\Delta x$ in the computational domain [109]. The direction of the repulsive force $\boldsymbol{e}_z$ is normal to the wall.

## 6.2 Near Wall Motion in a Newtonian Fluid

We first investigate the near wall swimming motion of a flagellum in a Newtonian fluid. Initially, the flagellum is located above the wall at $y_0 = 0.5$, with an initial angle $\theta_0 = -45^\circ$. Here, $\theta$ is measured with respect to the direction parallel to the wall, and the swimmer is heading towards the wall for $\theta < 0$. Figure 6.1 compares the trajectory of the center of the swimmer ($s = l/2$) with different amplitudes. The high frequency oscillations in the curves show the variation of the swimmer's center in each undulatory cycle. Three different near-wall swimming modes are observed

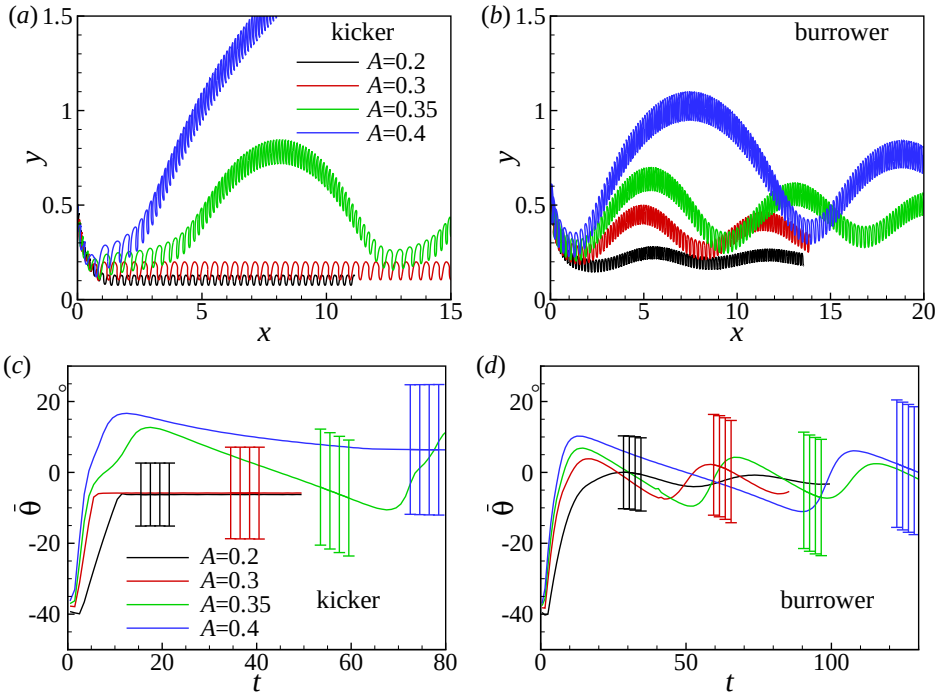


Figure 6.1. Trajectory of a near-wall ($a$) kicker and ($b$) burrower of different amplitudes in a Newtonian fluid. The swimmer is initially located at $y_0 = 0.5$ and $\theta_0 = -45°$. Time history of the orientation angle $\bar{\theta}$ averaged over each undulatory cycles for a ($c$) kicker and ($d$) burrower. Error bars show the range of temporal variation of the angles.

for the kicker swimmer. At $A \leq 0.3$, the kicker is stably attracted to the wall. The kicker swims close to the wall and periodically collides with it. This type of near-wall motion of an undulatory swimmer has been observed in simulations [242] and experiments for a sperm [223]. At $A = 0.35$, the kicker is weakly attracted to the wall and swims in a cyclic trajectory. The kicker stays near the wall in a few undulatory cycles and quickly escapes, and it takes a much longer time for the swimmer to swim back to the wall again. The average distance between the kicker and the wall is on the order of the swimmer size which is consistent with the results of Smith *et al.* [225]. Similar cyclic near-wall motion was also observed for a puller squirmer near a wall [49]. At high enough amplitude, the kicker eventually escapes the wall.

Therefore, the wall attraction of an undulatory flagellum is strongly affected by its undulation amplitude. The burrower swimmer is always weakly attracted to the wall and swims in a cyclic motion. The amplitude of its cyclic trajectory slowly decreases. The pusher-type swimmers are more strongly attracted towards the wall than the pullers. Wall attraction is weakened at higher amplitudes for both swimmer types. On the other hand, the far-field hydrodynamic analysis for a swimmer parallel to the wall shows that a force dipole pusher is attracted to the wall by its image, while the puller moves away from its image.

The weak attraction of an undulatory swimmer towards the wall can be understood in the light of the orientational angle of the swimmer. Fig. 6.1($c$) and ($d$) show the time history of the swimmer's angle averaged over each undulatory cycle, and error bars show the range of its temporal variation. As the swimmer approaches the wall, its head first contacts with the wall and the angle of the swimmer quickly increases. For the kickers of $A = 0.2$ and 0.3, the final average angle is negative $\bar{\theta} \simeq -6^{\circ}$ and the kicker is stably attracted to the wall. In this swimming mode, both the head and the tail of the kicker periodically collides with the wall. For a kicker with larger amplitudes, its scattering angle is positive, meaning the swimmer initially escapes the wall. Positive scattering angle is observed for the burrower, which is related to its decreasing wave amplitude from the head to tail. The wall effect slowly reduces the angel of the swimmer. Note that for the swimmer with large amplitudes, for example kicker of $A = 0.35$, there is no contact between the swimmer's tail and the wall, and the hydrodynamic interaction is responsible for the swimmer's attraction towards the wall. The strength of this hydrodynamic interaction determines the near-wall swimming mode of the swimmer. For a kicker of $A = 0.35$ and a burrower, the orientation angle eventually becomes negative and the swimmer gets back to the wall. While for a kicker of $A = 0.4$, its initial scattering angle is large and the wall effect becomes negligible as it swims away from the wall. Therefore, the wall contact, the initial scattering angle of the swimmer and the hydrodynamic effects are all important to the near-wall motion of an undulatory swimmer.

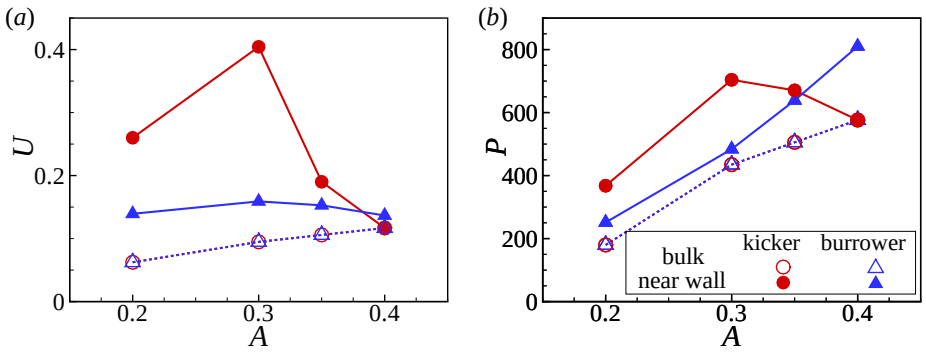


Figure 6.2. $(a)$ The swimming speed $U$ and $(b)$ power consumption $P$ of swimmers in a Newtonian fluid as a function of the swimmer's amplitude $A$.

The wall attraction strongly affects the swimming performance of an undulatory flagellum. In figure 6.2, the swimming speed and the power consumption of swimmer in a bulk fluid and near a wall are compared. The power consumption is calculated by $P = \int_s \boldsymbol{u} \cdot \boldsymbol{f} dS$. In the bulk fluid, the swimming speed and the power consumption monotonically increases with the swimmer's amplitude. Due to symmetry, the performances of kicker and burrower swimmers are exactly the same. The wall attraction increases the swimming speed as well as the power consumption compared to a swimmer in a bulk fluid. The effects are stronger for a swimmer closer to the wall. These results are consistent with an infinitely long flagellum near a wall [64]. For both swimmer types, the maximum swimming speed occurs at $A = 0.3$. For the kicker, near-wall swimming speed is about 4 times its speed in a bulk fluid, and its power consumption increases about 60%. These results indicate that the undulatory swimmer can optimize its swimming performance near the wall by tuning its undulation amplitude.

### 6.3 Near Wall Motion in Non-Newtonian Fluids

Figures 6.3($a$) and ($b$) compare the trajectories of a swimmer of $A = 0.2$ and 0.4 in a Newtonian and inelastic shear-thinning fluids. The swimmer is initially located at $y_0 = 0.5$ and $\theta_0 = -45°$. Stronger wall attraction is observed for both kicker and burrower in an inelastic shear-thinning fluid. The kicker of $A = 0.4$ no longer escapes the wall and it swims in a cyclic trajectory in a shear-thinning fluid at $Cu = 1$. Further increasing the Carreau number to $Cu = 3$ does not affect kicker's trajectory. The shear-thinning effect decreases the distance of a burrower away from the wall and a stable attraction is observed for burrower of $A = 0.2$. The strong wall attraction is mainly related to the scattering angle of the swimmer. The shear-thinning viscosity decreases the scattering angle of the swimmer from the wall (see figure 6.3($c$)). Therefore, it stays near the wall for a longer time. In figure 6.3($d$), we compare the normalized speed and power of a stably attracted swimmer of $A = 0.2$ for different values of Carreau numbers $Cu$. For both the swimmer types, the shear-thinning effects increase the swimming speed and reduce the power consumption, no matter whether the swimmer is in the bulk fluid or near the wall. The shear-thinning effects are the same for a kicker and burrower in the bulk fluid. The speed has a peak value at $Cu \sim 1$ due to the optimum effect of low-viscosity fluid corridors generated by shear-thinning viscosity near an undulatory flagellum as demonstrated in our previous work [53]. When attracted to the wall, swimmer's speed monotonically increases with increasing $Cu$. This speed enhancement is stronger for a swimmer near a wall. The power consumption roughly follows the same scaling law as the swimmer in the bulk fluid [53] and asymptotically approaches $P/P_N = 0.5$.

The fluid elasticity strongly affects the wall attraction of the swimmer. Stable wall attraction of a kicker of $A = 0.2$ is observed in a viscoelastic fluid at $De = 1$ and $\alpha = 0$ (see figure 6.4($a$)). Compared to the swimmer in a Newtonian fluid, the kicker in a viscoelastic fluid of $De = 1$ and $\alpha = 0$ has higher distance away from the wall. Later, we will see that this is due to the fact that the kicker swimmer has

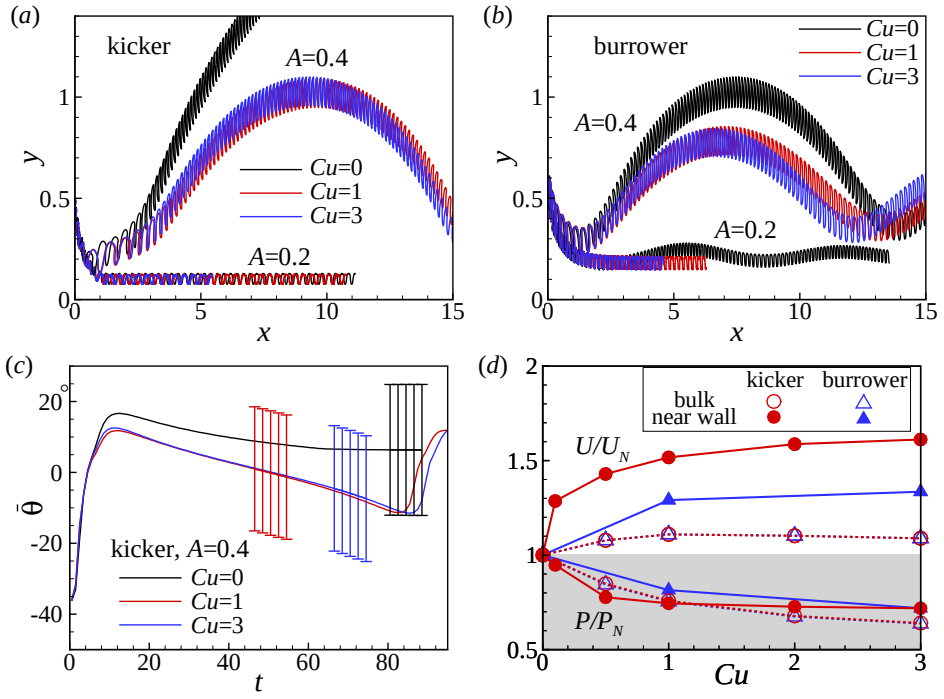


Figure 6.3. Trajectory of a near-wall swimming ($a$) kicker and ($b$) burrower of $A = 0.2$ and 0.4 in an inelastic shear-thinning fluid at $Cu = 1$. ($c$) Time history of the orientation angle $\bar{\theta}$ averaged over each undulatory cycle for a swimmer of $A = 0.4$. ($d$) The normalized swimming speed $U/U_N$ and power consumption $P/P_N$ of swimmers of $A = 0.2$ swimming in a bulk fluid and near a wall. Here, $U_N$ and $P_N$ are the swimming speed and power consumption in a Newtonian fluid, respectively.

a large orientation angle towards the wall in a constant-viscosity viscoelastic fluid. In a shear-thinning viscoelastic fluid, the near-wall behavior of the kicker is similar to its motion in a Newtonian fluid. The fluid elasticity has the same effects on the burrower, and a stable wall attraction is observed for a burrower in viscoelastic fluids (see 6.4($b$)). The non-Newtonian rheological behavior of the background fluid have similar effects on the wall attraction of a kicker and a burrower, but their effects on the swimming speed are different. In figure 6.4($c$), we compare the temporal evolution of the swimming speed of a kicker of $A = 0.2$ in different fluids along the wall during an undulatory cycle. The instantaneous speed of the swimmer depends on its undulatory

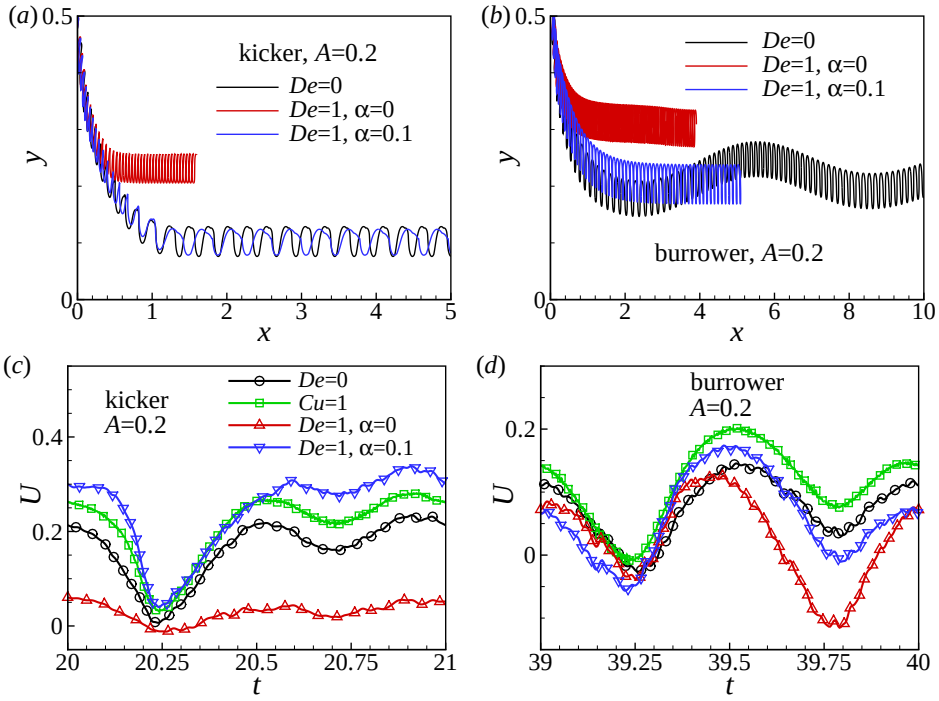


Figure 6.4. The trajectory of a near-wall swimming ($a$) kicker and ($b$) burrower of $A = 0.2$ in a Newtonian and viscoelastic fluids. Comparison of the swimming speed of a near-wall swimming ($c$) kicker and ($d$) burrower in different fluids.

phase and the waveform near the wall. The non-Newtonian fluid behavior does not affect the velocity profile but strongly affects the swimming speed. The kicker swims much slower in a constant viscosity viscoelastic fluid. Interestingly, the combination the fluid elasticity and the shear-thinning viscosity generates a strong speed boost, which is larger than in an inelastic shear-thinning fluid. Such a speed enhancement in a shear-thinning viscoelastic fluid is not observed for a burrower.

The polymer molecules are highly stretched in the region near the head of the swimmer, which generate a strong attraction of the swimmer to the wall (see figure 6.5($a$) and ($b$)). On the other hand, this effect reduces the wall contact force on the swimmer's head and prevents the swimmer to further reorient its angle away from the wall. This result is consistent with our previous finding on the permanent attraction

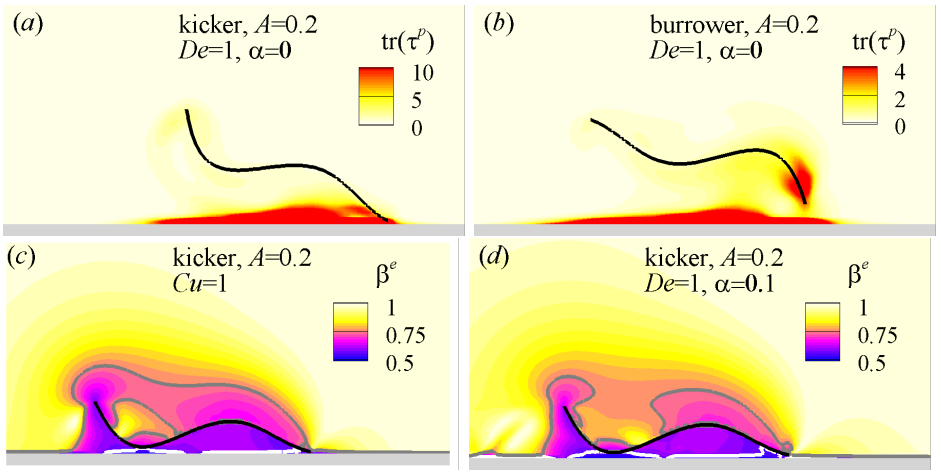


Figure 6.5. Polymer stretching around a near-wall swimming $(a)$ kicker and $(b)$ burrower of $A = 0.2$ in a viscoelastic fluid at $De = 1$ and $\alpha = 0$. The fluid viscosity distribution around a near-wall swimming kicker of $A = 0.2$ in $(c)$ an inelastic shear-thinning fluid at $Cu = 1$ and $(d)$ shear-thinning viscoelastic fluid at $De = 1$ and $\alpha = 0.1$. White and gray curves in $(c)$ and $(d)$ are the contourlines of $\beta^e = 0.55$ and 0.75, respectively.

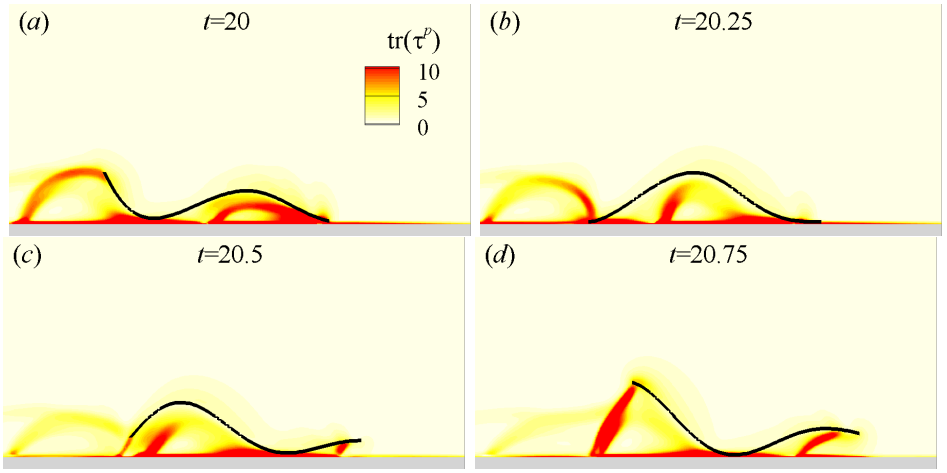


Figure 6.6. Time sequence of the polymer stretching around a near-wall swimming kicker of $A = 0.2$ in a shear-thinning viscoelastic fluid at $De = 1$ and $\alpha = 0.1$.

of a pusher squirmer in a viscoelastic fluid [50]. The undulatory motion of the kicker in an inelastic shear-thinning fluid reduces the effective viscosity of the fluid around the flagellum, creating a low viscosity fluid region which translates with the swimmer (see figure 6.5($c$)). The fluid viscosity on the wall side is much more reduced due to the strong shear rate inside the gap. Therefore, the interplay between the wall attraction and the shear-thinning effects leads to a strong speed enhancement for an undulatory swimmer as shown in figure 6.3($d$). In figure 6.5($d$), the distribution of effective viscosity in a shear-thinning viscoelastic fluid around the kicker, calculated using Eq. (5.3), is similar to an inelastic shear-thinning fluid. On the wall side, the shear-thinning effect in a viscoelastic fluid is stronger than the inelastic shear-thinning fluid. On the other side, the size of the low-fluid viscosity region around the kicker is also smaller in a viscoelastic fluid. Based on our previous argument on the swimming motion of an infinitely long flagellum in a shear-thinning fluid, both these effects favors the speed enhancement of the swimmer as seen in figure 6.4($c$). Another reason for the stronger speed enhancement of kicker in a shear-thinning viscoelastic fluid may be related to the effects of fluid elasticity. The polymer stretching around the near-wall swimming kicker is a highly dynamical process ( see figure 7.7). The undulatory motion of the head and the tail of the swimmer away from the wall strongly stretches the polymer molecules. As the swimmer swims along the wall, its entire body interacts with the strong polymer stretching region generated by its head. This interaction can lead to an attraction of the swimmer towards the wall which increases its swimming speed.

## 6.4 Summary and Discussion

We have numerically investigated the near-wall motion of an undulatory swimmer of finite length in Newtonian and non-Newtonian fluids. In a Newtonian fluid, three types of near-wall swimming modes are observed for the kicker depending on the amplitude of the undulatory flagellum. The kicker of small amplitude is stably

attracted to the wall and glides with a fast speed along the wall. In this type of swimming mode, both the head and the tail of the swimmer are in close contacts with the wall and the swimmer has a small negative angle towards the wall. This result is consistent with the observations for the near-wall swimming of a sperm [227]. The swimming speed and the power consumption are greatly increased by the wall attraction. At larger amplitudes, the kicker first escapes from the wall. The hydrodynamic interaction between the swimmer and the wall reorients the swimmer back towards the wall. It may then swim in a cyclic trajectory which slowly approaches a stable height. The swimmer is weakly attracted to the wall with its distance away from the wall on the same order as the swimmer size. This attraction is observed in simulation results of Smith *et al.* [225]. The kicker escapes the wall for large enough initial scattering angle. Cyclic trajectories are observed for the burrowers studied in this work. These results show that both the flagella contact with the wall and the hydrodynamic interactions are crucial in determining the near-wall behavior of an undulatory swimmer.

Non-Newtonian fluid rheology affects both the wall attraction of a swimmer and the swimming performance of a swimmer near the wall. Shear-thinning viscosity of the fluid slightly enhances the wall attraction, mainly by reducing the scattering angle of the swimmer. It greatly increases the swimming speed by creating a low-viscosity fluid region around the swimmer. This mechanism is the same as swimming in a bulk environment. The effects of fluid elasticity is more complex. In a constant-viscosity viscoelastic fluid, it enhances the wall attraction by generating a strong polymer stretching region near the head of the swimmer and inhibits the swimmer's reorientation. As a result, the swimmer's head is strongly attracted to the wall and swims slowly with a high inclination angle along the wall. In a shear-thinning viscoelastic fluid, the combination of the fluid elasticity and shear-thinning viscosity generates the strongest speed enhancement for the kicker. In this case, both the reduced viscosity near the swimmer and the interaction between the swimmer and the polymer molecules contribute to the speed enhancement. This strong speed enhancement is

closely related to the configuration of the near-wall swimmer and is not observed for the burrower. Cervical mucus has been shown to have both shear-thinning viscosity [207] and viscoelasticity [230]. Our results indicate that these properties lead to fast swimming motion of sperms near a wall in a shear-thinning viscoelastic fluid.

In the current study, the swimmer is modeled as a finite flagellum with a prescribed traveling wave form. The effects of non-Newtonian fluid rheology and wall contact on the wave form are not considered. Gagnon *et al.* have showed that the beating kinematics of a *C. elegans* in a shear-thinning fluid is the same as in a Newtonian fluid [214]. The fluid elasticity, on the other hand, strongly influences the beating pattern of cilia of a *Chlamydomonas* [243]. Interestingly, shape of the beating cilia of *Chlamydomonas* is also strongly modified by the wall contact, while the beating shape of a sperm is relatively less affected [223]. It also worth noting that the near-wall behavior of a swimmer depends on its initial configuration, especially its angle of incidence [70, 81]. Another important effect for the near-wall behavior in real scenarios is the interaction between the microswimmers, especially for the sperm cells which usually swim in high concentrations. All these details could have important effects on the near-wall behavior of a swimmer. Further studies are required to include these effects.

# 7. ELASTOHYDRODYNAMICS OF AN INTERNALLY DRIVEN FLAGELLUM

## 7.1 Motivation and Previous Works

Many small organisms and cells, such as bacteria, algae and sperm swim in a fluid using active motion of cilia and flagella. Many prokaryotic cells, such as bacteria, use a thin helical filament which rotates relative to the cell body to propel the cells. The eukaryotic cells usually have a thicker filament, which diameter is around 180nm [244] compared to the 20nm [17] for a prokaryotic filament, for example *E. coli* flagella. For the eukaryotic cells, almost the entire filament appendages undergoes a periodic deformation to generate the cellular self-propulsion [245]. The filament contains an axoneme, which consists of a ring-like arrangement of nine doublets of parallel elastic microtubules and one pair of microtubules in the center. The nexin proteins connects the nearby microtubule doublets and provides elastic links between them. The dynein molecular motors which locate in between the neighbouring microtubules generate local sliding displacements between adjacent microtubules in the presence of ATP [131, 246]. The global sliding of the microtubules is suppressed because the microtubules pair is rigidly connected at one end. Therefore, a bending deformation of the filament occurs because of the local sliding motion [247].

Axonemal cilia and flagella can generate different periodic beating and waving forms. The waveforms of the filament and the swimming motion of the organism are determined by the interaction between the flagella internal force, the passive elastic force generated due to the deformation of the structure, and the external effects, such as hydrodynamic forces. For *Paramecium* and *Volvox*, a large number of cilia on the surface deform in a coordinated manner and generate a propagating wave on the surface [248]. Cilia are also found on the inside surface of lungs where their coordinated deformation moves the mucus and particles up toward the nasal passage

[249]. The bi-flagellated alga *Chlamydomonas* uses two cilia in front of its body to pull itself forward. The waveform of a cilium has an asymmetric beat pattern, which consists a power stroke and recovery stroke. In the power stroke, the cilium extends at the base and sweeps back similar to the arms of a person in a breaststroke swimming. In the recovery stroke, the flagellum folds and generates less drag. For a sperm, the bending wave of its flagellum propagates from the head towards the tail with the amplitude increasing. The flagella can either beat in a three-dimensional waveform of conical shape or a nearly planar wave form [221]. The flagellar waveform can also be asymmetric for hyperactivated sperm [250]. Many nematode swimmers, such as *C. elegans*, have a different body structure and a much larger body size compared to sperm and bacteria, while they also use a propagating wave along their body for locomotion. For *C. elegans*, its waving amplitude decreases from the head to the tail.

The details of controlling mechanism for the flagellar and ciliary beats and their interaction with the surrounding fluid environment are still not fully understood [131]. Fluid rheology is found to greatly affect the waving form of the flagellum and cilia and the swimming speed of the organisms. In cervical mucus, the bending deformation of the filament is confined to its distal portion and show a smaller amplitude and wavelength compared to those in a Newtonian fluid [251]. Similar phenomena were also observed for *Chlamydomonas* in a viscoelastic fluid, where the deformation of the cilia at the proximal side is suppressed [243]. For *C. elegans*, the shear-thinning viscosity does not affect its waving form and the swimming speed [214], while the flow field around the swimmer and the power consumption are greatly affected [53, 233]. The filament deformation can also be affected by the contact force when collides with a wall surface [223]. The beating pattern of the filament is suggested to be a self-organized mechanism, where the filament spontaneously oscillates because of the interplay of the dynein motors and the elastic microtubules [36, 252]. Camalet and Jülicher [37, 54] proposed an internally driven filament model which assumes a sliding force distribution along the filament. Their model showed that a spontaneous oscillating instability occurs for the filament via a Hopf bifurcation [54]. Different

dynein motor coordination models were developed to match with the experimental data of the wave shape of sperms [39]. The results show that the model of load dependent detachment rate of the motors best fits the experimental observations [39].

Despite of the complexity of the internally driven mechanism, a simpler model has been used to describe the sliding force distribution along the filament and study the hydrodynamics of the bending flagellum and cilia [208,231,242,253]. This model assumes a deterministic forcing mechanism for the filament and models a chemical signaling that periodically regulates the activated and deactivated state of the dynein motors [254, 255]. Theoretical works assume an internal sliding force in the form of a traveling wave [231, 253] and use a resistive force theory to account for the hydrodynamic force [11]. For a hinged flagellum in a fluid of high viscosity or fluid elasticity, beating deformation is found to be concentrated at the distal end of the flagellum similar to observations in experiments [253]. Fauci and Peskin [55] proposed a numerical model with a preferred curvature along the flagellum to investigate the hydrodynamics of an undulatory swimmer. This model has been successfully applied to investigate the interaction between a flagellum and a wall surface [66], synchronization of two flagella [235, 256], calcium signaling of the flagellum beating [257], sperm detachment from the epithelium [229]. A recent study shows that the swimming speed of an undulatory flagellum can either be enhanced or hindered by fluid elasticity depending on the bending stiffness of the swimmer [208]. A stiff swimmer swims slower, while a soft swimmer can swim faster if its amplitude increases from the head to the tail. However, the details of the interaction between active bending motion of the flagellum and the hydrodynamic forces are still poorly understood.

In this work, we investigate the elastohydrodynamics of a self-driven undulatory swimmer in a viscous fluid using two-dimensional direct numerical simulations. We simulate the swimmer as a finite-length flagellum driven by an internal sliding force, and two types of swimmer, kicker and burrower are studied to model the motion

of sperm and *C. elegans*, respectively. The effects of the bending stiffness of the swimmer, the internal sliding force, and the inertial effects are considered.

## 7.2 Elastohydrodynamics of an Internally Driven Flagellum

The flagellum of length $L$ and radius $a$ is internally driven by a distributed sliding force [37] and deforms within a plane. For the fluid, the Navier-Stokes equations are solved on an Eulerian grid

$$\rho\frac{d\boldsymbol{u}}{dt} = -\nabla p + \mu\nabla^2\boldsymbol{u} + \boldsymbol{f}_h, \qquad \nabla\cdot\boldsymbol{u} = 0, \tag{7.1}$$

where $\boldsymbol{f}_h$ is the hydrodynamic force exerted on the fluid by the elastic flagellum. The governing equation for the elastic flagellum is [258]

$$\rho_L\frac{\partial^2\boldsymbol{X}}{\partial t^2} = -\boldsymbol{F}_h + \boldsymbol{F}_e, \tag{7.2}$$

where $\rho_L$ is the line density of the elastic filament which is negligible because the thickness of the flagellum is small. The fluid and the elastic structure are coupled together by force conservation and no-slip no-penetration boundary conditions

$$\boldsymbol{f}_h(\boldsymbol{x}) = \int_L \boldsymbol{F}_h(\boldsymbol{X})\delta(\boldsymbol{x}-\boldsymbol{X})ds, \qquad \boldsymbol{U}(\boldsymbol{X}) = \int_V \boldsymbol{u}(\boldsymbol{x})\delta(\boldsymbol{x}-\boldsymbol{X})dV, \tag{7.3}$$

where the integrations are done over the flagellum $L$ and entire fluid domain $V$, respectively. $\delta$ is the delta function.

On the right hand side of Eq. (7.2), two forces (per length) are the hydrodynamic force acting on the flagellum $-\boldsymbol{F}_h$ and the elastic force $\boldsymbol{F}_e$. The elastic force is calculated by the variation of the distributed elastic energy $E_e$ given as [37]

$$E_e = \frac{k_b}{2}\kappa^2 + \frac{k_s}{2}(\xi-1)^2 - a\kappa F^i, \tag{7.4}$$

which includes the bending energy, the stretching energy and the energy corresponding to the relative sliding motion of neighboring microtubule doublets inside the flagellum [37]. $k_b$ and $k_s$ are the bending and stretching stiffness, respectively. $\kappa$ is the signed curvature of the filament, $\xi = |\partial\boldsymbol{X}/\partial s|$ is the extension rate of the flagellum,

$a$ is the thickness of the flagellum. $F^i(s) = -\int_s^L f^i(s')ds'$ is the integration of the distributed internal force $f^i$ along the flagellum [37], where $s = 0$ is at the head of the flagellum and $s = L$ is at the tail. In most of previous studies [66, 235] and the current work, $k_s$ has a large value to model an inextensible flagellum. In the current simulation, $\xi - 1$ is around 0.02%. For a strictly inextensible filament, $k_s$ becomes a Lagrange multiplier and needs to be determined from the inextensibility condition [258]. The distributed elastic force on the flagellum is calculated to be

$$\boldsymbol{F}_e = -\frac{\partial E_e}{\partial \boldsymbol{X}} = -k_b(\kappa - \kappa^0)\frac{\partial \kappa}{\partial \boldsymbol{X}} - k_s(\xi - 1)\frac{\partial \xi}{\partial \boldsymbol{X}} + a\kappa f^i \frac{\partial s}{\partial \boldsymbol{X}}, \tag{7.5}$$

where $\kappa^0 = aF^i/k_b$ is the target curvature [66]. In this work, two force distributions are imposed when changing the bending stiffness of the flagellum. In the first method, the target curvature $\kappa^0$ is imposed and the internal force density $F^i$ changes with bending stiffness $k_b$. In the second method, we fix the force density $F^i$ and change $\kappa^0$ for different bending stiffness $k_b$. The results are reported in dimensionless form by scaling, length by the wavelength of the flagellum $\lambda$, and time by waving period $T$, speed by the wave speed $c = \lambda/T$, and power by $\mu\lambda^2/T^2$. In a body-fixed coordinate system, the target shape of the flagellum has one complete waveform expressed as $y = Ax\cos[2\pi(x - t)]$ $(0 \leq x \leq 1)$ for kicker and $y = A(1 - x)\cos[2\pi(x - t)]$ for burrower, respectively. The target curvature is given as $\kappa^0_{A=0.2} = y''(x)/[1+y'(x)^2]^{3/2}$. For the kicker, most of its thrust is generated at the tail side and swimmer is a pusher. On the contrary, the burrower is a puller-type swimmer. In the current work, the nondimensional amplitude $A = 0.2$, and the total length of the flagellum is $L = 1.12$, the corresponding curvature is written as $\kappa^0_{A=0.2}$.

The Reynolds number of the swimmer is $Re = \rho\lambda^2/\mu T = 0.625$ and $6.25 \times 10^{-3}$. Another important dimensionless parameter for an elastic flagellum is the sperm number. For a two-dimensional undulating sheet, it is defined as [209, 259]

$$Sp = \lambda(\mu/k_bT)^{1/3}, \tag{7.6}$$

which is the ratio between the wavelength of the flagellum $\lambda$ and the elastohydrodynamic penetration length $(k_bT/\mu)^{1/3}$. In a dimensionless form, the target curvature

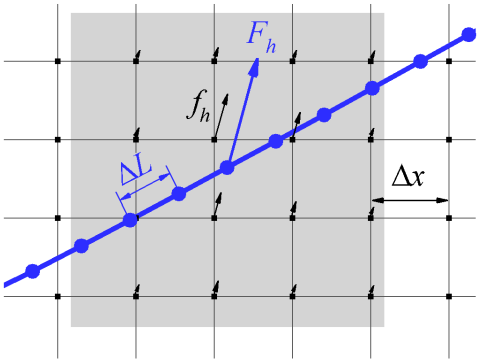


Figure 7.1. ($a$) Schematic of the immersed boundary method. Hydrodynamic forces (per length) $\boldsymbol{F}_h$ on the Lagrangian points (circles) are conservatively distributed to the body force $\boldsymbol{f}_h$ on the Eulerian grid (squares) inside the gray area.

and the sliding force are related to each other by $\kappa^0 = Sp^3 F_i a$, here $a$ and $F_i$ are the dimensionless thickness of the flagellum and the dimensionless sliding force. The sperm number also quantifies the ratio between the fluid stresses and bending stresses. For $Sp \ll 1$, the flagellum deformation is determined by the internally driven activity and the elastic deformation while its waveform is less affected by fluid stresses, i.e., the flagellum is stiff. In the limit of $Sp = 0$, the flagellum has a infinitely large bend stiffness and its shape and motion are prescribed. In contrast, for $Sp \gg 1$, the flagellum is soft and its deformation is strongly affected by the fluid stresses. The bending stiffness of sea urchin sperm flagella $k_b = 0.9 \times 10^{-21}\text{Nm}^2$ [260], the flagellum length $L = 30 - 45\mu\text{m}$, the wavelength $\lambda = 24 - 30\mu\text{m}$ [131], the period of the oscillation is around $T = 30\text{ms}$ [11], therefore its sperm number for three-dimensional undulations in water is $Sp = \lambda(\mu/k_b T)^{1/4} = 1.9 - 2.3$ in a water. For *C. elegans*, $k_b = 2 \times 10^{-15}\text{Nm}^2$ [261], $L = 1\text{mm}$, $\lambda = 2.5\text{mm}$, $U = 0.35\text{mm/s}$, $T = 0.5\text{s}$ [214], and the sperm number $Sp = 2.5$.

### 7.3 Numerical Method and Validation

In an immersed boundary (IB) method [262], the governing equations for the fluid and the elastic body are solved on Eulerian and Lagrangian grids, respectively (see figure 7.1). In our simulation, the flagellum is inside a region of uniform Eulerian grid spacing $\Delta x$ to ensure accuracy [262]. The flagellum is resolved by a line of uniformly distributed Lagrangian points with $\Delta L = L/N$ spacing, where $N$ is the number of points. The elastic energy is first discretized on each Lagrangian point $\boldsymbol{X}_j$ of the flagellum, then the elastic force $\boldsymbol{F}_e$ is calculated by taking the derivative of the discrete energy [66],

$$\begin{aligned} F_e(\boldsymbol{X}_j) = & \frac{k_b}{\Delta L^2}\left[(\kappa_j - \kappa_j^0)(\boldsymbol{n}_j + \boldsymbol{n}_{j-1}) - (\kappa_{j-1} - \kappa_{j-1}^0)\boldsymbol{n}_j - (\kappa_{j+1} - \kappa_{j+1}^0)\boldsymbol{n}_{j-1}\right] \\ & + \frac{k_s}{\Delta L}\left[(\frac{|\Delta \boldsymbol{L}_j|}{\Delta L} - 1)\boldsymbol{t}_j - (\frac{|\Delta \boldsymbol{L}_{j-1}|}{\Delta L} - 1)\boldsymbol{t}_{j-1}\right] \\ & - \frac{k_b}{2\Delta L}\left[\kappa_j(\kappa_{j+1}^0 - \kappa_{j-1}^0)\boldsymbol{t}_j - \kappa_{j-1}(\kappa_j^0 - \kappa_{j-2}^0)\boldsymbol{t}_{j-1}\right]. \end{aligned} \tag{7.7}$$

Note that in the last term, the sliding force is expressed in terms of target curvature. The discrete curvature and extension rate are

$$\kappa_j = \boldsymbol{n}_j \cdot \left(\frac{\boldsymbol{t}_j - \boldsymbol{t}_{j-1}}{\Delta L}\right), \qquad \xi_j = |\Delta \boldsymbol{L}_j|/\Delta L, \tag{7.8}$$

where $\Delta \boldsymbol{L}_j = \boldsymbol{X}_{j+1} - \boldsymbol{X}_j$. The discrete tangent unit vector is $\boldsymbol{t}_j = \Delta \boldsymbol{L}_j/|\Delta \boldsymbol{L}_j|$, the discrete normal unit vector $\boldsymbol{n}_j$ correspond to $\pi/2$ rotation of $\boldsymbol{t}_j$ in a counter clockwise direction. For the delta function, we use a second-order discretized version [262]

$$\delta(\boldsymbol{x} - \boldsymbol{X}) = \begin{cases} \frac{1}{16\Delta x^2}(1 + \cos\frac{\pi dx}{2})(1 + \cos\frac{\pi dy}{2}), & |dx| \le 2, |dy| \le 2 \\ 0, \quad \text{otherwise}, \end{cases} \tag{7.9}$$

where $\Delta x$ is the Eulerian grid spacing and $(dx, dy) = (\boldsymbol{x} - \boldsymbol{X})/\Delta x$.

Simulations are conducted using a finite volume method on a fixed staggered grid. The interpolation of the horizontal and vertical components of velocity and forces are based on different Eulerian grids. A conventional operator splitting method is applied

to enforce the continuity equation. The second-order TVD (total variation diminishing) Runge-Kutta method is used for time marching. The spatial derivatives in the convection term are evaluated using the QUICK (Quadratic Upstream Interpolation for Convective Kinetics) scheme and the diffusion terms are discretized using the central difference scheme. In the current study, we implement an explicit-time stepping immersed boundary method to solve the equations for undulating flagellum. In this simplest scheme of immersed boundary method, the fluid velocity and pressure are first updated keeping the structure fixed, and then the position of the structure is updated with the new velocity at the next time step. It is worth noting that for the current scheme, the simulation requires very small time steps to maintain stability when involving stiff elastic structures. An implicit-time stepping immersed boundary method has been proposed to resolve the problem [263, 264]. In the limit of $Sp = 0$, i.e. the flagellum has an infinitely large bending stiffness, its kinematics is prescribed and a distributed Lagrangian multiplier (DLM) method [108] is used to model the flagellum.

Simulation of prescribed motion of the flagellum using a DLM method has been validated in our previous studies [53]. In figure 7.2($a$), we compare our results of a stiff flagellum modeled using the IB and DLM methods. The results of the swimming motion of an internally driven stiff flagellum of $Sp = 0.5$ agrees well with the prescribed motion of a stiff flagellum of $Sp = 0$. We find the ratio of the Eulerian and Lagrangian grid mesh size affects the simulation results. In figure 7.2($b$), the swimming speed of the flagellum reaches a plateau for $\Delta x/\Delta L \leqslant 1$. For large $\Delta x/\Delta L$, the actual curvature profile along the flagellum strongly oscillates and the swimming speed of the flagellum deviates from the correct result.

## 7.4 Results and Discussion

We first investigate the swimming performance of an undulatory swimmer with fixed target curvature and different bending stiffness. In figure 7.8, the average swim-

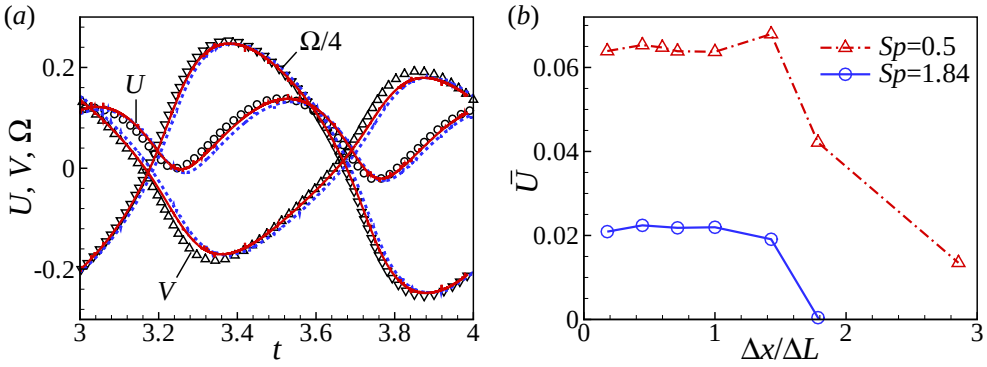


Figure 7.2. $(a)$ Comparison of the time history of velocity components and angular velocity of a kicker of $Sp = 0$ using DLM method (symbols) and a stiff kicker of $Sp = 0.5$ using IB method with $\Delta x = \Delta L = 0.01, \Delta t = 6.25 \times 10^{-6}$ (blue dashed lines) and $\Delta x = \Delta L = 0.005, \Delta t = 1.25 \times 10^{-6}$ (red solid lines). $(b)$ Effects of the ratio between Eulerian and Lagrangian grid spacing distance on the swimming speed of the flagellum swimmer, $\Delta x = 0.01$ and $\Delta t = 6.25 \times 10^{-6}$. The Reynolds number of the swimmer is $Re = 0.625$.

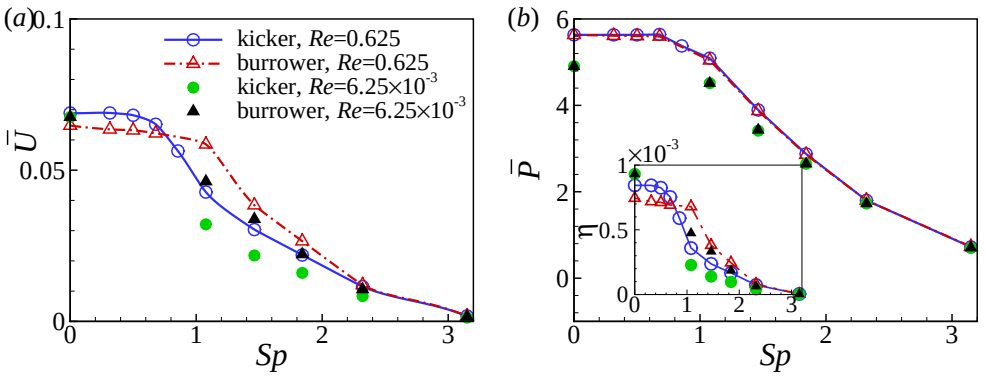


Figure 7.3. $(a)$ Average swimming speed $\bar{U}$, $(b)$ hydrodynamic power consumption $P$ and swimming efficiency $\eta$ of the kicker and burrower at a fixed target curvature $\kappa^0_{A=0.2}$ for different sperm number $Sp$.

ming speed $\bar{U}$, the hydrodynamic power consumption $\bar{P} = \int_0^1 dt \int_L \boldsymbol{F}_h \cdot \boldsymbol{U} ds$, and the efficiency $\eta = \bar{U}^2/\bar{P}$ for kicker and burrower are compared. At a fixed target curvature, all these variables monotonically increase with decreasing $Sp$. At $Sp = 0$,

the kicker and burrower has the same speed and power at $Re = 6.25 \times 10^{-3}$ because the kinematics of the two swimmers are exactly the same when viewed in a reversed time. At $Re = 0.625$, the kicker swims faster than the burrower when $Sp$ approaches zero. This result is consistent with the result of a squirmer at non-zero $Re$, where the inertial effects increase the speed of a pusher while decrease the speed of a puller [74]. The Stokes solution has the lowest energy dissipation compared to all the other incompressible flows with the same boundary conditions [111], and therefore higher energy consumption is required for the swimmers at $Re = 0.625$. At $Sp = 3.2$, the flagellum has a small body deformation and the swimming speed is small, which is only $2 - 3\%$ of the speed at $Sp = 0$. In the region in between, the burrower swims faster than the kicker at the same $Sp$. This phenomenon is observed for both low and high Reynolds numbers, indicating the existence of an optimal waving form for an elastic flagellum. The power consumptions for kicker and burrower, on the other hand, are similar for all $Sp$ even at $Re = 0.625$. These results show that the interaction between the hydrodynamic force and elastic force is important in determining the swimming performance of an undulatory flagellum.

In figure 7.4, we compare the time history of the swimming speed and power consumption for kicker and burrower in one undulatory time period as well as their trajectory of the center of mass. For the stiff swimmers at $Sp = 0.5$, both kicker and burrower reach the maximum swimming speed at around $T = 0$ and 0.5, where the swimmer exhibits a complete sine wave function along its body. Increasing $Sp$, the peak speed for a kicker gradually shifts to a later time. At $Sp = 1.84$, the peak speed occurs at around $T = 0.25$ and 0.75. Increasing $Sp$ does not greatly affect the peak-to-valley velocity difference for the kicker, while it generates a time period of high negative speed and leads to a slower swimming motion. A burrower, on the other hand, has a non-monotonic change in its peak speed with increasing $Sp$. A large reduction of the speed oscillation is observed for the burrower at larger sperm numbers, for example $Sp = 1.84$. Similar phenomena can also be observed for the power consumption. The power of burrower with $Sp = 1.08$ has a much smaller

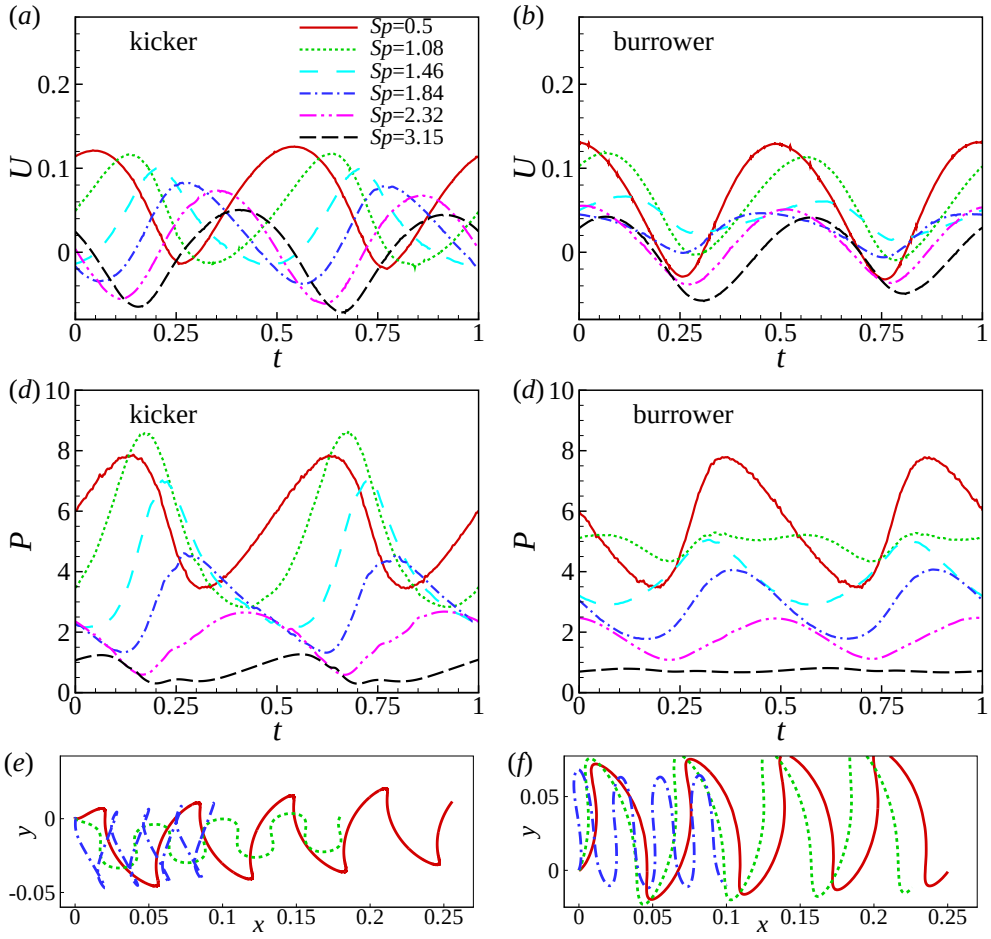


Figure 7.4. The time history of the $(a)$ swimming speed and $(b)$ power consumption for an undulatory kicker and burrower at $Re = 0.625$ for different sperm numbers. The trajectories of the center of mass of a $(e)$ kicker and $(f)$ burrower.

oscillation than the kicker. Therefore, a soft burrower not only swims faster than a kicker at the same $Sp$, it also has a more uniform energy consumption, which can be favorable for microorganisms. In figure 7.4$(e)$ and $(f)$, the center of mass of both kicker and burrower shows a zigzag trajectory, as observed in previous studies [265]. A burrower has a larger lateral oscillation than the kicker.

Figure 7.5 compares the curvature along the flagellum at $Sp = 0.5, 1.08$ and $1.84$. The target curvature for kicker and burrower shows a symmetry about the middle of

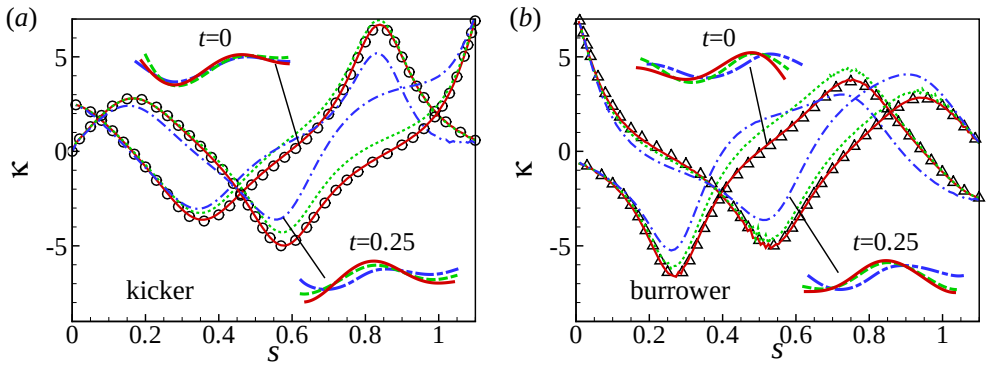


Figure 7.5. The curvature along the ($a$) kicker and ($b$) burrower of different $Sp$ at $t = 0$ and 0.25. Symbols show the target curvature, red solid lines, green dotted lines and blue dashdot lines show the curvature for flagellum at $Sp = 0.5, 1.08$ and 1.84, respectively. Inset: shape of the flagellum at $t = 0$ and 0.25. The Reynolds number is $Re = 0.625$.

the flagellum body at $s = 0.5$. The body shape of a stiff flagellum follows the target beat pattern, while a softer flagellum deviates from it. The deviation of curvature from the target curvature near the head ($s < 0.2$) is small for both swimmers. For a soft kicker, the curvature deviation mainly occurs at the tail side ($s > 0.6$). Since the tail side of the kicker has a larger amplitude and generates more thrust than the head side, the deviation from the target beat pattern results in a smaller swimming speed. On the contrary, a soft burrower has a large body deformation near the head, which generates a large thrust and a large swimming speed. A burrower also has a larger curvature deviation for $s > 0.2$.

The active and passive bending deformation of the flagellum strongly affects the local flow velocity and thus the swimming performance of the flagellum. In figure 7.6, the soft flagellum has a very different velocity distribution on it body compared with the stiff flagellum. A soft kicker generates a much weaker vorticity near the head than the stiff kicker, where a strong negative vorticity below the body leads to a large forward swimming speed. As a result, the local velocity for this segment of the soft kicker is negative. Near the tail of the soft kicker, the vorticity is enhanced

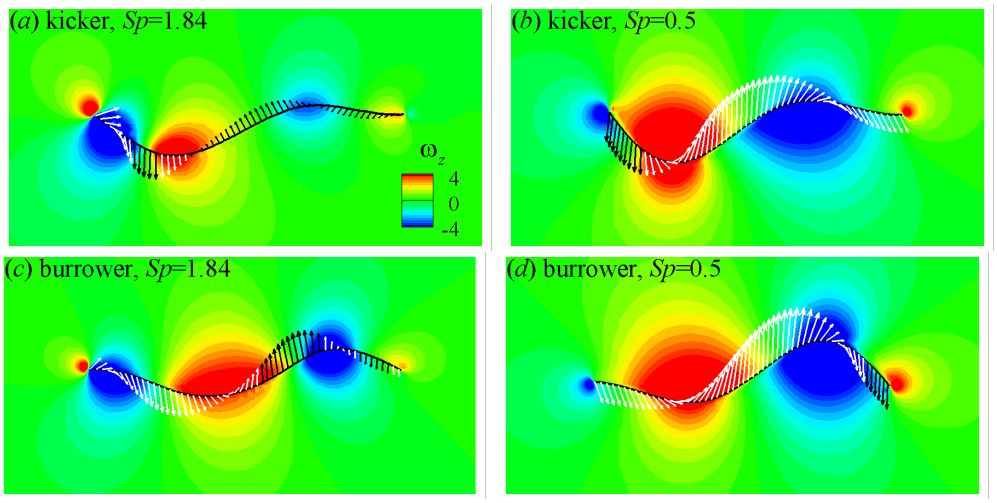


Figure 7.6. Flow field around the flagellum with a fixed target curvature $\kappa^0_{A=0.2}$ swimming from left to right at $t = 0$. Contour plots show the distribution of the vorticity $\omega_z$. Arrows show the velocity on the flagellum, where white and black colors corresponds to positive and negative local velocities, respectively. The Reynolds number is $Re = 0.625$.

and therefore the local velocity is positive. Generally, the region with local forward velocity is smaller than the region with local backward velocity, and the center of mass of soft kicker has a negative velocity at this time instant (see figure 7.4($a$)). Similar phenomena can be observed for the burrower. However, a strong positive vorticity region is generated above the soft burrower at the middle of the body, which leads to a large forward velocity for the flagellum. These results show that the details of the interaction between hydrodynamic effects from the fluid and the active and passive deformation of the flagellum is important for the flagellum swimming.

For the flagellum of a fixed sliding force, the target curvature $\kappa^0$ scales as $Sp^3$. Therefore, a stiff flagellum has a small undulatory amplitude and its swimming speed is small. A soft flagellum, on the other hand, strongly deforms, which leads to a lower swimming speed (see figure 7.7). In figure 7.8($a$), three different sliding forces in dimensionless form are considered $aF^i = 0.8\kappa^0_{A=0.2}, 0.32\kappa^0_{A=0.2}$ and $0.16\kappa^0_{A=0.2}$. Note that the corresponding target curvature of the flagellum is calculated by $\kappa^0 = Sp^3 aF^i$.

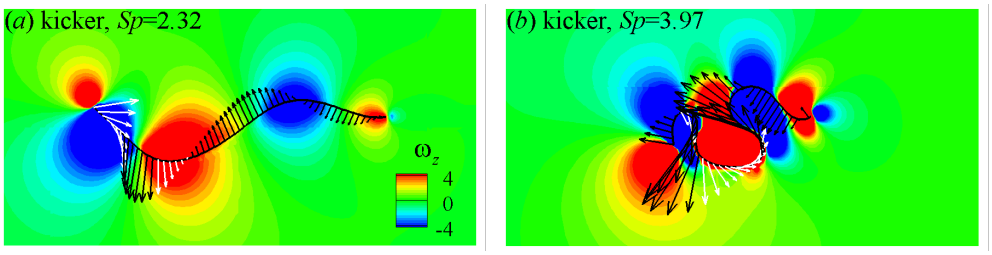


Figure 7.7. Flow fields around the flagellum with a fixed sliding force $aF_i = 0.16\kappa^0_{A=0.2}$ swimming from left to right at $t = 0$. Contour plots show the distribution of the vorticity $\omega_z$. Arrows show the velocity on the flagellum, where white and black colors correspond to positive and negative local velocities, respectively. The Reynolds number is $Re = 0.625$.

For a given internal force distribution $F^i$, the swimming speed $\bar{U}$ reaches a peak value at a certain $Sp$. The maximum speed is of the same order as the speed of a stiff flagellum. The maximum speed of the burrower is larger than the kicker for the same sliding force. For a burrower with $aF^i = 0.8\kappa^0_{A=0.2}$, the maximum swimming speed occurs around $Sp = 1.08$, the corresponding target curvature is $\kappa^0_{A=0.2}$. At $aF^i = 0.32\kappa^0_{A=0.2}$, the target curvature is $2\kappa^0_{A=0.2}$. Similar phenomenon also exists for the kicker. This means that a soft flagellum requires a larger target curvature in order to achieve a maximum swimming speed. The power consumption in figure 7.8($b$) monotonically increases with $Sp$. Note that the plot is in log scale, and the power increases substantially compared with the stiff flagella with a fixed target curvature (see figure 7.8($b$)). The efficiency also has a peak value for each fixed sliding force $F_i$. In many previous studies, the flagellum is modeled with a fixed target curvature and has a small $Sp$ so that the target beating pattern and swimmer kinematics are similar. However, most organisms have large $Sp$, e.g., *C. elegen*. We should note that the computed power consumption for a *C. elegen* deviates from experimental measurements.

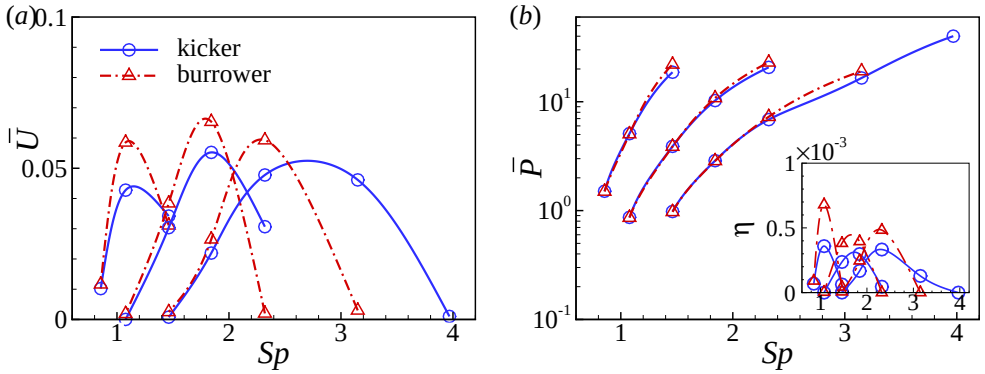


Figure 7.8. $(a)$ Average swimming speed $\bar{U}$, $(b)$ power consumption $P$ and swimming efficiency $\eta$ of the kicker and burrower at three fixed sliding forces $F^i$ and different $Sp$. The Reynolds number $Re = 0.625$, the sliding force is respectively $aF^i = 0.8\kappa^0_{A=0.2}, 0.32\kappa^0_{A=0.2}$ and $0.16\kappa^0_{A=0.2}$ from left to right.

## 7.5 Concluding Remarks

In this section, we numerically investigated the elastohydrodynamics of a self-driven undulatory swimmer. Based on the model developed by Camalet and Jülicher [37, 54], we show that the sliding force provides a target curvature to the flagellum, $\kappa^0 = Sp^3 aF_i$ for a two-dimensional flagellum. The numerical model of target curvature developed by Fauci and Peskin [55] can be recovered when neglecting the tangential contribution of the sliding force. Our numerical simulation of a stiff flagellum agrees well with the results of a flagellum with prescribed kinematics. Based on this model, we numerically model the swimming motion of an elastic kicker and burrower driven by a fixed target curvature or a fixed sliding force distribution. The sperm number $Sp$, which characterizes the stiffness of the flagellum, has important effects on the swimming performance in both cases. For a flagellum with a fixed target curvature, our results show that the swimming speed, power consumption and swimming efficiency monotonically decreases with $Sp$. A soft burrower has higher speed and efficiency than the kicker at the same $Sp$. The difference is related to the interplay between the flagellum elastic deformation and the hydrodynamic forces.

Particularly, weakened negative vorticity near the head of a soft flagellum reduces the swimming speed. A strong positive vorticity generated at the middle of the soft burrower induces a favorable flow for its swimming. For a flagellum with a fixed sliding force, we find that there exists an optimum $Sp$, where swimmer speed reaches its maximum. The power consumption greatly increases at high $Sp$. Our results show that the elastic deformation of the flagellum greatly affects the swimmer's performance.

# 8. COLLECTIVE MOTION OF MICROORGANISMS IN A VISCOELASTIC FLUID[1]

## 8.1 Motivation and Previous Works

The suspension of swimming microorganisms and their aggregation have received growing attention for their importance in pathology, reproduction and ecology [266]. The collective motion of microorganisms exhibits many turbulent-like behaviors, such as large-scale flow structures [267,268], strong fluctuations in velocity field [269], and enhanced diffusion and mixing [83]. The microorganisms exhibit locally correlated motions [270] and aggregations [267]. In contrast to the classic turbulence at high Reynolds numbers, which involves energy transfer across different length scales, the active turbulence is generated by the collective motion of microorganisms. The input energy is dissipated at the same length scale as it is produced [271,272]. Theoretical models based on continuum equations [273] and discrete self-propelled particles [41, 274, 275] have been proposed to investigate the stability and turbulent features of microswimmer suspensions and active nematics [276].

Microorganisms and spermatozoa often swim in non-Newtonian fluids which are viscoelastic [207]. Examples of these phenomena include bacteria forming biofilms by producing extracellular polymeric substances [42], spermatozoa racing through cervical mucus in the mammalian female reproductive tract [59], and bacteria abundance within oceanic gels of transparent exopolymer particles [206]. There has been a long debate about the effects of fluid elasticity on the speed of an isolated swimmer. Both an increase and a decrease in speed have been observed in previous studies depending on the propulsion mechanism and geometry of the microorganisms and

[1]This chapter has been reprinted (abstract/excerpt/figure) with permission from "Collective motion of microorganisms in a viscoelastic fluid", by G. Li and A. M. Ardekani, in Physical Review Letters, 117(11): 118001, 2016 (DOI: 10.1103/PhysRevLett.117.118001). Copyright (2016) by the American Physical Society.

fluid's rheological properties [135]. In a dilute suspension of microorganisms, fluid elasticity changes the wavelength of the most unstable disturbance [140] and leads to microorganism aggregation in an external vortical flow [139]. More recently, a continuum model is developed [277] to couple the internally driven active nematic to the polymer rheology. The results show that the polymer additives may have a calming effects on the active flow, while the full-coupling of the polymer and nematic orientations greatly increases the complexity of spontaneous flow. At high Reynolds numbers, polymer additives in a turbulent flow suppress the large-scale fluctuations [278], increase flow intermittency [279] and generate a significant drag reduction [280]. The interplay between stretching of polymer molecules and turbulent flow structures [281] is one of the key aspects of viscoelastic turbulence.

In this work, we present the first fully resolved numerical simulation of collective dynamics of microswimmers in viscoelastic fluids. The present work introduces fluid elasticity as a mean to tune the effective interactions between swimmers and consequently the turbulent properties. Different form the previous works [140, 277], we consider the hydrodynamics of the discrete rod-like swimmers in a continuum viscoelastic fluid. We show that the fluid elasticity has a stronger effect on a suspension of pushers than pullers. The polymer stress enhances the local aggregation and polar alignment of pushers. At large scales, polymers suppress the velocity fluctuations, break down the large-scale flow structures with a time period set by the polymer relaxation. Accordingly, energy spectra and induced mixing in an active turbulence are greatly modified by fluid elasticity.

## 8.2 Results and Discussion

We conduct two-dimensional simulations of $N$ identical slender rod-like swimmers in a viscoelastic fluid. Simulations are performed in a square box of size $L$ with periodic boundaries in all directions. The number density is defined as $c = Nl^2/L^2$. By imposing a slip velocity $U_s = U_0[\pm \tanh(10s/l) + 1]$ on the surface of the swimmer,

we consider both pushers (+) and pullers (-). Here, $U_0$ is the characteristic swimming speed, $l$ is the swimmer length, $s \in [-l/2, l/2]$ is the length measured from the head of the swimmer. In a Newtonian fluid, the swimming speed of an isolated pusher and puller is $U = U_0$; their induced velocity fields are also the same but in the opposite direction. Hereinafter, the results are normalized as follows: the length is scaled by $l$, velocity by $U_0$, time by $l/U_0$, and pressure and stress by $\rho\nu U_0/l$, where $\rho$ and $\nu$ are the fluid density and kinematic viscosity, respectively.

The dimensionless equations for conservation of momentum and mass are

$$Re\frac{D\boldsymbol{u}}{Dt} = -\nabla p + \nabla \cdot \boldsymbol{\tau} + \boldsymbol{f}, \qquad \nabla \cdot \boldsymbol{u} = 0, \tag{8.1}$$

where the Reynolds number $Re = Ul/\nu$ is $5 \times 10^{-3}$, $D/Dt$ is the material time derivative, $\boldsymbol{u}$ is the velocity vector, $p$ is the pressure and $\boldsymbol{\tau}$ is the deviatoric stress tensor. The forcing term $\boldsymbol{f}$ is calculated using a distributed Lagrange multiplier method to accurately satisfy the boundary conditions on the swimmer [108] (see more details in supplementary material). In a Newtonian fluid, the stress tensor is $\boldsymbol{\tau} = \dot{\boldsymbol{\gamma}}$, where $\dot{\boldsymbol{\gamma}} = \nabla\boldsymbol{u} + \nabla\boldsymbol{u}^{\mathrm{T}}$ is the shear rate tensor. To model an elastic fluid, the Oldroyd-B constitutive equation is used, in which $\boldsymbol{\tau}$ can be split into solvent and polymer contributions as $\boldsymbol{\tau} = \boldsymbol{\tau}^s + \boldsymbol{\tau}^p$, where $\boldsymbol{\tau}^s = \beta_s\dot{\boldsymbol{\gamma}}$ and

$$\boldsymbol{\tau}^p + De\,\overset{\triangledown}{\boldsymbol{\tau}^p} = (1-\beta_s)(\nabla\mathbf{u} + \nabla\mathbf{u}^{\mathrm{T}}), \tag{8.2}$$

where $\beta_s = 0.5$ is the ratio of the solvent viscosity to the zero-shear-rate viscosity of the polymeric solution. The Deborah number $De = \lambda/t_f$ is the ratio of the polymer relaxation time $\lambda$ to the characteristic flow time scale $t_f = l/U_0$. In a viscoelastic turbulence, the flow field is strongly affected by $De$. At $De \ll 1$, polymer molecules are essentially not deformed and the elastic effects are negligible. In contrast, at $De \gg 1$, elastic forces dominate. The notation $\triangledown$ represents the upper-convected derivative. The excluded volume effect is modeled by adding a linear repulsive force whenever the distance between any two points on two swimmers is smaller than the swimmer thickness.

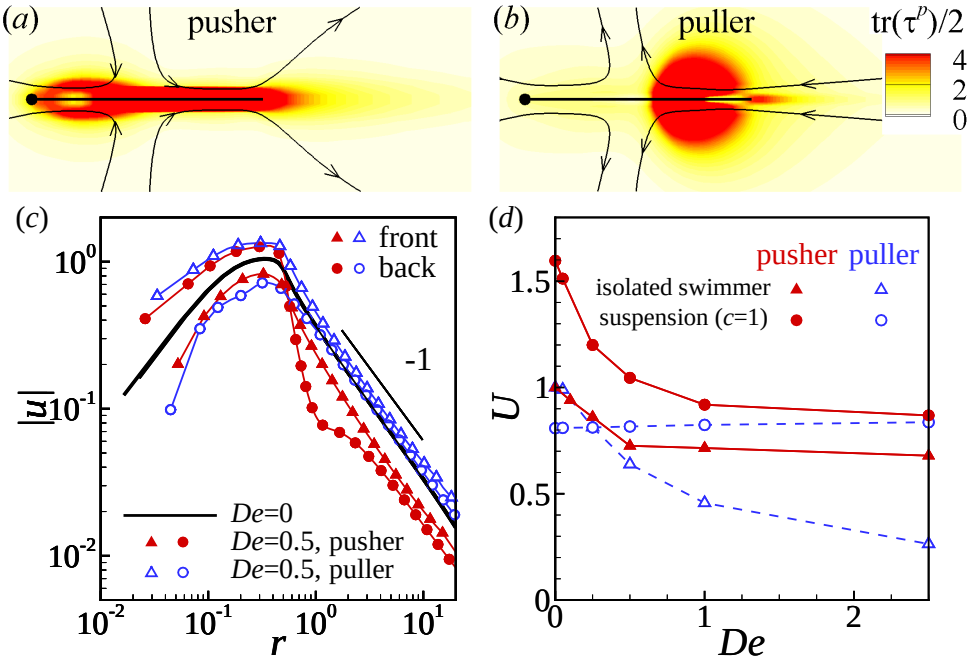


Figure 8.1. (color online). Elastic energy distribution $\mathrm{tr}(\boldsymbol{\tau}^p)/2$ around a ($a$) pusher and ($b$) puller as they swim to the left, $De = 0.5$. ($c$) The magnitude of the velocity field away from the isolated swimmer. ($d$) Swimming speed for an isolated swimmer (triangles) and suspension (circles) as a function of $De$.

The effects of fluid elasticity on a single swimmer are first investigated. For a pusher, polymers are tangentially stretched along the entire body [Fig. 8.1$a$], while for a puller, the high elastic energy is stored near the tail [Fig. 8.1$b$]. The flow field induced by the swimmers are affected by fluid elasticity [Fig. 8.1$c$]. In a Newtonian fluid, the magnitude of the velocity fields in front of and behind the swimmer are the same $|u| \sim 1/r$. Fluid elasticity breaks this symmetry and its effects on pushers and pullers are different. The same $1/r$ scaling law holds for pullers, while for pushers, velocity decreases much faster at the rear side of the swimmer. The polymer molecules are strongly stretched along the pusher, once they pass the swimmer, the polymer extension can not be supported any longer and the fluid elements contract along the swimming direction and expand in the normal direction. Therefore, streamlines

expand at the rear of the swimmer, and flow velocity along the swimmer direction dramatically decreases, similar to the "die swell" phenomenon [216]. Fluid elasticity does not affect the far-field velocity decay for either swimmers since the polymers are mainly deformed near the swimmer. Fluid elasticity hinders the swimming speed for both pushers and pullers for an isolated swimmer. The average swimming speed of pushers in a suspension monotonically decreases with $De$, while it is less affected for a suspension of pullers [Fig. 8.1$d$]. Therefore, the role of fluid elasticity on a suspension can be very different from its effects on a single swimmer.

In suspensions, the swimmers are initially uniformly distributed and have the same swimming direction. The nematic suspension is unstable for both swimmer types, and they form clusters. Fig. 8.2 shows the flow field at $t = 25$ which has reach a statistically steady state. In a Newtonian fluid, the flow induced by pushers is characterized by large scale structures as large as the size of computational domain. Pushers tend to align with their neighbors due to the lateral hydrodynamic attractions and they exhibit a local orientational order. The suspension of pullers in a film is very different from those in an unconfined suspension. In a bulk fluid, large scale flows are not observed and the pullers are randomly distributed regardless of their concentration [41]. Whereas in a film, the pullers aggregate at the front and form clusters [Fig. 8.2($b$)].

In a viscoelastic fluid [Fig. 8.2($c$) and ($d$)], the cluster type is not qualitatively affected, i.e. the aggregation of the swimmers is mainly determined by their swimming mechanism. The typical cluster size for pushers in a viscoelastic fluid is, however, larger and involves more swimmers compared to the Newtonian fluid. Fluid elasticity reduces the velocity fluctuations and suppresses the fluid mixing (see more details in supplementary material). Fluid elasticity reduces the size of large-scale flow structures in a suspension of pushers, which can be as large as the computational domain in a Newtonian fluid. These large-scale high-speed regions occasionally form in a viscoelastic fluid, but quickly break down into smaller patches. Fluid elasticity has much weaker effect on a suspension of pullers.

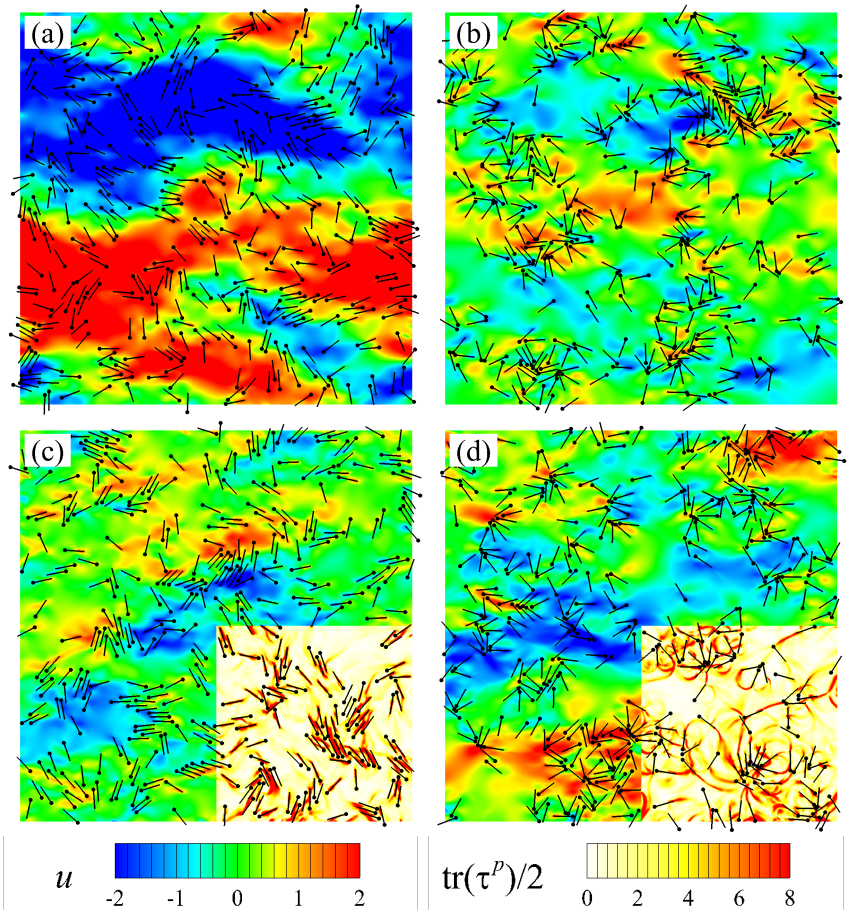


Figure 8.2. (color online). Flow field and distribution of swimmers at $t = 25$ for $(a, c)$ pushers and $(b, d)$ pullers. The number density is $c = 1$. $De = 0$ in $(a, b)$ and 2.5 in $(c, d)$, respectively. Contours in the main frame and the right-bottom quarter of $(c, d)$ show the horizontal velocity component $u$ and elastic energy $\mathrm{tr}(\boldsymbol{\tau}^p)/2$, respectively.

In Fig. 8.3$(a)$, the aggregation of swimmers are quantified using pair correlation functions $g(r)$ and $g(\theta)$, representing the probability of finding a swimmer at center-to-center distance $r$ and angle $\theta$ with respect to another swimmer. For pushers, $g(r)$ peaks at around $r = 0.2$, representing the strong tendency of lateral attraction. The peak value of $g(r)$ increases with $De$, showing an increase in attraction due to fluid elasticity. In the inset, the plot of $g(\theta)$ shows a tendency for polar alignment of pushers, and fluid elasticity further increases this effect. In general, fluid elasticity

enhances the aggregation of pushers, which is consistent with our results for two hydrodynamically interacting pushers (see more details in supplementary material). Shear flow in the gap between the two pushers generates a strong polymer stretching which enhances the attraction. This mechanism is similar to the polymer-enhanced wall attraction of a pusher-type squirmer [50].

The role of fluid elasticity on the flow coherent structures is characterized by the spatial and temporal correlation functions as $C_u(r) = \langle \boldsymbol{u}(\boldsymbol{x}+\boldsymbol{r}) \cdot \boldsymbol{u}(\boldsymbol{x}) \rangle / \langle \boldsymbol{u}^2(\boldsymbol{x}) \rangle$ and $C_u(\Delta t) = \overline{\boldsymbol{u}(t+\Delta t) \cdot \boldsymbol{u}(t)} / \overline{\boldsymbol{u}^2(t)}$. Here, $\langle\rangle$ and $-$ represent the average in space and time, respectively. In Fig. 8.3($b$), we compare the averaged correlation functions $\overline{C}_u(r)$ and $\langle C_u(\Delta t) \rangle$ for different suspensions. The spatial velocity correlation for a pusher suspension is weakened by fluid elasticity. The typical length of the averaged flow structures, which is characterized by the value of $r$ at which $\overline{C}_u(r) = 0$ only slightly decreases with $De$. Similarly, the shape of the temporal velocity correlation function is changed by fluid elasticity, while correlation time $\Delta t \simeq 5$ is less affected. Fluid elasticity reduces the velocity magnitude of some regions of the large-scale flow, while it is not strong enough to reverse the flow direction.

We now closely examine the instantaneous flow fields to better understand the interplay between polymer stretching, swimmer aggregation and large-scale flow structures in a suspension of pushers. The time variation of the kinetic and elastic energies in a suspension is written as

$$Re \frac{dK}{dt} + \frac{dE}{dt} = P - \varepsilon_K - \varepsilon_E, \tag{8.3}$$

where $K = \langle \boldsymbol{u}^2/2 \rangle$ and $E = \langle \mathrm{tr}(\boldsymbol{\tau}^p)/2 \rangle$ are the spatial averaged kinetic and elastic energies in the flow field. $P = \sum_i \int_l \boldsymbol{f} \cdot \boldsymbol{u} ds / L^2$ is the average power input generated by all the swimmers. $\varepsilon_K = \langle \beta_s \dot{\boldsymbol{\gamma}} : \dot{\boldsymbol{\gamma}} \rangle$ and $\varepsilon_E = E/De$ represent energy dissipations caused by the Newtonian solvent and polymer molecules, respectively. To quantify the pusher aggregation, we define a local polar order parameter $S_1 = \sum_i \sum_{j \neq i, r<1} \cos(\theta)$, where $r$ and $\theta$ are the distance and angle between pushers $i$ and $j$. Parameter $S_1$ provides information about the polar alignment of pushers, including the size and the number of clusters. For $N$ pushers aggregated in one cluster with perfect polar

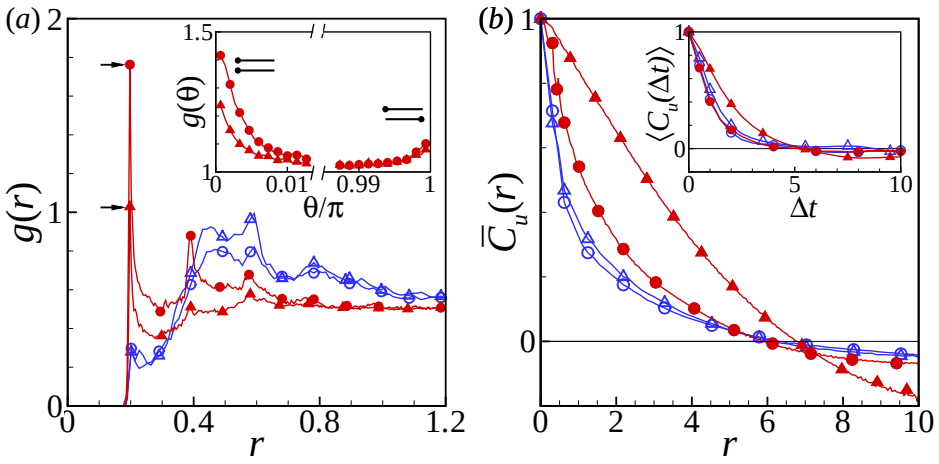


Figure 8.3. (color online). ($a$) Pair correlation functions $g(r)$ and $g(\theta)$ (inset) for pushers (red) and pullers (blue). Contour plots of $g(r,\theta)$ are given in the supplementary material. ($b$) Averaged spatial and temporal (inset) velocity correlations $\overline{C}_u(\boldsymbol{r})$ and $\langle C_u(\Delta t)\rangle$ of the induced flow field. The number density is $c = 1$. Solid triangle: pusher at $De = 0$, solid circle: pusher at $De = 2.5$, open triangle: puller at $De = 0$ and open circle: puller at $De = 2.5$.

alignment, $S_1 = N(N+1)$. Similarly, we define a local nematic parameter $S_2 = \sum_i \sum_{j\neq i, r<1} |\cos(\theta)|$. The size of instantaneous flow structure $r_c$ is determined by calculating $C_u(r_c) = 0$. At $De = 0$, $\overline{K} \simeq 1.8, \overline{S}_1 = 113.5, \overline{S}_2 = 1048.2$ and $\overline{r}_c \simeq 6.6$; at $De = 2.5$, $\overline{K} \simeq 0.4, \overline{S}_1 = 260.9, \overline{S}_2 = 1238.2, \overline{r}_c \simeq 5.9$, and $\overline{E} \simeq 2.6$. Fluid elasticity inhibits velocity fluctuations, enhances polar and nematic alignment of pushers, and slightly decreases the size of the average large-scale flow structures.

To better understand the results, we compare fluctuations for different variables, $a' = (a - \overline{a})/\overline{a}$, where $a$ is the variable of interest. In Fig. 8.4($a$), $K'$ and $r_c'$ are strongly correlated in a Newtonian fluid, meaning larger flow structures generate stronger velocity fluctuations. No obvious correlation between $S_1'$ and $r_c'$ is observed, indicating that the pusher aggregation is more related to the local hydrodynamic interaction among the swimmers, rather than large-scale flows. Both $K'$ and $r_c'$ oscillate with a typical time period $\Delta t \sim 4$, which is approximately the time it takes for a pusher to

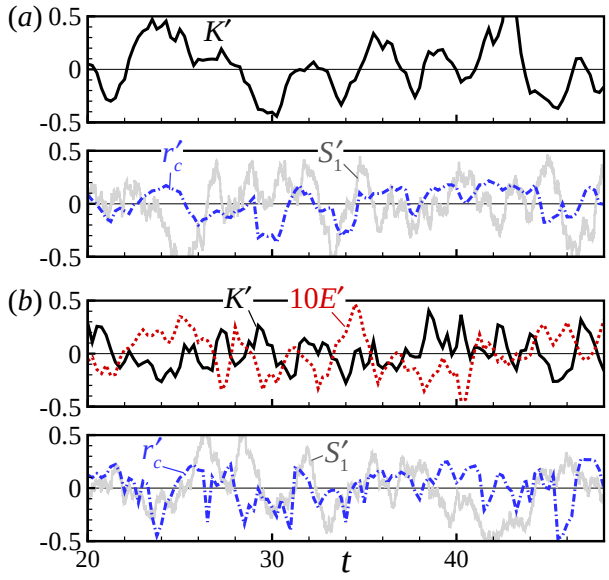


Figure 8.4. (color online). Time variation of the normalized kinetic energy $K'$, elastic energy $E'$ and flow structure size $r_c'$ of a pusher suspension at $c = 1$ in a $(a)$ Newtonian fluid and $(b)$ viscoelastic fluid at $De = 2.5$.

swim across large-scale flow structures. In Fig. 8.4$(b)$, $K'$ are $E'$ are anti-correlated with each other in a viscoelastic fluid. Note that because of the $Re$ factor in Eq. (3), the elastic energy strongly affects the kinetic energy, even though $E'$ is an order of magnitude smaller than $K'$. The time scale of fluctuations is approximately $\Delta t = 1 \sim 2$, which is close to the polymer relaxation time $\lambda = 2.5$. Polymer stretching in an active turbulence is a highly nonequilibrium process. Once the large-scale flow emerges, it starts to more strongly stretch polymer molecules in the flow field. The polymer stretching gradually reduces the velocity fluctuations and breaks down the large-scale flow structures. After the polymer molecules are relaxed, the velocity fluctuations are recovered and large-scale flow structures emerge again.

The modification of the flow coherent structures by fluid elasticity is also revealed in energy spectra. In Fig. 8.5, we compare the energy spectrum for different suspensions. For all the cases, a roughly universal $k^{-4}$ power-law is observed at high wavenumbers $k > k_l = 2\pi$, due to the shape of rod-like swimmers [275]. At low

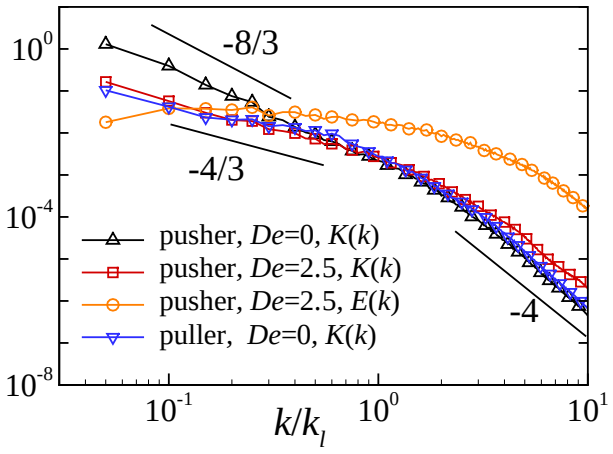


Figure 8.5. (color online). Energy spectra $K(k)$ and $E(k)$ in a microswimmer suspension at $c = 1$.

wavenumbers, the asymptote varies with the swimmer type and the fluid environment. For a suspension of pushers in a Newtonian fluid, we derive the same scaling $K(k) \sim k^{-8/3}$ as in a bacterial suspension [271]. In a viscoelastic fluid, the kinetic energy reduces to $k^{-4/3}$ at low wavenumbers and slightly increases at high wavenumbers $k > k_l$, showing that polymer molecules extract energy from large scales and partially release it at small scales. The interaction between polymer molecules and large scale flows effectively causes a polymer-induced kinetic energy cascade. This mechanism is the same as in a viscoelastic turbulent flow at high $Re$ [282], except that for an active turbulence in a viscoelastic fluid, this is the only energy cascade. The elastic energy has a much more flat distribution over $k < k_l$, indicating the polymer stretching by the large scale flows. This is similar to the viscoelastic turbulence at high Reynolds numbers [283]. The kinetic energy dissipation is $\varepsilon_K(k) = 2k^2K(k) \sim k^{-2/3}$ for a pusher suspension in a Newtonian fluid. The viscous dissipation is mainly caused by the large-scale flow structures, consistent with the measurements in a bacterial suspension [284]. In a viscoelastic fluid, polymers add an extra dissipation $\varepsilon_E$ to the fluid and $\varepsilon_K(k) \sim k^{2/3}$ at $k < k_l$, i.e. the strongest viscous dissipation occurs at the swimmer length scale.

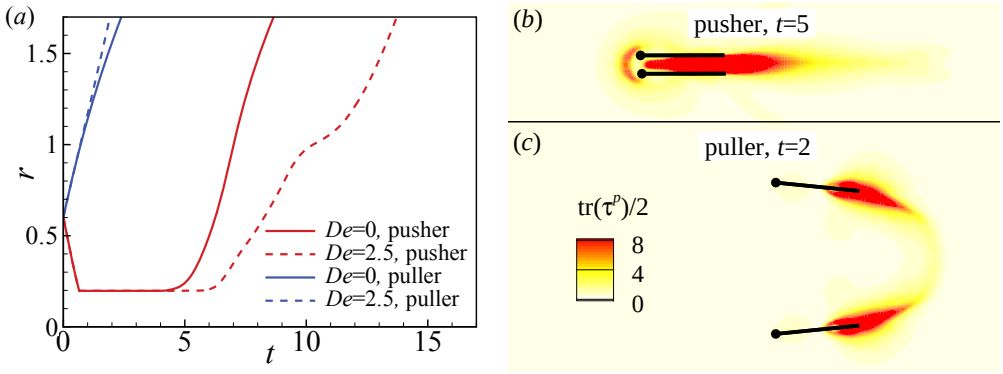


Figure 8.6. (color online). ($a$) Time history of the distance between two pushers which are initially swimming in the same direction and parallel to each other. Polymer stretching around the ($b$) pushers and ($c$) pullers in a viscoelastic fluid at $De = 2.5$.

To conclude, based on the fully-resolved numerical simulations of suspension of rod-like swimmers, we have shown that the effects of fluid elasticity on a suspension can be very different from its effect on a single swimmer. Particulary, fluid elasticity enhances the aggregation of pushers mainly due to the local hydrodynamics. Large-scale flow structures induce stronger polymer stretching, and the polymer relaxation breaks down the large flow structures and suppresses the velocity fluctuations. Our work has extended the studies of collective motion in Newtonian fluids to polymeric solutions. These results can be useful in understanding the behavior of swimming microorganisms in a more realistic fluid environment, such as bacteria in biofilm and oceanic exopolymer particles.

## 8.3 Supplemental Material

### 8.3.1 Effects of Fluid Elasticity on Two Swimmers

To investigate the effects of fluid elasticity on the pusher aggregation, we conduct simulations of two swimming pushers and pullers in Newtonian and viscoelastic fluids. The two swimmers are initially parallel to each other and swim in the same direction.

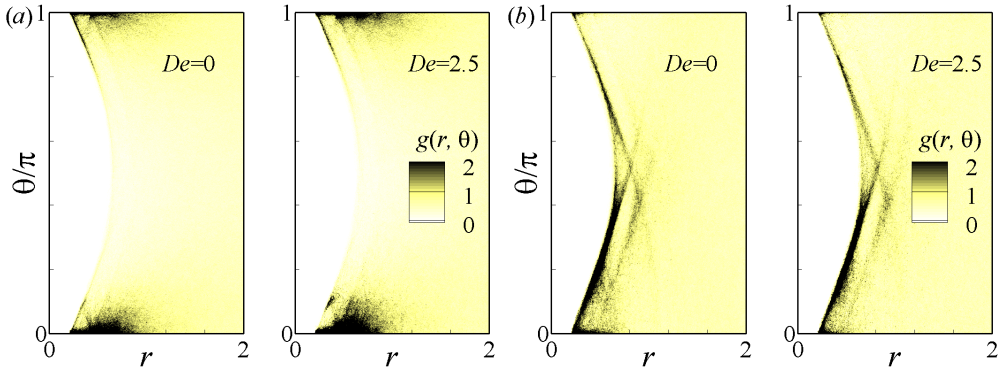


Figure 8.7. (color online). The pair correlation function $g(r,\theta)$ of swimmers in a suspension of $(a)$ pushers and $(b)$ pullers.

The initial lateral center-to-center distance is $r = 0.6$. As shown in Fig. 8.6$(a)$, the two pushers are gradually attracted to each other, swim together for a while and eventually separate. The two pullers, on the other hand, repel each other. The pushers contact time increases from 3.6 at $De = 0$ to 5.1 $De = 2.5$, showing the enhancement of pusher attraction by fluid elasticity. In Fig. 8.6$(b)$, the strong shear in the gap between the two pushers generates a strong polymer stretching which enhances the attraction. This mechanism is similar to the polymer-enhanced wall attraction of a pusher-type squirmer discussed in our earlier work [50].

### 8.3.2 Effects of Fluid Elasticity on a Suspension of Swimmers

Effects of fluid elasticity on aggregation of swimmers in a suspension is quantified using the pair correlation function $g(r,\theta)$ at different $De$ (Fig. 8.7). The pair correlation function is defined as

$$g(r,\theta) = \frac{L^2\pi}{N(N-1)V(r_{i,j})\theta_{i,j}} \sum_{i=1}^{N} \sum_{\substack{j=1 \\ i\neq j}}^{N} \langle \delta(r_{i,j}-r)\delta(\theta_{i,j}-\theta)\rangle, \tag{8.4}$$

where

$$\delta(r_{i,j}-r) = \begin{cases} 1, & r-\frac{\Delta r}{2} \leq r_{i,j} < r+\frac{\Delta r}{2}, \\ 0, & \text{otherwise}, \end{cases} \tag{8.5}$$

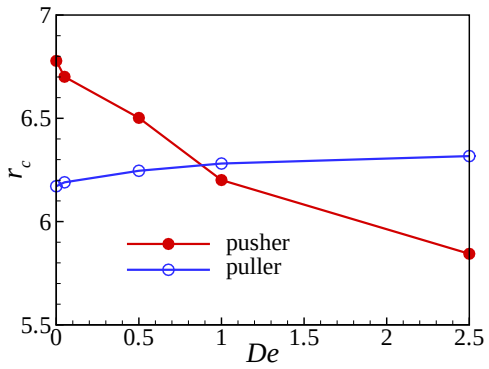


Figure 8.8. (color online). The size of the time-averaged flow structures in a suspension of swimmers at different $De$. The number density is $c = 1$.

and $\delta(\theta_{i,j} - \theta)$ is similarly defined. $r_{i,j}$ and $\theta_{i,j}$ are the center-to-center distance and angle between swimmers $i$ and $j$, respectively, and $V(r_{i,j}) = \pi[(r_{i,j} + \Delta r/2)^2 - (r_{i,j} - \Delta r/2)^2]$. As we have shown in the main text, pushers show a strong tendency of lateral attraction, and the polar alignment is stronger than the apolar alignment. Fluid elasticity enhances the aggregation and the polar alignment of the pushers. Pullers are attract to each other with a preferred angle smaller than $\pi/2$. The pair correlation functions in a suspension of pullers are less affected by fluid elasticity. In Fig. 8.8, the size of the time-averaged flow structures $r_c$, determined by $\overline{C}_u(r_c) = 0$, decreases with $De$ in the suspension of pushers, while it slightly increases for the suspension of pullers.

Based on the induced velocity field, we calculate the advection and diffusion of a scalar field $\phi$ initialized as $\phi|_{t=0} = \sin(2\pi x/L)$ to quantify mixing. The corresponding Péclet number is $Pe = Ul/D = 100$, where $D$ is the diffusivity. From Fig. 8.9, we clearly see that the mixing in a pusher suspension at $De = 0$ is much faster than the other cases. In Fig. 8.10($a$), the probability distribution function of horizontal component of velocity $u$ in a viscoelastic fluid is narrower for suspension of pushers, while for pullers, the effect is opposite, and it is much weaker. The time evolution of the spatial average of the scalar norm $\langle|\phi|\rangle$ is illustrated in Fig. 8.10($b$). Once an

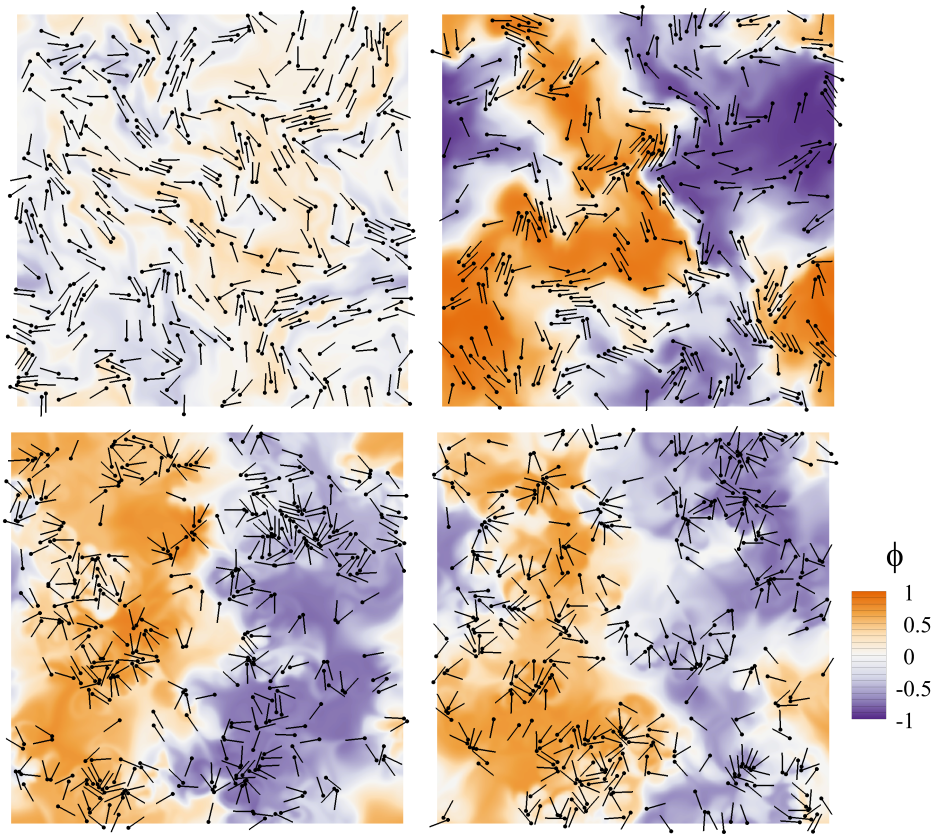


Figure 8.9. (color online). Scalar field $\phi|_{t=0} = \sin(2\pi x/L)$ is passively advected by the velocity field of the suspension at $t = 25$. $(a)$ pushers at $De = 0$, $(b)$ pushers at $De = 2.5$, $(c)$ pullers at $De = 0$, and $(d)$ pullers at $De = 2.5$. The number density is $c = 1$.

instability from the initial nematic state develops, $\langle|\phi|\rangle$ drops much faster than the pure diffusion case due to the mixing induced by active turbulence. Fluid elasticity reduces fluid mixing in the suspension of pushers, but has a weaker effect on the suspension of pullers. The spatial average of scalar norm for a diffusion process follows $\langle|\Phi|\rangle(t) = \langle|\Phi_0|\rangle \exp[-(2\pi/L)^2 Dt]$, where $L = 20$ is the domain size, $D = 0.01$ is the diffusivity. Similar exponential law exists in an active turbulence after turbulent flow structures develop. The equivalent diffusivity is calculated by $D = \int_0^\infty \langle \boldsymbol{u}(t)^2 \rangle dt$. For a velocity field with a Gaussian distribution, $D = \sigma^2$, where $\sigma$ is the standard deviation. From Fig. 8.10$(a)$, we derive $\sigma = 1.3$ for the suspension of pushers in a

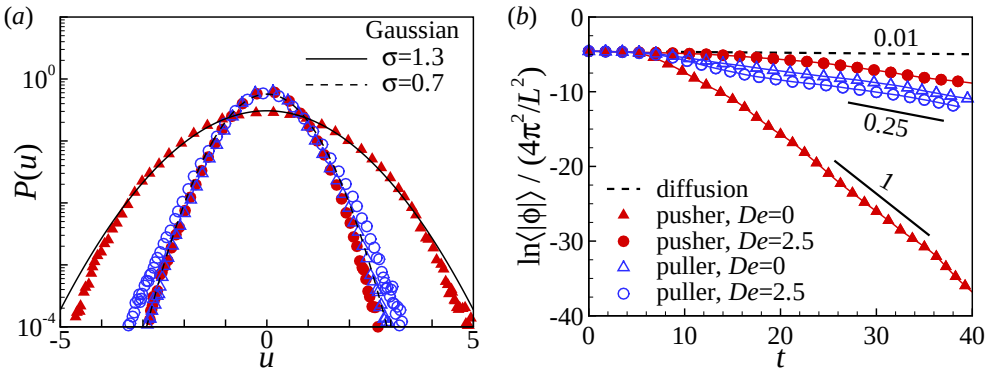


Figure 8.10. (color online). ($a$) The probability distribution function $P(u)$ of the horizontal velocity component $u$ of the flow field. Here, $\sigma$ is the standard deviation of the Gaussian distribution. ($b$) Time evolution of the spatial average of scalar norm, $\langle|\phi|\rangle$. The number density is $c = 1$.

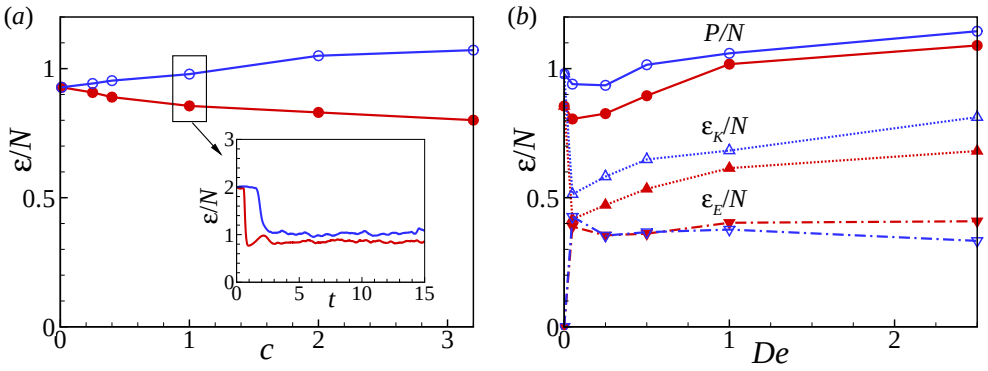


Figure 8.11. (color online). ($a$) Number-averaged energy dissipation $P/N$ of suspension of swimmers in a Newtonian fluid at various cell concentrations. Inset: time history of $P/N$ of suspensions at $c = 1$. ($b$) Number-averaged energy dissipations $P/N$, $\varepsilon_K/N$ and $\varepsilon_E/N$ of suspension of swimmers at $c = 1$ at various $De$. $\varepsilon_K$ and $\varepsilon_E$ are the energy dissipation caused by Newtonian solvent and polymer molecules, respectively. Red solid symbols: pusher, blue open symbols: puller.

Newtonian fluid and 0.7 for other cases. These values are close to what we obtained from Fig. 8.10($b$).

At last, we characterize the effects of fluid elasticity on the energetics of the microswimmer suspensions. In a statistically steady state, the time variations of the kinetic and elastic energies are zero, and all of the input power eventually dissipates, i.e. $P = \varepsilon_K + \varepsilon_E$, where $\varepsilon_K$ and $\varepsilon_E$ are the energy dissipation caused by the Newtonian solvent and polymer molecules, respectively. In Fig 8.11($a$), the number-averaged energy dissipation $P/N$ in a Newtonian fluid decreases with increasing pusher concentration, while it increases for pullers. This observation is opposite to the simulation results only considering the far-field hydrodynamic interactions [275], indicating the key role of the near-field hydrodynamics. The power consumption is initially high when the swimmers are in a nematic phase, but it quickly drops as they start to lose their initial order ( see inset of Fig. 8.11($a$)). Therefore, collective swimming of pushers is not only advantageous for achieving higher speed, but also reduces the overall energy consumption.

In Fig. 8.11($b$), polymers add an extra dissipation $\varepsilon_E$ to the fluid, they affect the power consumption of both pusher and puller suspensions in a similar way. At low $De$, the power consumption is slightly decreased. Polymer stretching by swimmers is weak, the fluid is still Newtonian-like and the contribution of the solvent to dissipation is approximately the same as the contribution of polymer molecules ($\beta = 0.5$). For $De > 0.25$, the total dissipation increases and, at $De = 2.5$, it is about $20 \sim 30\%$ larger than the one in a Newtonian fluid. The trend is similar to the results of an isolated swimmer. The viscous dissipation increases with increasing $De$, while the polymer dissipation is less affected. Recall that $\varepsilon_E = E/De$. This result indicates that larger polymer relaxation time corresponding to larger $De$ compensates the effects of the stronger polymer elongation. This effect is similar to the observations in a viscoelastic turbulent flow at high Reynolds numbers [282].

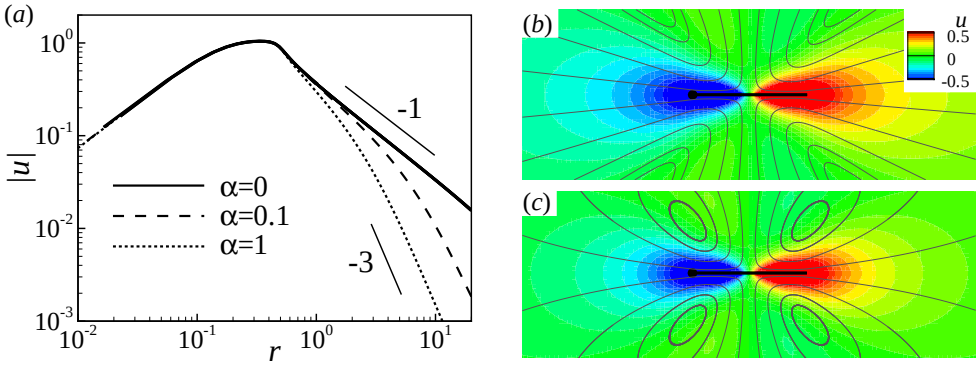


Figure 8.12. (color online). ($a$) The magnitude of the velocity field away from an isolated swimmer in a Newtonian fluid with different air/liquid friction coefficients. Flow field around a pusher swimmer in a Newtonian fluid with ($b$) $\alpha = 0$ and ($c$) $\alpha = 1$. Black lines are streamlines. Contours show the magnitude of horizontal velocity component $u$.

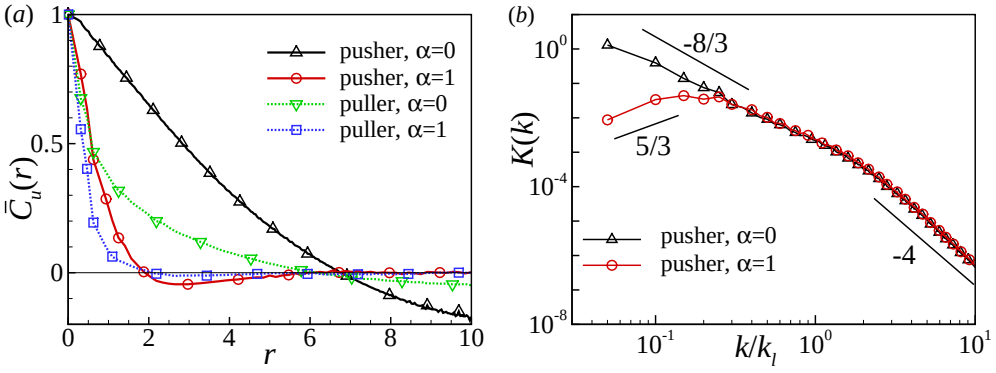


Figure 8.13. (color online). The effects of air/liquid friction on ($a$) averaged spatial velocity correlation $\overline{C}_u(\boldsymbol{r})$ and ($b$) the kinetic energy spectrum of a microswimmer suspension in a Newtonian fluid. The number density is $c = 1$.

### 8.3.3 Effects of Air-liquid Friction

The term $-\alpha \boldsymbol{u}$ is the dissipative term which models the friction between the film and the surrounding air [285]. This term is not necessary in models of an active turbulence because the viscous dissipation naturally maintains a finite energy level,

unlike a 2D turbulent flow at high Reynolds numbers. However, we find that it has important effects on both single swimmer and suspension dynamics. The air-liquid friction does not affect the swimming speed of a single swimmer, but the far-field velocity profile decays much faster, following $1/r^3$ [see Fig. 8.12($a$)], the same as swimming in a confined thin film [286]. Near the swimmers, the friction generates recirculation regions with closed streamlines. In a suspension, the flow structures are greatly reduced by air-liquid friction. In Fig. 8.13($a$), the typical vortical structures are greatly reduced to around $r_c \simeq 2$ for both pusher and puller suspensions, indicating that the size of the large scale flow structures are strongly affected by the far-field velocity field. For the energy spectrum, the friction term changes the kinetic energy distribution at small wavenumbers into $K(k) \sim k^{5/3}$, the same as a bacterial suspension in a confined chamber [271]. These results show that the friction breaks down the large scale flow structures.

# 9. SUMMARY AND PROPOSED WORK

## 9.1 Summary of Results

In this thesis, the swimming motion in complex fluids and complex environments is investigated by using direct numerical simulations. We mainly use a continuum model for the non-Newtonian fluid and a discretized description for swimmers using different swimmer models. We focus on the effects of the non-Newtonian fluid rheological properties, such as viscoelasticity and the shear-thinning viscosity on the hydrodynamics of microswimmers and inert particles. Our results show that the non-Newtonian fluid rheological properties have important effects on the microswimmers, including its swimming speed, the power consumption, the near-field and far-field velocity decay, the near-wall swimming behavior, interaction with the external flow field, and the collective motion of a suspension.

For a single squirmer in a Newtonian fluid, three different swimming modes are observed in the presence of inertial effect: the pusher and the puller with a weak pulling strength escape from the wall. As the strength of pulling effect increases, the puller swims along the wall keeping a constant distance and orientation angle, and at a higher strength, it bounces on the wall. Therefore, the puller swimmer can be trapped by a surface, however, at smaller Reynolds numbers, the wall attraction becomes weaker. For a suspension of squirmers, we found that they are all attracted to the walls, independent of the swimmer's type. The squirmers frequently approach and escape from the wall surface, but have a much higher probability to stay near the walls than swim in the bulk fluid. In the near-wall region, the squirmers mostly orient normal to the walls, the interactions between the squirmers affect the structure of the clusters.

The non-Newtonian behavior is found to greatly affect the near-wall motion of a squirmer. We find the pusher squirmer can be permanently trapped to the wall, due to a strong polymer stretching around the rear pole of the pusher, inducing an elastic drag which resists the locomotion of the swimmer. A neutral squirmer stays longer time near the surface, and a puller is less affected, they both eventually escape the wall. The fluid viscoelasticity is found to be the main reason for these affects, and the different behavior is due to the different polymer stretching around the squirmer.

For an inert particle in an external flow field of a channel flow, cross-streamline particle migration is observed due to various effects: inertia, elasticity, shear-thinning and secondary flow due to the non-circular cross-section of the channel. Inertia and viscoelastic effects compete with each other: inertial effects drive the particle away from the channel centerline, while viscoelastic effects drive the particle towards the centerline. Both the shear-thinning effect and the corresponding secondary flow tend to move the particle closer to the wall, and their effects are more pronounced with stronger inertia and elasticity.

We then compared the effects of viscoelasticity and shear-thinning visocity of the fluid on an undulatory swimmer. For a squirmer, both effects are found to hinder the swimming speed [95, 213]. However, for an undulatory swimmer, such as a sperm, there is a heated debate in the literature [134–138, 208, 231]. In a viscoelastic fluid, our simulation results are consistent with previous analytical works [135], in which the swimming speed and power consumption decrease with fluid viscoelasticity. In an inelastic shear-thinning fluid, we find the swimming speed to be enhanced, as long as the fluid viscosity near the flagellum is effectively thinned. The reason for the speed boost is similar to the case of a flagellum in a confined channel. Same results are also confirmed for a flagellum swimming in a heterogeneous fluid environment with particle suspensions.

The near-wall motion of an undulatory swimmer has some similarities to the near-wall motion of a squirmer. Depending on the undulatory amplitude, the swimmer can be strongly attracted to the wall, be weakly attracted to the wall with a relatively large

oscillating distance away from the wall, or escape from the wall. The contact between the swimmer and the wall and the hydrodynamic interaction are both important for the near-wall motion of the swimmer. In a non-Newtonian fluid, the shear-thinning viscosity is found to increase the swimming speed and to slightly enhance the wall attraction by reducing the swimmer's initial scattering angle. Similar as a pusher squirmer, the fluid elasticity leads to strong attraction of flagellum towards the wall and reduces its swimming speed. In a shear-thinning viscoelastic fluid, the combined shear-thinning effect and fluid elasticity results in an enhanced swimming speed for the kicker along the wall.

Fluid elasticity not only affects the swimming speed of a microswimmer and its near-wall motion, it also greatly affects the collective motion in a suspension, especially for the pusher swimmers. It enhances the attraction and the orientational ordering of the pusher swimmers. We find the polymer stress is strongly anti-correlated to the kinetic energy of the flow field, i.e., the induced polymer stresses break down the large-scale flow structures and suppress velocity fluctuations. From the energy spectrum, we observe that the polymer molecules extract energy from large scales and partially release it at small scales.

## 9.2 Recommendations for Future Works

Collective motion of self-propelling particles are of great interest for many years for its theoretical and practical importance [2]. At high particle concentrations, the induced fluid flow exhibits turbulent flow properties, such as large-scale flow structures [267, 268] and enhanced diffusion and mixing [83]. The self-propelling particles show locally correlated motions [270] and form clusters [267]. Active particles also undergo an activity-induced phase separation which closely resembles the equilibrium of a gas liquid coexistence [287, 288]. Recently, studies show that adding inert particles into a suspension of active particles can substantially change the onset of the phase separation [289, 290]. Our preliminary results show that clustering of mixture of

active and inert particles are formed without Brownian motions. Further work can be continued on this area to investigate the non-equilibrium phenomena of suspension of active and inert particles.

Fluid and nutrient mixing at microscales is important for microorganisms, however, mixing is not efficient in a low-Reynolds-number regime of a Newtonian fluid. In this thesis, we have shown that in a suspension of self-propelled particles, fluid mixing is inhibited by fluid elasticity mainly because the swimming speed of the swimmers are reduced. However, polymer solutions are found to destabilize the fluid in presence of the curved streamlines [291] or large enough disturbances [292]. Using a polymethyl methacrylate solution, previous experiments also demonstrated a rapid mixing of viscoelastic fluids in microchannels with an abrupt contraction [293]. Despite of these studies, the underlying physics are still not completely clear and numerical simulations of this phenomenon are needed. The major difficulty is the severe numerical instability at a high Weissenberg number. To overcome this difficulty, we implement an algorithm based on matrix-logarithm of the conformation tensor [294]. This method uses a tensor-logarithmic transformation of the conformation tensor for differential viscoelastic constitutive equations, which can be applied to a wide variety of constitutive laws. The core feature of this transformation is the decomposition of the velocity gradient, $\nabla \boldsymbol{u}$, into a traceless extensional component, $\mathbf{E}$, and a pure rotational component, $\mathbf{R}$. In the log-conformation representation, the evolution equation of the conformation tensor $\mathbf{C}$ is replaced by an equivalent evolution equation for the logarithm of the conformation tensor $\theta = \ln \nabla \mathbf{C}$. When necessary, an inverse transformation $\mathbf{C} = e^{\theta}$ is used to calculate $\mathbf{C}$. The logarithmic conformation tensor method has been implemented into our in-use code and future research can focus on to exploring the elasticity-related instability and fluid mixing.

In most part of this thesis, the kinematics of the microswimmers is imposed as a given condition. This model is the first step to learn the hydrodynamics of the low Reynolds number swimming and is useful to investigate the effects of non-Newtonian rheology and the hydrodynamic interactions between swimmers and surfaces. In

chapter 7, we investigated the elastohydrodynamics of an internally driven flagellum with a prescribed sliding force. However, experiments suggest that the dynein motor activity is not coordinated by a chemical signal but arises spontaneously because of the interplay of the dynein motors and the elastic microtubules [36, 252]. More details of the microorganisms, such as the self-organized oscillating mechanism of flagellum [36, 37], and the material properties of the swimmer, should be included to fully understand the interaction between the swimmer and the surrounding fluid environment. Interestingly, measurements of the *C. elegans* show its body behaves as a shear-thinning viscoelastic material [261]. Previous studies have shown that the stiffness of an undulatory flagellum has an important effect on its swimming speed in a viscoelastic fluid [208, 209]. Future studies may consider both the elastic and shear-thinning behavior of the swimmer's body as well as the internally driven mechanism. More advanced numerical codes need to be developed for the simulation of an elastic body inside a viscous fluid. To avoid very small time step required in an explicit-time stepping immersed boundary method, an implicit-time stepping method [232, 263, 264] needs to be implemented. Generally, the implicit version of the method needs to solve a matrix equation to update the position of the elastic body, and a generalized minimum residual method (GMRES) can be implemented [295].

Other numerical techniques are required to expand the parameter space for microorganism swimming in complex fluids. For the non-Newtonian fluid, there are mainly two types of models: the continuum model and the coarse-grained model. The continuum model is based on a polymeric stress field which is the ensemble average of polymer molecules inside an infinitely small volume of fluid. This method gives us a closed-form governing equation for the polymeric stress with proper boundary conditions. This equation is implemented in a CFD code solving Navier-Stokes equations and has been widely used in various studies on viscoelastic fluids, including the present thesis. However, this method suffers a major issue, called the "high-Weissenberg number problem" [296], i.e., the extensional viscosity, defined as the ratio of extensional stress to extensional strain rate, will become infinite for a non-shear-thinning vis-

coelastic fluid at finite strain rate and the numerical method becomes unsteady at high $Wi$. Some techniques, including the log-conformation method [294], which is the one implemented in the current thesis, the square-root method [297] and the polymer stress diffusion method [298] have been proposed to deal with this problem. These methods increase the upper limit of the $Wi$ allowed in simulations up to around 10 for Oldroyd-B fluid but are still limited for the microorganisms swimming in real viscoelastic material, for which $Wi \sim O(10^2)$ [135, 299].

In the coarse-grained modeling method, each molecule is represented as a string of beads connected by springs [216, 300]. Each bead represents a large number of polymer segments and has a given Stokes drag coefficient and a Brownian motion. The springs reflect the connectivity of the polymer chains and the effect of entropy which drives the chains toward an equilibrium coiled conformation. For efficiency, the strings in simulations usually include only two beads, i.e. the spring dumbbell model, which captures the longest time and length scales of the polymer chain. This method has some drawbacks, especially is limited to the dilute assumption for the polymeric solution [300]. On the other hand, it has several advantages compared to the continuum model. Firstly, this method can reach up to Weissenberg number of hundreds by increasing the stiffness of the spring [301] and thus avoids the difficulty encountered with a continuum model. Secondly, this method avoids any boundary conditions at an immersed boundary in a viscoelastic fluid. Currently, a continuum model of viscoelastic fluid with an immersed boundary method simply neglects the boundary condition for the polymer stress at the immersed boundary. Note that in the work of Teran *et al.* [136], a stress jump condition is mathematically proposed while may not be implemented in the numerical method [208, 235]. This simplification may still be acceptable for some simulations, such as the undulatory flagellum in a viscoelastic fluid validated in chapter 5, while it encounters issues for some other problems. For a coarse-grained model, a collision force for the bead can be implemented to accurately account for the effects of an immersed boundary. Lastly, the coarse-grained method

reveals the nature of the heterogeneous fluid environment around a microorganism, which may lead to important effects not captured using a continuum model.

# LIST OF REFERENCES

# LIST OF REFERENCES


[1] E. M. Purcell. Life at low reynolds number. *Am. J. Phys*, 45(1):3–11, 1977.

[2] D. L. Koch and G. Subramanian. Collective hydrodynamics of swimming microorganisms: Living fluids. *Annu. Rev. Fluid Mech.*, 43:637–659, 2011.

[3] E. Lauga and T. R. Powers. The hydrodynamics of swimming microorganisms. *Rep. Prog. Phys.*, 72(9):096601, 2009.

[4] J. Elgeti, R. G. Winkler, and G. Gompper. Physics of microswimmerssingle particle motion and collective behavior: a review. *Rep. Prog. Phys.*, 78(5):056601, 2015.

[5] G. Taylor. Analysis of the swimming of microscopic organisms. In *Proc. R. Soc. B*, volume 209, pages 447–461. The Royal Society, 1951.

[6] G. Taylor. The action of waving cylindrical tails in propelling microscopic organisms. In *Proc. R. Soc. B*, volume 211, pages 225–239. The Royal Society, 1952.

[7] M. Holwill and R. E. Burge. A hydrodynamic study of the motility of flagellated bacteria. *Arch. Biochem. Biophys.*, 101(2):249–260, 1963.

[8] M. J. Lighthill. On the squirming motion of nearly spherical deformable bodies through liquids at very small reynolds numbers. *Comm. Pure Appl. Math.*, 5(2):109–118, 1952.

[9] J. R. Blake. A spherical envelope approach to ciliary propulsion. *J. Fluid Mech.*, 46(01):199–208, 1971.

[10] J. R. Blake. Self propulsion due to oscillations on the surface of a cylinder at low reynolds number. *Bull. Aust. Math. Soc.*, 5(02):255–264, 1971.

[11] J. Gray and G. J. Hancock. The propulsion of sea-urchin spermatozoa. *J. Exp. Biol.*, 32(4):802–814, 1955.

[12] M. J. Lighthill. Flagellar hydrodynamics. *SIAM review*, 18(2):161–230, 1976.

[13] C. J. Brokaw. Non-sinusoidal bending waves of sperm flagella. *J. Exp. Biol.*, 43(1):155–169, 1965.

[14] C. J. Brokaw. Bending moments in free-swimming flagella. *J. Exp. Biol.*, 53(2):445–464, 1970.

[15] Y. Magariyama, S. Sugiyama, K. Muramoto, I. Kawagishi, Y. Imae, and S. Kudo. Simultaneous measurement of bacterial flagellar rotation rate and swimming speed. *Biophys. J.*, 69(5):2154, 1995.

[16] G. Li and J. X. Tang. Low flagellar motor torque and high swimming efficiency of caulobacter crescentus swarmer cells. *Biophys. J.*, 91(7):2726–2734, 2006.

[17] S. Chattopadhyay and X. Wu. The effect of long-range hydrodynamic interaction on the swimming of a single bacterium. *Biophys. J.*, 96(5):2023–2028, 2009.

[18] J. Higdon. The hydrodynamics of flagellar propulsion: helical waves. *J. Fluid Mech.*, 94(02):331–351, 1979.

[19] B. Rodenborn, C. Chen, H. L. Swinney, B. Liu, and H. P. Zhang. Propulsion of microorganisms by a helical flagellum. *Proc. Natl. Acad. Sci. U.S.A.*, 110(5):E338–E347, 2013.

[20] G. J. Hancock. The self-propulsion of microscopic organisms through liquids. In *Proc. R. Soc. B*, volume 217, pages 96–121. The Royal Society, 1953.

[21] G. K. Batchelor. Slender-body theory for particles of arbitrary cross-section in stokes flow. *J. Fluid Mech.*, 44(03):419–440, 1970.

[22] J. Lighthill. Reinterpreting the basic theorem of flagellar hydrodynamics. In *The Centenary of a Paper on Slow Viscous Flow by the Physicist HA Lorentz*, pages 25–34. Springer, 1996.

[23] J. Tillett. Axial and transverse stokes flow past slender axisymmetric bodies. *J. Fluid Mech.*, 44(03):401–417, 1970.

[24] J. B. Keller and S. I. Rubinow. Slender-body theory for slow viscous flow. *J. Fluid Mech.*, 75(4):705–714, 1976.

[25] J. Geer. Stokes flow past a slender body of revolution. *J. Fluid Mech.*, 78(03):577–600, 1976.

[26] R. E. Johnson. An improved slender-body theory for stokes flow. *J. Fluid Mech.*, 99(02):411–431, 1980.

[27] R. E. Johnson and C. J. Brokaw. Flagellar hydrodynamics. a comparison between resistive-force theory and slender-body theory. *Biophys. J.*, 25(1):113, 1979.

[28] A. J. Reynolds. The swimming of minute organisms. *J. Fluid Mech.*, 23(02):241–260, 1965.

[29] E. O. Tuck. A note on a swimming problem. *J. Fluid Mech.*, 31(02):305–308, 1968.

[30] A. T. Chwang and T. Y. Wu. A note on the helical movement of microorganisms. 178(1052):327–346, 1971.

[31] N. Phan-Thien, T. Tran-Cong, and M. Ramia. A boundary-element analysis of flagellar propulsion. *J. Fluid Mech.*, 184:533–549, 1987.

[32] B. Liu, K. S. Breuer, and T. R. Powers. Propulsion by a helical flagellum in a capillary tube. *Phys. Fluids*, 26(1):011701, 2014.

[33] H. C. Berg and L. Turner. Torque generated by the flagellar motor of escherichia coli. *Biophys. J.*, 65(5):2201–2216, 1993.

[34] V. A. Martinez, J. Schwarz-Linek, M. Reufer, L. G. Wilson, A. N. Morozov, and W. C. K. Poon. Flagellated bacterial motility in polymer solutions. *Proc. Natl. Acad. Sci. U.S.A.*, 111(50):17771–17776, 2014.

[35] C. W. Wilson, C. T. Nguyen, M. Chen, J. Yang, R. Gacayan, J. Huang, J. Chen, and P. Chuang. Fused has evolved divergent roles in vertebrate hedgehog signalling and motile ciliogenesis. *Nature*, 459(7243):98–102, 2009.

[36] F. Jülicher and J. Prost. Spontaneous oscillations of collective molecular motors. *Phys. Rev. Lett.*, 78(23):4510, 1997.

[37] S. Camalet and F. Jülicher. Generic aspects of axonemal beating. 2(1):24, 2000.

[38] C. J. Brokaw. Molecular mechanism for oscillation in flagella and muscle. *Proc. Natl. Acad. Sci. U.S.A.*, 72(8):3102–3106, 1975.

[39] I. H. Riedel-Kruse, A. Hilfinger, J. Howard, and F. Jülicher. How molecular motors shape the flagellar beat. *HFSP journal*, 1(3):192–208, 2007.

[40] J. R. Blake. Infinite models for ciliary propulsion. *J. Fluid Mech.*, 49(02):209–222, 1971.

[41] D. Saintillan and M. J. Shelley. Orientational order and instabilities in suspensions of self-locomoting rods. *Phys. Rev. Lett.*, 99(5):058102, 2007.

[42] L. Hall-Stoodley, J. W. Costerton, and P. Stoodley. Bacterial biofilms: from the natural environment to infectious diseases. *Nature Rev. Microbiol.*, 2(2):95–108, 2004.

[43] I. Klapper, C. J. Rupp, R. Cargo, B. Purvedorj, and P. Stoodley. Viscoelastic fluid description of bacterial biofilm material properties. *Biotechnol. Bioengng*, 80(3):289–296, 2002.

[44] J. N. Wilking, T. E. Angelini, A. Seminara, M. P. Brenner, and D. A. Weitz. Biofilms as complex fluids. *MRS Bull.*, 36(05):385–391, 2011.

[45] J. Rutllant, M. López-Béjar, and F. López-Gatius. Ultrastructural and rheological properties of bovine vaginal fluid and its relation to sperm motility and fertilization: a review. *Reprod. Domestic. Anim.*, 40(2):79–86, 2005.

[46] S. K. Lai, Y. Wang, D. Wirtz, and J. Hanes. Micro-and macrorheology of mucus. *Adv. Drug Deliv. Rev.*, 61(2):86–100, 2009.

[47] L. Rothschild. Non-random distribution of bull spermatozoa in a drop of sperm suspension. *Nature*, 198(488):1221, 1963.

[48] A. P. Berke, L. Turner, H. C. Berg, and E. Lauga. Hydrodynamic attraction of swimming microorganisms by surfaces. *Phys. Rev. Lett.*, 101(3):038102, 2008.

[49] G. Li and A. M. Ardekani. Hydrodynamic interaction of microswimmers near a wall. *Phys. Rev. E*, 90(1):013010, 2014.

[50] G. Li, A. Karimi, and A. M. Ardekani. Effect of solid boundaries on swimming dynamics of microorganisms in a viscoelastic fluid. *Rheol. Acta*, 53(12):911–926, 2014.

[51] G. Li, G. H. McKinley, and A. M. Ardekani. Dynamics of particle migration in channel flow of viscoelastic fluids. *J. Fluid Mech.*, 785:486–505, 2015.

[52] J. R. Vélez-Cordero and E. Lauga. Waving transport and propulsion in a generalized newtonian fluid. *J. Non-Newton. Fluid Mech.*, 199:37–50, 2013.

[53] G. Li and A. M. Ardekani. Undulatory swimming in non-Newtonian fluids. *J. Fluid Mech.*, 784:R4, 2015.

[54] S. Camalet, F. Jülicher, and J. Prost. Self-organized beating and swimming of internally driven filaments. *Phys. Rev. Lett.*, 82(7):1590, 1999.

[55] L. J. Fauci and C. S. Peskin. A computational model of aquatic animal locomotion. *J. Comput. Phys.*, 77(1):85–108, 1988.

[56] G. Li and A. M. Ardekani. Collective motion of microorganisms in a viscoelastic fluid. *Phys. Rev. Lett.*, 117(11):118001, 2016.

[57] R. M. Harshey. Bacterial motility on a surface: many ways to a common goal. *Annu. Rev. Microbiol*, 57(1):249–273, 2003.

[58] M. C. van Loosdrecht, J. Lyklema, W. Norde, and A. J. Zehnder. Influence of interfaces on microbial activity. *Microbiol. Rev.*, 54(1):75–87, 1990.

[59] S. S. Suarez and A. A. Pacey. Sperm transport in the female reproductive tract. *Human Reprod. Update*, 12(1):23–37, 2006.

[60] C. Montecucco and R. Rappuoli. Living dangerously: how helicobacter pylori survives in the human stomach. *Nat. Rev. Mol. Cell Biol.*, 2(6):457–466, 2001.

[61] C. W. Wolgemuth, N. W. Charon, S. F. Goldstein, and R. E. Goldstein. The flagellar cytoskeleton of the spirochetes. *J. Mol. Microbiol. Biotechnol.*, 11(3-5):221–227, 2006.

[62] M. W. Harman, S. M. Dunham-Ems, M. J. Caimano, A. A. Belperron, L. K. Bockenstedt, H. C. Fu, J. D. Radolf, and C. W. Wolgemuth. The heterogeneous motility of the lyme disease spirochete in gelatin mimics dissemination through tissue. *Proc. Natl. Acad. Sci. U.S.A.*, 109(8):3059–3064, 2012.

[63] S. Jung. Caenorhabditis elegans swimming in a saturated particulate system. *Phys. Fluids*, 22(3):031903, 2010.

[64] D. F. Katz. On the propulsion of micro-organisms near solid boundaries. *J. Fluid Mech.*, 64(01):33–49, 1974.

[65] D. F. Katz, J. R. Blake, and S. L. Paveri-Fontana. On the movement of slender bodies near plane boundaries at low reynolds number. *J. Fluid Mech.*, 72(03):529–540, 1975.

[66] L. J. Fauci and A. McDonald. Sperm motility in the presence of boundaries. *Bull. Math. Biol.*, 57(5):679–699, 1995.

[67] E. Lauga, W. R. DiLuzio, G. M. Whitesides, and H. A. Stone. Swimming in circles: motion of bacteria near solid boundaries. *Biophys. J.*, 90(2):400–412, 2006.

[68] G. Li and J. X. Tang. Accumulation of microswimmers near a surface mediated by collision and rotational brownian motion. *Phys. Rev. Lett.*, 103(7):078101, 2009.

[69] G. Li, J. Bensson, L. Nisimova, D. Munger, P. Mahautmr, J. X. Tang, M. R. Maxey, and Y. V. Brun. Accumulation of swimming bacteria near a solid surface. *Phys. Rev. E*, 84(4):041932, 2011.

[70] K. Drescher, J. Dunkel, L. H. Cisneros, S. Ganguly, and R. E. Goldstein. Fluid dynamics and noise in bacterial cell–cell and cell–surface scattering. *Proc. Natl. Acad. Sci. U.S.A.*, 108(27):10940–10945, 2011.

[71] A. Hamel, C. Fisch, L. Combettes, P. Dupuis-Williams, and C. N. Baroud. Transitions between three swimming gaits in paramecium escape. *Proc. Natl. Acad. Sci. U.S.A.*, 108(18):7290–7295, 2011.

[72] H. Jiang and T. Kiørboe. The fluid dynamics of swimming by jumping in copepods. *J. R. Soc. Interface*, page rsif20100481, 2011.

[73] S. Wang and A. M. Ardekani. Unsteady swimming of small organisms. *J. Fluid Mech.*, 702:286–297, 2012.

[74] S. Wang and A. M. Ardekani. Inertial squirmer. *Phys. Fluids*, 24(10):101902, 2012.

[75] G. Zilman, J. Novak, and Y. Benayahu. How do larvae attach to a solid in a laminar flow? *Mar. Biol*, 154(1):1–26, 2008.

[76] R. Zargar, A. Najafi, and M. Miri. Three-sphere low-reynolds-number swimmer near a wall. *Phys. Rev. E*, 80(2):026308, 2009.

[77] Y. Or and R. M. Murray. Dynamics and stability of a class of low reynolds number swimmers near a wall. *Phys. Rev. E*, 79(4):045302, 2009.

[78] D. G. Crowdy and Y. Or. Two-dimensional point singularity model of a low-reynolds-number swimmer near a wall. *Phys. Rev. E*, 81(3):036313, 2010.

[79] D. Crowdy and O. Samson. Hydrodynamic bound states of a low-reynolds-number swimmer near a gap in a wall. *J. Fluid Mech.*, 667:309–335, 2011.

[80] J. Dunstan, G. Mino, E. Clement, and R. Soto. A two-sphere model for bacteria swimming near solid surfaces. *Phys. Fluids*, 24(1):011901, 2012.

[81] S. E. Spagnolie and E. Lauga. Hydrodynamics of self-propulsion near a boundary: predictions and accuracy of far-field approximations. *J. Fluid Mech.*, 700:105–147, 2012.

[82] A. Sokolov and I. S. Aranson. Reduction of viscosity in suspension of swimming bacteria. *Phys. Rev. Lett.*, 103(14):148101, 2009.

[83] X. Wu and A. Libchaber. Particle diffusion in a quasi-two-dimensional bacterial bath. *Phys. Rev. Lett.*, 84(13):3017, 2000.

[84] A. Sokolov, R. E. Goldstein, F. I. Feldchtein, and I. S. Aranson. Enhanced mixing and spatial instability in concentrated bacterial suspensions. *Phys. Rev. E*, 80(3):031903, 2009.

[85] B. Cichocki, R. B. Jones, R. Kutteh, and E. Wajnryb. Friction and mobility for colloidal spheres in stokes flow near a boundary: The multipole method and applications. *J. Chem. Phys.*, 112(5):2548–2561, 2000.

[86] R. Pesché and G. Nägele. Stokesian dynamics study of quasi-two-dimensional suspensions confined between two parallel walls. *Phys. Rev. E*, 62(4):5432, 2000.

[87] S. Bhattacharya, J. Bławzdziewicz, and E. Wajnryb. Many-particle hydrodynamic interactions in parallel-wall geometry: Cartesian-representation method. *Phy. A*, 356(2):294–340, 2005.

[88] P. T. Underhill, J. P. Hernandez-Ortiz, and M. D. Graham. Diffusion and spatial correlations in suspensions of swimming particles. *Phys. Rev. Lett.*, 100(24):248101, 2008.

[89] P. T. Underhill and M. D. Graham. Correlations and fluctuations of stress and velocity in suspensions of swimming microorganisms. *Phys. Fluids*, 23(12):121902, 2011.

[90] J. P. Hernandez-Ortiz, C. G. Stoltz, and M. D. Graham. Transport and collective dynamics in suspensions of confined swimming particles. *Phys. Rev. Lett.*, 95(20):204501, 2005.

[91] J. P. Hernandez-Ortiz, P. T. Underhill, and M. D. Graham. Dynamics of confined suspensions of swimming particles. *J. Phys. Condens. Matter*, 21(20):204107, 2009.

[92] H. H. Wensink and H. Löwen. Aggregation of self-propelled colloidal rods near confining walls. *Phys. Rev. E*, 78(3):031409, 2008.

[93] I. Llopis and I. Pagonabarraga. Hydrodynamic interactions in squirmer motion: Swimming with a neighbour and close to a wall. *J. Non-Newton. Fluid Mech.*, 165(17):946–952, 2010.

[94] L. Zhu, M. Do-Quang, E. Lauga, and L. Brandt. Locomotion by tangential deformation in a polymeric fluid. *Phys. Rev. E*, 83(1):011901, 2011.

[95] L. Zhu, E. Lauga, and L. Brandt. Self-propulsion in viscoelastic fluids: Pushers vs. pullers. *Phys. Fluids*, 24(5):051902, 2012.

[96] K. Ishimoto and E. A. Gaffney. Squirmer dynamics near a boundary. *Phys. Rev. E*, 88(6):062702, 2013.

[97] T. Ishikawa, M. P. Simmonds, and T. J. Pedley. Hydrodynamic interaction of two swimming model micro-organisms. *J. Fluid Mech.*, 568:119–160, 2006.

[98] V. Magar and T. J. Pedley. Average nutrient uptake by a self-propelled unsteady squirmer. *J. Fluid Mech.*, 539:93–112, 2005.

[99] R. A. Lambert, F. Picano, W. Breugem, and L. Brandt. Active suspensions in thin films: nutrient uptake and swimmer motion. *J. Fluid Mech.*, 733:528–557, 2013.

[100] Z. Lin, J. Thiffeault, and S. Childress. Stirring by squirmers. *J. Fluid Mech.*, 669:167–177, 2011.

[101] A. Doostmohammadi, R. Stocker, and A. M. Ardekani. Low-reynolds-number swimming at pycnoclines. *Proc. Natl. Acad. Sci. U.S.A.*, 109(10):3856–3861, 2012.

[102] L. Zhu, E. Lauga, and L. Brandt. Low-reynolds-number swimming in a capillary tube. *J. Fluid Mech.*, 726:285–311, 2013.

[103] T. Ishikawa and T. J. Pedley. The rheology of a semi-dilute suspension of swimming model micro-organisms. *J. Fluid Mech.*, 588:399–435, 2007.

[104] T. Ishikawa and T. J. Pedley. Diffusion of swimming model micro-organisms in a semi-dilute suspension. *J. Fluid Mech.*, 588:437–462, 2007.

[105] T. Ishikawa, J. T. Locsei, and T. J. Pedley. Development of coherent structures in concentrated suspensions of swimming model micro-organisms. *J. Fluid Mech.*, 615:401–431, 2008.

[106] T. Ishikawa. Vertical dispersion of model microorganisms in horizontal shear flow. *J. Fluid Mech.*, 705:98–119, 2012.

[107] N. Sharma and N. A. Patankar. A fast computation technique for the direct numerical simulation of rigid particulate flows. *J. Comput. Phys.*, 205(2):439–457, 2005.

[108] A. M. Ardekani, S. Dabiri, and R. H. Rangel. Collision of multi-particle and general shape objects in a viscous fluid. *J. Comput. Phys.*, 227(24):10094–10107, 2008.

[109] R. Glowinski, T. W. Pan, T. I. Hesla, D. D. Joseph, and J. Periaux. A fictitious domain approach to the direct numerical simulation of incompressible viscous flow past moving rigid bodies: application to particulate flow. *J. Comput. Phys.*, 169(2):363–426, 2001.

[110] A. Doostmohammadi and A. M. Ardekani. Interaction between a pair of particles settling in a stratified fluid. *Phys. Rev. E*, 88(2):023029, 2013.

[111] S. Kim and S. J. Karrila. *Microhydrodynamics: principles and selected applications*. Courier Corporation, 2013.

[112] V. Mehandia and P. R. Nott. The collective dynamics of self-propelled particles. *J. Fluid Mech.*, 595:239–264, 2008.

[113] A. Sierou and J. F. Brady. Rheology and microstructure in concentrated noncolloidal suspensions. *J. Rheol.*, 46(5):1031–1056, 2002.

[114] B. Bunner and G. Tryggvason. Dynamics of homogeneous bubbly flows part 1. rise velocity and microstructure of the bubbles. *J. Fluid Mech.*, 466:17–52, 2002.

[115] A. S. Khair and N. G. Chisholm. Expansions at small reynolds numbers for the locomotion of a spherical squirmer. *Phys. Fluids*, 26(1):011902, 2014.

[116] A. M. Ardekani and R. H. Rangel. Numerical investigation of particle–particle and particle–wall collisions in a viscous fluid. *J. Fluid Mech.*, 596:437–466, 2008.

[117] G. A. O'Toole and R. Kolter. Flagellar and twitching motility are necessary for pseudomonas aeruginosa biofilm development. *Mol. Microbiol.*, 30(2):295–304, 1998.

[118] L. A. Pratt and R. Kolter. Genetic analysis of escherichia coli biofilm formation: roles of flagella, motility, chemotaxis and type i pili. *Mol. Microbiol.*, 30(2):285–293, 1998.

[119] P. I. Watnick and R. Kolter. Steps in the development of a vibrio cholerae el tor biofilm. *Mol. Microbiol.*, 34(3):586–595, 1999.

[120] K. P. Lemon, D. E. Higgins, and R. Kolter. Flagellar motility is critical for listeria monocytogenes biofilm formation. *J. Bacteriol.*, 189(12):4418–4424, 2007.

[121] P. M. Merritt, T. Danhorn, and C. Fuqua. Motility and chemotaxis in agrobacterium tumefaciens surface attachment and biofilm formation. *J. bacteriol.*, 189(22):8005–8014, 2007.

[122] T. Kim, B. M. Young, and G. M. Young. Effect of flagellar mutations on yersinia enterocolitica biofilm formation. *Appl. Environ. Microbiol.*, 74(17):5466–5474, 2008.

[123] A. Houry, R. Briandet, S. Aymerich, and M. Gohar. Involvement of motility and flagella in bacillus cereus biofilm formation. *Microbiology*, 156(4):1009–1018, 2010.

[124] H. H. Tuson and D. B. Weibel. Bacteria–surface interactions. *Soft Matter*, 9(17):4368–4380, 2013.

[125] L. L. Burrows. Pseudomonas aeruginosa twitching motility: type iv pili in action. *Annu. Rev. Microbiol.*, 66:493–520, 2012.

[126] T. Tolker-Nielsen, U. C. Brinch, P. C. Ragas, J. B. Andersen, C. S. Jacobsen, and S. Molin. Development and dynamics of pseudomonassp. biofilms. *J. Bacteriol.*, 182(22):6482–6489, 2000.

[127] H. Vlamakis, C. Aguilar, R. Losick, and R. Kolter. Control of cell fate by the formation of an architecturally complex bacterial community. *Genes Dev.*, 22(7):945–953, 2008.

[128] M. Wloka, H. Rehage, H. Flemming, and J. Wingender. Rheological properties of viscoelastic biofilm extracellular polymeric substances and comparison to the behavior of calcium alginate gels. *Colloid Polym. Sci.*, 282(10):1067–1076, 2004.

[129] T. Shaw, M. Winston, C. J. Rupp, I. Klapper, and P. Stoodley. Commonality of elastic relaxation times in biofilms. *Phys. Rev. Lett.*, 93(9):098102, 2004.

[130] E. Lauga. Life at high deborah number. *EPL*, 86(6):64001, 2009.

[131] C. Brennen and H. Winet. Fluid mechanics of propulsion by cilia and flagella. *Annu. Rev. Fluid Mech.*, 9(1):339–398, 1977.

[132] H. C. Berg and L. Turner. Movement of microorganisms in viscous environments. 1979.

[133] R. B. Kimsey and A. Spielman. Motility of lyme disease spirochetes in fluids as viscous as the extracellular matrix. *J. Infect. Dis.*, 162(5):1205–1208, 1990.

[134] X. N. Shen and P. E. Arratia. Undulatory swimming in viscoelastic fluids. *Phys. Rev. Lett.*, 106(20):208101, 2011.

[135] E. Lauga. Propulsion in a viscoelastic fluid. *Phys. Fluids*, 19(8):083104, 2007.

[136] J. Teran, L. Fauci, and M. Shelley. Viscoelastic fluid response can increase the speed and efficiency of a free swimmer. *Phys. Rev. Lett.*, 104(3):038101, 2010.

[137] B. Liu, T. R. Powers, and K. S. Breuer. Force-free swimming of a model helical flagellum in viscoelastic fluids. *Proc. Natl. Acad. Sci. U.S.A.*, 108(49):19516–19520, 2011.

[138] S. E. Spagnolie, B. Liu, and T. R. Powers. Locomotion of helical bodies in viscoelastic fluids: enhanced swimming at large helical amplitudes. *Phys. Rev. Lett.*, 111(6):068101, 2013.

[139] A. M. Ardekani and E. Gore. Emergence of a limit cycle for swimming microorganisms in a vortical flow of a viscoelastic fluid. *Phys. Rev. E*, 85(5):056309, 2012.

[140] Y. Bozorgi and P. T. Underhill. Effect of viscoelasticity on the collective behavior of swimming microorganisms. *Phys. Rev. E*, 84(6):061901, 2011.

[141] Y. Bozorgi and P. T. Underhill. Role of linear viscoelasticity and rotational diffusivity on the collective behavior of active particles. *J. Rheol.*, 57(2):511–533, 2013.

[142] A. M. Ardekani, R. H. Rangel, and D. D. Joseph. Motion of a sphere normal to a wall in a second-order fluid. *J. Fluid Mech.*, 587:163–172, 2007.

[143] G. D'Avino, G. Cicale, M. A. Hulsen, F. Greco, and P. L. Maffettone. Effects of confinement on the motion of a single sphere in a sheared viscoelastic liquid. *J. Non-Newton. Fluid Mech.*, 157(1):101–107, 2009.

[144] A. Despeyroux and A. Ambari. Slow motion of a sphere towards a plane through confined non-newtonian fluid. *J. Non-Newton. Fluid Mech.*, 167:38–45, 2012.

[145] S. Padhy, M. Rodriguez, E. S. G. Shaqfeh, G. Iaccarino, J. F. Morris, and N. Tonmukayakul. The effect of shear thinning and walls on the sedimentation of a sphere in an elastic fluid under orthogonal shear. *J. Non-Newton. Fluid Mech.*, 201:120–129, 2013.

[146] J. A. Tatum, M. V. Finnis, N. J. Lawson, and G. M. Harrison. 3d particle image velocimetry of the flow field around a sphere sedimenting near a wall: Part 1. effects of weissenberg number. *J. Non-Newton. Fluid Mech.*, 141(2):99–115, 2007.

[147] A. M. Ardekani, D. D. Joseph, D. Dunn-Rankin, and R. H. Rangel. Particle-wall collision in a viscoelastic fluid. *J. Fluid Mech.*, 633:475, 2009.

[148] D. A. Eisenberg, I. M. Klink, and R. J. Phillips. Axisymmetric sedimentation of spherical particles in a viscoelastic fluid: Sphere–wall and sphere–sphere interactions. *J. Rheol.*, 57(3):857–880, 2013.

[149] H. Giesekus. A simple constitutive equation for polymer fluids based on the concept of deformation-dependent tensorial mobility. *J. Non-Newton. Fluid Mech.*, 11(1-2):69–109, 1982.

[150] G. Schleiniger and R. J. Weinacht. A remark on the giesekus viscoelastic fluid. *J. Rheol.*, 35(6):1157–1170, 1991.

[151] W. R. DiLuzio, L. Turner, M. Mayer, P. Garstecki, D. B. Weibel, H. C. Berg, and G. M. Whitesides. Escherichia coli swim on the right-hand side. *Nature*, 435(7046):1271–1274, 2005.

[152] G. Li, L. Tam, and J. X. Tang. Amplified effect of brownian motion in bacterial near-surface swimming. *Proc. Natl. Acad. Sci. U.S.A.*, 105(47):18355–18359, 2008.

[153] S. Thutupalli, R. Seemann, and S. Herminghaus. Swarming behavior of simple model squirmers. 13(7):073021, 2011.

[154] F. Snijkers, G. D'Avino, P. L. Maffettone, F. Greco, M. A. Hulsen, and J. Vermant. Effect of viscoelasticity on the rotation of a sphere in shear flow. *J. Non-Newton. Fluid Mech.*, 166(7):363–372, 2011.

[155] N. Goyal and J. J. Derksen. Direct simulations of spherical particles sedimenting in viscoelastic fluids. *J. Non-Newton. Fluid Mech.*, 183:1–13, 2012.

[156] G. Segre. Radial particle displacements in poiseuille flow of suspensions. *Nature*, 189:209–210, 1961.

[157] K. Kang, S. S. Lee, K. Hyun, S. J. Lee, and J. M. Kim. Dna-based highly tunable particle focuser. *Nat. Commun.*, 4, 2013.

[158] E. J. Lim, T. J. Ober, J. F. Edd, S. P. Desai, D. Neal, K. W. Bong, P. S. Doyle, G. H. McKinley, and M. Toner. Inertio-elastic focusing of bioparticles in microchannels at high throughput. *Nat. Commun.*, 5, 2014.

[159] A. Karnis and S. G. Mason. Particle motions in sheared suspensions. xix. viscoelastic media. *Can. J. Chem. Eng.*, 10(2):571–592, 1966.

[160] F. Gauthier, H. L. Goldsmith, and S. G. Mason. Particle motions in non-newtonian media. ii. poiseuille flow. *Trans. Soc. Rheol.*, 15(2):297–330, 1971.

[161] W. Lee, H. Amini, H. A. Stone, and D. Di Carlo. Dynamic self-assembly and control of microfluidic particle crystals. *Proc. Natl. Acad. Sci. U.S.A.*, 107(52):22413–22418, 2010.

[162] H. Amini, E. Sollier, W. M. Weaver, and D. Di Carlo. Intrinsic particle-induced lateral transport in microchannels. *Proc. Natl. Acad. Sci. U.S.A.*, 109(29):11593–11598, 2012.

[163] A. Karnis, H. L. Goldsmith, and S. G. Mason. The flow of suspensions through tubes: V. inertial effects. *Can. J. Chem. Eng.*, 44(4):181–193, 1966.

[164] J. Matas, J. F. Morris, and É. Guazzelli. Inertial migration of rigid spherical particles in poiseuille flow. *J. Fluid Mech.*, 515:171–195, 2004.

[165] J. A. Schonberg and E. J. Hinch. Inertial migration of a sphere in poiseuille flow. *J. Fluid Mech.*, 203:517–524, 1989.

[166] J. Feng, H. H. Hu, and D. D. Joseph. Direct simulation of initial value problems for the motion of solid bodies in a newtonian fluid. part 2. couette and poiseuille flows. *J. Fluid Mech.*, 277:271–301, 1994.

[167] B. H. Yang, J. Wang, D. D. Joseph, H. H. Hu, T. Pan, and R. Glowinski. Migration of a sphere in tube flow. *J. Fluid Mech.*, 540:109–131, 2005.

[168] B. Chun and A. J. C. Ladd. Inertial migration of neutrally buoyant particles in a square duct: An investigation of multiple equilibrium positions. *Phys. Fluids*, 18(3):031704, 2006.

[169] Y. W. Kim and J. Y. Yoo. The lateral migration of neutrally-buoyant spheres transported through square microchannels. *J. Micromech. Microeng.*, 18(6):065015, 2008.

[170] X. Shao, Z. Yu, and B. Sun. Inertial migration of spherical particles in circular poiseuille flow at moderately high reynolds numbers. *Phys. Fluids*, 20(10):103307, 2008.

[171] D. Di Carlo, J. F. Edd, K. J. Humphry, H. A. Stone, and M. Toner. Particle segregation and dynamics in confined flows. *Phys. Rev. Lett.*, 102(9):094503, 2009.

[172] Y. Choi, K. Seo, and S. Lee. Lateral and cross-lateral focusing of spherical particles in a square microchannel. *Lab Chip*, 11(3):460–465, 2011.

[173] E. S. Asmolov. The inertial lift on a spherical particle in a plane poiseuille flow at large channel reynolds number. *J. Fluid Mech.*, 381:63–87, 1999.

[174] L. Zeng, S. Balachandar, and P. Fischer. Wall-induced forces on a rigid sphere at finite reynolds number. *J. Fluid Mech.*, 536:1–25, 2005.

[175] D. R. Gossett, H. T. K. Tse, J. S. Dudani, K. Goda, T. A. Woods, S. W. Graves, and D. Di Carlo. Inertial manipulation and transfer of microparticles across laminar fluid streams. *Small*, 8(17):2757–2764, 2012.

[176] D. Di Carlo. Inertial microfluidics. *Lab Chip*, 9(21):3038–3046, 2009.

[177] A. Karimi, S. Yazdi, and A. M. Ardekani. Hydrodynamic mechanisms of cell and particle trapping in microfluidics. *Biomicrofluidics*, 7(2):021501, 2013.

[178] M. A. Tehrani. An experimental study of particle migration in pipe flow of viscoelastic fluids. *J. Rheol.*, 40(6):1057–1077, 1996.

[179] B. P. Ho and L. G. Leal. Migration of rigid spheres in a two-dimensional unidirectional shear flow of a second-order fluid. *J. Fluid Mech.*, 76(04):783–799, 1976.

[180] G. D'Avino, G. Romeo, M. M. Villone, F. Greco, P. A. Netti, and P. L. Maffettone. Single line particle focusing induced by viscoelasticity of the suspending liquid: theory, experiments and simulations to design a micropipe flow-focuser. *Lab Chip*, 12(9):1638–1645, 2012.

[181] G. Romeo, G. D'Avino, F. Greco, P. A. Netti, and P. L. Maffettone. Viscoelastic flow-focusing in microchannels: scaling properties of the particle radial distributions. *Lab Chip*, 13(14):2802–2807, 2013.

[182] S. Yang, J. Y. Kim, S. J. Lee, S. S. Lee, and J. M. Kim. Sheathless elasto-inertial particle focusing and continuous separation in a straight rectangular microchannel. *Lab Chip*, 11(2):266–273, 2011.

[183] P. Y. Huang and D. D. Joseph. Effects of shear thinning on migration of neutrally buoyant particles in pressure driven flow of newtonian and viscoelastic fluids. *J. Non-Newton. Fluid Mech.*, 90(2):159–185, 2000.

[184] M. M. Villone, G. D'Avino, M. A. Hulsen, F. Greco, and P. L. Maffettone. Simulations of viscoelasticity-induced focusing of particles in pressure-driven micro-slit flow. *J. Non-Newton. Fluid Mech.*, 166(23):1396–1405, 2011.

[185] M. M. Villone, G. D'Avino, M. A. Hulsen, F. Greco, and P. L. Maffettone. Particle motion in square channel flow of a viscoelastic liquid: Migration vs. secondary flows. *J. Non-Newton. Fluid Mech.*, 195:1–8, 2013.

[186] J. Nam, H. Lim, D. Kim, H. Jung, and S. Shin. Continuous separation of microparticles in a microfluidic channel via the elasto-inertial effect of non-newtonian fluid. *Lab chip*, 12(7):1347–1354, 2012.

[187] G. D'Avino and P. L. Maffettone. Particle dynamics in viscoelastic liquids. *J. Non-Newton. Fluid Mech.*, 215:80–104, 2015.

[188] K. W. Seo, Y. J. Kang, and S. J. Lee. Lateral migration and focusing of microspheres in a microchannel flow of viscoelastic fluids. *Phys. Fluids*, 26(6):063301, 2014.

[189] C. Fetecau and C. Fetecau. Unsteady flows of oldroyd-b fluids in a channel of rectangular cross-section. *Int. J. Nonlinear Mech.*, 40(9):1214–1219, 2005.

[190] R. Guénette and M. Fortin. A new mixed finite element method for computing viscoelastic flows. *J. Non-Newton. Fluid Mech.*, 60(1):27–52, 1995.

[191] G. D'Avino, T. Tuccillo, P. L. Maffettone, F. Greco, and M. A. Hulsen. Numerical simulations of particle migration in a viscoelastic fluid subjected to shear flow. *Comput. Fluids*, 39(4):709–721, 2010.

[192] A. M. Leshansky, A. Bransky, N. Korin, and U. Dinnar. Tunable nonlinear viscoelastic focusing in a microfluidic device. *Phys. Rev. Lett.*, 98(23):234501, 2007.

[193] M. Zurita-Gotor, J. Bławzdziewicz, and E. Wajnryb. Swapping trajectories: A new wall-induced cross-streamline particle migration mechanism in a dilute suspension of spheres. *J. Fluid Mech.*, 592:447–469, 2007.

[194] G. D'Avino, P. L. Maffettone, F. Greco, and M. A. Hulsen. Viscoelasticity-induced migration of a rigid sphere in confined shear flow. *J. Non-Newton. Fluid Mech.*, 165(9):466–474, 2010.

[195] P. Y. Huang, J. Feng, H. H. Hu, and D. D. Joseph. Direct simulation of the motion of solid particles in couette and poiseuille flows of viscoelastic fluids. *J. Fluid Mech.*, 343:73–94, 1997.

[196] B. P. Ho and L. G. Leal. Inertial migration of rigid spheres in two-dimensional unidirectional flows. *J. Fluid Mech.*, 65(02):365–400, 1974.

[197] H. Lim, J. Nam, and S. Shin. Lateral migration of particles suspended in viscoelastic fluids in a microchannel flow. *Microfluid. Nanofluidics*, 17(4):683–692, 2014.

[198] J. Happel and H. Brenner. *Low Reynolds number hydrodynamics: with special applications to particulate media*, volume 1. Springer Science & Business Media, 2012.

[199] R. P. Chhabra. *Bubbles, drops, and particles in non-Newtonian fluids*. CRC press, 2006.

[200] M. T. Arigo, D. Rajagopalan, N. Shapley, and G. H. McKinley. The sedimentation of a sphere through an elastic fluid. part 1. steady motion. *J. Non-Newton. Fluid Mech.*, 60(2):225–257, 1995.

[201] D. Fabris, S. J. Muller, and D. Liepmann. Wake measurements for flow around a sphere in a viscoelastic fluid. *Phys. Fluids*, 11(12):3599–3612, 1999.

[202] A. Abedijaberi and B. Khomami. Sedimentation of a sphere in a viscoelastic fluid: a multiscale simulation approach. *J. Fluid Mech.*, 694:78–99, 2012.

[203] G. H. McKinley. Steady and transient motion of spherical particles in viscoelastic liquids. *Transport Processes in Bubble, Drops, and Particles*, pages 338–375, 2002.

[204] A. S. R. Duarte, A. I. P. Miranda, and P. J. Oliveira. Numerical and analytical modeling of unsteady viscoelastic flows: The start-up and pulsating test case problems. *J. Non-Newton. Fluid Mech.*, 154(2):153–169, 2008.

[205] M. T. Arigo and G. H. McKinley. The effects of viscoelasticity on the transient motion of a sphere in a shear-thinning fluid. *J. Rheol.*, 41(1):103–128, 1997.

[206] D. C. Smith, M. Simon, A. L. Alldredge, and F. Azam. Intense hydrolytic enzyme activity on marine aggregates and implications for rapid particle dissolution. *Nature*, 359(6391):139–142, 1992.

[207] S. H. Hwang, M. Litt, and W. C. Forsman. Rheological properties of mucus. *Rheol. Acta*, 8(4):438–448, 1969.

[208] B. Thomases and R. D. Guy. Mechanisms of elastic enhancement and hindrance for finite-length undulatory swimmers in viscoelastic fluids. *Phys. Rev. Lett.*, 113(9):098102, 2014.

[209] E. E. Riley and E. Lauga. Enhanced active swimming in viscoelastic fluids. *Europhys. Lett.*, 108(3):34003, 2014.

[210] W. R. Schneider and R. N. Doetsch. Effect of viscosity on bacterial motility. *J. bacteriol.*, 117(2):696–701, 1974.

[211] Y. Magariyama and S. Kudo. A mathematical explanation of an increase in bacterial swimming speed with viscosity in linear-polymer solutions. *Biophys. J.*, 83(2):733–739, 2002.

[212] T. D. Montenegro-Johnson, A. A. Smith, D. J. Smith, D. Loghin, and J. R. Blake. Modelling the fluid mechanics of cilia and flagella in reproduction and development. *Eur. Phys. J. E*, 35(10):1–17, 2012.

[213] T. D. Montenegro-Johnson, D.J. Smith, and D. Loghin. Physics of rheologically enhanced propulsion: Different strokes in generalized stokes. *Phys. Fluids*, 25(8):081903, 2013.

[214] D. A. Gagnon, N. C. Keim, and P. E. Arratia. Undulatory swimming in shear-thinning fluids: experiments with caenorhabditis elegans. *J. Fluid Mech.*, 758:R3, 2014.

[215] M. Dasgupta, B. Liu, H. C. Fu, M. Berhanu, K. S. Breuer, T. R. Powers, and A. Kudrolli. Speed of a swimming sheet in newtonian and viscoelastic fluids. *Phys. Rev. E*, 87(1):013015, 2013.

[216] R. B. Bird, R. C. Armstrong, and O. Hassager. Dynamics of polymeric liquids. vol. 1: Fluid mechanics. 1987.

[217] P. J. Carreau, D. De Kee, and R. P. Chhabra. *Rheology of polymeric systems: principles and applications*. Hanser Publishers Munich, 1997.

[218] D. P. Poppi, R. E. Hendricksen, and D. J. Minson. The relative resistance to escape of leaf and stem particles from the rumen of cattle and sheep. *J. Agric. Sci.*, 105(01):9–14, 1985.

[219] A. Einstein. Eine neue bestimmung der moleküldimensionen. *Ann. Phys.*, 324(2):289–306, 1906.

[220] A. D. Maude. Non-random distribution of bull spermatozoa in a drop of sperm suspension. *Nature*, 200:381, 1963.

[221] D. M. Woolley. Motility of spermatozoa at surfaces. *Reproduction*, 126(2):259–270, 2003.

[222] J. Yuan, D. M. Raizen, and H. H. Bau. Propensity of undulatory swimmers, such as worms, to go against the flow. *Proc. Natl. Acad. Sci. U.S.A.*, 112(12):3606–3611, 2015.

[223] V. Kantsler, J. Dunkel, M. Polin, and R. E. Goldstein. Ciliary contact interactions dominate surface scattering of swimming eukaryotes. *Proc. Natl. Acad. Sci. U.S.A.*, 110(4):1187–1192, 2013.

[224] G. Li, A. Ostace, and A. M. Ardekani. Hydrodynamic interaction of swimming organisms in an inertial regime. *Phys. Rev. E*, 94(5):053104, 2016.

[225] D. J. Smith, E. A. Gaffney, J. R. Blake, and J. C. Kirkman-Brown. Human sperm accumulation near surfaces: a simulation study. *J. Fluid Mech.*, 621:289–320, 2009.

[226] K. Ishimoto and E. A. Gaffney. A study of spermatozoan swimming stability near a surface. *J. Theor. Biol.*, 360:187–199, 2014.

[227] J. Elgeti, U. B. Kaupp, and G. Gompper. Hydrodynamics of sperm cells near surfaces. *Biophys. J.*, 99(4):1018–1026, 2010.

[228] M. P. Curtis, J. C. Kirkman-Brown, T. J. Connolly, and E. A. Gaffney. Modelling a tethered mammalian sperm cell undergoing hyperactivation. *J. Theor. Biol.*, 309:1–10, 2012.

[229] J. Simons, S. Olson, R. Cortez, and L. Fauci. The dynamics of sperm detachment from epithelium in a coupled fluid-biochemical model of hyperactivated motility. *J. Theor. Biol.*, 354:81–94, 2014.

[230] D. P. Wolf, L. Blasco, M. A. Khan, and M. Litt. Human cervical mucus. i. rheologic characteristics. *Fertil. Steril.*, 28(1):41–46, 1977.

[231] H. C. Fu, T. R. Powers, and C. W. Wolgemuth. Theory of swimming filaments in viscoelastic media. *Phys. Rev. Lett.*, 99(25):258101, 2007.

[232] R. D. Guy and B. Thomases. Computational challenges for simulating strongly elastic flows in biology. In *Complex Fluids in Biological Systems*, pages 359–397. Springer, 2015.

[233] D. A. Gagnon and P. E. Arratia. The cost of swimming in generalized Newtonian fluids: experiments with C. elegans. *J. Fluid Mech.*, 800:753–765, 2016.

[234] C. Datt, L. Zhu, G. J. Elfring, and O. S. Pak. Squirming through shear-thinning fluids. *J. Fluid Mech.*, 784:R1, 2015.

[235] J. C. Chrispell, L. J. Fauci, and M. Shelley. An actuated elastic sheet interacting with passive and active structures in a viscoelastic fluid. *Phys. Fluids*, 25(1):013103, 2013.

[236] S. Yazdi, A. M. Ardekani, and A. Borhan. Swimming dynamics near a wall in a weakly elastic fluid. *J. Nonlinear Sci.*, 25(5):1153–1167, 2015.

[237] S. Yazdi, A. M. Ardekani, and A. Borhan. Locomotion of microorganisms near a no-slip boundary in a viscoelastic fluid. *Phys. Rev. E*, 90(4):043002, 2014.

[238] S. Dabiri, J. Lu, and G. Tryggvason. Transition between regimes of a vertical channel bubbly upflow due to bubble deformability. *Phys. Fluids*, 25(10):102110, 2013.

[239] S. Dabiri and G. Tryggvason. Heat transfer in turbulent bubbly flow in vertical channels. 122:106–113, 2015.

[240] S. Dabiri, A. Doostmohammadi, M. Bayareh, and A. M. Ardekani. Rising motion of a swarm of drops in a linearly stratified fluid. *Int. J. Multiph. Flow*, 69:8–17, 2015.

[241] S. Dabiri and P. Bhuvankar. Scaling law for bubbles rising near vertical walls. *Phys. Fluids*, 28(6):062101, 2016.

[242] A. A. Evans and E. Lauga. Propulsion by passive filaments and active flagella near boundaries. *Phys. Rev. E*, 82(4):041915, 2010.

[243] B. Qin, A. Gopinath, J. Yang, J. P. Gollub, and P. E. Arratia. Flagellar kinematics and swimming of algal cells in viscoelastic fluids. *Sci. Rep.*, 5, 2015.

[244] F. D. Warner and P. Satir. The structural basis of ciliary bend formation radial spoke positional changes accompanying microtubule sliding. *J. Cell BioI.*, 63(1):35–63, 1974.

[245] D. Bray. *Cell movements: from molecules to motility*. Garland Science, 2001.

[246] M. Murase. *The dynamics of cellular motility*. John Wiley & Sons, 1992.

[247] F. D. Warner and D. R. Mitchell. Polarity of dynein-microtubule interactions in vitro: cross-bridging between parallel and antiparallel microtubules. *J. Cell Biol.*, 89(1):35–44, 1981.

[248] I. R. Gibbons. Cilia and flagella of eukaryotes. *J. Cell Biol.*, 91(3):107s–124s, 1981.

[249] M. A. Sleigh, J. R. Blake, and N. Liron. The propulsion of mucus by cilia. *Am. Rev. Respir. Dis.*, 137(3):726–741, 1988.

[250] H. Ho and S. S. Suarez. Hyperactivation of mammalian spermatozoa: function and regulation. *Reproduction*, 122(4):519–526, 2001.

[251] D. F. Katz, R. N. Mills, and T. R. Pritchett. The movement of human spermatozoa in cervical mucus. *J. Reprod. Fertil.*, 53(2):259–265, 1978.

[252] K. E. Machin. The control and synchronization of flagellar movement. *Proc. R. Soc. B*, 158(970):88–104, 1963.

[253] H. C. Fu, C. W. Wolgemuth, and T. R. Powers. Beating patterns of filaments in viscoelastic fluids. *Phys. Rev. E*, 78(4):041913, 2008.

[254] R. Rikmenspoel. The equation of motion for sperm flagella. *Biophys. J.*, 23(2):177, 1978.

[255] K. Sugino and Y. Naitoh. Simulated cross-bridge patterns corresponding to ciliary beating in paramecium. 1982.

[256] S. D. Olson and L. J. Fauci. Hydrodynamic interactions of sheets vs filaments: Synchronization, attraction, and alignment. *Phys. Fluids*, 27(12):121901, 2015.

[257] S. D. Olson, S. S. Suarez, and L. J. Fauci. Coupling biochemistry and hydrodynamics captures hyperactivated sperm motility in a simple flagellar model. *J. Theor. Biol.*, 283(1):203–216, 2011.

[258] W. Huang, S. J. Shin, and H. J. Sung. Simulation of flexible filaments in a uniform flow by the immersed boundary method. *J. Comput. Phys.*, 226(2):2206–2228, 2007.

[259] C. H. Wiggins and R. E. Goldstein. Flexive and propulsive dynamics of elastica at low reynolds number. *Phys. Rev. Lett.*, 80(17):3879, 1998.

[260] J. Howard. Mechanics of motor proteins and the cytoskeleton. 2001.

[261] M. Backholm, W. S. Ryu, and K. Dalnoki-Veress. Viscoelastic properties of the nematode caenorhabditis elegans, a self-similar, shear-thinning worm. *Proc. Natl. Acad. Sci. U.S.A.*, 110(12):4528–4533, 2013.

[262] C. S. Peskin. The immersed boundary method. *Acta Numer.*, 11:479–517, 2002.

[263] T. Y. Hou and Z. Shi. Removing the stiffness of elastic force from the immersed boundary method for the 2d stokes equations. *J. Comput. Phys.*, 227(21):9138–9169, 2008.

[264] T. Y. Hou and Z. Shi. An efficient semi-implicit immersed boundary method for the navier–stokes equations. *J. Comput. Phys.*, 227(20):8968–8991, 2008.

[265] A. Bilbao, E. Wajnryb, S. A. Vanapalli, and J. Blawzdziewicz. Nematode locomotion in unconfined and confined fluids. *Phys. Fluids*, 25(8):081902, 2013.

[266] J. W. Costerton, P. S. Stewart, and E. P. Greenberg. Bacterial biofilms: a common cause of persistent infections. *Science*, 284(5418):1318–1322, 1999.

[267] C. Dombrowski, L. Cisneros, S. Chatkaew, R. E. Goldstein, and J. O. Kessler. Self-concentration and large-scale coherence in bacterial dynamics. *Phys. Rev. Lett.*, 93(9):098103, 2004.

[268] N. H. Mendelson, A. Bourque, K. Wilkening, K. R. Anderson, and J. C. Watkins. Organized cell swimming motions in bacillus subtilis colonies: patterns of short-lived whirls and jets. *J. bacteriol.*, 181(2):600–609, 1999.

[269] L. H. Cisneros, R. Cortez, C. Dombrowski, R. E. Goldstein, and J. O. Kessler. Fluid dynamics of self-propelled microorganisms, from individuals to concentrated populations. 43(5):737–753, 2007.

[270] L. H. Cisneros, J. O. Kessler, S. Ganguly, and R. E. Goldstein. Dynamics of swimming bacteria: Transition to directional order at high concentration. *Phys. Rev. E*, 83(6):061907, 2011.

[271] H. H. Wensink, J. Dunkel, S. Heidenreich, K. Drescher, R. E. Goldstein, H. Löwen, and J. M. Yeomans. Meso-scale turbulence in living fluids. *Proc. Natl. Acad. Sci. U.S.A.*, 109(36):14308–14313, 2012.

[272] A. Creppy, O. Praud, X. Druart, P. L. Kohnke, and F. Plouraboué. Turbulence of swarming sperm. *Phys. Rev. E*, 92(3):032722, 2015.

[273] D. Saintillan and M. J. Shelley. Instabilities and pattern formation in active particle suspensions: kinetic theory and continuum simulations. *Phys. Rev. Lett.*, 100(17):178103, 2008.

[274] R. A. Simha and S. Ramaswamy. Hydrodynamic fluctuations and instabilities in ordered suspensions of self-propelled particles. *Phys. Rev. Lett.*, 89(5):058101, 2002.

[275] D. Saintillan and M. J. Shelley. Emergence of coherent structures and large-scale flows in motile suspensions. *J. R. Soc. Interface*, page rsif20110355, 2011.

[276] L. Giomi. Geometry and topology of turbulence in active nematics. *Phys. Rev. X*, 5(3):031003, 2015.

[277] E. J. Hemingway, A. Maitra, S. Banerjee, M. C. Marchetti, S. Ramaswamy, S. M. Fielding, and M. E. Cates. Active viscoelastic matter: From bacterial drag reduction to turbulent solids. *Phys. Rev. Lett.*, 114(9):098302, 2015.

[278] Y. Amarouchene and H. Kellay. Polymers in 2d turbulence: Suppression of large scale fluctuations. *Phys. Rev. Lett.*, 89(10):104502, 2002.

[279] G. Boffetta, A. Celani, and S. Musacchio. Two-dimensional turbulence of dilute polymer solutions. *Phys. Rev. Lett.*, 91(3):034501, 2003.

[280] C. M. White and M. G. Mungal. Mechanics and prediction of turbulent drag reduction with polymer additives. *Annu. Rev. Fluid Mech.*, 40:235–256, 2008.

[281] L. Xi and M.l D. Graham. Active and hibernating turbulence in minimal channel flow of newtonian and polymeric fluids. *Phys. Rev. Lett.*, 104(21):218301, 2010.

[282] P. C. Valente, C. B. da Silva, and F. T. Pinho. The effect of viscoelasticity on the turbulent kinetic energy cascade. *J. Fluid Mech.*, 760:39–62, 2014.

[283] E. De Angelis, C. M. Casciola, and R. Piva. Energy spectra in viscoelastic turbulence. *Physica D*, 241(3):297–303, 2012.

[284] T. Ishikawa, N. Yoshida, H. Ueno, M. Wiedeman, Y. Imai, and T. Yamaguchi. Energy transport in a concentrated suspension of bacteria. *Phys. Rev. Lett.*, 107(2):028102, 2011.

[285] M. Rivera and X. Wu. External dissipation in driven two-dimensional turbulence. *Phys. Rev. Lett.*, 85(5):976, 2000.

[286] T. Brotto, J. Caussin, E. Lauga, and D. Bartolo. Hydrodynamics of confined active fluids. *Phys. Rev. Lett.*, 110(3):038101, 2013.

[287] J. Stenhammar, A. Tiribocchi, R. J. Allen, D. Marenduzzo, and M. E. Cates. Continuum theory of phase separation kinetics for active brownian particles. *Phys. Rev. Lett.*, 111(14):145702, 2013.

[288] G. S. Redner, M. F. Hagan, and A. Baskaran. Structure and dynamics of a phase-separating active colloidal fluid. *Phys. Rev. Lett.*, 110(5):055701, 2013.

[289] S. C. Takatori and J. F. Brady. A theory for the phase behavior of mixtures of active particles. *Soft Matter*, 11(40):7920–7931, 2015.

[290] K. Yeo, E. Lushi, and P. M. Vlahovska. Dynamics of inert spheres in active suspensions of micro-rotors. 2016.

[291] A. Groisman and V. Steinberg. Elastic turbulence in a polymer solution flow. *Nature*, 405(6782):53–55, 2000.

[292] L. Pan, A. Morozov, C. Wagner, and P. E. Arratia. Nonlinear elastic instability in channel flows at low reynolds numbers. *Phys. Rev. Lett.*, 110(17):174502, 2013.

[293] H. Y. Gan, Y. C. Lam, and N. Nguyen. Polymer-based device for efficient mixing of viscoelastic fluids. *Appl. Phys. Lett.*, 88(22):224103–226100, 2006.

[294] R. Fattal and R. Kupferman. Constitutive laws for the matrix-logarithm of the conformation tensor. *J. Non-Newton. Fluid Mech.*, 123(2):281–285, 2004.

[295] Y. Saad and M. H. Schultz. Gmres: A generalized minimal residual algorithm for solving nonsymmetric linear systems. *SIAM J. Sci. Stat. Comput.*, 7(3):856–869, 1986.

[296] R. G. Owens and T.N. Phillips. *Computational rheology*, volume 14. World Scientific, 2002.

[297] N. Balci, B. Thomases, M. Renardy, and C. R. Doering. Symmetric factorization of the conformation tensor in viscoelastic fluid models. *J. Non-Newton. Fluid Mech.*, 166(11):546–553, 2011.

[298] B. Thomases and M. Shelley. Emergence of singular structures in oldroyd-b fluids. *Phys. Fluids*, 19(10):103103, 2007.

[299] D. J. Smith, E. A. Gaffney, H. Gadêlha, N. Kapur, and J. C. Kirkman-Brown. Bend propagation in the flagella of migrating human sperm, and its modulation by viscosity. *Cell Motil. Cytoskeleton*, 66(4):220–236, 2009.

[300] M. Doi and S. F. Edwards. *The theory of polymer dynamics*, volume 73. Oxford University Press, 1988.

[301] M. Somasi, B. Khomami, N. J. Woo, J. S. Hur, and E. S. G. Shaqfeh. Brownian dynamics simulations of bead-rod and bead-spring chains: numerical algorithms and coarse-graining issues. *J. Non-Newton. Fluid Mech.*, 108(1):227–255, 2002.

VITA

# VITA

## RESEARCH INTERESTS

Non-Newtonian and viscoelastic fluids, microorganism swimming, biological flows and biofluids, microfluidics and biomedical devices, vortical dynamics, computational fluid dynamics.

## EDUCATION

- **Purdue University** Aug. 2014–Dec. 2016
  **Ph.D.**, Mechanical Engineering, West Lafayette, IN
- **University of Notre Dame** Aug. 2012–Transferred Aug. 2014
  Aerospace and Mechanical Engineering, Notre Dame, IN
- **University of Science and Technology of China** Sep. 2009–Jul. 2012
  **M. S**, Theoretical and Applied Mechanics, Hefei, China
- **University of Science and Technology of China** Sep. 2005–Jul. 2009
  **B. S**, Theoretical and Applied Mechanics, Hefei, China

## JOURNAL PUBLICATIONS

**11.** G. Li and A. M. Ardekani, "Near wall motion of undulatory swimmers in non-Newtonian uids", ***European Journal of Computational Mechanics*** (submitted).

**10.** G. Li, A. Ostace and A. M. Ardekani, "The inertia effects on the hydrodynamic interactions of swimming organisms", ***Physical Review E*** 94(5), 053104, 2016.

**9.** G. Li and A. M. Ardekani, "Collective Motion of Microorganisms in a Viscoelastic Fluid", ***Physical Review Letters***, 117(11), 118001, 2016.

**8.** G. Li, G. H. McKinley and A. M. Ardekani, "Dynamics of particle migration in a channel flow of viscoelastic fluids", ***Journal of Fluid Mechanics***, 785, 486–505, 2015.

**7.** G. Li and A. M. Ardekani, "Undulatory swimming in non-Newtonian fluids", ***Journal of Fluid Mechanics***, 784, R4, 2015.

**6.** G. Li, A. Karimi and A.M. Ardekani, "Effect of solid boundaries on swimming dynamics of microorganisms in a viscoelastic fluid", ***Rheologica Acta***, 53(12), 911–926, 2014.

**5.** G. Li and A.M. Ardekani, "Hydrodynamic interaction of micro-swimmers near a wall", ***Physical Review E***, 90, 013010, 2014.

**4.** G. Li, N. Liu and X. Lu, "Dynamic performance and wake structure of flapping plates with different shapes", ***Acta Mechanica Sinica***, 30(6), 800–808, 2014.

**3.** G. Li and X. Lu, "Analysis of force and power of flapping plates", ***Journal of Fluid Mechanics***, 712, 598–613, 2012.

**2.** G. Li and X. Lu, "Numerical studies on locomotion performance of fishlike tail fins", ***Journal of Hydrodynamics***, 24, 488–495, 2012.

**1.** Z. Li, G. Li, H. Huang and X. Lu. "Lattice Boltzmann study of electro-hydrodynamic drop deformation with large density ratio", ***International Journal of Modern Physics C***, 22, 729–744, 2011.

## TEACHING EXPERIENCES

- **Purdue University**

  Fluid Mechanics — Aug. 2016–Dec. 2016

## AWARDS AND HONORS

- Ward A. Lambert Graduate Teaching Fellowship — Purdue University, 2016
- Outstanding Graduate Student Teaching Awards — University of Notre Dame, 2014
- Graduate student fellowship — University of Notre Dame, 2012
- Outstanding Graduate — University of Science and Technology of China, 2009